Novel Modes of Chemokine-Driven Leukocyte Migration

Cameron Robert Bastow

B.Sc. (Mol Bio)

Department of Molecular and Cellular Biology,
School of Biological Sciences,
The University of Adelaide

August 2021

THE UNIVERSITY of ADELAIDE

Declaration

I certify that this work contains no material which has been accepted for the award of any other degree or diploma in my name, in any university or other tertiary institution and, to the best of my knowledge and belief, contains no material previously published or written by another person, except where due reference has been made in the text. In addition, I certify that no part of this work will, in the future, be used in a submission in my name, for any other degree or diploma in any university or other tertiary institution without the prior approval of the University of Adelaide and where applicable, any partner institution responsible for the joint-award of this degree.

I give permission for the digital version of my thesis to be made available on the web, via the University's digital research repository, the Library Search and also through web search engines, unless permission has been granted by the University to restrict access for a period of time.

I acknowledge the support I have received for my research through the provision of an Australian Government Research Training Program Scholarship.

Signed,

Cameron Robert Bastow, B.Sc. (Mol Bio)

August 2021

Acknowledgements

Firstly, I'd like to thank my supervisor Prof Shaun McColl. Thank you for initially piquing my interest in immunology during my second year of undergraduate studies through a tutorial on regulatory T cells. Since then, you have always encouraged me to pursue immunology, ensured there was a position for me in your laboratory and made yourself available at any time to chat. On top of this, I greatly appreciate all of the occasions you have introduced me to fellow colleagues at conferences and all of the opportunities you have given me to mix with amazing national and international immunologists outside of work. These have been valuable in my development as a scientist and given me great confidence to discuss my work and ask questions. Lastly, I thank you for your understanding, support and encouragement throughout my disrupted thesis completion. Sorry for taking so long, I maintain that it was all part of an elaborate plan to meet Paris.

I would also like to acknowledge the important contributions of my co-supervisor Dr Iain Comerford. From the time I first started working with you during a Summer Vacation Scholarship in second year undergrad, you have always been patient with your teaching and instructed meticulous scientific technique that I conduct myself with today. You also knew when to step back and entrust me with the direction of my projects so I could develop my scientific independence, and for this I am very grateful. I would also like to thank you for inviting me to assist you in peer-reviewing manuscripts for publication as these were valuable lessons in critical reading. Lastly, thank you for proofing all forms of my written work, from conference abstracts to animal ethics and this thesis. This has both improved the quality of my writing and given me great confidence in my writing ability.

Next, I would like to thank all of my collaborators that provided helpful discussions, reagents or performed experimental techniques that have contributed to my studies. Firstly, thank you to Prof Carola Garcia de Vinuesa for supplying *Rag1*$^{-/-}$(*Sh2d1a*$^{-/-}$:*Foxp3*$^{\text{DTR-GFP}}$) chimeric mice and expert insight on the germinal centre reaction and underlying germinal centre T cell responses. Thank you for finding the time for these discussions amongst your busy schedule, I greatly appreciate all of the opportunities I have had to learn from you. Thank you to Prof Scott Mueller and Dr Sapna Devi for your efforts optimising and performing live imaging experiments, and for making me feel welcome during my visit to the lab to analyse these data. Thank you to Prof Ian Frazer for your expertise and assistance in setting up our skin graft experiments, and to Ms Lynn Tolley for flying to Adelaide to demonstrate and perform the grafting surgery. Thank you to our Animal Welfare Officer Dr Denise Noonan for supplying reagents and veterinary assistance during grafting surgery. I would also like to thank Prof Peter Hoffman, Dr Mark Condina and Dr Clifford Young for organising, optimising and performing our mass spectrometry experiments. Lastly, thank you to Dr Josef Nguyen for donating his spare time to irradiate mice for our bone marrow chimera experiments.

Thank you to the lab mother, Adriana for keeping the lab running and always dropping whatever you were doing to help me scrummage the fridges for reagents. Thank you for your help optimising and performing the western blots and immunoprecipitation experiments to detect all pesky forms of CCL21. You were also unfortunate enough to sit across from Ervin and I for multiple years, so I also thank you for your tolerance.

I would like to give a special thank you to Ervin. I would not be the scientist I am today without the fiery passion for cellular immunology and hard work ethic you demonstrated and taught me. Thank you for all the discussions, arguments and pep talks we shared in the lab, your "office", and whilst cruising around in the Dean (I hear that the Bay is going off). I sorely miss our discussions and hypothesising around the white board.

I'd like to thank all iterations of the McColl lab that I have endured during my candidature. Firstly, Mark and Michelle for making me feel welcome when I first joined the lab, and particularly Mark for introducing me to microscopy. Thank you to my colleagues Duncan, Kevin, Carly and Kerrie for making the lab an enjoyable place to be, especially when experiments weren't going as planned. Some of my favourite memories have been the national ASI conferences we have attended as a group, and all the time we spent outside of work, mostly drinking. Thank you to the new kids, Jaz, Jade, Tim, Todd, Caitlin and Maleika for maintaining the social agenda we had previously established in the lab. It was hard seeing all my close friends move on, but you made the process a bit easier and it has been a pleasure to help teach you and see the great scientists you have become.

Thank you to my biggest support, Mum. Thank you for providing for me throughout my PhD, I never had to worry about home life and that allowed me to focus so much on my work. You have dropped me off and picked me up from the lab at unreasonable hours on multiple occasions without hesitation. The amount of work I have achieved would not be possible without your contributions.

Actually lastly, thank you to my amazing girlfriend Paris. Thank you for all your encouragement to push me through the thesis writing process and for celebrating all my small achievements. Love you lots.

Contents

List of Figures and Videos

List of Tables

Abbreviations

(h:mm:ss): timestamp (hours:minutes:seconds)

(v/v): volume/volume

(w/v): weight/volume

µg: micrograms

µL: microlitres

µm: micrometres

7-AAD: 7-amino-actinomycin D

7α,25-HC: 7α,25-dihydroxycholesterol

Ab: Antibody

ACKR4: Atypical chemokine receptor 4, gene name *Ackr4*. Previously known as CCX-CKR, CCR11, *Ccrl2*

AID: Activation-induced cytidine deaminase

Alum: Aluminium potassium sulphate

ANOVA: Analysis of variance

BECs: Blood endothelial cells

BM: Basement membrane

BMDCs: Bone marrow-derived dendritic cells

bp: base pairs

BSA: Bovine serum albumin

BSA-NP$_x$: Bovine serum albumin haptenated with *x* 4-hydroxy-3-nitrophenylacetyl moieties

CCL21-Leu: CCL21 with leucine in amino acid position 65. Encoded by *Ccl21b*/*Ccl21c*

CCL21-Ser: CCL21 with serine in amino acid position 65. Encoded by *Ccl21a*

cDC: Conventional dendritic cells

cDNA: Complementary DNA

CKR: Chemokine receptor

cLECs: Ceiling lymphatic endothelial cells

CSR: Class switch recombination

d: day post immunisation, e.g. d4, d6

DAPI: 4′,6-diamidino-2-phenylindole

DC: dendritic cells

DermDN: Dermal double-negative stromal cells

dLN: draining lymph node

DMEM: Dulbecco's Modified Eagle Medium

DMSO: Dimethylsulfoxide

DTR: Diphtheria toxin receptor

DTT: Dithiothreitol

DTx: Diphtheria toxin

DZ: Dark zone

EDTA: Ethylenediaminetetraacetic acid

EFPB: Extrafollicular plasmablast

EGFP: Enhanced green fluorescent protein

ELISA: Enzyme-linked immunosorbent assay

EpiDN: Epidermal double-negative stromal cells

eYFP: Enhanced yellow fluorescent protein

FACS: Fluorescence activated cell sorting

FCS: Foetal calf serum

FITC: Fluorescein isothiocyanate

fLECs: Floor lymphatic endothelial cells

FM: Follicular mantle

FRC: Fibroblastic reticular cells

G: group, e.g., G1, G2

g: grams

GAG: glycosaminoglycan

GC: Germinal centre

GCB cell: Germinal centre B cell

GCT cell: Germinal centre T cell. Includes both T_{FH} and T_{FR} cell subsets

GFP: Green fluorescent protein

Ggg: S-geranylgeranyl-L-glutathione

gMFI: geometric mean fluorescence intensity

GRK: G protein-coupled receptor kinase

HEPES: 4-(2-hydroxyethyl)-1-piperazineethanesulfonic acid

HRP: Horse radish peroxidase

i.p.: intraperitoneal

i.v.: intravenous

IE: Interfollicular epithelium

IF: Infundibulum

Ig: Immunoglobulin

IgM^+PCs: IgM^+ plasma cells

IM: Isthmus

int: Intracellular

iPBS: inhibitory PBS

IRES: Internal ribosome entry site

kDA: kilodalton

kg: kilograms

LAS: Laboratory Animal Services

LC: Langerhans cell

LC-MS: Liquid chromatography mass spectrometry

LECs: Lymphatic endothelial cells

LLPCs: Long-lived plasma cells

LN: Lymph node

LPS: Lipopolysaccharide

LV: lymphatic vessel

Ly5.1: Also known as CD45.1 and B6.SJL-$Ptprc^aPepc^b$/BoyJ mice

LZ: Light zone

m/z: mass-to-charge ratio

M: molar

MEM: Minimum Essential Media

mg: milligrams

MHC-II: Major histocompatibility complex class II

mL: millilitres

mm: millimetres

mM: millimolar

moDC: Monocyte-derived dendritic cells

MRBCLB: Mouse red blood cell lysis buffer

MRC: Marginal reticular cells

mRNA: messenger ribonucleic acid

Neu5Ac: N-acetylneuraminic acid, epitope detected by the GL7 antibody

ng: nanograms

nL: nanolitres

nm: nanometres

NP: 4-hydroxy-3-nitrophenylacetyl

NP-KLH: 4-hydroxy-3-nitrophenylacetyl keyhole limpet hemocyanin

NP-PE: 4-hydroxy-3-nitrophenylacetyl R-phycoerythrin

NS: not significant

nTreg: natural T regulatory cells. Also known as thymic T regulatory cells

OCT compound: Optimal cutting temperature compound

OD450: Optical density at 450 nanometres

PALS: periarteriolar lymphatic sheath

PBS: Phosphate buffered saline

PCs: Plasma cells

pDC: Plasmacytoid dendritic cells

PFA: Paraformaldehyde

pg: picograms

PMSF: phenylmethylsulfonyl fluoride

psi: pound per square inch

PVDF: polyvinylidene fluoride

qPCR: quantitative polymerase chain reaction

rcf: relative centrifugal force

rm: recombinant mouse

ROIs: Regions of interest

RPMI: Roswell Park Memorial Institute

s.c.: subcutaneous

SAP: SLAM associated protein (gene: *Sh2d1a*)

sCCL21: Soluble CCL21

SCS: Subcapsular sinus

SDS-PAGE: Sodium dodecyl-sulfate polyacrylamide gel electrophoresis

SED: Subepithelial dome

SEM: Standard error of mean

SHM: Somatic hypermutation

SIP: Sphingosine-1-phosphate

SIV: Simian immunodeficiency virus

SRBC: Sheep red blood cells

swPC: Isotype-switched plasma cells

TBS: Tris buffered saline

T_{FH}: T follicular helper

T_{FR}: T follicular regulatory

TLR: Toll-like receptor

TMB: 3,3',5,5'-Tetramethylbenzidine

TPA: 12-O-tetradecanoylphorbol13-acetate

Treg: T regulatory cell. Encompasses both natural/thymic and peripheral T regulatory cells

TSLP: Thymic stromal lymphopoietin

TSU: Technical Services Unit

U: units

WT: Wildtype C57Bl6/J mice

PhD Publications

Bastow CR, Bunting MD, Kara EE, McKenzie DR, Caon A, Devi S, Tolley L, Mueller SN, Frazer IH, Harvey N, Condina MR, Young C, Hoffmann P, McColl SR, Comerford I. Scavenging of soluble and immobilized CCL21 by ACKR4 regulates peripheral dendritic cell emigration. Proc Natl Acad Sci USA. 2021 Apr 27;118(17):e2025763118. doi: 10.1073/pnas.2025763118.

Kara EE, **Bastow CR**, McKenzie DR, Gregor CE, Fenix KA, Babb R, Norton TS, Zotos D, Rodda LB, Hermes JR, Bourne K, Gilchrist DS, Nibbs RJ, Alsharifi M, Vinuesa CG, Tarlinton DM, Brink R, Hill GR, Cyster JG, Comerford I, McColl SR. Atypical chemokine receptor 4 shapes activated B cell fate. J Exp Med. 2018 Mar 5;215(3):801-813. doi: 10.1084/jem.20171067. Epub 2018 Jan 31.

McKenzie DR, Kara EE, **Bastow CR**, Tyllis TS, Fenix KA, Gregor CE, Wilson JJ, Babb R, Paton JC, Kallies A, Nutt SL, Brüstle A, Mack M, Comerford I, McColl SR. IL-17-producing γδ T cells switch migratory patterns between resting and activated states. Nat Commun. 2017 Jun 5;8:15632. doi: 10.1038/ncomms15632.

Kara EE, McKenzie DR, **Bastow CR**, Gregor CE, Fenix KA, Ogunniyi AD, Paton JC, Mack M, Pombal DR, Seillet C, Dubois B, Liston A, MacDonald KPA, Belz GT, Smyth MJ, Hill GR, Comerford I, McColl SR. CCR2 defines in vivo development and homing of IL-23-driven GM-CSF-producing Th17 cells. Nat Commun. 2015 Oct 29;6:8644. doi: 10.1038/ncomms9644.

Kara EE, Comerford I, Fenix KA, **Bastow CR**, Gregor CE, McKenzie DR, McColl SR. Tailored immune responses: novel effector helper T cell subsets in protective immunity. PLoS Pathog. 2014 Feb 20;10(2):e1003905. doi: 10.1371/journal.ppat.1003905.

Kara EE, Comerford I, **Bastow CR**, Fenix KA, Litchfield W, Handel TM, McColl SR. Distinct chemokine receptor axes regulate Th9 cell trafficking to allergic and autoimmune inflammatory sites. J Immunol. 2013 Aug 1;191(3):1110-7. doi: 10.4049/jimmunol.1203089. Epub 2013 Jun 24.

PhD conference proceedings

Bastow CR, Bunting M, Devi S, Kara E, McKenzie D, Tolley L, Frazer I, Mueller S, McColl S, Comerford I. The atypical chemokine receptor ACKR4 regulates dermal chemokine bioavailability and dendritic cell egress. Oral presentation at the Australasian Society for Immunology Conference (Brisbane, QLD, 2017)

Bastow CR, Bunting M, Devi S, Kara E, McKenzie D, Tolley L, Frazer I, Mueller S, McColl S, Comerford I. The atypical chemokine receptor ACKR4 regulates dermal chemokine bioavailability and dendritic cell egress. Oral presentation at the 13th Adelaide Immunology Retreat (Nurioopta, SA, 2017)

Bastow CR, Bunting M, Devi S, Kara E, McKenzie D, Mueller S, McColl S, Comerford I. The atypical chemokine receptor ACKR4 regulates dermal chemokine bioavailability and dendritic cell egress. Poster presentation at the International Congress of Immunology (Melbourne, VIC, 2016)

Bastow CR, Bunting M, Devi S, Kara E, McKenzie D, Tolley L, Frazer I, Mueller S, McColl S, Comerford I. The atypical chemokine receptor ACKR4 regulates dermal chemokine bioavailability and dendritic cell egress. Oral presentation at the 12th Adelaide Immunology Retreat (Wirrina Cove, SA, 2016)

Abstract

The mammalian immune system is made up of highly specialised and motile cells that protect the organism against pathogen colonisation and disease arising from oncogenic or autoimmune origins. Central to effective immune responses are extensive cell-cell interactions and communication between cells at the site of immune challenge and within specialised lymphoid organs. Hence, efficient migration and organisation of immune cells within tissues mediated by the dynamic expression of chemokine signalling proteins and complementary chemokine receptors underpins host immunity. Whilst much is known regarding the function of chemokines in leukocyte trafficking, recent advances have generated many outstanding questions. For example, how chemokine gradients are regulated in peripheral tissues is unknown. Recent studies have visualised immobilised CCL21 chemokine gradients *in situ* and subsequently identified the narrow functional range within which they are maintained to facilitate dendritic cell egress from the skin. The atypical chemokine receptor ACKR4 has demonstrated CCL21 scavenging activity in lymph nodes, yet a role for ACKR4 in regulating chemokine gradients in peripheral tissues is undetermined. Additionally, delineation of T follicular helper (T_{FH}) and T follicular regulatory (T_{FR}) cells specialised in supporting and suppressing antibody responses has significantly advanced our understanding of germinal centre reactions that drive the production of high-affinity antibodies and generate humoral immune memory. Whilst the microanatomical localisation of cell populations during antibody responses has been studied, the chemotactic cues that direct T_{FH}/T_{FR} cell migration remain incompletely characterised. Given the importance of dendritic cell trafficking for initiating adaptive immune responses and the critical role of T_{FH}/T_{FR} cells in governing antibody responses, these questions have direct relevance to understanding host protection against pathogens and improving vaccination strategies. These outstanding questions are therefore of high priority and explored in detail in this thesis.

Firstly, this study has identified several critical functions of ACKR4 in regulating CCL21 and subsequent dendritic cell migration *in vivo*. ACKR4 expression was demonstrated to be crucial for regulation of soluble CCL21 abundance in all barrier tissues examined. Within steady-state skin, ACKR4 also maintained functional immobilised CCL21 gradients and limited the dissemination of solubilised CCL21 to draining lymph nodes. ACKR4 function within radio-resistant cells regulated the abundance of both forms of CCL21, with the greatest *Ackr4* expression identified in dermal papillary fibroblasts. In the absence of ACKR4, cutaneous dendritic cell homing to lymphatic vessels and draining lymph nodes was significantly impaired. This study firmly establishes ACKR4 as a key regulatory component of chemokine gradients in barrier tissues essential for initiating adaptive immune responses.

Secondly, this study has identified multiple novel chemokine receptors expressed by germinal centre T cells, of which CCR6 expression was further investigated. Expression of

CCR6 was greater in T_{FR} cells compared to T_{FH} cells, however there was no intrinsic requirement for CCR6 in T_{FR} cell differentiation. CCL20, the sole ligand for CCR6, increased in the spleen following immunisation and facilitated T_{FR} cell migration *in vitro*, yet no gross differences in splenic Treg/T_{FR} cell localisation were observed in the absence of CCR6. Together, this work broadens the understanding of how cell migratory signals are maintained *in vivo*, shaping strategies aimed to modulate immune cell migration for health and prevention of disease; and identifies novel chemokine axes implicated in T_{FR} cell biology, adding to the understanding T_{FR} cell function and how defects in the biology of these cells may underpin autoantibody-driven autoimmune diseases.

Chapter 1
Introduction

Chapter 1 – Introduction

1.1 Overview

The mammalian immune system is crucial to an organism's survival against assault from a wide range of pathogens and protection against cancerous abnormal cell growth. Divided into two arms, the innate immune system responds to conserved foreign particles or danger signals to offer immediate broad protection; and the adaptive immune system elicits high-specificity and develops long-lived memory populations that rapidly respond to subsequent threats. Central to effective immune responses are extensive cell-cell interactions and communication between cells, both at the site of immune challenge and within secondary lymphoid organs. Hence, efficient migration of immune cells and proper organisation within tissues are key to rapid immune responses upon challenge. Organisation and trafficking of immune cells is largely mediated by a family of chemokine signalling proteins and complementary chemokine receptors dynamically expressed by leukocytes. Therapeutic manipulation of chemokine cues or the mechanisms that regulate chemokine cues have application in vaccination strategies and the treatment of cancer, chronic inflammatory diseases and autoimmune diseases, thus characterising the signals that govern leukocyte migration is an active field today.

1.2 The chemokine and chemokine receptor system

Immune cell migration is directed by small secreted proteins called chemokines, and their respective seven-transmembrane chemokine receptors. Chemokines are a large family of over 50 low-molecular weight chemotactic cytokines that direct cell migration. Whilst chemokines were initially named somewhat haphazardly based upon the settings in which they were discovered, new chemokine nomenclature has since systematically grouped these proteins into 4 groups depending of the configuration of four structurally important N-terminal cysteine residues. Subsequently, chemokines are designated either as CC, CXC (where X denotes a non-conserved amino acid), CX_3C, or XC (which lack the first and third cysteine residue), then L for ligand, and numbered in chronological order of identification of the human chemokine gene within the group[1,2]. In general, chemokines are secreted into the extracellular space to establish interpretable gradients that facilitate directional cell migration. The diffusibility of chemokines varies due to differences in their inherent affinity for glycosaminoglycans (GAGs) present in the extracellular environment, which facilitate immobilisation to extracellular surfaces[3,4]. Affinity for GAGs is determined by primary amino acid sequence, but can also be modified by post-transcriptional modification or proteolysis to fine-tune chemokine activity[5–7]. Importantly, the context in which chemokines are presented in the extracellular environment, soluble or immobilised, dictates signalling outcomes through their respective chemokine receptor.

Chemokines exert their function via binding complementary seven-transmembrane G protein-coupled chemokine receptors expressed by motile cells, predominantly

leukocytes. Chemokine receptors are broadly classified based on functionality, where conventional/typical chemokine receptors facilitate cell migration through pertussis toxin-sensitive $G_{\alpha i}$ small G proteins and β-arrestin-mediated signal transduction, and atypical chemokine receptors facilitate alternate chemokine regulatory functions as they lack the G protein interactions necessary for migratory signalling. Multiple chemokines can bind the same chemokine receptor, and multiple chemokine receptors, both conventional and atypical, can bind the same chemokine. Conventional chemokine receptors are named according to the predominant class of chemokine that they bind (CC, CXC, CX_3C or XC), designated R for receptor and are numbered chronologically in order of identification[1,2]. Like chemokines, chemokine receptors can be post-transcriptionally modified to alter sensitivity to ligands[8,9]. Together, chemokines and respective conventional chemokine receptors within the immune system are broadly classified as homeostatic or inflammatory depending on their function. Homeostatic chemokines are constitutively expressed during the steady-state and are important in leukocyte development, maturation, immune surveillance, tolerance, and leukocyte compartmentalisation in lymphoid organs and peripheral tissues. In contrast, inflammatory cytokines are highly expressed following inflammation to facilitate leukocyte migration to the site of immune challenge or to lymphoid tissue niches to perpetuate immune responses. As chemokine ligand promiscuity is largely observed with inflammatory chemokines, opposed to the more restricted binding repertoires of homeostatic chemokine receptors, it is hypothesised that this apparent redundancy in the inflammatory chemokine system is likely to combat subversion of the chemokine network by pathogens[10]. Upon ligand activation of conventional chemokine receptors, responding cells assume a polarised morphology, generate filamentous actin at their leading edge and cytoskeletal retraction at the trailing end to generate propulsion[11]. To facilitate directed cell migration, chemokines are displayed in interpretable soluble or immobilised gradients. Alternatively, chemokines can also enhance random motility[12]. The manner in which a chemokine is presented determines the chemotactic behaviour of responding cells. For example, immobilised chemokine gradients promote adhesion to extracellular surfaces[7]. Therefore, depending on how a chemokine is presented, chemokine receptor activation can trigger random or directed migration to a soluble chemokine, chemokinesis and chemotaxis respectively; random or directed migration on a surface of immobilised chemokine, haptokinesis and haptotaxis respectively; or integrin-mediated cell arrest[4,7,10,12,13]. Understanding the precise combination of these migratory processes during the elicitation of immune responses remains an active field of investigation.

1.3 Atypical chemokine receptors

In contrast to conventional chemokine receptors, atypical chemokine receptors cannot trigger cell migration due to the inability to couple to G proteins necessary for activating cell motility machinery. Rather, given their ability to bind chemokines and trigger receptor internalisation, atypical chemokine receptors have described roles in scavenging ligands to regulate chemokine abundance and distribution[14]. To date, four atypical chemokine receptors designated ACKR1-4 have been characterised[15], with CCRL2/CRAMB tentatively

designated ACKR5 and G protein-coupled receptor 182 (GPR182) awaiting designation following recent identification of scavenging activity for CXCL10, CXCL12 and CXCL13[16] (Table 1.1). ACKR1 and ACKR2 bind a broad range of inflammatory CC and CXC chemokines and have a key role in the resolution of inflammatory responses and limiting excessive, pathogenic leukocyte recruitment[17–20] (Table 1.1). In addition to scavenging, vascular endothelial cell-expressed ACKR1 transports chemokines from the basal to luminal side of vasculature to recruit circulating inflammatory leukocytes[21,22], whilst ACKR2 on lymphatic endothelial cells regulates both lymphatic vessel development and function[23,24]. Alternatively, ACKR3 and ACKR4 scavenge the homeostatic chemokines CXCL12; and CCL19, CCL21 and CCL25 respectively[25–27]. Both have described roles in generating or maintaining functional gradients of their respective ligands *in vivo*. ACKR3 generates necessary CXCL12 gradients for key developmental events during embryogenesis[28], and also modulates CXCR4 activity directly through the formation of heterodimers[29]. The *in vivo* function of ACKR4 is less well characterised and discussed in greater detail below. Lastly, ACKR5 is structurally similar to other atypical chemokine receptors, however does not bind chemokines nor scavenge its ligands[30]. Rather, ACKR5 presents its chemoattractant ligand chemerin on the cell surface to increase its local concentration and attract leukocytes expressing the functional migratory receptor CMKLR1[30,31]. Thus together, the atypical chemokine receptor family sculpts cell migration via chemokine ligand scavenging during both steady-state and inflammatory scenarios.

1.4 Outstanding questions in chemokine biology

Whilst much is already known about the function of chemokines in facilitating leukocyte trafficking, recent advances have generated many outstanding questions. One important question regards how chemokine gradients form and are maintained *in vivo*. Progress towards understanding this has come from studies of the chemokine CCL21, a ligand of both CCR7 and ACKR4. Recent studies have visualised and quantified immobilised CCL21 chemokine gradients *in situ*, and subsequently the narrow functional range within which they are maintained to facilitate dendritic cell egress from barrier tissues was identified[4,13]. How such immobilised gradients are regulated in peripheral tissues where CCL21 is constitutively expressed is unknown. Furthermore, multiple studies have identified additional post-transcriptional modulation of CCL21 activity via proteolytic cleavage, yet the importance of this modification *in vivo* remains uncharacterised[7,8,13,32–34]. Secondly, significant advances in the understanding of germinal centre responses have been achieved over the last decade following the delineation of distinct lineages of $CD4^+$ T cells specialised in supporting or suppressing antibody responses[35–44]. Subsequently, the inherent migratory events that facilitate T and B cell interactions underpinning the generation of antibody responses have been intensively studied. Whilst the microanatomical localisation of participating cell populations in antibody responses have been identified in multiple secondary lymphoid organs, the chemotactic cues that direct this migration remain incompletely characterised, particularly for germinal centre T (GCT) cell subsets. Given the importance of both CCR7-dependent peripheral dendritic cell trafficking in initiating adaptive immune responses and

subsequent antibody responses in host protection against invading pathogens and current vaccination strategies, these two outstanding questions are of high priority. The remainder of this introduction will outline the relevant biology of dendritic cell migration and the germinal centre response.

1.5 Dendritic cells

An appreciation for haptotactic chemokine gradients was first identified for dendritic cell trafficking from the skin[4], yet how these gradients are maintained remains unknown. Dendritic cells are a heterogenous population of innate immune cells that specialise in the uptake and presentation of foreign and self-antigen to T cells. Being at the interface of innate and adaptive immunity, dendritic cells play an essential role in tolerance and immune activation by trafficking antigen from peripheral sites to secondary lymphoid organs. Different dendritic cell subsets are defined by their ontogeny and are identified by surface phenotype, master transcription factor and/or anatomical location. Subsets differ in developmental origin, anatomical location, migratory and antigen presentation capacity, and broader function during immunological challenge. Accordingly, dendritic cells are now classified into the following subsets. First, conventional dendritic cells (cDCs) are the prototypical antigen presenting cell and excel in antigen capture and display for efficient naïve T cell activation or tolerogenic suppression[45]. cDCs are further divided based on their ability to prime CD8 cytotoxic T cells or CD4 T-helper responses effectively, cDC1 and cDC2 subsets respectively, and whether they are tissue-resident or migrate to lymphoid organs[45]. Alternatively, plasmacytoid dendritic cells (pDCs) have relatively poor antigen presentation capability, but are recognised for their ability to rapidly and robustly secrete type-1 interferon upon activation by viral products[46]. More recently, non-inflammatory functions of pDCs have been identified in thymocyte selection[47] and oral tolerance[48,49]. Monocyte-derived dendritic cells (moDCs) are generated in inflamed tissues from infiltrating monocytes and support local effector T cell responses[50]. Lastly, Langerhans cells reside in the epithelial layer of most barrier tissues and resemble a combination of tissue-resident macrophages and migratory dendritic cells[51]. They have demonstrated both immunogenic and tolerogenic functions depending on the immunological context[51]. The precise functions, developmental pathway and markers of each dendritic cell subset are outside of the scope of this thesis and reviewed elsewhere[45,46,50–52]. Additionally, dendritic cells are also described in terms of their level of activation/maturation. After lineage differentiation, immature dendritic cells reside in peripheral tissues and display high antigen uptake capacity, low surface peptide-MHC and costimulatory receptor expression. Upon encountering inflammatory stimuli, dendritic cells undergo a process of maturation where endocytic pathways are downregulated, and robust peptide-MHC is displayed on the cell surface with upregulated costimulatory molecules necessary for T cell activation[53]. Alternatively, maturation of dendritic cells in the absence of inflammatory stimuli occurs during the steady-state and has roles in peripheral T cell tolerance[54,55]. Whilst the signals that regulate this phenomenon *in vivo* remain incompletely characterised, inflammation-independent maturation of tolerogenic dendritic cells has been observed *in vitro* following

ligation of surface receptor TREM-2[56], activation with TSLP[57], and blocking E-cadherin interactions[58]. Coinciding with dendritic cell maturation is a drastic switch in migratory phenotype from tissue-tropic to lymphoid-homing chemokine receptor expression to facilitate homing to secondary lymphoid organs[59,60].

1.6 Chemokine receptor mediated dendritic cell egress

Dendritic cell egress from peripheral tissues to draining lymph nodes via the afferent lymphatics is facilitated by the chemokine receptor CCR7[55,61–66], which recognises the homeostatic chemokines CCL19 and CCL21. Immature dendritic cells do not express CCR7, however expression is rapidly upregulated upon activation[59,60,67]. Studies with CCR7-deficient mice have demonstrated the requirement for this chemokine receptor in the emigration of dendritic cells from a number of barrier tissues including the small intestine[63-65], skin[55,61,62] and lung[66]. Subsequently, *Ccr7*$^{-/-}$ mice display perturbed adaptive immune responses to inflammation[55,61,63], and impaired tolerogenic responses in the steady-state[55,64,66]. The contributions of CCR7 in the emigration of dendritic cells are best characterised in the skin as this is the tissue most amenable to live imaging. The role of CCR7 in cutaneous dendritic cell emigration is depicted in Figure 1.1. In the skin, CCL21 is constitutively produced by dermal lymphatic endothelial cells (LECs) and secreted into the extracellular environment[4,68,69]. The unique elongated C-terminal tail of CCL21, which contains extensive positively-charged amino acids, facilitates immobilisation to extracellular surfaces via interactions with negatively charged GAGs, particularly heparan sulfate moieties, which are littered throughout the interstitial space[4,7,70]. By diffusion and not the localisation of ligand binding sites, LEC-derived CCL21 forms immobilised gradients in the extracellular space orientated in increasing concentration towards lymphatic vessels[4]. These immobilised gradients are essential to guide CCR7-dependent migration of dendritic cells towards lymphatic vessels as their disruption *ex vivo* with heparinase blocks homing of dendritic cells to lymphatic vessels[4]. Similarly, saturation of cutaneous CCL21 abundance via transgenic overexpression of CCL21 *in vivo*, or ectopic addition of full-length CCL21 *ex vivo* impairs dendritic cell egress and lymphatic homing[4,71]. In addition to the immediate function of guiding dermal dendritic cells towards lymphatic vessels, CCR7 further contributes in multiple migratory events that underly migration of peripheral dendritic cells to the lymph node (as shown in Figure 1.1). Dendritic cells enter dermal lymphatic capillaries through preformed portals in the discontinuous basement membrane lining these vessels, then enter the lymphatic lumen through specialised button junctions[72,73]. Intracellular reserves of CCL21 concentrated within lymphatic endothelium adjacent to basement membrane portals are then secreted locally upon dendritic cell contact to facilitate transmigration[74,75] (Figure 1.1). As CCL21 is essential for initial homing to lymphatic vessels, it has been difficult to determine the function of CCL21 at the lymphatic vessel surface *in vivo* using *Ccr7*$^{-/-}$ dendritic cells or neutralising CCL21 antibodies. However, it is hypothesised that at this site, local CCL21 may direct dendritic cells to preformed portals in the discontinuous basement membrane, facilitate adhesion to the lymphatic endothelium, and/or propel dendritic cells into vessels to physically open button junctions[74,75]. Within the

lymphatic capillary lumen, immobilised CCL21 gradients generated by lymph flow direct dendritic cell migration downstream in the direction of draining lymph nodes[76]. However, upon reaching larger lymphatic collecting vessels downstream, dendritic cell emigration to the lymph nodes becomes passive as the increased lymph flow in these vessels is sufficient to propel cells[74,76,77]. Upon reaching the draining lymph node via the afferent lymphatics, dendritic cells are retained in the lymph node subcapsular sinus (SCS). This compartment is comprised of cells and fibres and acts as a physical barrier to arrest incoming cells based on their size[78]. Migration of dendritic cells out of the SCS and into the T-zone/paracortex is also facilitated by CCR7[79]. Here, immobilised gradients of CCL21 within the interfollicular regions underlying the SCS are proposed to mediate dendritic cell migration out of the SCS[80] (Figure 1.1).

Additional conventional chemokine receptors have supplementary, context-dependent functions in dendritic cell egress following inflammation. Epidermal Langerhans cells utilise CXCR4 following inflammation to exit the epidermis and migrate towards CXCL12 induced in dermal stromal cells[81,82]. Antagonism of CXCL12 *in vivo* resulted in a modest reduction in cutaneous dendritic cell accumulation in draining lymph nodes following skin hypersensitisation[81,82]. Inflammation also induces LEC basolateral secretion of soluble CX3CL1, which attracts emigrating dendritic cells via CX3CR1[83]. Observations *in vitro* support a function for basolateral-restricted CX3CL1 expression in facilitating transmigration across lymphatic endothelium, and loss of CX3CL1 *in vivo* resulted in significantly delayed arrival of cutaneous dendritic cells in the draining lymph node following skin hypersensitisation[83]. Other chemokines have also demonstrated CCR7/CCL21-dependent synergistic functions. Cutaneous allergen responses induce CCL8 expression in SCS macrophages that were required for dendritic cell egress from the SCS[84]. Here, CCL8-CCR8 engagement augmented CCL21-CCR7 chemotaxis rather than facilitating SCS egress itself[84]. Hence it was proposed that this mechanism may assist migrating dendritic cells that express low levels of CCR7 during allergen responses[84]. A similar mechanism was described for cutaneous CCL17 induced upon inflammation. Here, autocrine CCL17 augmented both CXCR4 and CCR7 mediated chemotaxis of dendritic cells in the skin, however, this effect was independent of the CCL17 receptor CCR4 on emigrating dendritic cells[85]. As dendritic cell tissue egress is often studied in the context of inflammation, it remains incompletely understood whether these additional chemokine axes also function during the steady-state in tolerogenic responses.

1.7 Contribution of CCR7 ligands to dendritic cell egress

Whilst CCR7 is essential for the migratory events that underpin dendritic cell egress from tissues, both CCR7 ligands CCL19 and CCL21 do not contribute equally to this process. During the steady-state, both CCL21 and CCL19 are highly expressed in the thymus and secondary lymphoid tissues[86–89], however CCL21 is also expressed in peripheral tissues during the steady-state[90–93]. In mice, tissue-tropic expression of CCL21 is established by

three genes that encode two functionally-identical isoforms of CCL21 differing by one amino acid in position 65[94,95]. Lymphoid CCL21-Serine (CCL21-Ser) production is driven by *Ccl21a* expression, whilst CCL21-Leucine (CCL21-Leu) is encoded by *Ccl21b*/*Ccl21c* expression in peripheral tissues[94,95]. Whilst low levels of CCL19 expression have been identified in the small intestine, colon, trachea, appendix and lung[86,96], the function of CCL19 outside of lymphoid tissues is poorly understood. Rather, CCL19 expression is induced in dendritic cells[97,98] and non-haematopoietic cells[96,99–101] by inflammation. In addition to distinct expression patterns, differences in the structure and biology of CCL19 and CCL21 induce unique signalling outcomes on CCR7 (Figure 1.2). Within the extracellular space, CCL21 tethers to GAGs via its unique charged C-terminal tail, whilst CCL19 remains soluble. Subsequently, immobilised CCL21 can trigger cell adhesion and haptotaxis in a β_2 integrin-dependent manner, whilst soluble CCL19 facilitates chemotactic responses[7]. Although CCL19 is approximately 100-fold less abundant than CCL21 in lymphoid tissues bar the spleen[102,103], CCL19 is 10-100-fold more potent than CCL21 in triggering CCR7-dependent chemotaxis[7,33,104]. Upon activation, chemokine receptors are phosphorylated by G protein-coupled receptor kinases (GRKs) to recruit β-arrestins that subsequently facilitate receptor desensitisation and internalisation. Both CCL19 and CCL21 trigger GRK6 mediated phosphorylation of CCR7, but additional phosphorylation is triggered by CCL19 through GRK3[105]. This results in robust β-arrestin recruitment and triggers CCR7 internalisation and desensitisation unique to CCL19 binding[106] (Figure 1.2). However, despite tailored signalling of CCL19 and CCL21 through CCR7, studies with *Ccl19*$^{-/-}$ mice have not found a role for CCL19 in steady-state dendritic cell egress from the skin or lungs[101,107]. Additionally, full-length CCL21 can also be post-translationally cleaved to remove the highly charged C-terminal tail to yield solubilised CCL21[7,32]. Given the differences in signalling between full-length and cleaved soluble CCL21[7–9,33], the latter is considered a pseudo third ligand of CCR7 (Figure 1.2). In addition to mediating immobilisation on GAGs, the elongated C-terminal tail of full-length CCL21 also participates in weak interactions with the chemokine domain resulting in the adoption of an autoinhibitory conformation[9,33]. Thus, upon proteolytic cleavage, soluble CCL21 displays enhanced chemotactic potency like CCL19[33]. However, compared to full-length CCL21, migration triggered by soluble CCL21 is less persistent[8]. Despite similarities to CCL19 in chemotactic potency, soluble CCL21 induces limited β-arrestin recruitment to CCR7, thus does not induce CCR7 receptor desensitisation[8,33]. CCL21 is cleaved *in vitro* by plasmin and activated dendritic cells via an uncharacterised serine protease, and solubilised CCL21 has been detected in lymph nodes following inflammation *in vivo*[7,32]. However, the precise contribution of soluble CCL21 in dendritic cell egress remains uncharacterised.

Regardless of the role of soluble CCL21, the contribution of immobilised CCL21 gradients have been demonstrated by studies with mice deficient in key signalling molecules that distinguish between the activity of full-length and cleaved CCL21. In addition to proteolytic cleavage, autoinhibitory conformations adopted by full-length CCL21 can also be uncoupled by interactions between sialic acid moieties and the charged C-terminal tail of CCL21[9]. These interactions promote full-length CCL21 to adopt an active conformation CCL21

similar to soluble CCL21, but without chemokine cleavage and solubilisation[9]. Interestingly, the sialyltransferase ST8SIA4 is upregulated in during the maturation of bone marrow-derived dendritic cells (BMDCs) and subsequently polysialylates multiple dendritic cell proteins including CCR7[9,108]. Mature migratory dendritic cells within steady-state lymph nodes also have detectable surface polysialylation that is further enhanced under inflammatory conditions[9]. *In vitro*, ST8SIA4-deficient BMDCs cannot migrate to full-length CCL21, however maintain normal sensitivity to soluble CCL21 and CCL19[9]. Dendritic cell egress from the skin is impaired in *St8sia4*$^{-/-}$ mice during both the steady-state and following inflammation[9]. Subsequently, the transfer of *St8sia4*$^{-/-}$ BMDCs *in vivo* demonstrated that intradermal homing to lymphatic vessels required polysialylation-mediated detection of full-length CCL21[9]. Conversely, injection of *St8sia4*$^{-/-}$ BMDCs into larger collector lymphatic vessels did not impair migration from the SCS to the paracortex, suggesting that immobilised CCL21 is not essential in SCS exit[9]. These observations are supported by similar studies with *Grk6*$^{-/-}$ mice. GRK6 is activated downstream of both CCL19 and full-length CCL21 ligation of CCR7, however it is only essential for CCR7 phosphorylation and signal termination downstream of full-length CCL21[13,105]. *In vitro*, GKR6 is dispensable for chemotaxis to soluble CCL21 and CCL19, but is required for haptotactic migration to immobilised CCL21[13]. In ear crawl in assays, fewer *Grk6*$^{-/-}$ BMDCs entered ear sheets, and entrance of BMDCs into the dermis was aligned with lymphatic vessels where immobilised CCL21 concentration was the greatest[13]. Experiments have not been performed to determine whether *Gkr6*$^{-/-}$ BMDCs can enter the lymphatic vessels *in vivo*, however like *St8sia4*$^{-/-}$ BMDCs, they are capable of migrating in the lymph node following afferent lymphatic vessel injection[13]. Therefore, despite immobilised gradients of CCL21 being identified in the lymph node interfollicular region[80], studies of *St8sia*$^{-/-}$ and *Grk6*$^{-/-}$ dendritic cells suggest that these immobilised gradients may be redundant in lymph node entry given the soluble CCL19 and CCL21 also present in lymph nodes.

1.8 Regulation of CCR7 ligands by ACKR4

Whilst the importance of CCR7 ligands in the egress of dendritic cells has been widely reported, few studies have investigated how these ligands are regulated in this context. Importantly, regulation of CCR7 ligands is critical as models of *in vivo* and *ex vivo* CCL21 overexpression have highlighted significant dendritic cell migration defects[4,71] and CCR7 responsiveness can be regulated by CCL19-mediated receptor occupancy and internalisation[109]. Here, the function of atypical chemokine receptors has been of great interest given their described roles in scavenging chemokine ligands. The atypical chemokine receptor ACKR4 (formally known as CCX-CKR and CCRL1) binds the homeostatic CCR7 ligands CCL19 and CCL21, and the CCR9 ligand CCL25[26,27]. During the preparation of this thesis, two additional ACKR4 ligands in CCL20[110,111] and human CCL22[111] were also identified. These reports challenge initial studies characterising ACKR4 ligands[26,27,112] and whether ACKR4 regulates these chemokines *in vivo* remains unknown. Unlike conventional chemokine receptors, ACKR4 does not activate signal transduction pathways involving Erk1/Akt or Src kinases, nor induce calcium flux or cell migration upon

ligand binding[27,112–114]. Rather, ligand binding triggers rapid internalisation and endocytic trafficking of both CCL19 and CCL21 mediated by dynamin and caveolae[115,116] (Figure 1.2). The resulting effect is rapid scavenging of ligands without desensitisation of the receptor[112,115,116]. Through this process, ACKR4 has also demonstrated the ability to generate functional chemokine gradients *in vitro* from homogenous extracellular chemokine when ACKR4 expression was polarised to one side of a chemotaxis chamber[80]. Like CCR7, cleaved CCL21 is a more potent ligand for ACKR4 than full-length CCL21 by means of β-arrestin1 recruitment[34]. Whilst the *in vitro* scavenging activity of ACKR4 has been readily reproduced, its contribution to regulating ligand abundance *in vivo* is widely debated. Expression of *Ackr4* was first identified in multiple lymphoid and non-lymphoid tissues, and haematopoietic cells by northern blot[26,27]. Subsequent generation of an *Ackr4*^{EGFP} reporter mouse strain validated expression in murine skin, lymph nodes, small intestine and thymus, but refuted extensive haematopoietic expression[112]. ACKR4 expression has since been characterised in ceiling LECs (cLECs) within the lymph node SCS[80]; distinct populations of thymic epithelial cells in the cortex, subcapsular zone and cortico-medullary junction[117]; and most recently, keratinocytes and minor populations of LECs and haematopoietic cells in the skin[100]; submucosal fibroblasts in the small intestine[118]; germinal centre B cells[119–121]; tumour-associated fibroblasts[122]; and cardiac fibroblasts[123].

Initial studies with ACKR4-deficient mice identified aberrant dendritic cell trafficking from the skin during the steady-state[112], thus multiple studies have investigated the function of ACKR4 in regulating dendritic cell trafficking. Our laboratory originally identified aberrant accumulation of CCL21 in the sera and lymph nodes of *Ackr4*$^{-/-}$ mice[102], however this was refuted in a later study by Ulvmar *et al.* where no differences in CCL21 levels in the lymph node were observed[80]. Rather, the study by Ulvmar *et al.* identified ACKR4 expression in lymph node cLECs lining the SCS, disrupted immobilised CCL21 gradients within lymph node interfollicular zones, and impaired migration of dendritic cells out of the SCS of *Ackr4*$^{-/-}$ mice[80]. Thus, ACKR4 expression by cLECs was implicated in sequestering parenchymal CCL21 within the interfollicular regions to construct gradients orientated towards the lymph node paracortex essential for dendritic cell migration from the SCS to the T cell zone. During this PhD project, Bryce *et al.* validated decreased dermal and epidermal dendritic cell subsets in the draining lymph node of *Ackr4*$^{-/-}$ mice during the steady-state and reported a similar defect following cutaneous inflammation[100]. This study identified no difference in steady-state cutaneous CCL21 or CCL19 abundance, however after inflammation, both CCL21 and CCL19 were hyperabundant in *Ackr4*$^{-/-}$ skin[100]. Utilising *Ackr4*$^{-/-}$*Ccl19*$^{-/-}$ mice, Bryce *et al.* demonstrated that defects in homeostatic dendritic cell egress from *Ackr4*$^{-/-}$ skin were independent of CCL19, and perturbed egress following inflammation in *Ackr4*$^{-/-}$ mice was rescued by compound CCL19-deficiency[100]. Cutaneous ACKR4 was subsequently attributed the role of regulating CCL19 induced during inflammation to maintain efficient dendritic cell egress, however the mechanism of ACKR4 in regulating dendritic cell steady-state egress was not determined. Conversely, a study by Thomson *et al.* identified no effect of ACKR4-deficiency on dendritic cell trafficking from the small intestine to the mesenteric lymph node during the steady-state or following

intraperitoneal (i.p.) administration of TLR7/8 agonist R848[118]. Similarly, CCR9-dependent plasmacytoid dendritic cell gut homing was intact in *Ackr4*$^{-/-}$ mice, suggesting no function of ACKR4 in regulating constitutive CCL25 expression in the gut[118]. However, quantitation of intestinal CCL21, CCL19 and CCL25 was not performed in this study. Contrary to these observations, our laboratory recently identified profound effects of ACKR4-deficiency within mammary tissue in a mouse model of breast cancer[122]. Loss of ACKR4 resulted in a significant accumulation of CCL21 and dendritic cells, resulting in a greater influx of cytotoxic T cells that restricted cancer growth[122]. These observations were dependent on CCL21 hyperabundance as they were reproduced by injection of ectopic CCL21 into the mammary pad of wildtype animals and abrogated by neutralisation of CCL21 in *Ackr4*$^{-/-}$ mice[122].

1.9 Summary- Peripheral ACKR4 function

Several important questions remain unanswered or contested regarding the function of ACKR4 in regulating CCR7-ligand abundance and distribution *in vivo*. Whilst the importance of the CCR7-CCL21 chemokine axis in governing dendritic cell egress from peripheral tissues is well documented, the role of peripheral ACKR4 expression in regulating ligand abundance *in vivo* remains controversial. Importantly, as ACKR4 has been demonstrated to regulate immobilised CCL21 gradients in the lymph node interfollicular zones, whether ACKR4 performs a similar role in regulating peripheral haptotactic CCL21 gradients necessary for dendritic cell egress is unknown. Here, comprehensively characterising the cell populations that express ACKR4 would assist in understanding the mechanisms by which ACKR4 may regulate chemokine abundance in peripheral tissues. Through deciphering the contributions of ACKR4 in CCR7-dependent migration, the mechanisms by which ACKR4-deficiency perturbs steady-state cutaneous dendritic cell emigration can be determined.

1.10 The function of chemokine receptors in GCT cell biology

Unlike the inter-tissue dendritic cell trafficking events that precede adaptive immune system activation, the precise migratory events that establish germinal centre responses elicited by the adaptive immune system within secondary lymphoid organs are regulated by multiple chemokine axes and chemotactic lipid mediators. The germinal centre is a dynamic lymphoid niche within secondary lymphoid organs that supports immunoglobulin gene mutagenesis in antigen-specific B cells and subsequent selection of B cell clones with increased affinity for antigen. Ultimately, the germinal centre response generates antigen-specific B cells with increased affinity for the antigen and generates long-term immunity to the pathogen through the formation of memory T- and B cell subsets and long-lived antibody-secreting plasma cells (LLPCs). Thus, the germinal centre reaction underpins both current vaccination strategies and host protection against invading pathogens, and when perturbed, can contribute to the pathogenesis of lymphomas[124] or a number of antibody-mediated autoimmune diseases[125]. Importantly, the success of the germinal centre rests on

highly coordinated interactions between germinal centre B cells (GCB cells) and T follicular helper cells (T_{FH} cells), whilst governance of this process is performed by T follicular regulatory cells (T_{FR} cells) to limit the generation of autoantibodies. Thus, characterising the dynamic shifts in chemotactic cues underpinning germinal centre responses will assist in understanding this process and offer new targets for therapeutic manipulation when antibody responses go awry.

1.11 T follicular helper cells

The requirement of T cells for sufficient B cell antibody production was first recognised following classical transfer experiments where the co-transfer of both thymus- and bone marrow-derived cells into immunodeficient mice was essential for robust antibody responses against protein antigen[126,127]. Since this observation, a distinct subset of $CD4^+$ T cells termed T_{FH} cells have been defined by expression of the master transcription factor Bcl6 and chemokine receptor CXCR5 necessary for their germinal centre localisation[35–41]. Bcl6 is a transcriptional repressor that is both necessary and sufficient to drive T_{FH} differentiation through antagonising expression of the master transcription regulators T-bet, GATA-3 and RORγt which drive T_H-1, T_H-2 and T_H-17 differentiation respectively, and repressing the antagonistic effector T cell transcription factor Blimp-1 and several miRNA clusters which down-regulate key T_{FH} molecules[38–40,128]. The T_{FH} cell development program is also characterised by repeated antigen exposure necessary to maintain Bcl6 expression[129]. Programming of T_{FH} cells is initiated by dendritic cells in the T cell zone and favours $CD4^+$ T cells with the greatest affinity for peptide-MHC-II[130]. The precise signals and additional transcription factors that drive T_{FH} differentiation at this stage are outside the scope of this thesis and reviewed elsewhere[131]. Notably, Bcl6 expression induced by dendritic cell priming is transient and insufficient to maintain the T_{FH} program, thus essential secondary antigen-specific activation is provided by activated cognate B cells at the T-B border[129,132-134]. Long-lasting motile interactions with cognate B cells facilitated through homotypic binding of SLAM family member adhesion molecules and intracellular SLAM-associated protein (SAP) signalling induce sufficient Bcl6 expression to maintain the T_{FH} population for the duration of the germinal centre response[135–137]. Additionally, interactions between B cell-expressed ICOSL and T_{FH} cell-expressed ICOS induces expression of the transcription factor c-maf required for optimal T_{FH} differentiation and expression of the cytokines IL-4, IL-21 and IL-10 crucial for B cell antibody responses[138-140].

T_{FH} cells are essential to support the formation antibody responses by i) instructing cognate antigen-activated B cells to undergo class-switch recombination (CSR) and seed the germinal centre, ii) providing selective survival signals to GCB cells with the greatest affinity for antigen following random immunoglobulin diversification, and iii) instructing the differentiation of high-affinity GCB cells into memory B cells and LLPCs. These processes are regulated by multiple cytokines and contact-dependent signalling receptors. Whilst high Bcl6 expression drives the expression of a distinct T_{FH}-polarised transcriptome,

early differentiating T_{FH} cells with low Bcl6 expression exhibit greater plasticity and express intermediate patterns of T_{FH}, T_H-1, T_H-2, T_H-17 and T regulatory (Treg) cell related genes[41]. Notably, T_{FH} cells are capable of expressing a variety of cytokines tailored to the nature of the pathogen, including IFN-γ[41,141,142], IL-4[41,137,141–143], IL-5 and IL-13[144], IL-17[138,145] and IL-10[142]. For example, infection with helminth *Nippostrongylus brasiliensis* resulted in an expansion of IL-4-producing T_{FH} cells, a population demonstrated to promote IgG1 isotype-switching in cognate B cells required to limit parasite fecundity and provide protective immunity[141,146]. Thus, through a broad cytokine palette, T_{FH} cells tailor CSR events in cognate B cells to select heavy immunoglobulin chains with biological properties suited to the nature of pathogen and site of infection[141]. Unique to the germinal centre reaction is the process of somatic hypermutation (SHM), whereby GCB cells rapidly divide and incorporate random point mutations enriched within immunoglobulin hypervariable genes targeted by the enzyme activation-induced cytidine deaminase (AID) to diversify their affinity for antigen[147,148]. Whilst this process is central to establishing competition between GCB cell clones for limited T_{FH} help ensuring selection of the highest-affinity clones, it also poses significant risks in the unintended generation of autoreactive antibodies[125,149,150] or oncogenic mutations leading to lymphoma[124,151]. For this reason, GCB cells are inherently highly apoptotic and die by default from deleterious off-target mutations or unfavourable immunoglobulin mutations that reduce antigen binding, uptake and subsequent presentation on MHC-II. This pro-apoptotic cell program is induced in GCB cells by the signature T_{FH} cell cytokine IL-21 which induces GCB cell Bcl6 expression necessary for upregulating pro-apoptotic mediators, tolerance to DNA-mutagenesis and repression of the master transcription factor Blimp-1 which drives plasma cell differentiation[152–160]. Conversely, GCB cell survival is mediated through a combination of T_{FH} cell-delivered IL-4 and contact-dependent CD40L ligation of GCB cell CD40 which induces expression of the anti-apoptotic factor Bcl-XL and rescues cells from apoptosis[161,162]. Critically, competition for T_{FH} cell interaction and survival signalling drives high-affinity GCB cell selection and differentiation[163], thus the number of T_{FH} cells must be limited to establish a basis for competition. Here, T_{FH} cell PD-1 expression assists in limiting the expansion of the T_{FH} cell population and ensures correct T_{FH} cell positioning in the germinal centre[164–166]. Lastly, T_{FH} cells deliver differentiation signals to high-affinity GCB cells, where IL-21 or IL-10 signalling in the absence of CD40 ligation drives LLPC differentiation through the upregulation of Blimp-1[167–169], and IL-9 signalling drives memory GCB cell formation through STAT1[170]. Similarly, memory T_{FH} cells form following the collapse of the germinal centre response, however the signals that drive this process remain poorly characterised. Additionally, populations of T_{FH} cells may exit lymphoid tissues and enter the circulation, or develop in ectopic lymphoid structures in chronically inflamed tissues. T_{FH} cells in these situations are outside of the scope of this thesis, but have been extensively reviewed[125,131].

1.12 Early migratory events following antigen exposure

Multiple migratory events orchestrate the germinal centre response, delivering cells to the correct lymphoid niches to facilitate cognate cellular interactions and support their full

differentiation, selection and survival (depicted in Figure 1.3 and 1.4). Within lymphoid tissues, naïve T cells and B cells are segregated into the T-zone and B cell follicles respectively, by distinct chemokines expressed by the underlying stromal cells. Naïve T cell expression of CCR7 facilitates localisation to T-zones via CCL19/CCL21 expressed by the network of fibroblastic reticular cells (FRCs) in this location[87]. Alternately, B cell localisation to follicles is driven by CXCR5 expression and CXCL13 production by FRCs and marginal reticular cells (MRCs)[171]. During the early stages of the humoral immune response, antigen-specific T and B cells rapidly overcome segregation by reversing this pattern of chemokine receptor expression to colocalise at the interface of the T and B cell zones (Figure 1.3). Specifically, antigen encounter by B cells in the follicle rapidly upregulates CCR7 expression which drives relocation to the T-B border[172,173]. Additionally, activated B cells upregulate the G protein-coupled receptor EBI2[174–176] which recognises the chemoattractant oxysterol 7α,25-dihydroxycholesterol (7α,25-HC)[177,178]. Whilst 7α,25-HC distribution has not been measured directly, expression of the enzymes that generate this oxysterol are enriched in the outer-follicle, thus it is inferred that 7α,25-HC is most abundant at the follicle perimeter and reduced in the follicle centre[179]. Accordingly, upregulated EBI2 uniformly distributes activated B cells along the T-B border and prevents penetration into the T-zone[175,176] (Figure 1.3). Early activated B cells also transiently upregulate CCR6[180-183]. In Peyer's patches, CCR6 facilitates relocation of antigen-specific B cells to the subepithelial dome (SED) for crucial interactions with dendritic cells that drive antibody isotype-switching to IgA[184]. However, the function of early CCR6 upregulation by B cells during antibody responses in other lymphoid tissues remains unknown. Concurrently, dendritic cell priming of antigen-specific T cells towards a T_{FH} differentiation pathway induces CXCR5 and EBI2 expression necessary for relocation to the T-B border[185–187] (Figure 1.3). Additionally, T-zone retention signals may be further relieved by Bcl6-mediated repression of the constitutively-expressed T cell adhesion ligand PSGL-1[188], which is capable of binding CCR7 ligands and enhancing CCR7-mediated chemotaxis[189].

1.13 Cell interactions at the T-B border and B cell differentiation trifurcation

At the T-B border, early-T_{FH} cells form long-lived mobile conjugates with cognate antigen-specific B cells to gain signals necessary for commitment to the T_{FH} differentiation program[132–134,173,190]. In turn, T_{FH} cells trigger cognate B cell expansion, immunoglobulin CSR, and direct the differentiation B cells into an early memory, transient extrafollicular plasmablast (EFPB), or germinal centre lineage (Figure 1.3). Cognate B cells undergo a brief population expansion at the T-B border or may relocate to the interfollicular areas for a proliferative burst and further interactions with cognate T_{FH} cells[132,191,192]. However, the significance of relocation to the interfollicular zone and the signals that promote this remain incompletely characterised. Our laboratory has demonstrated a role for intrinsic B cell ACKR4 function to fine-tune sensitivity to CCR7 ligands and regulate migration to the interfollicular areas[120]. In competitive models, activated B cells from ACKR4-deficient mice outcompete wildtype B cells and proliferate to preferentially seed both the EFPB and GCB cell compartments[120]. During these extensive cell interactions, cytokines secreted by T_{FH}

cells in conjugates stimulate CSR within cognate B cells to produce a range of isotype-switched antibodies with distinct biological functions tailored to the nature of the pathogen[141]. Whilst it was long considered that CSR occurred within the germinal centre, it was recently demonstrated that it occurs prior to fate decisions that instruct the entry of activated B cells into the germinal centre or EFPB compartment[193]. Whilst the anatomical niche that CSR occurs within was not determined in that study, it is likely this process occurs at the T-B border or within interfollicular areas. Lastly, T_{FH} cells license the trifurcation of activated B cell differentiation down one of three lineages. By an unknown mechanism, a small population of cognate B cells with unaltered germline-encoded specificity return to the circulation as early memory B cells, increasing the pool of naïve B cells with specificity for the antigen[194]. Return to the circulation by early memory B cells is believed to be facilitated by the acquisition of a $CXCR5^{+}CCR7^{-}$ naïve B cell migratory phenotype[194,195] (Figure 1.3). Alternatively, activated B cells may be instructed to differentiate into a transient population of EFPBs which secrete an immediate source of protective, relatively low-affinity antibodies[196]. B cells destined for this fate may first relocate to the outer-follicle by maintained EBI2 expression and downregulated CCR7 to undergo proliferation[132] (Figure 1.3). Ultimately, EFPBs upregulate CXCR4 which facilitates migration to the medullary cords in the lymph nodes or splenic junction zones[197,198] (Figure 1.3). Lastly, cognate B cells selected for affinity maturation relocate to the follicle centre to seed the germinal centre.

1.14 Germinal centre organisation

Entry of activated B cells to the nascent germinal centre is mediated by down-regulation of CCR7 and EBI2, and retained expression of CXCR5[198,199]. Importantly, down-regulation of EBI2 enables B cells to congregate in the centre of the follicles to initiate germinal centre formation[174,198] (Figure 1.3). GCB cells are further confined within the germinal centre boundary by the expression of two lipid-sensing G protein-coupled receptors, S1PR2[200] and P2YR8[201,202] that inhibit cell migration upon binding their ligands sphingosine-1-phosphate (SIP)[200] and S-geranylgeranyl-L-glutathione (Ggg)[203], respectively. Like EBI2 ligand 7α,25-HC, these lipid metabolites are limited in the follicle centre and present in the greatest concentration in the outer-follicle, thus restrict escape of GCB cells into the outer-follicle[200–204] (Figure 1.4). The germinal centre is further compartmentalised by the polar expression of two chemokine axes, CXCR5 and CXCL13 in the light zone, and CXCR4 and CXCL12 in the dark zone[199] (Figure 1.4). GCB cells within the light zone are termed centrocytes, whilst dark zone resident GCB cells are referred to as centroblasts. Knock-out studies have revealed that the segregation of light and dark zones is dependent on the expression of CXCL12 by a distinct population of dark zone reticular stromal cells[199] and CXCR4 by centroblasts, as both centrocytes and centroblasts express comparable levels of CXCR5[163]. Therefore, the cycling of GCB cells between these two compartments central to affinity maturation is regulated by dynamic CXCR4 expression dictated by a timed cellular program[205]. Similar to GCB cells, T_{FH} cells also downregulate EBI2[187] and upregulate S1PR2[206] during primary antibody responses to localise to and restrict movement within germinal centres (Figure 1.4). T_{FH} cell-expression of CXCR5 enriches for their positioning

within the light zone to provide selective survival signals to GCB cells with greater antigen affinity[186]. CXCR4 expression has been reported by T_{FH} cells[40,207], with one study demonstrating CXCR4 defined T_{FH} localisation within the dark zone[208]. However, the importance of T_{FH} cell CXCR4 expression is unknown, as is the function of T_{FH} cells residing in the dark zone.

1.15 Egress of germinal centre products

The key products of the germinal centre reaction are the generation of high-affinity, isotype-switched memory B cells and LLPCs that confer long-term protection and rapid secondary response to future pathogen exposure. Following positive-selection in the germinal centre, developing plasma cells downregulate CXCR5 and CCR7, and upregulate CXCR4 expression for redirection to the lymph node medullary cords or splenic red pulp[197] (Figure 1.4). Alternatively, some LLPCs exit lymphoid tissues by upregulating S1PR1 which facilitates migration into S1P-rich lymph and blood[209,210]. Subsequent migration to the bone marrow is driven by CXCR4 expression[197], whilst migration to peripheral inflammatory sites or tissues is governed by inflammatory or tissue-tropic chemokine receptors, respectively[211,212]. Germinal centre-derived memory B cells express both CXCR4 and CXCR5, downregulate S1PR2 and upregulate EBI2 and CCR6[170,195,213]. Here, the downregulation of S1PR2 and upregulation of EBI2 likely facilitates the egress from the germinal centre niche, whereas CCR6 expression is redundant in this process[170,213]. Within lymphoid tissues, memory B cells localise sites of antigen drainage such as the peri-subcapsular space in lymph nodes[214] (Figure 1.4). Memory B cells in this location express both CCR6 and CXCR3[214], which may facilitate localisation to this area given CCL20 expression in the lymph node SCS[215] and CXCR3 ligand expression in the interfollicular zones[216]. Like LLPCs, memory B cells can express tissue-tropic chemokine receptors to localise to barrier tissues such as the lung and lamina propria of the gut[217–219]. Memory T_{FH} cells can also localise to the outer-follicle and peri-subcapsular space in lymph nodes where they have a $CCR7^{+}CXCR5^{-}EBI2^{+}$ migratory phenotype[187] (Figure 1.4). Within this space, memory T_{FH} cells interact with memory B cells upon secondary infection to rapidly trigger proliferation and plasma cell differentiation[214]. Interestingly, following secondary antigen exposure, memory T_{FH} cells display a different migratory capacity to primary T_{FH} cells characterised by frequent shuttling between follicles and germinal centres due to maintained EBI2 expression[187]. The implications of such shuttling behaviour remain undetermined.

1.16 T follicular regulatory cells

There is a growing appreciation that $Foxp3^{+}$ Treg cells are capable of co-opting differentiation pathways of canonical T helper subsets to exhibit a subset-specific regulatory capacity[220]. Accordingly, three independent groups demonstrated that thymus-derived natural Tregs (nTreg) utilize the developmental pathway of T_{FH} cells to gain the capacity to migrate into the germinal centre and regulate the humoral response[42–44]. This specialised subset, termed T_{FR} cells has a transcriptome similar both to T_{FH} cells: CXCR5, PD-1, ICOS

and Bcl6; and activated Treg cells: Foxp3, CTLA4, GITR, and Blimp-1, however, T_{FR} cells are more closely related to activated Tregs due to expression of Blimp-1 and lack of B-helper molecules CD40L, IL-4 and IL-21[42,43]. Akin to T_{FH} cells, T_{FR} cell differentiation is a multi-step process that requires costimulatory CD28 and ICOS signalling[43,221,222], Bcl6 expression[42,43], initial dendritic cell activation[223], and subsequent SAP-dependent B cell interaction[43,223]. Yet unlike T_{FH} cells, T_{FR} cell differentiation must balance reciprocally antagonistic Bcl6 expression necessary for germinal centre localisation cues, with Blimp-1 expression necessary for Treg lineage stability and suppression mediators[224]. Here gradual downregulation of the IL-2Rα chain throughout T_{FR} cell differentiation limits IL-2 stimulation and subsequent STAT5 activation which represses Bcl6[225–227]. Additional factors driving the formation of T_{FR} cells outside the focus of this thesis are reviewed elsewhere[228,229]. Given their differentiation from nTregs, T_{FR} cells display oligoclonal specificity for self-antigen[230] and are preferentially induced by immunisation with self-antigens[227,231]. Thus, during antibody responses to foreign antigens, both recruitment into the germinal centre and suppressive capacity of T_{FR} cells are independent of specificity to the immunising antigen[223,230]. How nTreg clones are selected for T_{FR} cell differentiation and subsequent recruitment into the germinal centre remains unknown, however bystander activation of nTregs may explain this phenomenon. Notably, under some conditions T_{FR} cells can differentiate from naïve T cells, thus display specificity for the immunising antigen[232]. This is context dependent and has been observed following immunisation with incomplete Freund's adjuvant, previously implicated in generation of tolerogenic responses[233,234]. Whether *in vivo* conditions can drive the development of T_{FR} cells that recognise foreign antigen remains unknown, however it is postulated that this may be important at barrier sites for tolerance to commensal bacteria[229]. Indeed, gut-lymphoid T_{FR} cells drive diversification of IgA against commensal bacteria necessary for a healthy gut microbiome[164].

The function of T_{FR} cells has been intensively studied throughout the course of this thesis and has since become widely contested. Initially, T_{FR} cells were attributed with regulating the size of T_{FH} and GCB cell populations[42–44]. This has since been challenged following the generation of *Foxp3*^{Cre}*Bcl6*^{fl} mice that prevent full T_{FR} cell differentiation and produce no significant differences in T_{FH} or GCB cell populations[225,235,236]. Similarly, the effect of T_{FR} cell depletion on antibody responses to foreign antigen are widely debated. Various studies have demonstrated decreased antigen-specific antibody production[43,236] and/or decreased affinity[43,164] following T_{FR} cell depletion, whilst other groups have shown increased antigen-specific antibody production[42,44,226,237,238]. Together, these studies demonstrate that T_{FR} cell function may differ depending on the anatomical site, as antibody responses to antigen delivered from mucosal sites are significantly diminished in the absence of T_{FR} cells[164,236]. Secondly, given the multistep differentiation of T_{FR} cells, these studies have demonstrated that the timing of T_{FR} cell depletion determines its effect on the germinal centre response. Early depletion of T_{FR} cells prior to germinal centre formation augments T_{FH} and GCB cell populations, antigen-specific and total immunoglobulin, and the outgrowth of autoreactive antibodies[237]. Alternatively, depletion of T_{FR} cells after the establishment of the germinal centre has little effect[237]. Importantly, early T_{FR} cell CXCR5 upregulation is driven by

NFAT2[239], thus genetic approaches blocking T_{FR} cell differentiation via targeted Bcl6 deficiency expression may not impair the earliest stages of their differentiation[229]. Lastly, the most recent studies have revealed that T_{FR} cells play an important role in supressing the expansion of non-specific antibodies[225,236,237], and autoreactive antibody clones[225,235,237,238,240]. How T_{FR} cells perform these functions remains an active area of investigation. Two groups have demonstrated the requirement for T_{FR} cell CTLA-4 expression in restricting T_{FH} cell, GCB cell and autoantibody outgrowth[241,242]. Whether T_{FR} cells limit the germinal centre response directly through interactions with GCB cells, or indirectly through T_{FH} cells is yet to be revealed, as is whether T_{FR} cells are capable of exercising the self-antigen-specific negative selection of GCB cells which have developed auto-reactive antibodies via SHM. Here, a detailed understanding of T_{FR} cell trafficking throughout the germinal centre response would add to the understanding of this population.

1.17 Summary- GCT cell migratory cues

The last two decades have provided great insight to the molecular signalling pathways and migratory events that govern antibody responses. However, the factors facilitating some migratory events and their biological importance remain incompletely understood. Whilst the discovery of CXCR5 expression by T cells with B cell helper function was a was a major step in the identification of *bona fide* T_{FH} cells, CXCR5 expression is only essential for the enrichment in the germinal centre light zone, not germinal centre entry[186]. Whilst down-regulation of CCR7 is essential for their egress from the T-zone[185,186], CXCR5-deficient T cells still localise to the T-B border and spread throughout germinal centres following immunization[186]. Similarly, CXCR5-deficient T_{FR} cells are capable of localising to the germinal centre[243]. Therefore, additional migratory axes must contribute to the migration of GCT cell subsets to the appropriate niches throughout the antibody response. Unlike T_{FH} cells, the localisation of T_{FR} cells during each phase of the humoral response is less well characterised. Given that T_{FR} cells display the same differentiation kinetics as T_{FH} cells and also express CXCR5, it has been assumed that T_{FR} cells colocalise with T_{FH} cells throughout the germinal centre response. However, the anatomical localisation of T_{FR} cells during the antibody response has not been intensively studied. Rather, few T_{FR} cells have been directly visualised in germinal centres[42–44,221,243,244]. Therefore, the migratory signals that control the localisation of T_{FR} cells remain incompletely understood.

1.18 The Research Project

Significant advances in the understanding of leukocyte trafficking have generated multiple open questions regarding the regulation of immobilised chemokine gradients and the chemotactic cues underpinning GCT cell localisation. Identification of narrow CCL21 haptotactic gradients essential for dendritic cell egress from cutaneous tissue highlight the importance of chemokine regulation in normal immune function. The atypical chemokine receptor ACKR4 is broadly expressed within peripheral tissues and when perturbed, impairs

steady-state dendritic cell egress from the skin via an unknown mechanism. Within the lymph node, ACKR4 regulates CCL21 abundance in interfollicular zones required for dendritic cell SCS egress, yet it is unknown whether peripheral ACKR4 regulates haptotactic gradients in peripheral sites. This leads to the following hypothesis that is investigated in Chapter 3.

Hypothesis: ACKR4 regulates CCR7 ligand abundance and distribution in barrier tissues to guide dendritic cell egress during the steady-state

This will be addressed by the following aims:

Aim 1: Investigate the abundance of chemokine ligands in *Ackr4*$^{-/-}$ barrier tissues

Aim 2: Identify ACKR4-expressing cells and their contribution to chemokine regulation

Aim 3: Determine the mechanism of perturbed dendritic cell egress from steady-state skin in *Ackr4*$^{-/-}$ mice

Concurrently, the chemotactic cues that guide GCT cell trafficking remain incompletely understood. Canonical CXCR5 expression by both T_{FH} and T_{FR} cells is necessary for optimal germinal centre localisation, however it is redundant in many of the relocalisation events prior to formation of the germinal centre. Furthermore, given the recent identification of T_{FR} cells, many of the migratory cues governing their relocation are inferred from the localisation of T_{FH} cells throughout the response as these subsets share similar differentiation programs. For these reasons, the following hypothesis has been formulated for study in Chapter 4.

Hypothesis: Additional chemokine receptors complement CXCR5 to direct GCT cell localisation during the germinal centre response

This will be addressed by the following aims:

Aim 1: Identify additional chemokine receptors expressed by GCT cell populations

Aim 2: Elucidate relevant chemokine ligand expression and localisation in the spleen during the germinal centre response

Aim 3: Identify the function of additional chemokine receptors on GCT cells

Table 1.1: Atypical chemokine receptor nomenclature and ligands

Receptor	Aliases	Ligands	Receptor function
ACKR1	DARC, Duffy, CD234	CCL2, CCL5, CCL7, CCL11, mCCL13, mCCL14, CCL17, CXCL1, CXCL2, CXCL3, CXCL5, mCXCL6, mCXCL8, CXCL11	Chemokine scavenging[17] and transcytosis[21,22]
ACKR2	D6, CCBP2	CCL2, CCL3, mCCL3L1, CCL4, mCCL4L1 CCL5, mCCL7, mCCL8, CCL11, hCCL12, mCCL13, mCCL14, CCL17, CCL22	Chemokine scavenging[18–20]
ACKR3	CXCR7, RDC-1	CXCL11, CXCL12[25]	Chemokine scavenging[28] and chemokine receptor modulation[29]
ACKR4	CCX-CKR, CCRL1, CCR11	CCL19, CCL21, CCL25[26,27], CCL20[110], hCCL22[111]	Chemokine scavenging[112,115,116]
ACKR5	CCRL2, CRAMB	Chemerin	Ligand presentation[30,31]
GPR182		CXCL10, CXCL12, CXCL13	Chemokine scavenging[16]

Table adapted from[10,14,15]

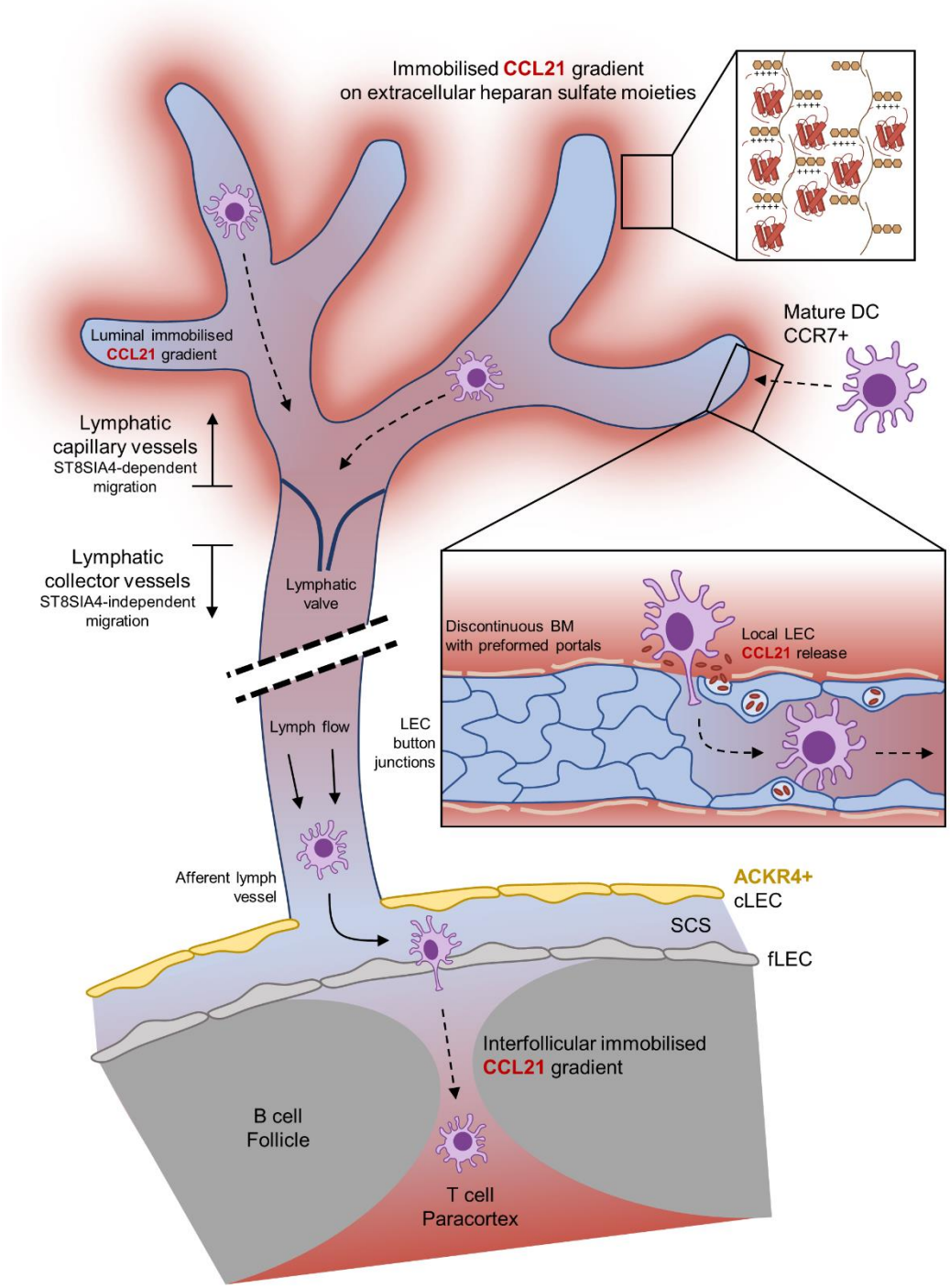
Immobilised CCL21 gradient
on extracellular heparan sulfate moieties
Luminal immobilised
CCL21 gradient
Mature DC
CCR7+
Lymphatic
capillary vessels
ST8SIA4-dependent
migration
Lymphatic
collector vessels
ST8SIA4-independent
migration
Lymphatic
valve
Discontinuous BM
with preformed portals
Local LEC
CCL21 release
LEC
button
junctions
Lymph flow
Afferent lymph
vessel
ACKR4+
cLEC
SCS
fLEC
Interfollicular immobilised
CCL21 gradient
B cell
Follicle
T cell
Paracortex

Figure 1.1: Functions of CCR7 and CCL21 in cutaneous dendritic cell egress

LECs lining lymphatic capillary vessels constitutively secrete CCL21 (red) into the extracellular space. Here, CCL21 becomes immobilised on heparan sulfate moieties and generates immobilised gradients steepest proximal to the lymphatic vessel surface. Upon maturation, cutaneous dendritic cells upregulate CCR7 and migrate towards lymphatic vessels. At the lymphatic vessel surface, dendritic cells first cross the discontinuous basement membrane (BM) through preformed portals, then enter the lymphatic lumen through unique button junctions between LECs. Local secretion of intracellular stores of CCL21 by LECs may guide dendritic cells to BM portals, facilitate adhesion to LECs, or propel dendritic cells to open button junctions. Within the lymphatic capillary vessel lumen, immobilised CCL21 gradients direct dendritic cells downstream. Upon entering larger lymphatic collector vessels, dendritic cell egress is passively facilitated by increased lymph flow maintained by lymphatic valves. After arrival in the lymph node SCS from afferent lymph vessels, dendritic cells enter the T cell paracortex via immobilised CCL21 gradients in the interfollicular space. The interfollicular immobilised CCL21 gradient is maintained by ACKR4 expressed on cLECs lining the SCS.

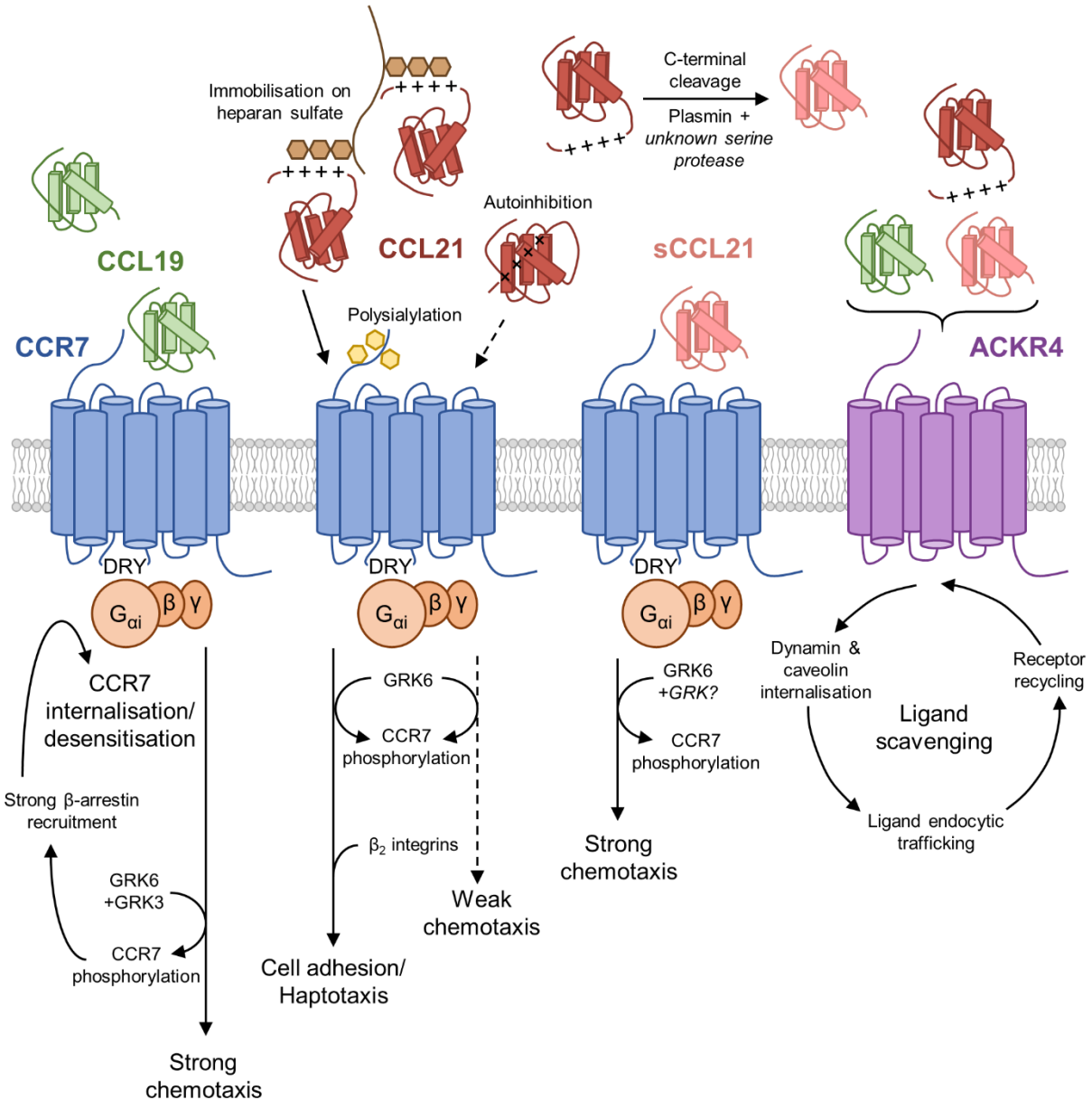
Immobilisation on heparan sulfate
C-terminal cleavage
Plasmin + unknown serine protease
CCL19
CCL21
Autoinhibition
sCCL21
Polysialylation
CCR7
ACKR4
DRY
Gαi
β
γ
CCR7 internalisation/ desensitisation
Strong β-arrestin recruitment
GRK6 +GRK3
CCR7 phosphorylation
Strong chemotaxis
GRK6
CCR7 phosphorylation
β2 integrins
Cell adhesion/ Haptotaxis
Weak chemotaxis
GRK6 +GRK?
CCR7 phosphorylation
Strong chemotaxis
Dynamin & caveolin internalisation
Receptor recycling
Ligand scavenging
Ligand endocytic trafficking

Figure 1.2: Signalling characteristics of CCL19 and CCL21 through CCR7 and ACKR4

The chemokine receptor CCR7 has two chemokine ligands, CCL19 and CCL21, with distinct signalling properties. CCL19 is a soluble ligand that facilitates robust cell migration and uniquely triggers CCR7 desensitisation downstream of extensive CCR7 phosphorylation by GRK3/GRK6 and robust β-arrestin recruitment. Conversely, CCL21 contains an elongated, positively-charged C-terminal tail that facilitates immobilisation on GAGs including heparan sulfate, or adoption of an autoinhibitory conformation. CCR7 sensitivity to full-length CCL21 requires ST8SIA4-mediated N-terminal receptor polysialylation and is dependent on GRK6 signal termination via CCR7 phosphorylation. Immobilised CCL21 triggers β2 integrin-dependent cell adhesion or haptotaxis to immobilised gradients, whilst unbound full-length CCL21 may trigger weak chemotaxis *in vitro*. Lastly, the extended C-terminal tail of CCL21 can be proteolytically cleaved by plasmin or an unidentified serine protease to produce soluble CCL21 (sCCL21). This pseudo-third CCR7 ligand promotes strong chemotaxis like CCL19, and cannot trigger CCR7 desensitisation like CCL21. CCR7 phosphorylation downstream of sCCL21 is mediated by GRK6 and an unidentified GRK, as demonstrated in studies with *Grk6*$^{-/-}$ BMDCs. CCL19, CCL21 and sCCL21 are all ligands for the atypical chemokine receptor ACKR4. Due to the lack of a conserved DRY motif, ACKR4 cannot recruit $G_{\alpha i}$ G proteins necessary for cell migration. Rather, ACKR4 scavenges ligands via dynamin and caveolin-mediated endocytic trafficking.

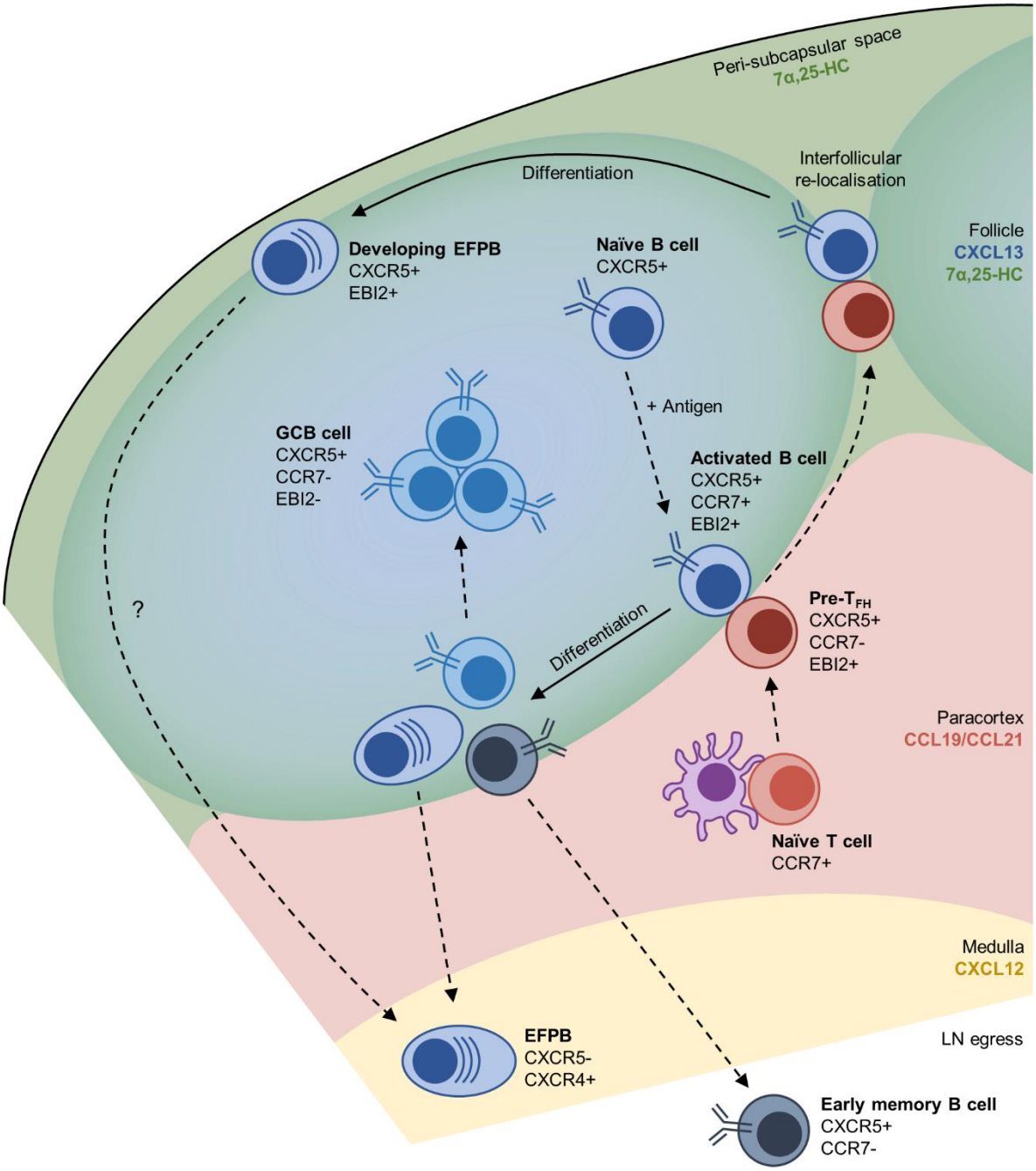
Peri-subcapsular space
7α,25-HC
Differentiation
Interfollicular
re-localisation
Follicle
CXCL13
7α,25-HC
Developing EFPB
CXCR5+
EBI2+
Naïve B cell
CXCR5+
+ Antigen
GCB cell
CXCR5+
CCR7-
EBI2-
Activated B cell
CXCR5+
CCR7+
EBI2+
?
Differentiation
Pre-T$_{FH}$
CXCR5+
CCR7-
EBI2+
Paracortex
CCL19/CCL21
Naïve T cell
CCR7+
Medulla
CXCL12
LN egress
EFPB
CXCR5-
CXCR4+
Early memory B cell
CXCR5+
CCR7-

Figure 1.3: Activated T and B cell migration in the lymph node preceding germinal centre formation

Depicted are known migratory events and phenotypes of activated T and B cells in the lymph node prior to the formation of the germinal centre. The distribution of CXCL13 (blue), 7α,25-HC (green), CCL19/CCL21 (red) and CXCL12 (yellow) are highlighted in each compartment, notably the gradient of 7α,25-HC strongest in the outer-follicle. Naïve T and B cells are segregated into the paracortex and follicle by the CCL19/CCL21:CCR7 and CXCL13:CXCR5 chemokine axes, respectively. Upon binding native antigen, activated B cells upregulate CCR7 and EBI2 to facilitate migration and distribution along the T-B border. Dendritic cells presenting cognate antigen peptides in the context of MHC-II initiate an early T_{FH} developmental program in responding T cells, marked by downregulation of CCR7 and expression of CXCR5 and EBI2 to facilitate T-B border homing. Extensive cognate T and B cell interactions at the T-B border may relocate to the interfollicular areas. Pre-T_{FH} cells direct the differentiation of cognate B cells into EFPBs, early memory B cells and GCB cells. EFPB differentiation can occur in the outer-follicle, but ultimately, EFPBs reside within the medulla due to CXCR4 expression. It is unknown whether EFPBs in the outer-follicle seed medullary EFPBs. Early memory B cells resume the migratory phenotype of naïve B cells, exit the lymph node and enter the circulation. Lastly, GCB cells downregulate CCR7 and EBI2 to migrate to the centre of the follicle to initiate the formation of germinal centres.

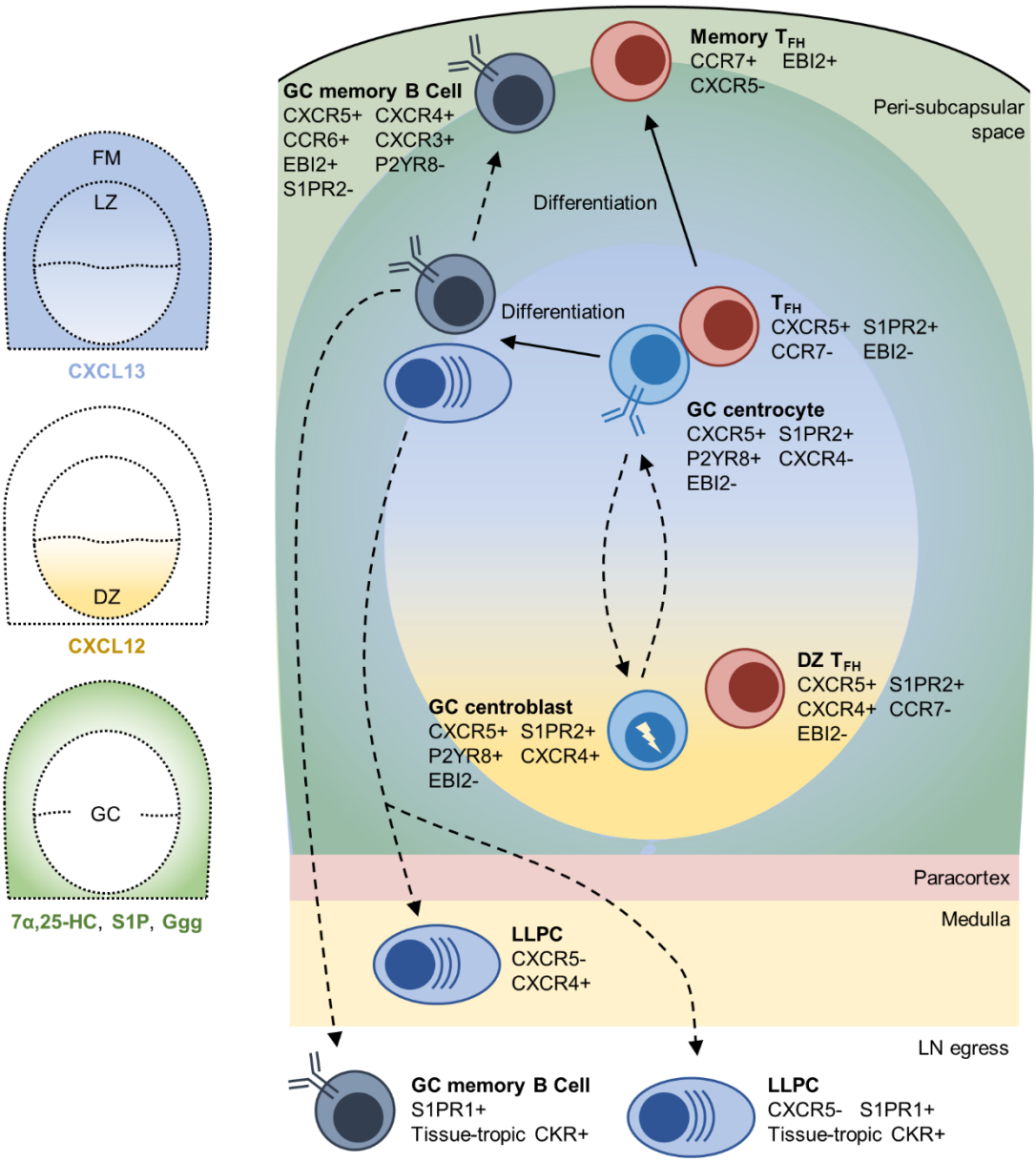
FM
LZ
CXCL13
DZ
CXCL12
GC
7α,25-HC, S1P, Ggg
GC memory B Cell
CXCR5+ CXCR4+
CCR6+ CXCR3+
EBI2+ P2YR8-
S1PR2-
Memory TFH
CCR7+ EBI2+
CXCR5-
Peri-subcapsular space
Differentiation
Differentiation
TFH
CXCR5+ S1PR2+
CCR7- EBI2-
GC centrocyte
CXCR5+ S1PR2+
P2YR8+ CXCR4-
EBI2-
DZ TFH
CXCR5+ S1PR2+
CXCR4+ CCR7-
EBI2-
GC centroblast
CXCR5+ S1PR2+
P2YR8+ CXCR4+
EBI2-
Paracortex
Medulla
LLPC
CXCR5-
CXCR4+
LN egress
GC memory B Cell
S1PR1+
Tissue-tropic CKR+
LLPC
CXCR5- S1PR1+
Tissue-tropic CKR+

Figure 1.4: Lymph node germinal centre compartmentalisation and migratory events

Depicted are known migratory events and phenotypes of germinal centre populations. The distribution of CXCL13 (blue); CXCL12 (yellow); and the lipid mediators 7α,25-HC, S1P and Ggg (green) within the follicular mantle (FM), light zone (LZ) and dark zone (DZ) are highlighted. T_{FH} cells reside within the LZ owing to CXCR5 expression, however $CXCR4^{+}$ T_{FH} cells have been visualised in the DZ. T_{FH} egress from the germinal centre is restricted by chemorepulsive S1PR2 signalling induced by S1P outside of the germinal centre. LZ centrocyte and DZ centroblast localisation is regulated by dynamic CXCR4 expression. Similarly, GCB cell migration is confined within the germinal centre by chemorepulsive S1PR2 and P2YR8 signalling induced by S1P and Ggg, respectively. Within the LZ, GCB cells receive signals from T_{FH} cells to differentiate into GC memory B cells and LLPCs. GC memory B cells downregulate germinal centre retention receptors S1PR2 and P2YR8 and relocate to the outer-follicle/peri-subcapsular space aided by EBI2 expression. Upregulation of CXCR3 and CCR6 may contribute to this relocalisation as their ligands CXCL9 and CCL20 are expressed in interfollicular zones and the peri-subcapsular space of lymph nodes, respectively (not depicted). Alternatively, GC memory B cells can upregulate S1PR1 and tissue-tropic chemokine receptors (CKRs) to leave the LN and traffic to peripheral tissues. LLPCs generated in the germinal centre may reside in the medulla via CXCR4 expression, or migrate to peripheral tissues like GC memory B cells. Memory T_{FH} cells generated following the resolution of the germinal centre response lose CXCR5 expression and upregulate CCR7 and EBI2. Memory T_{FH} cells reside in the outer-follicle/peri-subcapsular space, however the signals retaining memory T_{FH} cells in this location remain incompletely characterised.

Chapter 2
Materials and Methods

Chapter 2 – Materials and Methods

2.1 Reagents and solutions

Standard lab reagents and stock solutions were obtained from Technical Services Unit (TSU), School of Biological Sciences, University of Adelaide, unless stated otherwise. Endotoxin-free phosphate buffered saline (PBS; Institute of Medical and Veterinary Science, Adelaide) was used for preparation of solutions required for animal use.

2.1.1 0.05% Saponin

0.05% (w/v) saponin (Sigma-Aldrich) was dissolved in sterile MilliQ water and stored at 4°C.

2.1.2 1-4% Paraformaldehyde

1% or 4% (w/v) paraformaldehyde (Sigma-Aldrich) was dissolved in PBS overnight at 60°C with mixing. The pH was subsequently adjusted to 7.2 and solution stored at 4°C.

2.1.3 10% Alum

10% (w/v) of aluminium potassium sulphate (BDH Chemicals) was dissolved in sterile MilliQ water and stored at room temperature.

2.1.4 1X Permeabilisation buffer

A 1X working solution was made fresh by diluting 10X Permeabilisation Buffer (eBioscience; 00-8333-56) with MilliQ water.

2.1.5 B300.19 media

RPMI 1640 (Gibco) supplemented with 10% (v/v) heat-inactivated foetal calf serum (FCS), 200mM L-glutamine (Gibco), 1mM sodium pyruvate (Gibco), 1X MEM non-essential amino acids (Gibco), 10mM HEPES (Gibco), 54μM β-mercaptoethanol (Sigma) and 0.2U/mL penicillin/streptomycin (Gibco).

2.1.6 Chemotaxis buffer

RPMI 1640 supplemented with 25mM HEPES and 0.5% (w/v) bovine serum albumin (BSA; Sigma-Aldrich) prepared fresh as required.

2.1.7 Digestion buffer

DMEM (Gibco) supplemented with 5% (v/v) heat-inactivated FCS, 2.5mM calcium chloride, 10mM HEPES and 0.2U/mL penicillin/streptomycin. Digestion buffer was supplemented with enzymes described in text immediately prior to digestive incubation.

2.1.8 ELISA coating buffer

PBS was supplemented with 28.6mM sodium carbonate (Sigma-Aldrich) and 11.9mM sodium bicarbonate (Sigma-Aldrich), then pH adjusted to 9.6.

2.1.9 FACS buffer
PBS was supplemented with 1% (w/v) BSA and 0.04% (v/v) sodium azide (Sigma-Aldrich).

2.1.10 Inhibitory PBS (iPBS)
PBS supplemented with protease inhibitor cocktail (Sigma-Aldrich) and 1.6mM phenylmethylsulfonyl fluoride (PMSF; Sigma-Aldrich).

2.1.11 Mouse red cell lysis buffer (MRCLB)
155mM ammonium chloride in MilliQ water, and 170mM Tris-HCl (pH 7.65) in MilliQ water were combined in a 9:1 ratio. The pH was subsequently adjusted to 7.2, then the solution was filter-sterilised and stored at 4°C, or pre-warmed to 37°C for use.

2.1.12 PBS Azide
PBS was supplemented with 0.04% (v/v) sodium azide (Sigma-Aldrich).

2.1.13 R10 media
RPMI 1640 without phenol red (Gibco) was supplemented with 10% (v/v) heat-inactivated FCS and 0.2U/mL penicillin/streptomycin. For BMDC crawl-in experiments, R10 media was further supplemented with 10mM HEPES.

2.1.14 Tailtip lysis buffer
MilliQ water with 100mM Tris-HCl (pH 8.5), 5mM EDTA, 0.2% (v/v) SDS and 200mM sodium chloride. Immediately prior to use, 0.1mg/ml Proteinase K (Bioline) was added and mixed thoroughly.

2.2 Animals and procedures

2.2.1 Mice
Ccr6$^{-/-}$, *Ackr4*$^{-/-}$, *Foxp3*^{GFP}, *Foxp3*$^{DTR\text{-}GFP}$, *Sh2d1a*$^{-/-}$ and *Rag1*$^{-/-}$ mice are described elsewhere[102,245–249]. C57Bl/6J (wildtype, WT) mice and B6.SJL.*Ptprca* (Ly5.1) mice were obtained from Laboratory Animal Services (LAS), University of Adelaide, or the Animal Resource Centre, Western Australia. *Ccr6*$^{-/-}$*Foxp3*^{GFP} and Ly5.1*Ackr4*$^{-/-}$ mice were generated at LAS by crossing the relevant strains. All mice were housed in individually ventilated cages under specific pathogen-free conditions at LAS. At experimental endpoints, mice were humanely killed by CO_2 asphyxiation immediately prior to tissue harvest. All experiments received approval from the University of Adelaide Animal Ethics Committee.

2.2.2 Genotyping
Tailtips were excised from weaned mice and stored at -20°C until use. To extract genomic DNA, tailtips were incubated in 100µL tailtip lysis buffer overnight at 55°C, heat-shocked at 96°C for 5 minutes then diluted with 500µL MilliQ water. Samples were centrifuged at 13,000rcf prior to use, and stored long-term at 4°C. Genotype was determined by polymerase chain reaction with MyTaq DNA Polymerase kit (Bioline) and relevant primers (Sigma-Aldrich; see **Table 2.1**) on a MyCycler (Bio-Rad). Samples were run on 1.5% (w/v) agarose

gels (VWR) and amplicons were visualised via GelRed staining on a ChemiDoc MP Imaging System (Bio-Rad). *Foxp3*^{GFP} and *Ccr6*$^{-/-}$*Foxp3*^{GFP} strains were maintained by breeding hemizygous males with homozygous females. Homozygosity was determined via flow cytometry on blood Tregs as heterozygous females contained half as many GFP^{+} Tregs as homozygous females.

2.2.3 Bone Marrow Reconstitutions

Mice over the age of 8 weeks old and >20g in weight were used as bone marrow hosts. Host mice were lethally irradiated in double-bagged acrylic poly(methyl methacrylate) mouse holders with two consecutive doses of 500 Rads at the Royal Adelaide Hospital by Senior Radiation Therapist, Dr. Josef Nguyen. For reconstitution, bone marrow was harvested into ice-cold PBS from the femur and tibia of donor mice under sterile conditions using a 23G needle (BD). Cells were pelleted by centrifugation at 300rcf for 6 minutes, then red blood cells were lysed by incubation with 10mL of pre-warmed MRCLB 37°C, 5% CO_2 for 5 minutes. The MRCLB was diluted with cold PBS then washed off by centrifugation at 300rcf for 6 minutes. Cells were counted and bone marrow samples were resuspended to $2.5x10^7$ cells/mL in PBS, and mixed to generate ratios described in text if required. Irradiated mice were injected with 200µL of bone marrow cell suspension ($5x10^6$ cells total) intravenously (i.v.) via the tail-vein on the day following irradiation. Chimeric mice had their cages changed daily for the first 2 weeks following irradiation and were afforded wet food to limit weight loss. Successful reconstitution was determined by flow cytometry on blood leukocytes harvested by tail-vein bleeding 6 weeks after reconstitution. Chimeric mice were used in experiments 8 weeks post-reconstitution. *Rag1*$^{-/-}$(*Sh2d1a*$^{-/-}$:*Foxp3*$^{DTR-GFP}$) chimeras were generated by collaborator Prof. Carola Garcia de Vinuesa's group, Australian National University, Canberra, then sent to Adelaide after the resting period for the remainder of the experiment.

2.2.4 Skin grafting

Skin grafting experiments were performed with Lynn Tolley, University of Queensland, Diamantina Institute, under sterile conditions at LAS, University of Adelaide, as previously described[250]. Briefly, skin donor mice were euthanised, then ear tissue was harvested and mechanically split into dorsal and ventral halves for grafting. Host mice were anaesthetised via i.p. injection of 80:10mg/kg ketamine and xylazine in saline, then shaved between the front and back legs on their right flank. Incisions in the flank skin down to the panniculus carnosus were cut in the shape of ear sheets and separated by approximately 2mm of host skin, then the tissue was removed. Graft tissue was laid on resulting graft beds and trimmed accordingly. Mice were bandaged and received 0.1mg/kg Temgesic in saline subcutaneously (s.c.) as an analgesic. Bandages were removed after seven days, and mice were rested for a further 5 weeks with daily monitoring throughout.

2.2.5 Perfusion

For chemokine leach out assays, euthanised mice were perfused with 10mL of PBS through the right ventricle using a 10mL syringe and 27G needle (BD).

2.3 Immunisation strategies and inflammation models

2.3.1 Sheep Red Blood Cells (SRBCs)

SRBCs in Alsever's solution (Applied Biological Products) were washed three times in endotoxin-free PBS by centrifugation at 450rcf for 15 minutes at 4°C with aspiration. Washed SRBCs were counted and resuspended to $1x10^{10}$ cells/ml in endotoxin-free PBS. Mice were immunised i.p. with $2x10^{9}$ (200µl) SRBCs and analysed at the time points described in text.

2.3.2 4-hydroxy-3-nitrophenylacetyl keyhole limpet hemocyanin (NP-KLH)/Alum

NP-KLH (Biosearch Technologies) was resuspended to 1mg/ml in sterile MilliQ water and stored protected from light at 4°C. Aliquots of 1mg/ml NP-KLH were diluted to 50µg/100µL per mouse in MEMα (Gibco) supplemented with 25mM HEPES. The antigen-MEMα solution was further diluted 1:1 with an equal volume of 10% Alum. Using pH indicator strips (BDH Chemicals), the pH was adjusted to 6.5 with 1M NaOH. Alkalinisation was accompanied by the formation of a precipitate and transient change in solution colour from yellow to a light pinkish hue whilst mixing. If the solution remained pink, 1M HCl was added to revert the colour change and increase pH back towards 6.5. After buffering, the remaining volume of the tube was made up with endotoxin-free PBS and the antigen solution was centrifuged at 480rcf for 10 minutes at 4°C. Supernatant was aspirated and the NP-KLH/Alum pellet was washed three times in endotoxin-free PBS. NP-KLH/Alum was resuspended in endotoxin-free PBS to 50µg/100µL after the final wash. Mice were immunised i.p. with 50µg (100µl) NP-KLH/Alum and analysed at the time points described in text.

2.3.3 FITC Paint

A 10% (w/v) solution of FITC (Sigma-Aldrich) in DMSO was prepared, then diluted to 1% FITC in a 1:1 mix of acetone:dibutyl phthalate. Mice were anaesthetised via isoflurane inhalation, and 10µL of 1% FITC was slowly pipetted onto the desired area.

2.4 Molecular analyses

2.4.1 RNA extraction via TRIzol

Large, snap frozen tissue samples were homogenized with a mortar and pestle under liquid nitrogen, decanted, and mixed with 1ml TRIzol (Ambion) per 100mg starting tissue. RNA was extracted according to manufacturer's protocol.

2.4.2 RNA extraction via RNeasy kits

RNA was extracted from sorted cells using either the QIAGEN RNeasy Micro Kit ($<5x10^{5}$ cells) or QIAGEN RNeasy Mini Kit ($5x10^{5}$-$1x10^{7}$ cells) according to manufacturer's protocol, including on-column DNase digest. RNA was extracted from small, snap-frozen tissue samples <30mg in weight using the QIAGEN RNeasy Mini Kit according to manufacturer's protocol. Fibrous tissues were homogenized with a mortar and pestle under liquid nitrogen, decanted, then mixed with Buffer RLT supplemented with 10µl/mL β-mercaptoethanol. Soft organs were mechanically homogenized with the blunt-end of a

syringe in Buffer RLT supplemented with 10µl/mL β-mercaptoethanol. On-column DNase digest was performed as per manufacturer's instructions.

2.4.3 cDNA synthesis

1µg or 2µg RNA was reverse-transcribed into cDNA using the Transcriptor First Strand cDNA Synthesis Kit (Roche), or High-Capacity cDNA Reverse Transcription Kit (Applied Biosciences) respectively, according to manufacturer's instructions. Reverse Transcriptase-negative controls were generated for all samples to identify DNA contamination.

2.4.4 Quantitative polymerase chain reaction (qPCR)

Quantitative PCR was performed with the SYBR Green I Master Kit (Roche) or Power SYBR Green Master Mix (Applied Biosystems) according to manufacturer's instructions. Reactions were performed in a total volume of 10µl with 1µM primer pairs (Sigma-Aldrich; see **Table 2.2**) in 384-well plates (Sarstedt). Primers were designed with Primer Express 3.0 software (Thermo Fisher Scientific) and specificity was confirmed with NCBI Primer-BLAST and sorted positive-control cell populations when possible. Data was analysed with LightCycler 480 SW 1.5.1 (Roche), and relative expression was calculated by the $2^{-\Delta CT}$ method, where $\Delta CT = Ct_{Target} - Ct_{Housekeeping\ Gene}$. Reverse Transcriptase-negative controls were run for all samples to identify DNA contamination.

2.4.5 Leach out protein collection

Tissues were harvested, weighed, immersed in iPBS in 1.5mL Eppendorf tubes, minced, then incubated for 3 hours at 4°C with shaking. Where necessary, hair was shaved off tissues with a surgical blade. Samples were subsequently centrifuged at 5000rcf for 8 minutes and supernatant was transferred to a new 1.5mL Eppendorf and stored at -80°C until use.

2.4.6 Chemokine quantification via ELISA

High-binding polystyrene EIA/RIA 96-well plates (Costar) were coated with 100µL of capture antibody (see **Table 2.3**) diluted in ELISA coating buffer and incubated overnight at 4°C. Wells were subsequently washed four times with 0.05% (v/v) Tween20 in PBS, then blocked with 200µL 3% (w/v) BSA in PBS for 2 hours at room temperature. After washing, 100µL of protein standards and diluted samples were plated in duplicate and incubated for two hours at room temperature. Washing was repeated and 100µL detection antibody (see **Table 2.3**) diluted in 1% (w/v) BSA in PBS was incubated for two hours at room temperature. The plate was washed, and incubated with 1X Avidin-HRP (eBioscience) or 0.1µg/mL Streptavidin-HRP (Rockland) diluted in 1% BSA for 45 minutes at room temperature. Washing was repeated and HRP was developed with 100µL 1X TMB ELISA Substrate Solution (eBioscience) until samples appeared within the linear range of the protein standard. Colour development was stopped with 75µL 1M orthophosphoric acid (AnalaR), and plates were analysed at 450nm with a Biotrak II plate reader (Amersham Biosciences). Concentration of chemokines was interpolated from standard curves generated with GraphPad Prism 6 after subtracting blanks.

2.4.7 Generation of cleaved CCL21

Cleaved CCL21 was generated by incubating 200ng of recombinant mouse CCL21 (R&D Systems) with $6x10^5$ BMDCs (generated as described below) for 12 hours at 37°C, 5% CO_2, as described elsewhere[7]. Culture supernatants containing CCL21 were directly separated by gel electrophoresis without immunoprecipitation.

2.4.8 Immunoprecipitation of endogenous CCL21

Immunoprecipitation experiments were designed by Cameron Bastow and performed by Adriana Caon. Tissue supernatants were prepared as above from inguinal, axillary and deep cervical lymph nodes. CCL21 was immunoprecipitated from supernatants with Protein G Dynabeads (Invitrogen) washed in 0.02% (v/v) Tween20 and loaded with polyclonal goat anti-CCL21 (R&D; AF457). Lymph node CCL21 was pooled from two mice by sequentially immunoprecipitating individual supernatants, then samples were extensively washed.

2.4.9 Protein gel electrophoresis and western blots

Electrophoresis and western blot experiments were designed/analysed by Cameron Bastow and performed by Adriana Caon. Samples were resuspended in 2X Laemmli sample buffer (Bio-Rad) with 1M DTT, then separated on 4-12% Bolt SDS-PAGE Gels (Invitrogen) in MES Buffer (Invitrogen). Full-length and cleaved CCL21 were identified by molecular ladders and controls. For mass spectrometry analysis, gel bands were visualised with Oriole stain (Bio-Rad), excised, then stored at 4°C in Eppendorf tubes until processed. For western blot analyses, gels were semi-dry transferred to 0.2µm PVDF membranes in discontinuous Tris-CAPS buffer, then blocked with 3% BSA, 1X Tris buffered saline (TBS), 0.1% (v/v) Tween20. Membranes were incubated with biotinylated polyclonal goat anti-CCL21 (R&D Systems; AF457) or monoclonal rat anti-CCL21 (R&D Systems; MAB457), washed in 1X TBS, 0.1% Tween20, incubated with streptavidin-HRP or HRP-conjugated anti-rat IgG (Jackson ImmunoResearch; 712-036-150), then washed and developed with Immobilon Crescendo Western HRP substrate (Millipore). Some membranes were reprobed with polyclonal rabbit anti-CCL21 (Peprotech; 500-P114) and HRP-conjugated anti-rabbit IgG (Invitrogen; 31460). Blots were imaged on a Bio-Rad ChemiDoc MP with Image Lab 6.0 software. Percentage of cleaved CCL21 was calculated using the Volume tool in Image Lab 6.0.

2.4.10 Liquid Chromatography Mass Spectrometry (LC-MS) analysis

LC-MS experiments were designed/analysed by Cameron Bastow, and performed/analysed by Dr. Clifford Young, Dr. Mark Condina and Prof. Peter Hoffman, University of South Australia. Gel bands containing cleaved CCL21 were processed by in-gel digestion as previously described[251], with the resulting tryptic peptides desalted by ZipTips (Merck Millipore). LC-MS analysis was performed on an Ultimate 3000 RSLCnano system coupled to an Orbitrap Exploris 480 mass spectrometer (Thermo Scientific). Samples were resuspended in 20% acetonitrile and 0.1% formic acid before injection onto a 25cm fused silica analytical column (75µm internal diameter packed in-house with 1.9µm C18 particles) heated at 50°C. Peptide elution was performed at a 300nL/min flow rate using a 10 minute linear gradient (20 to 56% acetonitrile in 0.1% formic acid). A targeted MS/MS method[252]

was employed to detect the triply charged carboxyamidomethylated peptides of CCL21-Ser (KQEPSLGCPIPAILFSPR) and CCL21-Leu (KQEPSLGCPIPAILFLPR), with their respective abundances represented by the intensities of PIPAILFSPR (m/z 900.53016) and PIPAILFLPR (m/z 926.58220) fragment ions acquired at resolution 30000 (m/z 200).

2.4.11 Anti-NP antibody ELISA

Vinyl 96-well assay plates (Costar) were coated with 50µL of 10µg/mL BSA-NP_{32} or BSA-NP_5 (Biosearch Technologies Inc.) diluted in ELISA coating buffer and incubated overnight at 4°C. Wells were subsequently washed four times with 0.05% (v/v) Tween20 in PBS, then blocked with 150µL 2% (w/v) skim milk in PBS for 2 hours at room temperature. After washing, 50µL of sera in duplicate, serially diluted 1/3 from a starting concentration of 1/100 was added to wells and incubated for 2 hours at room temperature. Wells were washed and bound anti-NP IgG was detected by incubation with 50µL of 80ng/mL anti-IgG-HRP in 2% skim milk/PBS for 2 hours at room temperature. After washing, HRP was detected with 75µL of 1X TMB ELISA Substrate Solution (eBioscience) until low dilutions became saturated and a gradient was observed across serial dilutions. Colour development was stopped with 50µL of 1M orthophosphoric acid, and plates were analysed at 450nm with a Biotrak II plate reader. Absorbance values from pre-immunisation sera were subtracted from experimental absorbance values.

2.5 Organ/Tissue harvest and cellular analyses

2.5.1 Blood

For flow cytometry analysis, blood was harvested into heparinised tubes (BD). 100-200µL of blood was then incubated in 10mL pre-warmed MRBCLB at 37°C, 5% CO_2 for 5 minutes. The cell suspension was centrifuged at 300rcf for 6 minutes at 4°C, then cells were resuspended in PBS for flow cytometric staining.

For sera analyses, blood was collected into 1.5mL Eppendorf tubes and allowed to clot at room temperature for 6 hours, or at 4°C overnight. Clotted blood was pelleted by centrifugation at 5000rcf for 8 minutes, then sera was collected and stored at -80°C until use.

2.5.2 Spleen

For flow cytometric analysis and sorting, spleens were harvested into 3mL PBS on ice, then mechanically disrupted through 70µm filters (BD) with the flat end of a 3mL syringe plunger (BD). Cell suspensions were homogenised by pipetting, topped up to 10mL with PBS and centrifuged at 300rcf for 6 minutes at 4°C. Supernatant was aspirated and the cell pellet was resuspended in 3mL of pre-warmed MRCLB and incubated at 37°C, 5% CO_2 for 5 minutes. The cell suspension was diluted with cold PBS to a final volume of 10mL and centrifuged at 300rcf for 6 minutes at 4°C. Cells were counted and resuspended to $7.5x10^6$ cells/mL in PBS for flow cytometric staining.

For imaging experiments, spleens were excised, trimmed of fat, and segmented to fit in Tissue-Tek cryomolds (Sakura). Tissues were immediately embedded in OCT compound

(Sakura) and snap-frozen with liquid nitrogen. Tissue moulds were stored covered at -80°C until required for sectioning.

2.5.3 Lymph node

For flow cytometric analysis of dendritic cells, lymph nodes were harvested into 1mL of digestion buffer supplemented with 1mg/mL collagenase (Sigma-Aldrich), gently minced and incubated for 30 minutes at 37°C, 5% CO_2. Samples were subsequently homogenised via pipetting, filtered through 70μm cell strainers and washed in PBS with centrifugation at 300rcf for 6 minutes at 4°C. Cells were counted and resuspended to $7.5x10^6$ cells/mL in PBS for flow cytometric staining.

2.5.4 Bone Marrow

For flow cytometric analysis and culture of BMDCs, bone marrow was flushed out of the femur with PBS using a 23G needle (BD). Bone marrow was homogenised via pipetting, filtered through a 70μm cell strainer, and then washed in PBS at 300rcf for 6 minutes at 4°C. The cell pellet was resuspended in 5mL of pre-warmed MRCLB and incubated at 37°C, 5% CO_2 for 5 minutes. The cell suspension was diluted with cold PBS and centrifuged at 300rcf for 6 minutes at 4°C. Cells were counted and resuspended to $7.5x10^6$ cells/mL in PBS for flow cytometric staining or $2.5x10^6$ cells/mL in R10 media for BMDC culture. For culturing, all steps were performed under sterile conditions with sterile instruments and reagents.

2.5.5 Ear sheets

For flow cytometric analysis or sorting, ears were harvested from the point of contact with the scalp. Ears were weighed, mechanically split into dorsal and ventral halves using forceps, and incubated dermis side down on 20mM EDTA/PBS for 2 hours at 37°C, 5% CO_2. Ear sheets were dried and the epidermis was peeled from the dermis in one continuous sheet. Separate single cell suspensions were prepared from both the dermis and epidermis after mincing and incubation in digestion buffer supplemented with 85μg/mL Liberase TM (Roche) and 30U/mL DNase-I (Sigma-Aldrich) at 37°C for 1.5 hours with mixing every 30 minutes. Fragments of tissue that became stuck in the pipette during mixing, particularly epidermis, were returned to digest buffer to minimise cell loss. Dermal and epidermal sheets from one mouse were digested separately in 500μL digest media, or for sorting experiments, all epidermal sheets from 5 mice were pooled and digested in 1.5mL digest media. Cell suspensions were passed through 70μm cell strainers (BD Biosciences), diluted to a final volume of 10mL in PBS, washed by centrifugation at 320rcf for 10 minutes, counted, and resuspended to $7.5x10^6$ cells/mL in PBS for flow cytometric staining.

For whole-mount imaging and BMDC crawl in experiments, ears were harvested above the cartilage of the inner ear to ensure ear sheets were completely flat. Ears were mechanically split with forceps, ensuring the inner layer of fat and cartilage remained on the dorsal side to be discarded, as only ventral halves were used for imaging given that they have fewer hair follicles. Ventral sheets were subsequently processed as described below.

2.5.6 Dorsal/Ventral skin

For flow cytometric analysis or sorting, the dorsal and ventral skin of mice was first shaved with a scalpel, then excised. The skin was then placed epidermis side down on a flat surface, and the subcutaneous fat was scored and scraped to remove as much as possible. Skin from one mouse was minced in 1.5mL of digestion buffer supplemented with 85µg/ml Liberase TM and 30U/ml DNase-I, then incubated at 37°C for 1.5 hours with mixing every 30 minutes. Fragments of tissue that became stuck in the pipette during mixing were returned to digest buffer to minimise cell loss. Cell suspensions were filtered through 70µm cell strainers, diluted to a final volume of 10mL in PBS, washed by centrifugation at 320rcf for 10 minutes, counted, and then resuspended to $7.5x10^6$ cells/mL in PBS for flow cytometric staining.

For imaging experiments, dorsal skin was shaved, and excised along a sagittal plane in strips before being mounted subcutaneous fat-side down on nitrocellulose paper. Samples were then bent to in a concave shape to counter rolling up when placed in OCT compound, and trimmed to fit inside Tissue-Tek cryomolds. Alternatively, mouse lip/chin skin was used as sections contained a greater density of hair follicles and less fat than sagittal dorsal skin sections. Here, skin was shaved, then the lower lip and skin down to the neck was excised and mounted epidermis side-up on nitrocellulose paper. All skin samples were embedded in Tissue-Tek cryomolds with OCT compound, and then snap-frozen with liquid nitrogen. Tissue moulds were stored covered at -80°C until required for sectioning.

2.5.7 Flow cytometric staining

Throughout staining, samples and reagents were kept protected from light on ice or at 4°C, and incubation steps were performed for 20 minutes with mixing, unless otherwise noted. Samples were plated in 96-well U-bottom cell culture plates (Costar) at a density of $1.5x10^6$ cells per well. Multiple wells of a sample were plated when analysing rarer cell populations, e.g. T_{FR} cells. Samples for cell sorting were stained in 15mL Falcon tubes (BD) at $7.5x10^6$ cells/mL and treated as "multiples of $1.5x10^6$ cells/well". All primary and secondary/miscellaneous staining reagents used are listed in **Table 2.4** and **Table 2.5**, respectively. Cells were initially stained with a viability dye in PBS at room temperature. Then cells were washed with FACS buffer, Falcon tubes: 300rcf for 6 minutes, or plates: 400rcf for 3 minutes, and resuspended in 50µL of 200µg/mL murine γ-globulin (Rockland) in FACS buffer to block endogenous Fcγ receptors. Importantly, if IgG was going to be analysed on B cell populations, cells were blocked with rat γ-globulin (Rockland) instead. Cells were then stained in the following order, omitting steps that were not required. First, cells were incubated with 10µL of unconjugated primary antibodies diluted in FACS buffer. After washing, cells were incubated with 50µL of an anti-rat secondary antibody diluted in FACS buffer supplemented with 200µg/mL murine γ-globulin and 1/100 dilution of normal mouse serum to detect unconjugated primary antibodies. To block unbound secondary antibody sites and permit use of other fluorophore conjugated antibodies, cells were washed, then blocked with 50µL of 200µg/mL rat γ-globulin in FACS buffer. Then cells were incubated with 10µL of fluorophore or biotin-conjugated antibody cocktails diluted in FACS buffer. After washing, biotinylated antibodies were detected by incubation with a suitable

streptavidin reagent diluted in FACS buffer. For intracellular or intranuclear staining, cells were washed with PBS azide, then permeabilised with 100µL of Cytofix/Cytoperm (BD) or 100µL of 1X fixation/permeabilisation buffer (eBioscience) respectively, for 20 minutes or overnight. After washing in 1X permeabilisation buffer, cells were resuspended in 50µL of 1X permeabilisation buffer and stained with 10µL of antibody cocktails diluted in 1X permeabilisation buffer. Samples were washed in 1X permeabilisation buffer, then PBS azide, before being resuspended in 1% PFA for acquisition. Samples were acquired on a BD LSRII or BD FACSAria within 3 days of staining. For acquisition of dendritic cells or stromal populations, samples were acquired with a 100µm nozzle at 30psi.

2.5.8 Cell sorting

Cells sorting was performed on a BD FACSAria. Lymphocytes were sorted with a 70µm nozzle at 70psi, whilst stromal cells were sorted with a 100µm nozzle at 30psi. Samples were kept at 4°C at all times, and purity >90% was determined post-sort. Importantly, when sorting for biological assays, sodium azide was omitted from all reagents.

2.5.9 MACs purification

Regulatory CD4 T cells were MACS-purified from steady-state hosts using the mouse $CD4^+CD25^+$ Regulatory T cell Isolation Kit (Miltenyi Biotec) as per manufacturer's instructions, under sterile conditions.

2.5.10 *In vitro* Chemotaxis

Splenocytes were rested in complete RPMI at a density of $1x10^7$ cells/mL for 3 hours at 37°C, 5% CO_2. For CCL19 chemotaxis, rested splenocytes were harvested and resuspended to $1x10^7$ cells/mL in fresh, pre-warmed chemotaxis buffer. Recombinant CCL19 was diluted to 75ng/mL in pre-warmed chemotaxis buffer with anti-CCL19 or control sera (generated in-house[120]) at concentrations described in text, then 150µL was loaded into the lower chambers of 96-well HTS Transwell plates (Corning). 50µL of rested splenocytes ($5x10^5$ cells total) were subsequently loaded into upper permeable supports (5.0µm pore size, polycarbonate membrane) and incubated for 3 hours at 37°C, 5% CO_2.

For CCL20 chemotaxis, rested splenocytes were harvested and resuspended to $2x10^7$ cells/mL in fresh, pre-warmed chemotaxis buffer. Recombinant CCL20 was diluted to concentrations described in text with pre-warmed chemotaxis buffer, then 600µL was loaded into the lower chambers of 24-well HTS Transwell plates (Corning). 100µL of rested splenocytes ($1x10^7$ cells total) were subsequently loaded into upper permeable supports (5.0µm pore size, polycarbonate membrane, only 12 supports/24-well plate) and incubated for 3 hours at 37°C, 5% CO_2. Following the incubation, permeable supports were removed from Transwell plates and the undersides of the membrane were washed once to remove any migrated cells that were attached. Cells were subsequently harvested for flow cytometric staining. Prior to flow cytometric acquisition, 20µL of CountBright beads (ThermoFisher) were added to each sample to quantitate the number of migrated cells.

Migration index was calculated as:

$$\frac{\#\text{ of migrated cells in sample} \div x \text{ beads}}{\#\text{ of cells in no chemokine control} \div x \text{ beads}}$$

2.6 Cell culture

2.6.1 BMDC generation

BMDCs were generated as described elsewhere[253]. Briefly, harvested bone marrow was resuspended in R10 media to $2.5x10^6$ cells/mL, and 1mL was plated in 100mm bacterial culture Petri dishes with 9mL of R10 media supplemented with 20ng/mL recombinant GM-CSF (Biolegend). Cells were cultured for 3 days at 37°C, 5% CO_2, then topped up with an additional 10mL R10 media supplemented with 20ng/mL recombinant GM-CSF, and incubated for a further 3 days. After 6 days of culture, 10mL of media was carefully removed off the top and another 10mL R10 media supplemented with 20ng/mL recombinant GM-CSF was added. To activate BMDCs, loosely-adherent cells and cells in suspension were harvested after 9 days, centrifuged at 300rcf for 5 minutes, and resuspended to 10mL/100mm petri dish in R10 media supplemented with 20ng/mL recombinant GM-CSF and 200ng/mL LPS. 5mL of cells were plated in 60mm tissue culture dishes (BD) and incubated overnight at 37°C, 5% CO_2 for use the following day. Alternatively, immature BMDCs were frozen after 9 days of culture at a concentration of $5x10^6$ cells/mL in 9:1 (v/v) FCS and DMSO then stored in liquid nitrogen for future use. Defrosted BMDCs were activated following the above protocol after washing with R10 media and resuspending cells to $3x10^5$ cells/mL.

2.6.2 B300.19 culture

The B300.19 cell line, previously generated from murine pre-B cells[254], and a stably transfected, ACKR4 over-expressing B300.19 cell line (B300.19-ACKR4) were defrosted from liquid nitrogen storage, washed with B300.19 media and grown in non-adherent culture within T25 flasks (Corning) overnight at 37°C, 5% CO_2. Cells were split into T75 flasks (Corning) the following day and maintained until use. B300.19 cell lines were utilised in this study given their minimal endogenous chemokine receptor expression.

2.7 Immunofluorescent staining and Image Acquisition

2.7.1 Sectioning and immunofluorescent staining

Tissues sections of 12µm thickness were cut at -17°C on a Shandon cryotome and mounted on polysine coated slides (Thermo Scientific). Mounted sections were stored in the cryotome until all cutting was complete, then samples were air-dried at room temperature for 30 minutes. Samples were fixed and/or permeabilised by one of the following methods, as stated in text: 1) Fixed and permeabilised in ice-cold acetone for 10 minutes, air-dried until residual acetone had evaporated, then re-hydrated in TBS for 5 minutes at room temperature; 2) fixed in ice-cold 4% PFA for 20 minutes at 4°C, then washed in TBS; 3) fixed in ice-cold 4% PFA, washed, then fixed and permeabilised in ice-cold acetone as described; or 4) fixed in ice-cold 4% PFA, washed, then permeabilised in 0.05% saponin and washed in TBS. Sections were then blocked with 40µL of 1% (w/v) BSA, 2% (v/v) normal mouse, rat or goat serum in TBS for 1 hour in a humid chamber at room temperature. Slides were then washed

through three changes of TBS for 2 minutes each. Sections were then stained in a humid chamber, protected from light at room temperature unless otherwise noted, in the following order omitting steps that were not required. All primary and secondary reagents are listed in **Table 2.6**. First, sections were incubated with unconjugated primary antibodies diluted in 40µL of 1% BSA/TBS for 2 hours or overnight at 4°C. Several unconjugated antibodies could be used in tandem if they were derived from different host species and secondary reagents did not display cross-reactivity. Similarly, fluorescently conjugated antibodies could be included in this step if they were derived from a different host species and did not interfere with secondary detection. After washing, unconjugated antibodies were detected by incubation with 40µL of secondary antibodies diluted in 1% BSA/TBS for 2 hours. Washing was repeated, then unbound secondary antibody sites were blocked following a 45 minute incubation with 40µL of 1% BSA/TBS supplemented with 2% (v/v) of the primary antibodies species' serum. After washing, fluorescently conjugated and biotinylated antibodies were incubated on sections in 40µL of 1% BSA/TBS for 2 hours or overnight at 4°C. Slides were washed and biotinylated antibodies were detected by incubation with 40µL of streptavidin conjugates diluted in 1% BSA/TBS for 1 hour. After a final wash, slides were partially air-dried upright in a covered slide box until residual TBS from washes had evaporated but sections were still damp. Sections were mounted with Vectashield antifade mounting medium (Vector Laboratories) and an appropriately-sized coverslip (Deckgläser). Coverslips were sealed with nail polish and stored at 4°C in the dark until required for imaging.

2.7.2 Whole-mount immunofluorescent staining

Ventral ear sheets were incubated dermis-side down in 48-well plates (Costar) with 150µL of 1% BSA in PBS with anti-CCL21 and anti-LYVE-1 or anti-CD31 (see **Table 2.6**) overnight at 4°C. Ear sheets were subsequently washed three times in PBS and incubated for 4 hours at 4°C with secondary reagents diluted in 400µL of 1% BSA in PBS. After washing, ear sheets were fixed in 1% PFA for 20 minutes at 4°C, then were blotted dry and mounted dermis-side up on polysine coated slides with square coverslips and Vectashield antifade mounting medium. Coverslips were sealed with nail polish and slides were stored at 4°C in the dark until imaging that day.

2.7.3 BMDC ear sheet crawl in

BMDC crawl in assays were performed as described elsewhere[253], with minor modifications. Ventral ear sheets were incubated dermis-side down in 48-well plates with anti-LYVE-1 in 150µL of R10 media at room temperature for 45 minutes. Ear sheets were subsequently washed with PBS three times, then stained with secondary reagents in 400µL of R10 media at room temperature for 45 minutes. During this incubation, LPS-activated BMDCs were harvested and fluorescently labelled with Cell Proliferation Dye eFluor670 (eBioscience) as per manufacturer's protocol. BMDCs were subsequently filtered through a 50µm filter (BD) and resuspended to $1x10^6$ cells/mL in pre-warmed R10 media supplemented with 10mM HEPES ready for use. Ear sheets were washed, then mounted flat, dermis-side up in the middle of 35mm petri dishes (Costar). A 7x15x2mm metal washer was then centred and mounted flat on the ear sheet, then the outside edge was sealed with heated 1.5% agarose.

Once the agar had set, 150µL of BMDCs were carefully added to the centre of the washer to avoid spilling, then samples were incubated with the lids on for 45 minutes at 37°C, 5% CO_2. After the incubation, residual BMDC media was removed from the centre of the washer, the apparatus was dismantled and tissue washed in PBS. Ear sheets were then fixed in 1% PFA for 20 minutes at 4°C, and then mounted for imaging as described above.

For CCL19 neutralised BMDC ear sheet crawl in, ear sheets were incubated in 150µL of 2mg/mL anti-CCL19 (generated in-house[120]) or control pre-bleed IgG for 45 minutes at 4°C. Ear sheets were then blotted dry and mounted for BMDC migration. After migration, dismantling and washing, ear sheets were fixed in 1% PFA for 20 minutes at 4°C, then lymphatic vessels were stained and samples mounted for imaging as described above.

2.7.4 Confocal Microscopy

Images were acquired on a Leica TCS SP5 confocal microscope with a 10x harmonically corrected plan-apochromat with NA 0.4, or 20x harmonically corrected plan-apochromat with NA 0.7 water objective, using Leica Application Suite: Advance Fluorescence (LAS: AF) software and sequential scanning between frames. Images were processed with LAS: AF Lite Version 2.6.3 (Leica), FIJI (Image J, National Institutes of Health), and/or Adobe Photoshop CS6 Version 13.0 (Adobe) for presentation, with brightness and contrast adjustments applied equally across images.

2.7.5 Intravital Imaging

Intravital imaging experiments were designed/analysed by Cameron Bastow and designed/performed by Dr. Sapna Devi and Prof Scott Mueller at the Doherty Institute, Melbourne. BMDCs were defrosted and activated overnight with LPS as described above. Activated BMDCs were harvested and labelled with 5µM CellTrace Violet (Molecular Probes) at 37°C for 10 minutes. 1-2x10^6 labelled BMDCs mixed with 50ng LPS in a final volume of 60µL was injected s.c. into the footpad of anesthetised WT or *Ackr4*$^{-/-}$ recipient mice. To label lymphatic vessels, 5µg of anti-LYVE-1-AF594 (R&D Systems, conjugated in-house with AlexaFluor594 Monoclonal Antibody Labelling Kit, Invitrogen) was co-injected s.c. into the footpad. Using a modified version of a published protocol[74], intravital imaging of the footpad was performed between 12-21 hours post-injection. Briefly, mice were anaesthetised via isoflurane inhalation and the hair around the hind paws was removed. Mice were maintained on a heat pad and kept at a core temperature of 37°C. The hind paw was placed on an elevated metal slide and vacuum grease was applied around the footpad. The footpad was then immersed in PBS before cover-slipping. For visualisation of blood vasculature, 50µL of 0.1% Evans Blue (Sigma) dissolved in PBS was administered i.v. Time-lapse imaging was performed using an upright FVMPE-RS multiphoton microscope (Olympus) equipped with at 25x/1.0 NA water immersion lens, enclosed in a custom-built environmental chamber (Precision Plastics) that was maintained at 35°C with heated air. Fluorescence excitations were performed at 800nm using an InSight pulsed infrared laser (Spectra Physics). Image stacks were acquired every minute over a one-hour imaging period. Raw imaging data were processed with Imaris 7 (Bitplane).

2.8 Image analyses

2.8.1 CCL21 gradient calculations

Using FIJI (Image J, National Institutes of Health), Z-stack images were split into single channels and collapsed into a max projection image. Lymphatic vessel masks were generated after applying thresholds to LYVE-1 single channel images and removing outlying noise. Using the "Distance Map" function in FIJI, a new image was generated from lymphatic vessel masks where the grey value of each pixel was equal to the distance of the pixel from the nearest lymphatic vessel mask. By applying sequential thresholds to this distance map, multiple regions of interest (ROIs) 10pixels in width (7.6μm) and increasing in distance from the initial lymphatic vessel mask by 10pixel increments were delineated. These ROIs were then applied to the respective max projection CCL21 single channel image to calculate the mean grey value within these areas, then CCL21 mean grey values were normalized to the average CCL21 intensity across all wildtype images within each independent experiment. Only distances up to 90μm were analysed given the reported increase in CCL21 staining background at greater distances[4]. Distance values were plotted using the upper distance of the respective mask range, i.e. the distance range of 0-7.6μm is plotted at x=7.6μm. Here, the distance of 0μm is the range -7.6-0μm from lymphatic vessel masks, i.e. within the lymphatic vessel mask.

2.8.2 BMDC crawl in assay

Max projection images and lymphatic masks were generated as described above. Two ROIs were then set for LYVE-1-positive and -negative staining areas. These ROIs were then applied to the respective max projection of the BMDC Cell Proliferation Dye eFluor670 images to calculate mean grey intensity values within these areas. Data were then expressed as the ratio of Cell Proliferation Dye eFluor670 mean grey intensity inside:outside LYVE-1^+ masks.

2.8.3 Two-photon BMDC tracking

Images were imported and processed in Imaris 8.1.2 (Bitplane). First, images were corrected for drift using the "Spots" function and static blood vasculature visualised by Evans Blue Dye, as required. Then lymphatic vessels identified by LYVE-1 staining were rendered in 3D, and a distance transformation was performed using the Matlab extension on the outside surface of the vessels. This generated a new channel where the grey value of each pixel was equal to the distance of the pixel from the nearest lymphatic vessel within a 3D space. All BMDCs that could be reliably followed were manually tracked using the "Spots" function within Imaris. Mean speed, and track straightness, length and duration were calculated using the statistics tools in Imaris. BMDC distance from the nearest lymphatic vessel was calculated from the mean intensity of the BMDC within the distance transformation channel generated as described above at each timepoint. Displacement relative to nearest lymphatic vessel was calculated by:

$$\text{initial distance from nearest LV - final distance from nearest LV } (\mu m)$$

Subsequently, velocity towards lymphatic vessel was calculated by:

$$\frac{\text{displacement relative to nearest LV } (\mu m)}{\text{track duration } (min)}$$

And lymphatic vessel homing efficiency was determined by:

$$\frac{\text{displacement relative to nearest LV } (\mu m)}{\text{track length } (\mu m)}$$

2.8.4 Foxp3 cell enumeration

Images were first stitched together in FIJI using the "MosaicJ" plugin when applicable. Then ROIs for the periarteriolar lymphatic sheath (PALS) and B cell follicles were drawn manually based on CD4 and IgD staining, respectively. Germinal centres were identified by the lack of IgD staining in areas surrounded by IgD^+ follicular mantles, then ROIs were drawn manually. The T-B border was defined as the area of the PALS ≤50μm from an adjacent follicle or germinal centre perimeter[132] using the "Distance Map" function in FIJI. The T-zone was then defined as the area of the PALS minus the T-B border. $Foxp3^+$ cells were automatically identified using the "Analyse Particles" function with a minimum size of 70pixels-squared. Larger cell aggregates were manually excluded from analysis. The number of $Foxp3^+$ cells in each ROI and the area of each zone were subsequently calculated for analyses.

2.9 Statistical Analyses

Data was presented and analysed in GraphPad Prism 7 with statistical tests described in text.

Table 2.1: Genotyping primers

Primer	Sequence 5' → 3'	Final Concentration (µM)	Annealing Temperature (°C)
CCR6 Genotyping- WT amplicon: 375bp, Mutant amplicon: 300bp			57.9
Ccr6 forward	TCTGCACTAGTGAGAGTGTG	1	
Ccr6 reverse	GTCATCACCACCATAATGTTG	0.5	
Ccr6 mutant reverse	GAACGAGATCAGCAGCCTCT GTTCC	0.5	
CXCR5 Genotyping- WT amplicon: 311bp, Mutant amplicon: 241bp			58
Cxcr5 forward	CGGAGATTCCCCTACAGGAC	0.8	
Cxcr5 reverse	GATCTTGTGCAGAGCGATCA	0.8	
Cxcr5 mutant reverse	AATTCGCCAATGACAAGACG	0.8	
ACKR4 Genotyping- WT amplicon: 325bp, Mutant amplicon: 630bp			60
Ackr4 forward	TTTCTTCCACGTTCTGTCTCTG	0.8	
Ackr4 reverse	GCTCATCAAGATGCCCAACA	0.4	
Ackr4 mutant reverse	TTTGGCAAAGAATTCACTCCT C	0.4	
GFP Genotyping- GFP amplicon: 344bp			67
Gfp forward	CCTACGGCGTGCAGTGCTTCA GC	1	
Gfp reverse	CGGCGAGCTGCACGCTGC	1	

Table 2.2: qPCR primers

Target	Forward 5' → 3'	Reverse 5' → 3'
Ackr1	CCTGAACCCCAGACTGAATATTG	TCCCCAAAGTCCCACACTGA
Ackr2	CTG CAT GAG CCT GGA CAA ATA C	AAC TGG GCC TTC GGT CTG T
Ackr3	GCTACAAACTGCTCAGCACTGAA	TCCTGGGCTGTGGTTTGC
Ackr4	AATGCTAGGTGCACTCCCATCT	CCGATTTCCAGCATCTGAATG
Ackr5	TTGTGCAAGGATACAGGGTGTT	CAATACCACAAGACACTGTCGTG
Axin2	GGTTCCGGCTATGTCTTTGC	CAGTGCGTCGCTGGATAACTC
Bcl6	GCACTGGGCAAACACAACAT	AGCGTGCCGGGTAAACTG
Ccl19	CCTGGGTGGATCGCATCA	TGCCTTTGTTCTTGGCAGAA
Ccl20	TGCTTTTTTGGGATGGAATTG	TGCAGTGATGTGCAGGTGAA
Ccl21	GCAAAGAGGGAGCTAGAAAACAGA	TGGACGGAGGCCAGCAT
Ccl25	GACTGCTGCCTGGGTTACCA	CCTAGCATGCCGGAGAACA
Ccr1	TGGGAGTTCACTCACCGTACCT	TCCACTGCTTCAGGCTCTTGT
Ccr2	GTTCATCCACGGCATACTATCAAC	GCCCCTTCATCAAGCTCTTG
Ccr3	TTGCCTACACCCACTGCTGTAT	TTTCCGGAACCTCTCACCAA
Ccr4	GCAACACTGCAAGAATGAGAAGA	GACCACCACGGCGAAGAT
Ccr5	CATCCGTTCCCCCTACAAGA	GGAACTGACCCTTGAAAATCCA
Ccr6	CCTGGGCAACATTATGGTGGT	CAGAACGGTAGGGTGAGGACA
Ccr7	CATTGCCTATGACGTCACCTACA	GAAGGCATACCAGAAAGGGTTGA
Ccr8	GCTCGCTCAGATAATTGGTCTTC	CGTGACGTTGGGCTCCAT
Ccr9	CAGTTCTGAGGAGGATGCTTGA	AACCCAGCTGCACTGATGATC
Ccr10	CCTCTACTCGGCCTCTTTCCA	CGGTCGGCGCTGATACAG
Cx3cr1	ATCAGCATCGACCGGTACCT	CTGCACTGTCCGGTTGTTCAT
Cxcr1	TGTCCCACATATTTGGCTTCCT	GCCCGTAGCAGACCAGCAT
Cxcr2	GCCCTGACCTTGCCTGTCT	TGCACAGGGTTGAGCCAAA
Cxcr3	TACCTTGAGGTTAGTGAACGTCA	CGCTCTCGTTTTCCCCATAATC
Cxcr4	ACCTCTACAGCAGCGTTCTCATC	TGTTGGTGGCGTGGACAATA
Cxcr5	GGGCTCCATCACATACAATATGG	GAATCTCCGTGCTGTTACTGTAGAAG
Cxcr6	CCGGCAGGCTAAGTGGAA	CACCCAAATGAGCAAGCAAA
Gapdh	ACCCAGAAGACTGTGGATGG	CAGTGAGCTTCCCGTTCAG

Il21	CTATGAAAATGACTTGGATCCTGAAC	CATGCTCACAGTGCCCCTTT
Lef1	TGGAGATGGAAGCTTGTTGAAA	CAGGGTAAGGTTGCTGTCAGTGT
Rplp0	TGCAGATCGGGTACCCAACT	ACGCGCTTGTACCCATTGA
Xcr1	CATGACCATCCACCGATACCT	GCTGCCCACACACATGATGT

Table 2.3: ELISA antibodies

Specificity	Conjugate	Isotype	Clone	Source	Final Concentration (µg/mL)
CCL19	purified	rat IgG2a	87102	R&D (MAB880)	2
	biotin	goat IgG	polyclonal	R&D (BAF880)	0.2
CCL20	purified	rabbit Ig	polyclonal R13 d26	in-house[255]	0.484
	biotin	rabbit Ig	polyclonal R13 d26	in-house[255]	2.96
total CCL21	purified	goat IgG	polyclonal	R&D (AF457)	1
	biotin	goat IgG	polyclonal	R&D (BAF457)	0.05
full-length CCL21	purified	rat IgG2b	59106	R&D (DuoSet, MAB457)	2
CCL25	purified	rat IgG2a	89827	R&D (MAB4811)	2
	biotin	goat IgG	polyclonal	R&D (BAF481)	0.05
mouse IgG	HRP	goat IgG	polyclonal	Thermo	0.08

Table 2.4: Flow Cytometry antibodies

Specificity	Conjugate	Isotype	Clone	Source	Final Concentration (µg/mL)
ACKR4	PE	mouse IgG2b	13E11	Prof. Joe Chiba, conjugated in-house	1µL/2x10^5 cells
B220 (CD45R)	FITC	rat IgG2a	RA3-6B2	BD	2.08
	PE-CF594	rat IgG2a	RA3-6B2	BD	0.66
	PerCP-Cy5.5	rat IgG2a	RA3-6B2	BD	0.83
	PE-Cy7	rat IgG2a	RA3-6B2	BD	0.83
	BV421	rat IgG2a	RA3-6B2	BD	0.83
	BV510	rat IgG2a	RA3-6B2	Biolegend	0.33
CCR6	purified	rat IgG2a	140706	R&D	8.33
	PE	rat IgG2a	140706	R&D	10µL/well
CD3ε	PE-Cy7	arm ham IgG	145-2C11	eBioscience	0.83
CD4	PE	rat IgG2a	H129.19	BD	0.83
	PE-Cy7	rat IgG2a	RM4-5	BD	0.83
	V450	rat IgG2a	RM4-5	BD	0.83
	BV786	rat IgG2a	RM4-5	BD	0.83
CD26	PE-Cy7	rat IgG2a	H194-112	Biolegend	1.11
CD31	FITC	rat IgG2a	MEC 13.3	BD	4.17
CD38	APC	rat IgG2a	90	eBioscience	0.67
CD44	biotin	rat IgG2b	IM7	BD	2.08
	FITC	rat IgG2b	IM7	BD	2.08
	PE	rat IgG2b	IM7	eBioscience	0.83
CD45	PE	rat IgG2b	30-F11	BD	0.83
CD45.2	biotin	mouse IgG2a	104	BD	2.08
	PerCP-Cy5.5	mouse IgG2a	104	eBioscience	0.83
	PE-Cy7	mouse IgG2a	104	Biolegend	0.83
CD90.2 (Thy1.2)	APC	rat IgG2a	53-2.1	BD	0.83
CD138	PE	rat IgG2a	281-2	BD	0.83
	APC	rat IgG2a	281-2	BD	0.83
CD140α (PDGFRα)	BV421	rat IgG2a	APA5	BD	1.11

Specificity	Conjugate	Isotype	Clone	Source	Final Concentration (µg/mL)
CXCR5	purified	rat IgG2a	2G8	BD	4.17
	biotin	rat IgG2a	2G8	BD	8.33
EpCAM (CD326)	purified	rat IgG2a	G8.8	BD	2.08
Erythrocytes	PE	rat IgG2b	Ter119	BD	0.83
Fas (CD95)	PE-Cy7	arm ham IgG	Jo2	BD	0.83
Foxp3	FITC	rat IgG2a	FJK-16s	eBioscience	3.33
	PerCP-Cy5.5	rat IgG2a	FJK-16s	eBioscience	1.33
gp38 (podoplanin)	biotin	syr ham IgG	eBio8.1.1	eBioscience	2.78
I-A[b]	BV421	mouse IgG2a	AF6-120.1	BD	0.83
I-A/I-E	biotin	rat IgG2a	2G9	BD	2.08
IgD	PerCP-eFluor710	rat IgG2a	11-26c	eBioscience	0.67
	APC	rat IgG2a	11-26c	eBioscience	0.83
	BV421	rat IgG2a	11-26c.2a	Biolegend	0.83
IgD[b]	biotin	mouse IgG1	217-170	BD	2.08
IgG1 (intracellular)	PE-Cy7	rat IgG	M1-14D12	eBioscience	0.83
IgM (intracellular)	FITC	rat IgG2a	eB121-15F9	eBioscience	2.78
LYVE-1	purified	rat IgG2a	223322	R&D	5.21
GL7 (Neu5Ac)	FITC AF647	rat IgM rat IgM	GL7 GL7	BD BD	2.78 0.83
Neuropillin-1 (CD304)	BV421	rat IgG2a	3E12	Biolegend	0.10
PD-1 (CD279)	PE	arm ham IgG	J43	eBioscience	0.83
	PE-Cy7	arm ham IgG	J43	eBioscience	0.83
PSGL-1 (CD162)	PE	rat IgG1	2PH1	BD	0.83
Sca-1 (Ly-6A/E)	FITC	rat IgG2a	D7	eBioscience	2.08
TCRβ	PE	arm ham IgG	H57-597	eBioscience	0.66

Table 2.5: Additional Flow Cytometry reagents

Product	Conjugate	Isotype	Source	Final Concentration (µg/mL)
anti-human IgG	biotin	goat Ig	Jackson ImmunoResearch	1/100
anti-rat IgG	AF488	goat Ig	Molecular Probes	10
	FITC	donkey Ig	Jackson ImmunoResearch	1/625
	PE	donkey Ig	Jackson ImmunoResearch	1/625
	AF647	goat Ig	Molecular Probes	10
ELC-Fc	human Fc		Prof. Jason Cyster	15µL/well
Fixable Viability Stain FVS780			BD	1/1000
LIVE/DEAD Fixable Near-IR Dead Cell Stain Kit			Molecular Probes	1/1000
LIVE/DEAD Fixable Blue Dead Cell Stain Kit			Molecular Probes	1/500
$NP_{(24)}$	PE		Biosearch Technologies	50
Streptavidin	PE		BD	1
	PerCP-Cy5.5		BD	1
	AF647		Jackson ImmunoResearch	1
	BV421		Biolegend	1
	V450		BD	1
	BV510		BD	1

Table 2.6: Immunofluorescence antibodies

Specificity	Conjugate	Isotype	Clone	Source	Final Concentration (µg/mL)
ACKR4	purified	goat IgG	C-16	Santa Cruz	4
	purified	mouse IgG2b	13E11	Prof. Joe Chiba	1
	purified	mouse IgG2a	2F11	Prof. Joe Chiba	1
	biotin	mouse IgG2b	13E11	Prof. Joe Chiba, biotinylated in-house	5
	biotin	mouse IgG2a	2F11	Prof. Joe Chiba, biotinylated in-house	5
B220 (CD45R)	FITC	rat IgG2a	RA3-6B2	BD	1.25
CCL20	biotin	goat IgG	BAF760 (Cat#)	R&D	5
CCL21	biotin	goat IgG	BAF457 (Cat#)	R&D	4
CD4	AF647	rat IgG2a	RM4-5	BD	0.67
	V450	rat IgG2a	RM4-5	BD	0.5
CD16/32	FITC	rat IgG2b	2.4G2	BD	3.33
CD31	purified	rat IgG2a	MEC 13.3	BD	0.78
Cytokeratin 5	purified	rabbit IgG	EP1601Y	Abcam	0.35
EpCAM (CD326)	purified	rat IgG2a	G8.8	BD	5
Foxp3	biotin	rat IgG2a	FJK-16s	eBioscience	5
IgM	FITC	rat IgG2a	eB121-15F9	eBioscience	2.5
IgD	APC	rat IgG2a	11-26c	eBioscience	1
LYVE-1	purified	rat IgG2a	223322	R&D	2.5
GL7 (Neu5Ac)	FITC	rat IgM	GL7	BD	5
Vimentin	purified	rabbit IgG	D21H3	Cell Signalling Technology	1/200
anti-goat IgG	AF488	donkey		Molecular Probes	5
anti-mouse IgG	Cy3	donkey		Jackson ImmunoResearch	1/200

Specificity	Conjugate	Isotype	Clone	Source	Final Concentration (µg/mL)
anti-rabbit Ig	Cy3	donkey		Jackson ImmunoResearch	1/150
	Cy5	donkey		Jackson ImmunoResearch	1/150
anti-rat IgG	FITC	donkey		Jackson ImmunoResearch	2
	AF488	goat		Molecular Probes	8
	AF647	goat		Molecular Probes	8
	BV421	goat		Biolegend	1/30
Streptavidin	AF546			Molecular Probes	1
	AF647			Jackson ImmunoResearch	1.875

Chapter 3
Results- ACKR4 regulates peripheral CCL21

Chapter 3 - Results - ACKR4 regulates peripheral CCL21

3.1 Overview

The CCR7-CCL21 chemokine axis governs multiple migratory processes essential for dendritic cell egress from barrier tissues. Primarily, extracellular immobilised gradients of CCL21 generated by LECs guide mature dendritic cells towards lymphatic vessels[4]. Immobilised CCL21 gradients are configured within a narrow functional range[13], however the mechanisms that regulate gradients in peripheral tissues remains unknown. The atypical chemokine receptor ACKR4 scavenges CCR7 ligands CCL19 and CCL21[26,27], regulates CCL21 gradients in the lymph node[80], and is expressed in multiple barrier tissues[100,112,118]. Yet it is unknown whether ACKR4 in peripheral tissues regulates CCL21 abundance and/or distribution at these sites.

3.2 CCL19 and CCL21 abundance is dysregulated in ACKR4-deficient tissues

To investigate a role for ACKR4 in chemokine scavenging in barrier tissues, chemokine leach out assays were performed on a variety of epithelial tissues, making comparisons between wildtype and *Ackr4*$^{-/-}$ mice. The skin, lungs, small intestine and vagina from steady-state adult mice were harvested, weighed, and the quantity of ACKR4 ligands CCL21, CCL19 and CCL25 that leached out of these tissues after 3 hours was quantified by ELISA. Increased CCL21 abundance was previously reported in the circulation of *Ackr4*$^{-/-}$ mice[102], thus cardiac perfusion was performed prior to harvesting tissues to remove circulating blood and minimise the impact of serum CCL21 on the quantitation of CCL21 in tissues. As the levels of chemokines specifically in barrier tissues was of interest, Peyer's patches were removed from the small intestine to not confound the results with any CCL19 and CCL21 present in secondary lymphoid tissue. Strikingly, CCL21 was hyperabundant by approximately 2-10-fold in all ACKR4-deficient barrier tissues assayed (Figure 3.1.A). In addition, approximately 2-fold more CCL19 leached out of ACKR4-deficient dorsal and ear skin than wildtype skin, however no difference in CCL19 abundance between ACKR4-deficient and wildtype mice was observed at other barrier sites (Figure 3.1.A). There was no statistically significant difference in the abundance of the small intestine-tropic chemokine CCL25 between ACKR4-deficient and wildtype mice (Figure 3.1.A), suggesting that ACKR4 does not regulate CCL25 at this site. Together, these data indicate that ACKR4 regulates chemokine levels at barrier sites, and appears to have a more pronounced role in the regulation of CCL21 than CCL19 or CCL25.

The observation that ACKR4-deficient mice exhibited hyperabundant CCL21 in the skin was contrary to a published report[100] and highlighted another example of disparity in CCL21 quantification in ACKR4-deficient mice between our laboratory and others[80,102,103,117]. A notable technical difference between the studies were the different ELISA capture antibodies

utilised. Therefore, the ability of these antibodies to detect all endogenous forms of murine CCL21 was compared. To generate both forms of CCL21 *in vitro* to test the binding capacity of these antibodies, full-length (12kDA) recombinant CCL21 was incubated with activated BMDCs which have been reported to process full-length CCL21 into its cleaved (8kDA) form[7]. These forms of CCL21 were then size-discriminated via western blot and detected with the different ELISA capture antibodies. Both full-length and cleaved CCL21 were detected with the polyclonal goat anti-CCL21 antibody used in Figure 3.1.A and in previous publications from our laboratory[102,103,122] (Figure 3.1.B). Importantly, the monoclonal rat antibody, a component of the R&D Systems murine CCL21 ELISA DuoSet kit utilised by other investigators[80,100,117] only detected full-length CCL21 (Figure 3.1.B). Reblotting western membranes with a third commercial antibody previously used by Schumann and colleagues[7] confirmed that cleaved CCL21 was present but not detected by the monoclonal rat antibody (Figure 3.1.B). Utilising the rat monoclonal antibody from the R&D Systems CCL21 ELISA DuoSet as the capture antibody on the same tissue supernatants in Figure 3.1.A reproduced the ELISA data reported by Bryce et al., with no difference in full-length CCL21 between wildtype and ACKR4-deficient skin[100] (Figure 3.1.C). This demonstrated that the different capture antibodies used by different groups was likely responsible for the prior conflicting CCL21 measurements observed in *Ackr4*$^{-/-}$ mice. More importantly, this clearly demonstrated that ACKR4 regulates the abundance of cleaved, soluble CCL21 in barrier tissues.

Having established new methods to distinguish full-length and cleaved forms of CCL21 by ELISA, quantitation of serum CCL21 was revisited to determine the relative contributions of these forms to the hyperabundant CCL21 previously observed in the serum of *Ackr4*$^{-/-}$ mice[102]. Consistent with data previously reported[102], CCL21 was detectable in wildtype sera and was approximately 8-fold greater in the serum of ACKR4-deficient mice when utilising the polyclonal goat antibody that binds both forms of CCL21 (Figure 3.1.D). However, no CCL21 was detected in sera of wildtype or *Ackr4*$^{-/-}$ mice when utilising the monoclonal rat antibody that only binds full-length CCL21 (Figure 3.1.D). This implied that cleaved soluble CCL21 is the dominant form present in blood and this form is hyperabundant in the circulation of *Ackr4*$^{-/-}$ mice. Given the elevated abundance of soluble CCL21 in all barrier tissues and the blood of *Ackr4*$^{-/-}$ mice, the abundance of CCL21 was measured in other major organs as the full extent of chemokine dysregulation in *Ackr4*$^{-/-}$ mice was unknown. Subsequently, the amount of CCL21 that leached out from heart, kidneys, liver and spleen of wildtype and *Ackr4*$^{-/-}$ mice was determined by ELISA. Consistent with previous data[102] there was no difference in CCL21 abundance in the spleen between wildtype and *Ackr4*$^{-/-}$ mice (Figure 3.1.E). CCL21 was hyperabundant by approximately two-fold in ACKR4-deficient heart, kidney and liver compared to wildtype organs (Figure 3.1.E). This suggested that ACKR4 function may be required within these internal organs to regulate the abundance of local CCL21, or alternatively, that peripheral CCL21 could accumulate at these sites due to hyperabundance in the blood. However, if these differences are due to excess CCL21 entering these organs from the blood, it is unknown why no differences in CCL21 are apparent in spleen as it is a highly vascularised organ. In summary, these data have resolved

an outstanding issue in the literature regarding the role of ACKR4 in regulation of CCL21 *in vivo.* The reported discrepancies appear to be due to different ELISA capture antibodies which distinguish between the full-length and cleaved forms of CCL21. The data here point to a role for ACKR4 in regulating soluble CCL21, particularly in barrier tissues. Therefore, a more detailed investigation of the role of ACKR4 in regulating CCL21 at these sites followed.

3.3 Post-translational accumulation of chemokines in *Ackr4*$^{-/-}$ mice is consistent with a loss of ACKR4-scavenging function

It was unknown whether perturbed dermal chemokine abundance in *Ackr4*$^{-/-}$ mice was due to a loss of scavenging function or other differences in chemokine expression resultant of ACKR4-deficiency. It was reasoned that if local ACKR4 expression regulated CCL21 abundance in the tissue, tissues with the greatest *Ackr4* expression would display the greatest extent of CCL21 dysregulation. To test this, the levels of *Ackr4* mRNA were determined in multiple barrier tissues harvested from steady-state wildtype mice. As anticipated, there was a significant positive correlation between the extent of CCL21 hyperabundance in *Ackr4*$^{-/-}$ tissues and the relative level of *Ackr4* transcript expressed by wildtype mice in that tissue (Figure 3.2.A). This strongly suggested that the extent of ligand over-abundance in ACKR4-deficient barrier tissues was linked to the level of *Ackr4* expression normally present at that site, which lend credence to the hypothesis that ACKR4 scavenges chemokines locally at barrier sites. Another possible explanation for the changes in chemokine levels observed in *Ackr4*$^{-/-}$ mice was that production of these chemokines was increased in the absence of ACKR4. Therefore, the relative expression levels of mRNAs encoding *Ccl21*, *Ccl19* and *Ccl25* were measured in wildtype and *Ackr4*$^{-/-}$ tissues to determine whether differences in chemokine abundance could be accounted for by altered chemokine transcription in *Ackr4*$^{-/-}$ mice. No statistically significant differences were observed for any of these chemokine transcripts between wildtype and ACKR4-deficient tissues (Figure 3.2.B), indicating that the increases in protein abundance of these chemokines was post-transcriptionally regulated, again consistent with the notion of local chemokine scavenging. Conceivably, increased chemokine levels may arise from an increase in the frequency of the cellular source of that chemokine. In the case of CCL21 in skin, the predominant cellular source is LECs[4,68,69], thus single cell suspensions were prepared from wildtype and ACKR4-deficient ears and LECs ($CD45^{-}Ter119^{-}gp38^{+}CD31^{+}$) were enumerated. There were no differences in the density of LECs between wildtype and ACKR4-deficient skin (Figure 3.2.C). Altogether, the data are consistent with local ACKR4 regulating the abundance of homeostatic CCL19 and CCL21 at barrier sites post-transcriptionally through ligand scavenging.

3.4 ACKR4 regulates dermal CCL21 gradients

A key advance in understanding the molecular mechanisms that guide dendritic cell egress from the skin was the visualisation and measurement of immobilized extracellular CCL21

gradients at this site via whole-mount immunofluorescence[4]. Whilst no difference in full-length CCL21 was observed via ELISA in *Ackr4*$^{-/-}$ mice (Figure 3.1.C), the leach-out assays used for ELISA analyses likely bias towards the detection of soluble CCL21 as a greater proportion of immobilized CCL21 would be retained within tissues. Thus to determine whether ACKR4 shaped functional immobilised CCL21 gradients in skin, the method developed by Weber *et al.* was utilised and applied to ear sheets from wildtype and *Ackr4*$^{-/-}$ mice in the steady-state. Briefly, whole ear sheets were split into dorsal and ventral halves, then stained with saturating concentrations of anti-CCL21 without fixation or permeabilisation to visualise only extracellular CCL21, and lymphatic vessels were visualised by LYVE-1 staining. Notably, the goat polyclonal anti-CCL21 antibody previously demonstrated to bind both full-length and cleaved CCL21 (Figure 3.1.B) is required to visualise CCL21 in this assay. Whilst full-length and cleaved CCL21 cannot be distinguished by this antibody, conceptually it is unlikely that significant quantities of soluble chemokine would remain in these tissue samples given the extended processing time and washing steps involved. Indeed, addition of exogenous cleaved CCL21 to wildtype ear sheets does not increase CCL21 fluorescence intensity[4]. In wildtype tissue (Figure 3.3.A, top panel), CCL21 staining was most intense in close proximity to LYVE-1^{+} lymphatic vessels, whereas large areas between lymphatic vessels were devoid of CCL21 staining (highlighted in single-stained image with asterisks). Strikingly, hyperabundant immobilised CCL21 was visible in ACKR4-deficient ear sheets, both on LYVE-1^{+} lymphatic vessels and within interstitial spaces (Figure 3.3.A, bottom panel). Quantifying the amount of CCL21 in images by mean grey intensity revealed that ACKR4 was required to control CCL21 abundance within LYVE-1^{+} lymphatic vessel areas (Figure 3.3.B). By calculating the intensity of CCL21 as the distance from nearest lymphatic vessel edge increased, the CCL21 gradient could be measured and compared between ACKR4-sufficient and -deficient tissues. As previously reported in wildtype tissue[4], CCL21 intensity was greatest at the lymphatic vessel edge and was significantly decreased in areas distant from lymphatic vessels (Figure 3.3.C). In *Ackr4*$^{-/-}$ tissue, a gradient of CCL21 most intense at the lymphatic vessel edge was also detected, however the intensity of CCL21 was 2-3-fold greater in *Ackr4*$^{-/-}$ tissue compared to wildtype tissue at each distance measured from lymphatic vessels (Figure 3.3.C). These data demonstrated that, in addition to regulating solubilised CCL21, ACKR4 also regulates the abundance of immobilised full-length CCL21 in the skin. Contrary to observations in the lymph node[80], ACKR4 was not required to generate an immobilised CCL21 gradient, but rather regulated the overall abundance of CCL21 throughout these gradients. This supported the findings of Weber and colleagues which suggested that gradient formation occurred via chemokine diffusion from the lymphatic endothelium and was not dictated by distribution of immobilisation sites[4].

Whilst heparin sulphate has previously been identified as the key agent responsible for immobilizing CCL21 in interstitial areas, immunofluorescent staining on ear sheets had also identified high expression of heparin sulphate on the surface of blood capillaries[4]. This was of particular interest as aberrant CCL21 deposits visualised in *Ackr4*$^{-/-}$ ear tissue appeared to decorate fine vessels that did not stain with anti-LYVE-1 antibodies (Figure 3.3.A, bottom

panel, highlighted with arrows). A similar staining pattern was observed after the addition of exogenous recombinant CCL21 to wildtype ear sheets in the study by Weber and colleagues[4]. Therefore, to determine whether hyperabundant CCL21 in ACKR4-deficient skin had accumulated aberrantly on the surface of blood capillaries, ear sheets were stained with anti-CD31 to visualise both blood capillaries and lymphatic vessels. In wildtype tissue, CCL21 was identified in close proximity to large lymphatic vessels that were present in the deeper dermal areas predominantly occupied by blood capillaries (Figure 3.4.A, top panel). Little CCL21 was observed associated with, or in close proximity to, $CD31^+$ blood capillaries (Figure 3.4.A, top panel, highlighted with arrows). Loss of ACKR4 resulted in accumulation of CCL21 throughout the deeper dermal areas occupied by blood vasculature, and deposits of CCL21 were observed lining blood capillaries (Figure 3.4.A, bottom panel, highlighted with arrows). Quantitation of CCL21 in these images demonstrated that CCL21 did not form a gradient towards $CD31^+$ vessels, consistent with the role for CCL21 in lymphatic homing, and that CCL21 was 2-3-fold greater in *Ackr4*$^{-/-}$ tissue compared to wildtype tissue at all distances from $CD31^+$ vessels (Figure 3.4.B). These results highlight a key role for ACKR4 in limiting aberrant binding of CCL21 to blood vasculature in the dermis.

3.5 Radio-resistant ACKR4 expression regulates chemokine abundance

The cellular compartment in which ACKR4 operates to control chemokines in barrier tissues is not well understood as ACKR4 expression has been visualised in multiple cutaneous cell populations of both stromal and haematopoietic origin with *Ackr4*^{EGFP} mice[100,112]. To investigate cutaneous ACKR4 expression, bone marrow chimeras were generated, hereby denoted as: bone marrow donor genotype → stromal host genotype, to determine whether the ligand scavenging activity of ACKR4 functioned within a haematopoietic or stromal/radio-resistant cell type. Lethally irradiated Ly5.1 or Ly5.1*Ackr4*$^{-/-}$ hosts were reconstituted with wildtype or *Ackr4*$^{-/-}$ bone marrow to generate chimeric mice where ACKR4-deficiency was restricted to the haematopoietic or stromal compartment. After 8 weeks recovery following bone marrow reconstitution, ear sheets were harvested from resting chimeras and CCL21 was both visualised by confocal microscopy and quantified via ELISA. Chimeric mice displayed reduced overall abundance of CCL21 (Figure 3.5.A,B) compared to non-irradiated mice (Figure 3.1.A, 3.3.A), however this difference is likely attributable to dose-dependent irradiation-induced destruction of LECs[256], the cellular source of CCL21 in the skin, which is known to result in skin lymphatic dysfunction in bone marrow chimeric mice[257]. Regardless, observations with broad knock-out mice (Figure 3.3.A) were recapitulated in chimeras, as hyperabundant CCL21 was visualised in chimeras with ACKR4-deficiciency in both the haematopoietic and stromal compartment: *Ackr4*$^{-/-}$→Ly5.1*Ackr4*$^{-/-}$ (Figure 3.5.A, top right panel), relative to wildtype controls: WT→Ly5.1 chimeras (Figure 3.5.A, top left panel). Haematopoietic ACKR4-deficiency: *Ackr4*$^{-/-}$→Ly5.1 (Figure 3.5.A, bottom left panel) had no effect on CCL21 abundance compared to control WT→Ly5.1 chimeras. However, stromal/radio-resistant expression of ACKR4: WT→Ly5.1*Ackr4*$^{-/-}$ (Figure 3.5.A, bottom right panel) was required

to regulate CCL21 abundance. These imaging experiments were supported by ELISA detection of CCL21 that leached-out of ear tissue from chimeric mice. There was no impact of haematopoietic ACKR4-deficiency on the quantity of CCL21 leaching out of tissue from chimeric mice assayed by ELISA (Figure 3.5.B). However, ACKR4-deficiency in stromal/radio-resistant cells alone resulted in hyperabundant CCL21 and recapitulated the phenotype observed in *Ackr4*$^{-/-}$ mice (Figure 3.5.B). Together, these data unequivocally show that ACKR4 expression in the stromal/radio-resistant compartment is required for regulation of CCL21 distribution and abundance in dermal tissue.

3.6 Dermal fibroblasts express the greatest *Ackr4* mRNA in the skin

Of the stromal cell populations in the skin, ACKR4 expression had previously been identified in keratinocytes and a small proportion of LECs using an *Ackr4*^{EGFP} reporter mouse[100]. To test whether this was a faithful representation of *Ackr4* expression in stromal cells from skin of wildtype mice, the major dermal and epidermal cell populations were sorted by FACS for detection of *Ackr4* transcript by qPCR. Within the ear dermis, four major stromal cell populations can be identified using a previously described panel of antibodies for categorising lymph node stroma[258], and anti-CD90 (Figure 3.6.A). Like lymph node stroma, blood endothelial cells (BECs) and LECs can be identified by expression of CD31 and gp38 (BECs: CD31^{+}gp38^{-}; LECs: CD31^{+}gp38^{+}). However, CD31-negative cells expressed a range of gp38 thus were not easily divided into two populations as observed in the lymph node. Nonetheless, within the CD31-negative population, fibroblasts were identified by CD90 and expression of the pan-fibroblast marker CD140α. Dermal cells negative for CD31, CD140α and CD90 were termed “dermal double-negative cells” (dermDN). The role of these cells in both lymph nodes and skin is unknown, however within the lymph node this population resembles smooth-muscle cells and is known to contain integrin-α7^{+} pericytes and a small population of calponin-1^{+} subcapsular cells[258]. It is likely the skin dermDN population contained smooth-muscle cells[259], but the phenotyping performed here could not definitively determine whether they were pericytes. Within ear epidermis digests, Langerhans cells were identified by expression of CD45 and high expression of MHC-II (Figure 3.6.B). Langerhans cells were important to include in the analysis as they are radio-resistant[260], thus survive lethal radiation and are present within bone marrow chimeras as the same genotype as the stroma, which was demonstrated to be the functional source of ACKR4 (Figure 3.5). Keratinocyte populations were delineated by expression of Sca-1 and EpCAM as published elsewhere[261], with minor variations. Interfollicular epidermal keratinocytes (IE: Sca-1^{+}EpCAM^{lo}) formed the majority of CD45^{-}MHC-II^{-} stroma, whilst keratinocyte subpopulations resident within the upper hair follicle including the isthmus (IM: EpCAM^{hi}Sca-1^{-}) and infundibulum (IF: Sca-1^{+}EpCAM^{mid}), were gated together as they were not easily distinguishable with the panel utilized (Figure 3.6.B). Epidermal double negative cells (EpiDN: Sca-1^{-}EpCAM^{mid}) contained keratinocytes resident within the bulge of the hair follicle[261]. Given the prolonged sample preparation time required for sorting these skin stromal populations, *Ackr4* expression was also measured in whole epidermis and dermis samples for comparison with

sorted populations as a quality control. Unexpectedly, *Ackr4* mRNA was over two-fold greater in the dermis than the epidermis (Figure 3.6.C), in contrast to a published study where the greatest cutaneous ACKR4 expression was identified in keratinocytes using *Ackr4*^{EGFP} mice[100]. Within sorted populations, the greatest *Ackr4* expression was identified in dermal fibroblasts, and approximately 7-fold lower expression in IE keratinocytes and the mixed dermDN population (Figure 3.6.C). The finding that dermal cell types had higher *Ackr4* expression than epidermal cell types was consistent with the bulk analysis of these compartments and provided confidence that the prolonged sample preparation time had not adversely impacted RNA quality. Whilst ACKR4 expression by fibroblasts was not identified by the study utilising the *Ackr4*^{EGFP} mouse, ACKR4 expression has previously been identified in primary human dermal fibroblasts, specifically papillary fibroblasts separated from deeper dermal reticular fibroblasts by dermatome[262]. To determine whether ACKR4 expression was restricted to papillary fibroblasts in mice, published surface markers utilised to identify postnatal dermal fibroblast subpopulations were adopted to sort fibroblast subpopulations from adult skin. In postnatal skin, four populations of fibroblasts can be identified based on expression the of CD26, Sca-1 and Dlk1: papillary fibroblasts ($CD26^{+}Sca\text{-}1^{-}$), reticular fibroblasts ($CD26^{-}Dlk^{+}Sca\text{-}1^{-}$), and two populations of hypodermal fibroblasts ($Dlk^{+}Sca\text{-}1^{+}$ and $Dlk^{-}Sca\text{-}1^{+}$)[263]. Expression of Dlk1 does not persist in adult skin so it was not included to sort fibroblasts subpopulations[263]. To identify these populations in adult mice, flank skin was used as it provided a greater number of fibroblasts for sorting. At this site, gp38 and CD140α were expressed by all fibroblasts, whereas CD90 utilised in ear skin fibroblast preparations was only expressed by a fraction of fibroblasts at this site (Figure 3.6.D), thus was not included for sorting. Subsequently, four subpopulations of fibroblasts in adult dorsal skin were identified by CD26 and Sca-1 expression (Figure 3.6.E). Similar to postnatal skin, $CD26^{+}Sca\text{-}1^{-}$ cells were adult papillary fibroblasts as confirmed by high expression of postnatal papillary fibroblast genes *Lef1* and *Axin2* (Figure 3.6.F). Whilst not definitely identified in adult skin, it is likely that Sca-1-positive fibroblast populations are hypodermal fibroblasts, and $CD26^{-}Sca\text{-}1^{-}$ cells are reticular fibroblasts based on the reported CD26 expression profiles in postnatal skin[263]. In line with previously published human data[262], *Ackr4* expression within fibroblast subpopulations was restricted to papillary fibroblasts (Figure 3.6.G). Together, these data identified that the greatest *Ackr4* transcript in the radio-resistant compartment of the skin was present in the dermis, particularly within fibroblasts. *Ackr4*-expressing fibroblasts could be further defined with markers synonymous with murine postnatal papillary fibroblasts, the fibroblast subset observed to express *Ackr4* transcript in humans. Within the epidermis, keratinocytes expressed the greatest level of *Ackr4* transcript, in-line with a study utilising the *Ackr4*^{EGFP} reporter mouse strain[100], although the levels of expression in the epidermis were found to be much less than that in the dermis.

3.7 Atypical chemokine receptor expression by dermal fibroblast subpopulations

Whilst CCL21 is essential for mature dendritic cell egress from peripheral sites, multiple other chemokines have been identified to play supplementary roles in this process[81–83].

Interestingly CD26, one marker which identified papillary fibroblasts, is a transmembrane dipeptidyl peptidase that has been demonstrated to cleave and alter the biological activity of some chemokines[264,265]. Expression of CD26 along with ACKR4 therefore implicates a potential role for papillary fibroblasts in directing immune cell trafficking within the skin via regulating the availability or activity of multiple chemokines. To determine whether papillary fibroblasts may act as a "chemokine-sink" to broadly regulate chemokine availability in the skin, we interrogated the expression of all known atypical chemokine receptors within dermal fibroblasts populations by qPCR. Whilst papillary fibroblasts did not express any atypical chemokine receptors other than *Ackr4*, hypodermal fibroblast populations highly expressed *Ackr1*, *Ackr2* and *Ackr3*, and thus may regulate the availability of their respective ligands *in vivo* (Figure 3.6.H). While these observations were not followed up further in the present study, they are discussed in Chapter 5.1.

3.8 Limited efficacy of antibody reagents for ACKR4 detection by flow cytometry

Given the disparity described above between *Ackr4* gene expression data and the reported findings using *Ackr4*^{EGFP} reporter mice, direct detection of ACKR4 protein was attempted by flow cytometry. Here, the anti-ACKR4 13E11 clone generated by the Chiba laboratory[266] was utilized as it recognises an extracellular N-terminal epitope, whereas the commercial anti-ACKR4 Santa Cruz C-16 clone recognises an intracellular C-terminal epitope. The 13E11 antibody clone demonstrated specificity for murine ACKR4 by flow cytometry by staining a B300.19 cell line stably transfected to overexpress murine ACKR4 to a much greater extent than the parental B300.19 cell line (Figure 3.7.A, B). Importantly, this staining was performed after treating B300.19 cells with the same rigorous enzymatic digestion required for the preparation of skin samples, thus demonstrating that the antigenic epitope is not cleaved or substantially modified during the processing steps required for skin sample preparation. Steady-state ear skin was then harvested from both wildtype and *Ackr4*$^{-/-}$ mice for flow cytometry analysis with the latter serving as the negative staining control for all cell populations. No specific staining for ACKR4 was observed with the 13E11 antibody for any of the dermal (Figure 3.7.C) or epidermal (Figure 3.7.D) cell populations compared to *Ackr4*$^{-/-}$ controls. As ACKR4 is known to cycle between the plasma membrane and endomembrane compartments[116], it was possible that low level surface ACKR4 expression was insufficient for detection by flow cytometry, thus detection of ACKR4 was next pursued via microscopy on tissue sections.

3.9 Limited efficacy of antibody reagents for ACKR4 detection by immunofluorescence imaging

ACKR4 expression had previously been visualised via immunofluorescent imaging[80,100,117,118], thus multiple anti-ACKR4 antibody clones were assayed on skin sections harvested from several anatomical sites and prepared by various methods for antibody staining. Transverse lip sections were used to image the skin as they contained a greater density of hair follicles compared to sagittal dorsal skin sections, allowing the

visualisation keratinocyte subpopulations in hair follicles. No ACKR4-specific staining was observed in wildtype sections above background identified with *Ackr4*$^{-/-}$ tissue using antibody clones generated by the Chiba laboratory[266] (Figure 3.8.A). Similarly, the Santa Cruz C-16 clone utilised elsewhere[80,100,117] did not produce a specific ACKR4 signal above background staining observed in *Ackr4*$^{-/-}$ tissue (Figure 3.8.B). Identical results were obtained with sagittal dorsal skin sections and fixed/permeabilised whole-mount ear tissue. To circumvent possible masking of antigen epitopes by acetone or paraformaldehyde fixation, whole unfixed ear sheets were stained to identify ACKR4 in its native state. Here, the Santa Cruz C-16 clone could not be used as it detected an intracellular epitope. Again, staining with antibody clones from the Chiba laboratory did not reveal any ACKR4-specific staining within the skin (Figure 3.8.C). Despite extensive efforts to identify ACKR4 expression in skin harvested from several sites, extensive background staining was observed with all antibodies in *Ackr4*$^{-/-}$ tissue, thus the use of antibodies was not suitable for detection of ACKR4 via flow cytometry or microscopy. Unfortunately, alternate methods attempted to detect ACKR4 in skin cell suspensions without antibodies through CCL19-Fc binding or *in vitro* chemokine scavenging were also unsuccessful despite repeated attempts. Having exhausted a plethora of methods to detect ACKR4 protein or ACKR4 function to no avail, further attempts to support *Ackr4* mRNA expression data were not pursued in the present study. Possible means to circumvent these issues in future studies are discussed in Chapter 5.1.

3.10 Dendritic cell migration in *Ackr4*$^{-/-}$ ear sheets is perturbed *in vitro*

Disruption of CCL21 haptotactic gradients by ectopic CCL21 expression *in vivo*, or addition of exogenous recombinant CCL21 *ex vivo*, perturbs egress and lymphatic homing of skin-resident dendritic cells[4,71]. Additionally, dendritic cell accumulation in skin-draining lymph nodes during the steady-state and after inflammation is perturbed in ACKR4-deficient mice[80,100,112]. Therefore, it was tested whether dysregulated CCL21 gradients present in ACKR4-deficient skin would impede dendritic cell homing to local lymphatic vessels. To do this, an *ex vivo* ear crawl-in assay was utilised. Here, LPS-activated, GM-CSF-derived BMDCs were fluorescently labelled, then incubated atop the dermal side of split ventral ear sheets. BMDCS subsequently enter the dermis and migrate towards LYVE-1^{+} lymphatic vessels in a CCR7-dependent manner, utilising the endogenous CCL21 gradient[4]. Thus, ear sheets were prepared from wildtype and *Ackr4*$^{-/-}$ mice, then wildtype BMDCs were incubated atop both to visualise the migratory behaviour of activated dendritic cells responding to the different immobilised CCL21 gradients established in these hosts. After a 45 minute incubation, most wildtype BMDCs had entered wildtype ear sheets and homed or attached to lymphatic vessels (Figure 3.9.A, top panel), as areas between vessels were largely void of BMDCs. Strikingly, lymphatic homing of wildtype BMDCs was significantly impaired in *Ackr4*$^{-/-}$ tissue, evident by the large number of BMDCs still within interstitial areas between lymphatic vessels (Figure 3.9.A, bottom panel). To enumerate BMDC migration and attachment to lymphatic vessels, the mean grey intensity of labelled BMDCs inside and outside of lymphatic vessel areas was compared between ACKR4-sufficient and

deficient ear sheets. A significantly increased ratio of BMDC mean grey intensity measured in wildtype tissue indicated that a greater number of BMDCs were associated with lymphatic vessels when ACKR4 was present (Figure 3.9.B). This demonstrated that ACKR4-deficient skin exhibited an impaired functional chemokine gradient for dendritic cell migration to lymphatic vessels, and that defective dendritic cell egress from the skin likely contributes to reduced dendritic cell accumulation in lymph nodes of *Ackr4*$^{-/-}$ mice.

3.11 Hyperabundant CCL19 does not affect dendritic cell migration in *Ackr4*$^{-/-}$ ear sheets

ACKR4-deficiency in skin during the steady-state resulted in hyperabundance of both CCR7 ligands, CCL19 and CCL21 (Figure 3.1.A). Whilst studies with *Ccl19*$^{-/-}$ mice indicated no physiological role for CCL19 in dendritic cell egress from skin[107], addition of exogenous CCL19 has been reported to disrupt dendritic cell egress from skin[267]. CCL19 has a greater potency for triggering CCR7 than CCL21, and CCL19 binding to CCR7 induces receptor desensitisation[7,33,104,106]. It was therefore possible that despite approximately 50-fold less CCL19 than CCL21 being present in *Ackr4*$^{-/-}$ skin, hyperabundant CCL19 may also contribute to defective lymphatic homing of dendritic cells in *Ackr4*$^{-/-}$ ear sheets in addition to aberrant CCL21 gradients. To determine whether hyperabundant CCL19 contributed to aberrant BMDC lymphatic homing in *Ackr4*$^{-/-}$ ear sheets, the BMDC crawl-in protocol was modified to permit neutralisation of dermal CCL19 prior to BMDC migration. Of the two ventral ear sheets harvestable from a single *Ackr4*$^{-/-}$ mouse, one was incubated in an excess of polyclonal anti-CCL19 serum and the second was incubated with pre-immunisation control serum. Thus, results could be analysed as paired comparisons as this experimental design controls for mouse-to-mouse variance in dermal CCL19 between donor mice. Importantly, this approach is only possible with CCL19 and not CCL21, as CCL19 is dispensable for dendritic cell egress, whilst neutralisation of the essential CCL21 signal completely abrogates dendritic cell lymphatic homing[107]. After a 45 minute crawl-in incubation, there was no observable difference in the distribution of wildtype BMDCs in *Ackr4*$^{-/-}$ ear sheets treated with control immunoglobulin (Figure 3.10.A, top panel) or neutralising anti-CCL19 (Figure 3.10.A, bottom panel). Quantitation of BMDC mean grey intensity inside:outside lymphatic areas revealed that neutralising CCL19 did not rescue the impaired lymphatic homing of BMDCs in *Ackr4*$^{-/-}$ tissue (Figure 3.10.B). Importantly, neutralising polyclonal anti-CCL19 serum blocked migration to CCL19 *in vitro* (Figure 3.10.C), the amount of antibody used for neutralising CCL19 *ex vivo* was in excess of a saturating concentration, and neutralising anti-CCL19 did not display cross-reactivity with CCL21 or impair migration to CCL21 *in vitro*. Therefore, by process of elimination, these data implicate hyperabundant CCL21 rather than CCL19 as the cause of impaired BMDC migration in ACKR4-deficient skin.

3.12 Lymphatic vessel homing of dendritic cells is impaired in *Ackr4*$^{-/-}$ skin *in vivo*

To visualise the migratory behaviour of dendritic cells in ACKR4-deficient skin in real-time and *in vivo*, two-photon microscopy was performed. Preliminary bone marrow chimera experiments with wildtype and *Ackr4*$^{-/-}$ hosts reconstituted with *Itgax*^{eYFP} bone marrow to visualise endogenous dendritic cells revealed that *in situ* activation of dermal dendritic cells via s.c. LPS injection was not homogenous, thus tracking a sufficient number of emigrating dendritic cells for statistical analysis with this model would require long imaging sessions that raise a number of technical challenges. To circumvent this, LPS-stimulated GM-CSF-derived BMDCs were used to model CCR7-dependent egress as they could be homogenously activated *in vitro* and injected in large numbers for robust cell tracking. Indeed, similar transfer approaches have been previously utilised due to the same limitations observed when activating endogenous dendritic cells[74,77]. Consequently, a published model was adopted where 1-2x10^6 fluorescently labelled, LPS-activated, wildtype BMDCs were injected s.c. into the footpads of wildtype and *Ackr4*$^{-/-}$ mice with 50ng LPS and fluorescently labelled anti-LYVE-1 antibody for visualisation of lymphatic vessels[74,77]. After 18-21 hours, mice were anaesthetised and secured for two-photon imaging of transferred BMDCs and lymphatic vessels within exposed tissue around the ankle as this site has minimal hair follicles and subcutaneous fat, lending itself to intravital imaging. Evans Blue dye was injected i.v. immediately prior to imaging for visualisation of blood vessels. At these time points, the majority of BMDCs in wildtype tissue had entered lymphatic vessels, whereas more BMDCs appeared within interstitial areas of *Ackr4*$^{-/-}$ tissue, as per *ex vivo* ear sheet crawl-in experiments. Furthermore, BMDCs in wildtype tissue could be visualised migrating towards, attaching to and entering lymphatic vessels (Figure 3.11.A, top panel, highlighted with arrows, and Video 3.1). Few BMDCs in *Ackr4*$^{-/-}$ tissue displayed these normal migratory patterns, however numerous BMDCs within close proximity to lymphatic vessels were visualised migrating away from, or perpendicular to, lymphatic vessels (Figure 3.11.A, middle panel, highlighted with arrow, and Video 3.2). Interestingly, some BMDCs in *Ackr4*$^{-/-}$ hosts were observed sending out long processes to attach to and crawl along blood capillaries despite close proximity to lymphatic vessels (Figure 3.11.A, bottom panel, highlighted with arrows, and Video 3.3). Hyperabundant CCL21 on the surface and in close proximity to blood capillaries was observed in whole-mount *Ackr4*$^{-/-}$ ear sheets (Figure 3.4.A, B), thus these BMDCs may have responded to aberrant accumulation of CCL21 at these sites *in vivo*. The absence of CCL21 decorating blood vessels in wildtype tissue (Figure 3.4.A, B) may explain why this migratory behaviour was not observed in wildtype hosts. These qualitative real-time observations supported our initial crawl-in experiments and identified aberrant migratory paths that wildtype BMDCs were taking in ACKR4-deficient skin which could delay tissue egress.

To evaluate quantitative data from the intravital imaging experiments, all migrating BMDCs that could be followed across an extended period of time throughout imaging were manually tracked to determine cell speed and track straightness. As CCL21 directs migration towards lymphatic vessels, the distance and displacement of all tracked BMDC from the nearest

lymphatic vessel was also calculated. Plotting the distance travelled by individual BMDCs relative to the nearest lymphatic vessel over time revealed that the majority of BMDCs in wildtype tissue moved towards lymphatic vessels as tracks were positive, whereas migration of BMDCs in *Ackr4*$^{-/-}$ tissue was less uniform as BMDC tracks were both positive and negative (Figure 3.11.B). To permit statistical comparisons on a sufficient number of cells, BMDC tracks ≥20 mins in duration were included, with the first 20 minutes of longer tracks analysed. Comparing average BMDC migration within a host across time revealed that after 11 minutes BMDCs had migrated significantly closer to lymphatic vessels in wildtype hosts, whereas there was no significant net movement of BMDCs towards lymphatic vessels within the first 20 minutes of tracking in *Ackr4*$^{-/-}$ hosts (Figure 3.11.C, WT $p<0.05$). Comparing average BMDC migration between wildtype and *Ackr4*$^{-/-}$ hosts across time revealed that after only 10 minutes of tracking, BMDCs had migrated significantly closer towards lymphatic vessels in wildtype hosts than *Ackr4*$^{-/-}$ hosts, and this was maintained up to 20 minutes (Figure 3.11.C, statistical significance indicated by asterisks). Previously, *in silico* modelling had indicated that cells must be within sufficient proximity to lymphatic vessels to sense the immobilized CCL21 gradient[4], and both two-photon imaging and BMDC crawl-in experiments had demonstrated that BMDCs take longer to migrate towards and enter lymphatic vessels in *Ackr4*$^{-/-}$ tissue. Importantly, there was no difference in the starting distance from lymphatic vessels of tracked BMDCs between host strains (Figure 3.11.D), thus results were not a product of BMDCs not being within the same proximity of lymphatic vessels between host strains despite the delayed lymphatic homing observed in *Ackr4*$^{-/-}$ tissue. There was no statistically significant difference in average speed or track straightness of BMDCs between hosts (Figure 3.11.E, F). However, as CCL21 functions to direct activated dendritic cells towards lymphatic vessels, it was important to study these parameters relative to lymphatic vessels, thus the velocity and lymphatic vessel homing efficiency of BMDCs between wildtype and *Ackr4*$^{-/-}$ hosts was determined. BMDCs in wildtype hosts on average displayed a positive velocity of approximately 1µm/min, indicating they generally migrated towards lymphatic vessels (Figure 3.11.G). In contrast, the velocity of BMDCs in *Ackr4*$^{-/-}$ hosts was significantly lower than in wildtype hosts and individual tracked BMDCs displayed a range of positive to negative velocities. Here, velocities <0µm/min indicated migration away from lymphatic vessels and velocities of ≈0µm/min indicated perpendicular migration to, or no net migration towards or away from lymphatic vessels. Lymphatic vessel homing efficiency was also calculated to demonstrate the track straightness of BMDCs towards the nearest lymphatic vessel. As values approach 1, tracks are increasingly direct towards lymphatic vessels (i.e. most efficient), whereas values approaching -1 indicate increasingly direct tracks away from lymphatic vessels (i.e. least efficient). Again, values ≈0 indicate migration perpendicular to, or no net migration towards or away from lymphatic vessels. BMDCs in wildtype hosts were significantly more efficient at directional migration towards lymphatic vessels than BMDCs in ACKR4-deficient mice (Figure 3.11.H). Taken together, these data suggest that whilst activated dendritic cells in *Ackr4*$^{-/-}$ skin migrate in path-persistent tracks at the same speed as emigrating dendritic cells in wildtype hosts (Figure 3.11.E, F), they are unable to be guided towards lymphatic vessels by immobilized CCL21 as efficiently (Figure 3.11.G, H). This would increase the time

required to migrate towards and attach to lymphatic vessels, consistent with the earlier results using ear crawl-in systems (Figure 3.9).

3.13 Skin-restricted ACKR4-deficiency is sufficient to impair dendritic cell emigration to lymph nodes

To date, all studies investigating the effect of ACKR4 deficiency on peripheral dendritic cell lymph node trafficking have been conducted in global *Ackr4*$^{-/-}$ mice[80,100,112]. Whilst a defect in dendritic cell trafficking has been attributed to dysregulated CCL21 gradients within the interfollicular areas of the lymph node due to a loss of ACKR4 function in lymph node cLECS[80], data generated here has identified an upstream dendritic cell migratory defect in the skin (Figure 3.9-3.11). Therefore, to isolate and measure the contribution of cutaneous ACKR4 activity on dendritic cell egress, a model to restrict ACKR4-deficiency to the skin whilst preserving ACKR4 expression and function within cLECs was required. This was achieved via transplantation of wildtype or *Ackr4*$^{-/-}$ skin onto wildtype recipients. First, wildtype or *Ackr4*$^{-/-}$ ear sheets were grafted onto wildtype mice to determine whether transplanted *Ackr4*$^{-/-}$ skin on a wildtype host retained a hyperabundant CCL19 and CCL21 phenotype (Figure 3.12.A). Two ear sheets were grafted onto recipient mice to maximize the surface area of ACKR4-deficient tissue and limit potential sequestering of hyperabundant ligands by surrounding endogenous host ACKR4. After a six-week recovery period to ensure lymphatic repair[268], grafts and contralateral flank skin were harvested and the quantity of CCL19 and CCL21 leached out of these tissues was measured. There was no difference in the quantity of CCL19 or CCL21 in control contralateral host flank skin between wildtype and *Ackr4*$^{-/-}$ graft recipients (Figure 3.12.B). However, the quantity of both CCL19 and CCL21 was approximately 3-fold higher in *Ackr4*$^{-/-}$ grafts compared to wildtype grafts (Figure 3.12.B). A possible caveat of this system is that differences in graft success or resolution of inflammation between wildtype and *Ackr4*$^{-/-}$ grafts could affect results. However, any effect of ACKR4-deficency on tissue engraftment was minimized by an extended 6 week recovery period, at the conclusion of which there was no difference in the appearance or size between wildtype and *Ackr4*$^{-/-}$ grafts (Figure 3.12.C). This finding also demonstrated that hyperabundant CCL19 and CCL21 in the skin was driven by local stromal ACKR4-deficiency and independent of elevated CCL21 observed in the circulation of *Ackr4*$^{-/-}$ mice (Figure 3.1.D).

To study the effect of skin-restricted ACKR4 deficiency on dendritic cell egress, wildtype and *Ackr4*$^{-/-}$ skin was grafted onto Ly5.1 hosts, then after 6 weeks recovery, grafts were painted with 1% FITC to induce maturation of dendritic cells and permit their identification in draining lymph nodes after uptake of FITC and emigration (Figure 3.12.D). Only CD45.1^{+} host-derived migratory dendritic cells were analysed to exclude CD45.2^{+} dendritic cells of graft origin which would be wildtype or ACKR4-deficient. The number of emigrated dendritic cells were calculated per unit of graft weight to control for small variances in graft sizes between hosts, then normalised to the number of emigrated dendritic cells observed in

graft-draining lymph nodes from wildtype grafts to permit the pooling of results from three independent experiments (Figure 3.12.E). As anticipated, very few to no $FITC^+$ dendritic cells were observed in the contralateral lymph nodes of hosts grafted with either wildtype or *Ackr4*$^{-/-}$ tissue (Figure 3.12.E). However, emigrated dendritic cells from wildtype grafts accumulated in graft-draining lymph nodes 2 days post-FITC paint (Figure 3.12.E). Conversely, there was no statistically significant increase in the number of $FITC^+$ dendritic cells in the graft-draining lymph node of *Ackr4*$^{-/-}$ graft recipients compared to contralateral lymph nodes, and there were significantly fewer emigrated dendritic cells in the graft-draining lymph node of *Ackr4*$^{-/-}$ graft recipients compared to wildtype graft recipients (Figure 3.12.E). Therefore, ACKR4-deficiency in the skin significantly impeded mature dendritic cell accumulation in the draining lymph node.

3.14 Skin ACKR4 is required to regulate CCL21 abundance in skin-draining lymph nodes

Given the striking hyperabundance of CCL21 in ear tissue of *Ackr4*$^{-/-}$ mice (Figure 3.1.A and 3.3.A) and the increased CCL21 detected within lymphatic vessels at this site (Figure 3.3.B), it was investigated whether excessive CCL21 in the skin of *Ackr4*$^{-/-}$ mice could drain via the lymphatics and pollute the lymphatic reservoir of CCL21. Indeed, excess CCL21 in the lymph nodes of *Ackr4*$^{-/-}$ mice had previously been reported by our laboratory[102], and visualized by another group[80]. Consistent with soluble CCL21 leaching in from the skin through the lymphatics, skin-draining lymph nodes from steady-state *Ackr4*$^{-/-}$ mice contained a greater proportion of cleaved CCL21 compared to wildtype mice (Figure 3.13.A, B). To identify the source of aberrant soluble CCL21 in lymphoid tissues, the unique tissue-tropic expression of CCL21 isoforms present in mice was exploited[94,95]. Here, peripheral CCL21-Leu expression driven by the *Ccl21b*/*Ccl21c* alleles could be distinguished from lymphoid tissue-derived CCL21-Ser by mass spectrometry as unique peptides containing the single amino acid difference are generated upon trypsin digest. Thus, mass spectrometry was performed on immunoprecipitated cleaved CCL21 from skin-draining lymph nodes of steady-state wildtype and *Ackr4*$^{-/-}$ mice to determine the relative abundance of peripheral CCL21-Leu. Whilst this assay was technically challenging due to the hydrophobic nature of the only unique CCL21-Ser/Leu peptides, mass spectrometry experiments successfully detected both CCL21-Ser and CCL21-Leu within the cleaved CCL21 fraction (Figure 3.13.C). Subsequently the relative peptide intensity of each isoform was determined, then calculated as a ratio of CCL21-Leu:CCL21-Ser for comparison between biological samples. A greater ratio of CCL21-Leu:CCL21-Ser was detected in *Ackr4*$^{-/-}$ skin-draining lymph nodes (Figure 3.13.D), consistent with increased cleaved CCL21 leaching from the skin into the lymph nodes.

Previously, dysregulated lymph node CCL21 accumulation observed in *Ackr4*$^{-/-}$ mice was attributed to loss of ACKR4-function in cLECs[80]. However, the data here identified dysregulated dermal CCL21 in *Ackr4*$^{-/-}$ mice and implicated this source of CCL21 in the

pollution of downstream lymph nodes. Thus to determine the contribution of peripheral ACKR4 in regulating lymph node CCL21 abundance, CCL21 was quantified in the supernatant of digested graft-draining lymph nodes 2 days after graft FITC painting, with contralateral lymph nodes used as a control (Figure 3.12.D). Importantly, the skin transplant model used here restricted ACKR4-deficiency to the skin whilst maintaining intact cLEC ACKR4 expression, thus the effect of hyperabundant dermal chemokines on the draining lymph node chemokine environment could be determined for the first time. Within wildtype graft recipients, there was no statistically significant difference in the quantity of CCL21 in graft-draining or control contralateral lymph nodes (Figure 3.13.E). Strikingly, there was a greater quantity of CCL21 in the graft-draining lymph nodes of *Ackr4*$^{-/-}$ graft recipients compared to control contralateral lymph nodes, and compared to graft-draining lymph nodes of wildtype graft recipients (Figure 3.13.E). CCL19 levels were below the limit of detection in graft-draining lymph nodes, thus it could not be determined whether hyperabundant dermal CCL19 also contributed to dysregulated CCL19 observed in the lymph nodes of *Ackr4*$^{-/-}$ mice[102]. As cLEC ACKR4 function was intact in the model, this demonstrated that excessive CCL21 accumulated in skin-draining lymph nodes downstream of dysregulated CCL21 abundance in ACKR4-deficient grafts. Furthermore, this demonstrated that ACKR4 function on cLECs alone was not sufficient to regulate lymph node CCL21 abundance as functional ACKR4 in skin was required, challenging the interpretation of the study by Ulvmar and colleagues attributing lymph node CCL21 dysregulation in *Ackr4*$^{-/-}$ to loss of ACKR4 in cLECs. Together, these data are consistent with excessive cleaved CCL21-Leu leaching out of ACKR4-deficient skin and accumulating in lymph nodes. As cLEC ACKR4 function was intact in skin graft experiments, this was the first study to identify the importance of peripheral ACKR4 in regulating downstream CCL21 abundance independent of cLEC ACKR4 function.

3.15 Conclusions

Global ACKR4 deficiency resulted in elevated abundance of CCL21 in the serum, at barrier sites including the skin, lung, small intestine and vagina, and some internal major organs including the heart, liver and kidney, but not the spleen. Elevated levels of CCL19 were only detected in the skin, and abundance of CCL25 in the small intestine was unaltered by ACKR4 deficiency. As hyperabundance of CCL21 in *Ackr4*$^{-/-}$ skin contradicted published work, further biochemical analysis on different ELISA capture antibodies utilised by laboratories revealed varying abilities to bind endogenous full-length and cleaved forms of CCL21. Leveraging these reagents, hyperabundant CCL21 in tissue leach-out assays with *Ackr4*$^{-/-}$ skin was demonstrated to be cleaved, soluble CCL21. Ligand hyperabundance in barrier tissues was not due to transcriptional changes, nor an increase in the cellular source of CCL21, consistent with ACKR4 regulating chemokine abundance post-transcriptionally via ligand scavenging. Loss of ACKR4 function also resulted in the dysregulation of immobilised CCL21 gradients in the skin, revealing that ACKR4 also regulates the abundance of full-length CCL21. ACKR4 functioned within radio-resistant cells to regulate the abundance of both forms of CCL21 within steady-state skin, and tissue-grafting

experiments demonstrated that dermal chemokine accumulation in ACKR4-deficient skin occurred independently of elevated CCL21 levels in the sera of *Ackr4*$^{-/-}$ mice. Contrary to expression profiling using *Ackr4*^{EGFP} mice where keratinocytes were determined as the major source of ACKR4[100], dermal expression of *Ackr4* mRNA was greater than that measured in the epidermis, with the highest expression identified in a subset of dermal fibroblasts akin to papillary fibroblasts. The migration of wildtype BMDCs was significantly impaired in *Ackr4*$^{-/-}$ skin independent of hyperabundant CCL19 and due to reduced velocity and track directness towards the nearest lymphatic vessel. Furthermore, this migratory defect in the skin alone was sufficient to impair accumulation of mature dendritic cells in the draining lymph node when ACKR4 deficiency was restricted to the skin. Strikingly, skin graft experiments further demonstrated that skin ACKR4 was required to limit the leaching of dermal CCL21 into draining lymph nodes when cLEC ACKR4 function was intact. This observation was supported by greater cleaved, peripheral CCL21-Leu detected in the skin-draining lymph nodes of *Ackr4*$^{-/-}$ mice. Together, this body of work demonstrated the widespread function of barrier ACKR4 in regulating chemokine gradients essential for steady-state host immunity.

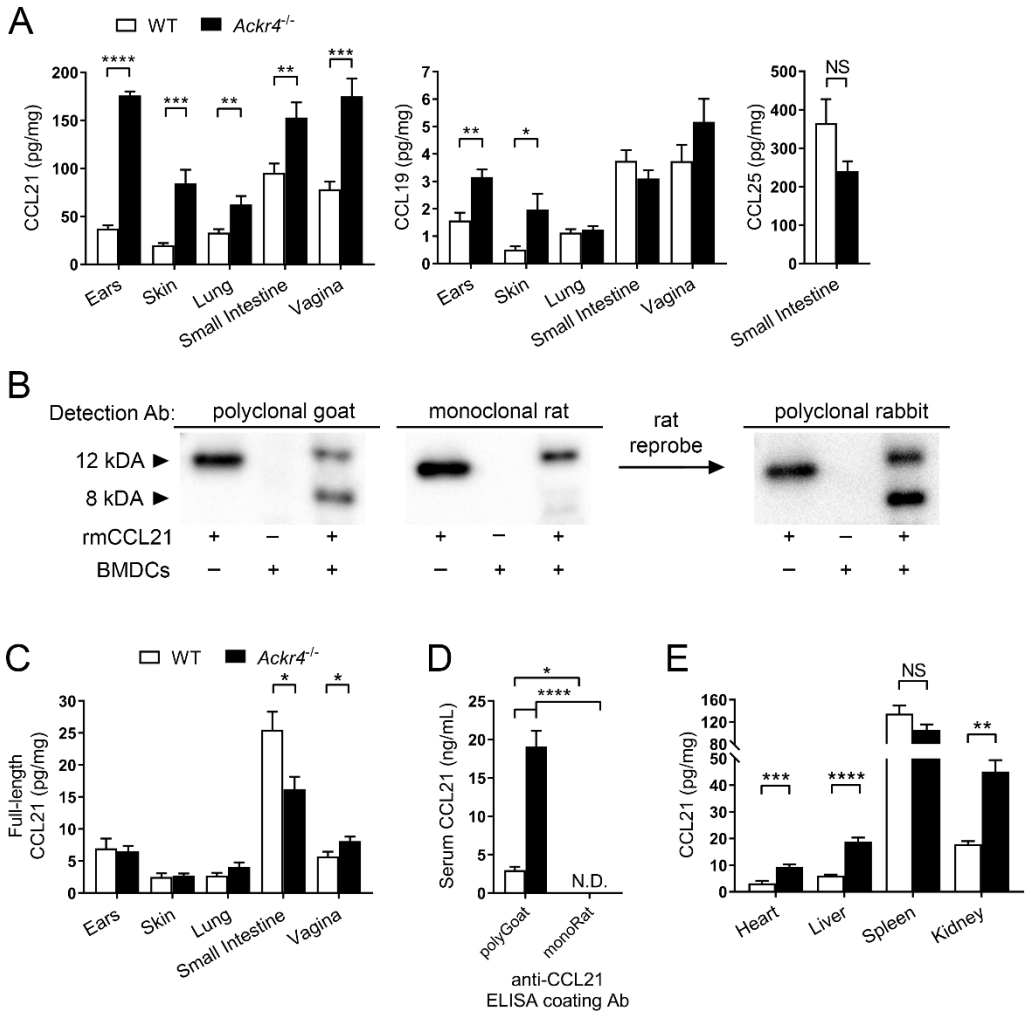

Figure 3.1: CCL19 and CCL21 protein are hyperabundant in ACKR4-deficient tissues

(A) Quantity of total CCL21, CCL19 and CCL25 (pg/mg) leached out of steady-state barrier tissues from WT and *Ackr4*$^{-/-}$ mice, as determined by ELISA. **(B)** Detection of full-length (12kDA) and BMDC-cleaved (8kDA) recombinant-mouse CCL21 with different commercial antibodies by western blot. Membranes probed with the monoclonal rat antibody were subsequently reprobed with another commercial antibody. **(C)** Quantity of full-length CCL21 (pg/mg) leached out of steady-state barrier tissues from (A), as determined by ELISA. **(D)** Quantity of CCL21 (ng/mL) in the blood of steady-state WT and *Ackr4*$^{-/-}$ mice, as determined by ELISA with the annotated capture antibodies. **(E)** Quantity of total CCL21 (pg/mg) in the heart, liver, spleen and kidney from steady-state WT and *Ackr4*$^{-/-}$ mice, as determined by ELISA. (A, C, E) Data pooled from two independent experiments, n=5-10 mice/strain ±SEM, two-tailed unpaired Student's t test between strains for a given tissue. (B) Data representative of two independent experiments. (D) Data from WT n=6, *Ackr4*$^{-/-}$ n=4, two-way ANOVA with Sidak's multiple comparison test. *p<0.05, **p<0.01, ***p<0.001, ****p<0.0001.

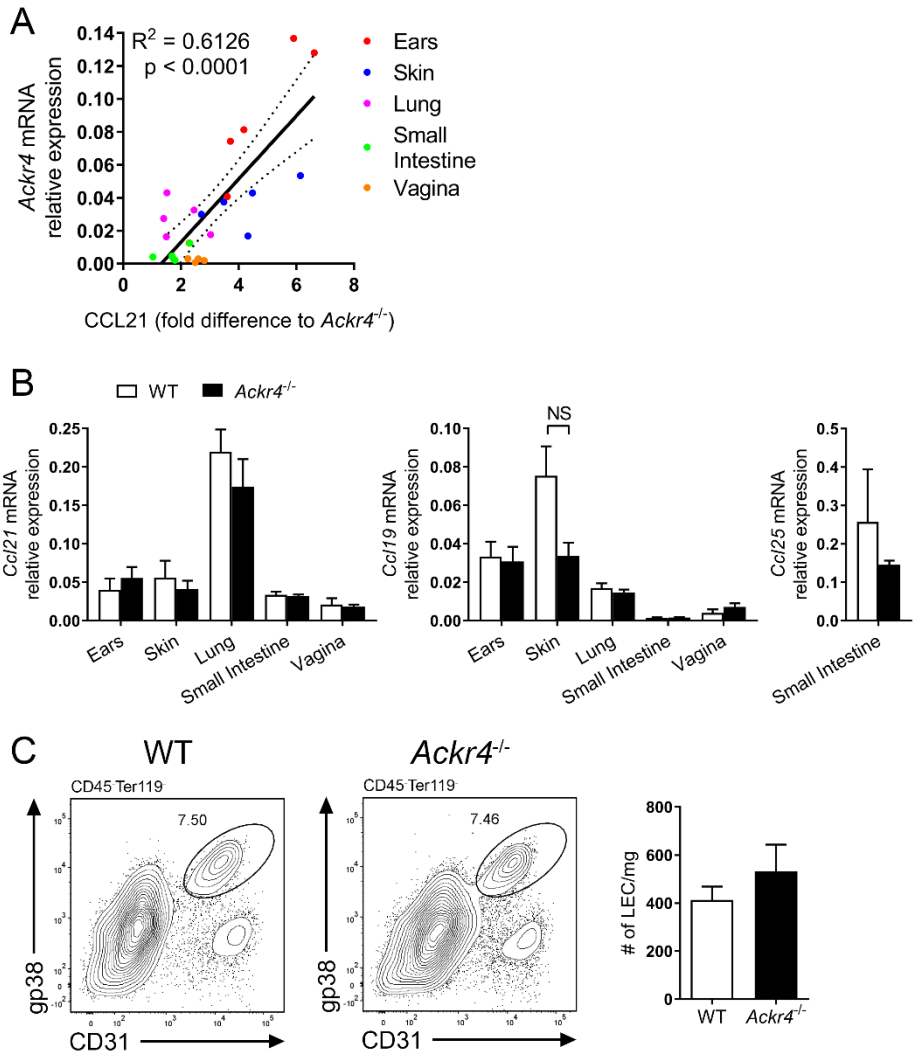

Figure 3.2: CCL19 and CCL21 abundance in barrier tissues is regulated by ACKR4 scavenging

(A) Linear correlation between *Ackr4* mRNA expression in WT tissue (relative to *Rplp0*), and fold-difference of CCL21 abundance for a given tissue between WT and *Ackr4*$^{-/-}$ mice. **(B)** Expression of *Ccl21*, *Ccl19* and *Ccl25* mRNA transcripts relative to *Rplp0* in steady-state barrier tissues from WT and *Ackr4*$^{-/-}$ mice. **(C)** Representative gating strategy for LECs (CD45^{-}Ter119^{-}CD31^{+}gp38^{+}) and number of LECs per mg ear tissue in steady-state WT and *Ackr4*$^{-/-}$ mice. (A-C) Data pooled from two independent experiments, n=5-10 mice/strain ±SEM, two-tailed unpaired Student's t test, except (A), linear regression with 95% confidence interval (dotted lines). For graphs in (B) with multiple tissues, two-tailed unpaired Student's t test was performed between strains for a given tissue.

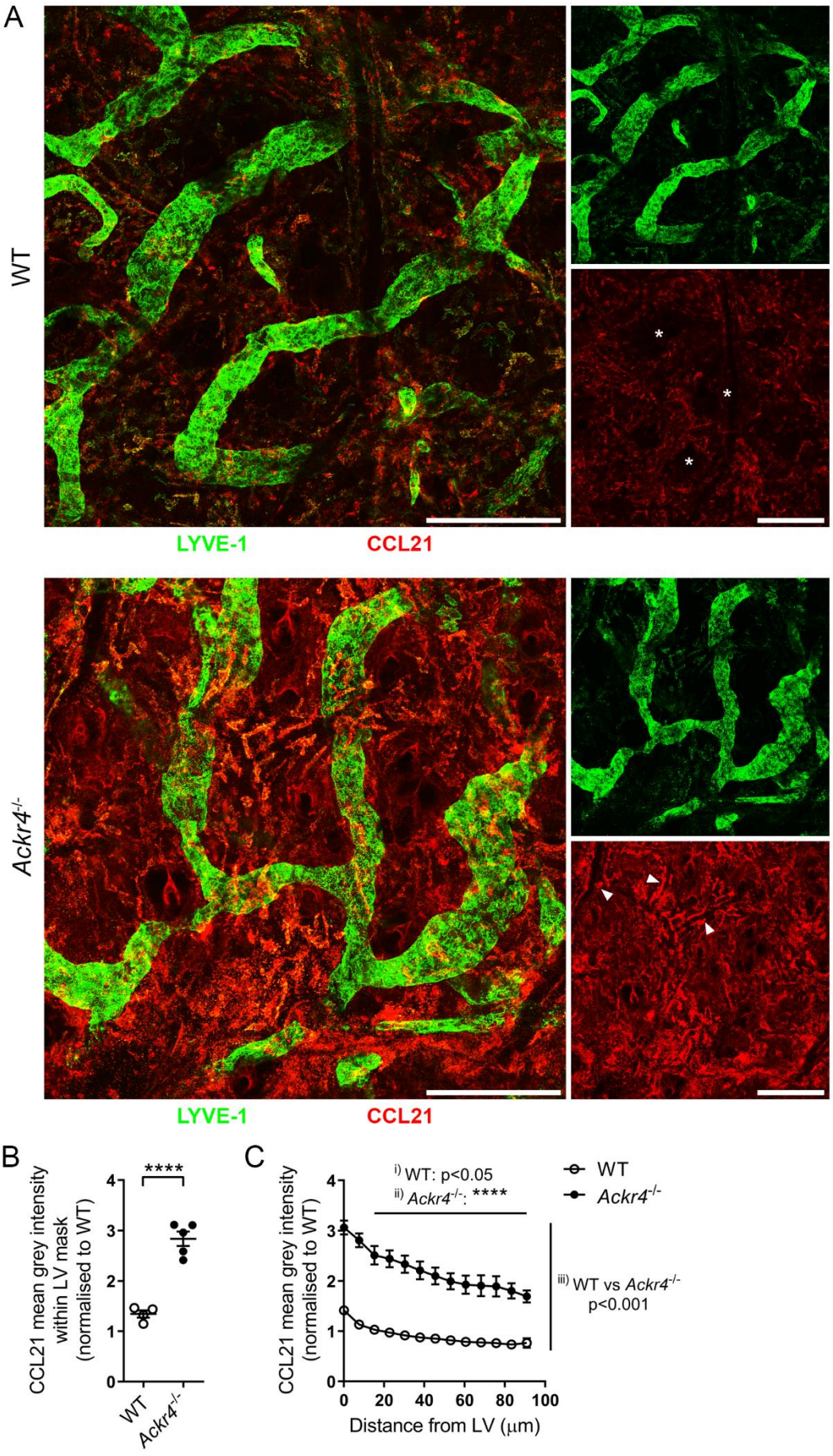
A
WT
LYVE-1
CCL21
Ackr4-/-
LYVE-1
CCL21
B
CCL21 mean grey intensity within LV mask (normalised to WT)
****
WT
Ackr4-/-
C
CCL21 mean grey intensity (normalised to WT)
i) WT: p<0.05
ii) Ackr4-/-: ****
iii) WT vs Ackr4-/- p<0.001
WT
Ackr4-/-
Distance from LV (μm)

Figure 3.3: ACKR4 regulates intradermal CCL21 gradients

(A) Representative Z-stack projections of unfixed, non-permeabilised whole-mount ear sheets from steady-state WT (top) and *Ackr4*$^{-/-}$ mice (bottom), stained LYVE-1 (green) and CCL21 (red), with single channel images (right). Areas of interest are denoted by asterisks and arrows referred to in text. Scale bar: 200μm. Images representative of two independent experiments, WT n=4, *Ackr4*$^{-/-}$ n=5. **(B)** Quantitation of CCL21 mean grey intensity (normalised to WT intensity) within lymphatic vessel masks from (A). Each dot represents the average of technical replicates per biological replicate, ±SEM, two-tailed unpaired Student's t test. **(C)** Quantitation of CCL21 mean grey intensity (normalized to average WT intensity) at defined distances from the nearest lymphatic vessel from images in (A). Each dot represents the average of biological replicates, within which technical replicates were averaged, ±SEM, two-way ANOVA with Sidak's multiple comparison test for i) CCL21 intensity between a defined distance and the vessel edge (i.e. 0 μm) in WT tissue, ii) CCL21 intensity between a defined distance and the vessel edge *Ackr4*$^{-/-}$ tissue, or iii) CCL21 intensity between WT and *Ackr4*$^{-/-}$ tissue at a defined interstitial distance. ****p<0.001.

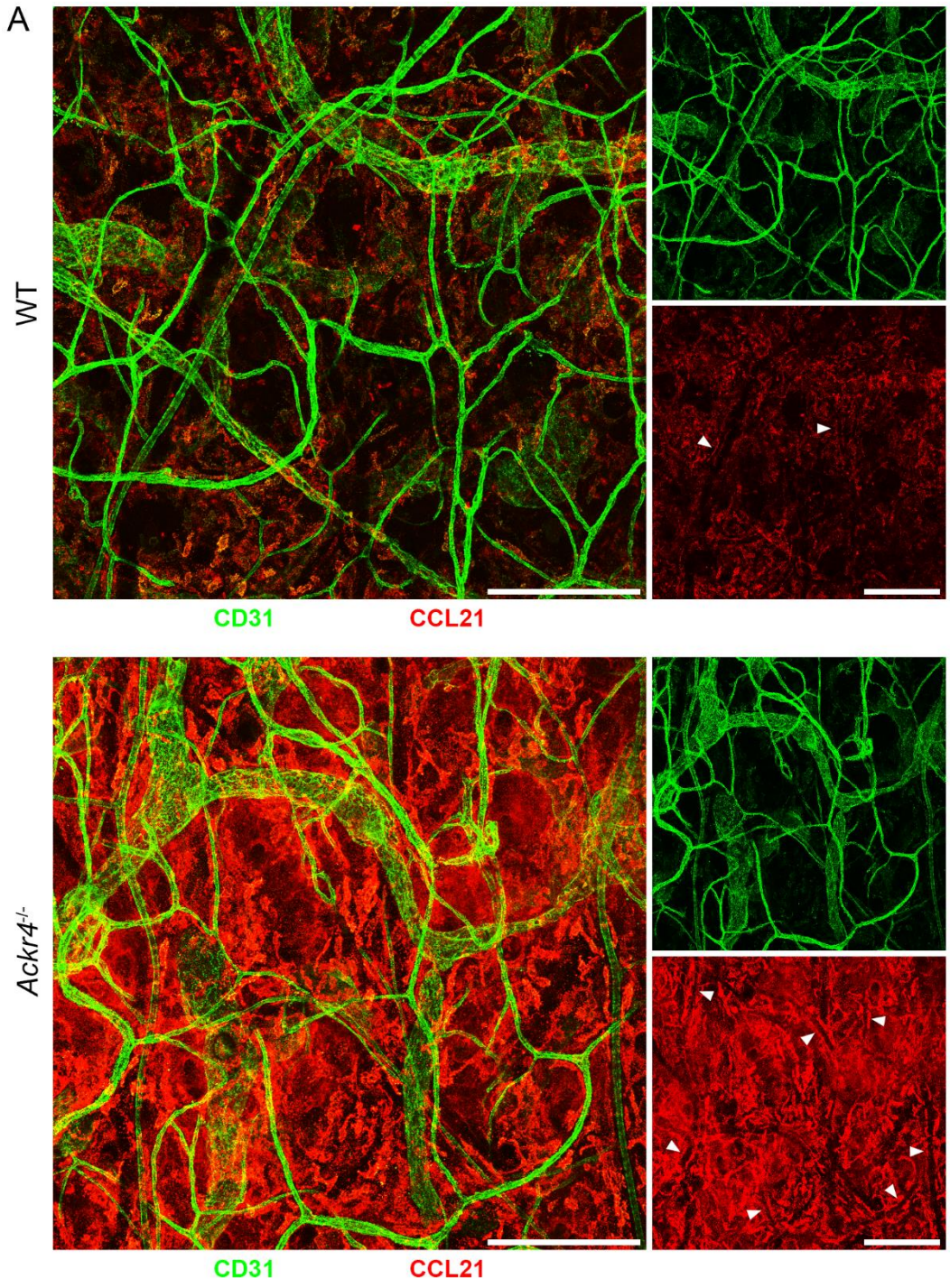
A
WT
CD31
CCL21
Ackr4-/-
CD31
CCL21
B
i) WT: NS
ii) Ackr4-/-: NS
WT
Ackr4-/-
iii) WT vs Ackr4-/-
p<0.001
CCL21 mean grey intensity (normalised to WT)
0
1
2
3
4
0
20
40
60
80
Distance from CD31+ vessel (μm)

Figure 3.4: ACKR4 restricts CCL21 accumulation at the surface of blood vasculature

(A) Representative Z-stack projections of unfixed, non-permeabilised whole-mount ear sheets from steady-state WT and *Ackr4*$^{-/-}$ mice, stained CD31 (green) and CCL21 (red), with single channel images (right). Areas of interest are denoted by arrows referred to in text. Scale bar: 200μm. Images representative of WT n=2, *Ackr4*$^{-/-}$ n=3. **(B)** Quantitation of CCL21 mean grey intensity (normalized to average WT intensity) at defined distances from the nearest CD31^{+} vessel from images in (A). Each dot represents the average of biological replicates, within which technical replicates were averaged, ±SEM, two-way ANOVA with Sidak's multiple comparison test for i) CCL21 intensity between a defined distance and the vessel edge (i.e. 0 μm) in WT tissue, ii) CCL21 intensity between a defined distance and the vessel edge in *Ackr4*$^{-/-}$ tissue, or iii) CCL21 intensity between WT and *Ackr4*$^{-/-}$ tissue at a defined interstitial distance.

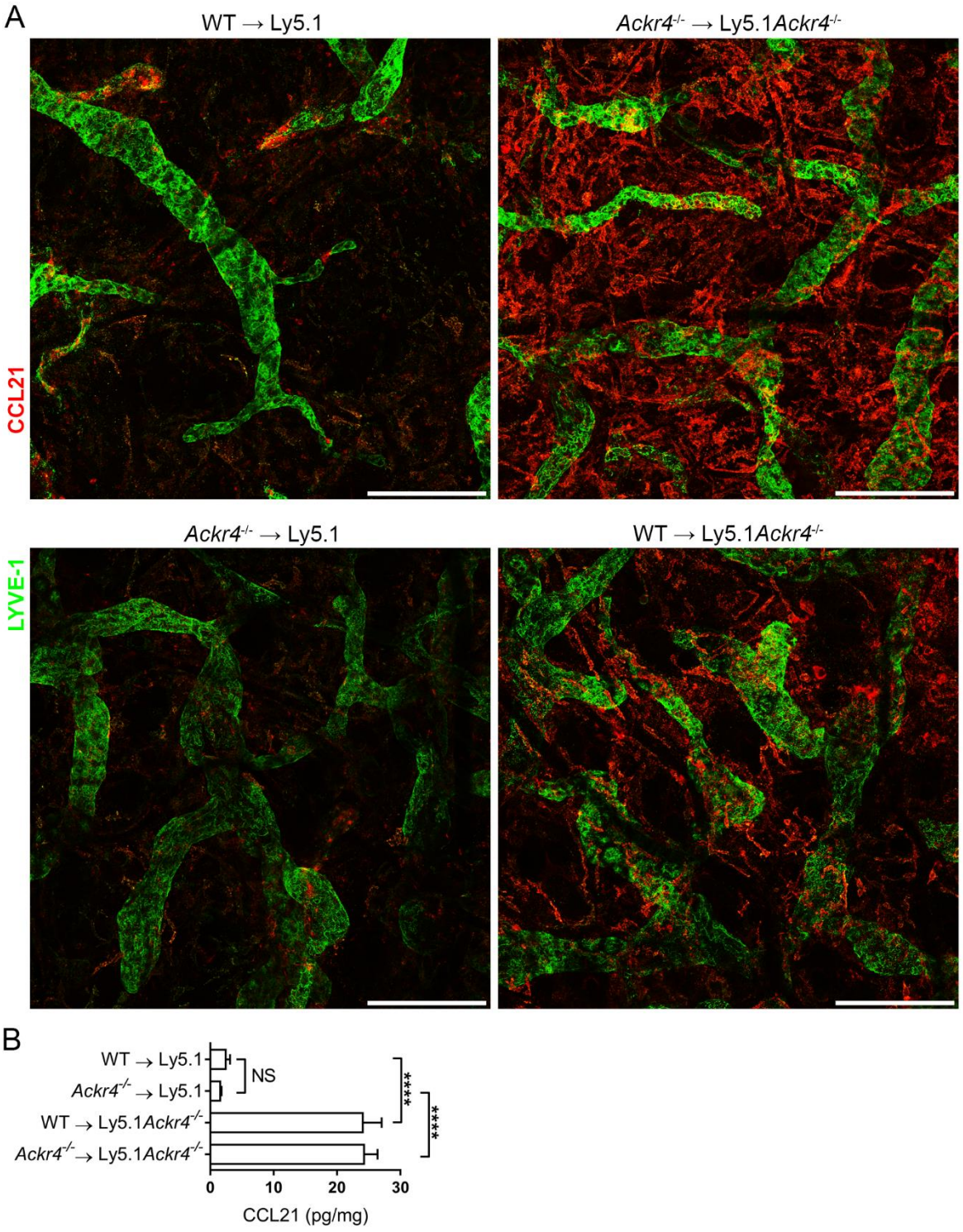
A
WT → Ly5.1
Ackr4-/- → Ly5.1Ackr4-/-
CCL21
Ackr4-/- → Ly5.1
WT → Ly5.1Ackr4-/-
LYVE-1
B
WT → Ly5.1
Ackr4-/- → Ly5.1
WT → Ly5.1Ackr4-/-
Ackr4-/- → Ly5.1Ackr4-/-
NS
****
****
0
10
20
30
CCL21 (pg/mg)

Figure 3.5: Radio-resistant ACKR4 expression regulates dermal CCL21

(A) Representative Z-stack projections of unfixed, non-permeabilised whole-mount ear sheets from indicated bone marrow chimeras, stained LYVE-1 (green) and CCL21 (red). Scale bar: 200μm. Images representative of 3 mice/chimera. **(B)** Quantity of total CCL21 (pg/mg) leached out of ear tissue from chimeric mice, as determined by ELISA. WT→Ly5.1 n=3, *Ackr4*$^{-/-}$→Ly5.1 and WT→Ly5.1*Ackr4*$^{-/-}$ n=4, *Ackr4*$^{-/-}$→Ly5.1*Ackr4*$^{-/-}$ n=5, ±SEM, one-way ANOVA with Tukey's multiple comparisons test. ****p<0.0001.

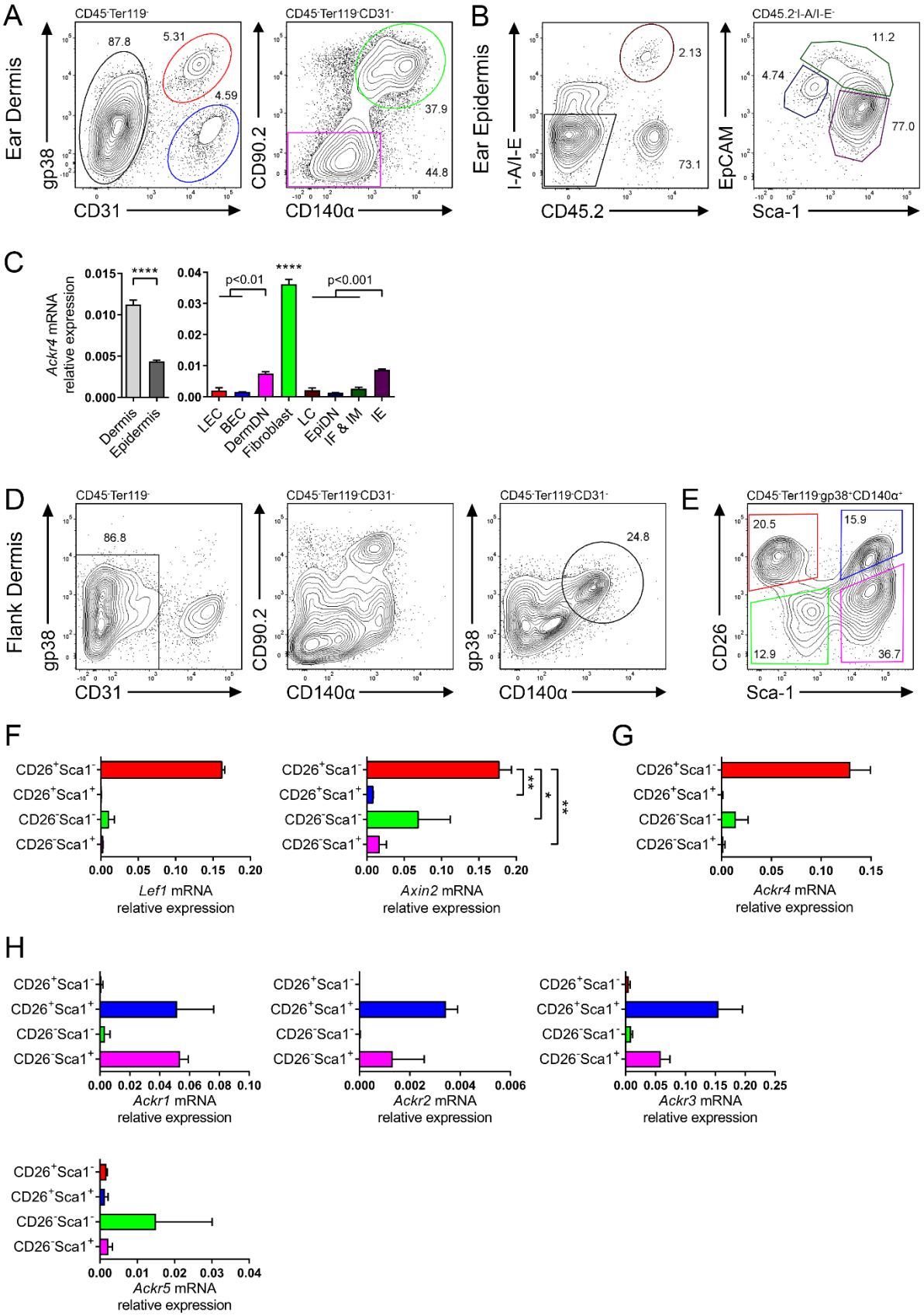
A
Ear Dermis
CD45-Ter119-
87.8
5.31
4.59
gp38
CD31
CD45-Ter119-CD31-
37.9
44.8
CD90.2
CD140α
B
Ear Epidermis
2.13
73.1
I-A/I-E
CD45.2
CD45.2-I-A/I-E-
11.2
4.74
77.0
EpCAM
Sca-1
C
Ackr4 mRNA relative expression
****
p<0.01
****
p<0.001
Dermis
Epidermis
LEC
BEC
DermDN
Fibroblast
LC
EpiDN
IF & IM
IE
D
Flank Dermis
CD45-Ter119-
86.8
gp38
CD31
CD45-Ter119-CD31-
CD90.2
CD140α
CD45-Ter119-CD31-
24.8
gp38
CD140α
E
CD45-Ter119-gp38-CD140α+
20.5
15.9
12.9
36.7
CD26
Sca-1
F
CD26+Sca1-
CD26+Sca1+
CD26-Sca1-
CD26-Sca1+
Lef1 mRNA relative expression
Axin2 mRNA relative expression
G
Ackr4 mRNA relative expression
H
Ackr1 mRNA relative expression
Ackr2 mRNA relative expression
Ackr3 mRNA relative expression
Ackr5 mRNA relative expression

Figure 3.6: Dermal papillary fibroblasts express the greatest *Ackr4* mRNA in the skin

(A) Representative sorting strategy for BECs ($CD45^-Ter119^-CD31^+gp38^-$), LECs ($CD45^-Ter119^-CD31^+gp38^+$), DermDN cells ($CD45^-Ter119^-CD31^-CD140\alpha^-CD90.2^-$), and fibroblasts ($CD45^-Ter119^-CD31^-CD140\alpha^+CD90.2^+$) from steady-state WT ear dermis. **(B)** Representative sorting strategy for Langerhans cells (LC: $CD45.2^+I\text{-}A/I\text{-}E^+$), EpiDN cells ($CD45.2^-I\text{-}A/I\text{-}E^-EpCAM^{mid}Sca\text{-}1^-$), IE keratinocytes ($CD45.2^-I\text{-}A/I\text{-}E^-EpCAM^{lo}Sca\text{-}1^+$), and IF and IM keratinocytes (IF: $CD45.2^-I\text{-}A/I\text{-}E^-EpCAM^{mid}Sca\text{-}1^+$; IM: $CD45.2^-I\text{-}A/I\text{-}E^-EpCAM^{hi}Sca\text{-}1^-$) from steady-state WT ear epidermis. **(C)** *Ackr4* mRNA relative to *Rplp0* transcript in whole dermis and epidermis (left) and sorted dermal and epidermal radio-resistant populations (right). **(D)** Representative gating strategy for dermal fibroblasts from steady-state flank dermis. **(E)** Representative sorting strategy for adult fibroblast subpopulations delineated by CD26 and Sca-1 in steady-state flank dermis. **(F)** Expression of postnatal papillary fibroblast mRNA transcripts relative to *Rplp0* in sorted adult fibroblast subpopulations. **(G)** Expression of *Ackr4* mRNA transcripts relative to *Rplp0* in sorted fibroblast subpopulations. **(H)** Expression of all other atypical chemokine receptor mRNA transcripts relative to *Rplp0* in sorted fibroblast subpopulations. (A-C) Data pooled from 3 independent experiments, 5 pooled mice/experiment, ±SEM, one-way ANOVA with Tukey's multiple comparisons test, except whole dermis and epidermis *Ackr4* expression, data pooled from 2 independent experiments, n=7-8 mice total, ±SEM, two-tailed unpaired Student's t test. (D) Data representative of 2 independent experiments, n=2 mice. (E) Data representative of 3 independent experiments, 3 pooled mice/experiment. (F) Data representative of 2 independent experiments, 3 pooled mice/experiment, ±SD, one-way ANOVA with Tukey's multiple comparison test. (G, H) Data pooled from 3 independent experiments, 3 pooled mice/experiment, ±SEM. *p<0.05, **p<0.01, ****p<0.0001.

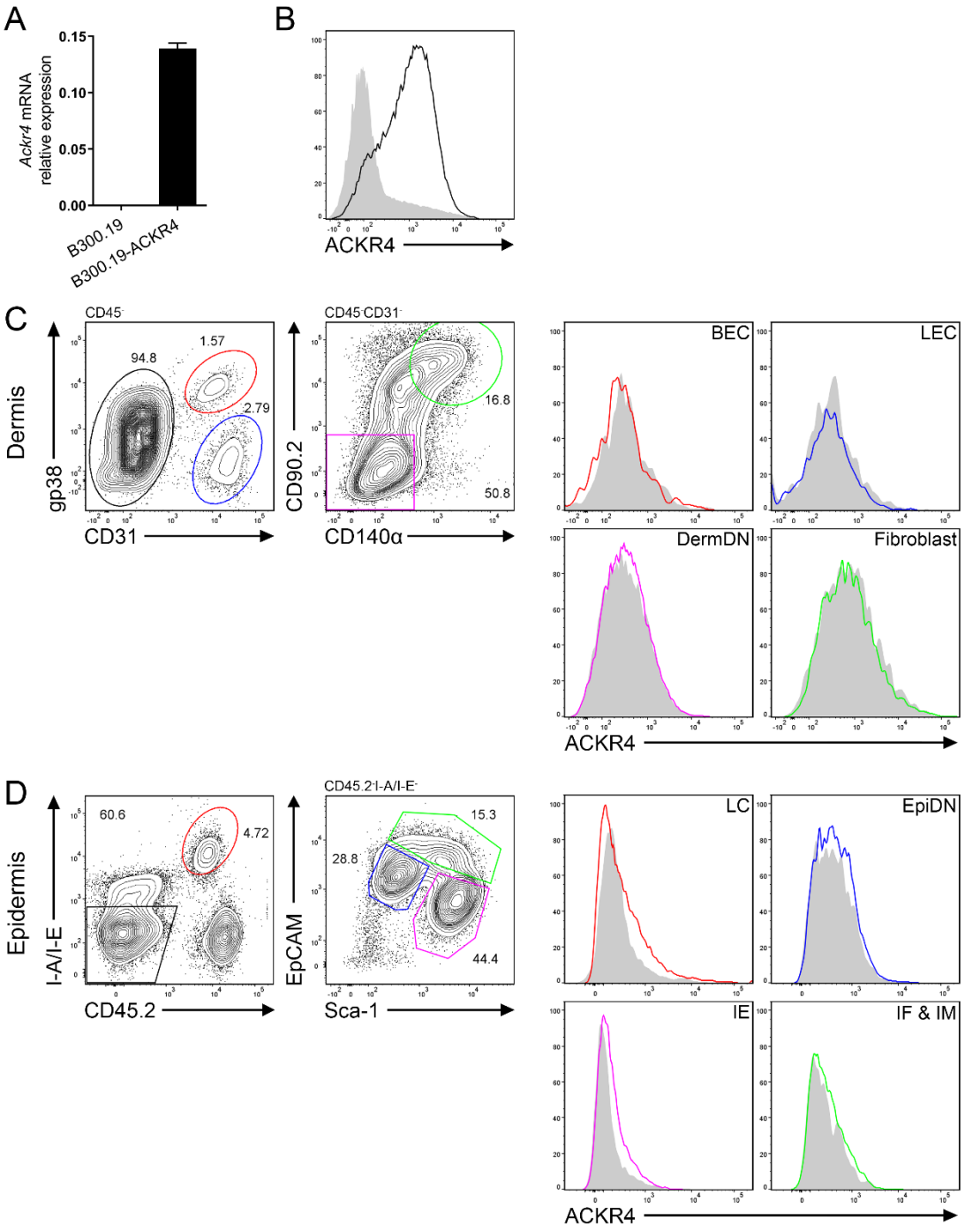
A
Ackr4 mRNA relative expression
0.15
0.10
0.05
0.00
B300.19
B300.19-ACKR4
B
ACKR4
C
CD45-
Dermis
gp38
CD31
94.8
1.57
2.79
CD45-CD31-
CD90.2
CD140α
16.8
50.8
BEC
LEC
DermDN
Fibroblast
ACKR4
D
Epidermis
I-A/I-E
CD45.2
60.6
4.72
CD45.2-I-A/I-E-
EpCAM
Sca-1
15.3
28.8
44.4
LC
EpiDN
IE
IF & IM
ACKR4

Figure 3.7: Antibody detection of ACKR4 on skin populations via flow cytometry

(A) Expression of *Ackr4* mRNA transcript relative to *Rplp0* in B300.19 and ACKR4-transduced B300.19 (B300.19-ACKR4) cells, ±SD. **(B)** Flow cytometric staining of cell lines in (A), B300.19 (filled grey) B300.19-ACKR4 (black line), with anti-ACKR4 clone 13E11 after skin digest treatment. **(C)** Representative gating strategy for major stromal populations in steady-state ear dermis, and detection of ACKR4 via clone 13E11 in WT (coloured line) and *Ackr4*$^{-/-}$ (filled histogram) mice for each population. **(D)** Representative gating strategy for major stromal/radio-resistant populations in steady-state ear epidermis, and detection of ACKR4 via clone 13E11 in WT (coloured line) and *Ackr4*$^{-/-}$ (filled histogram) mice for each population. (C, D) Representative of 2 independent experiments, WT n=8, *Ackr4*$^{-/-}$ n=4 total.

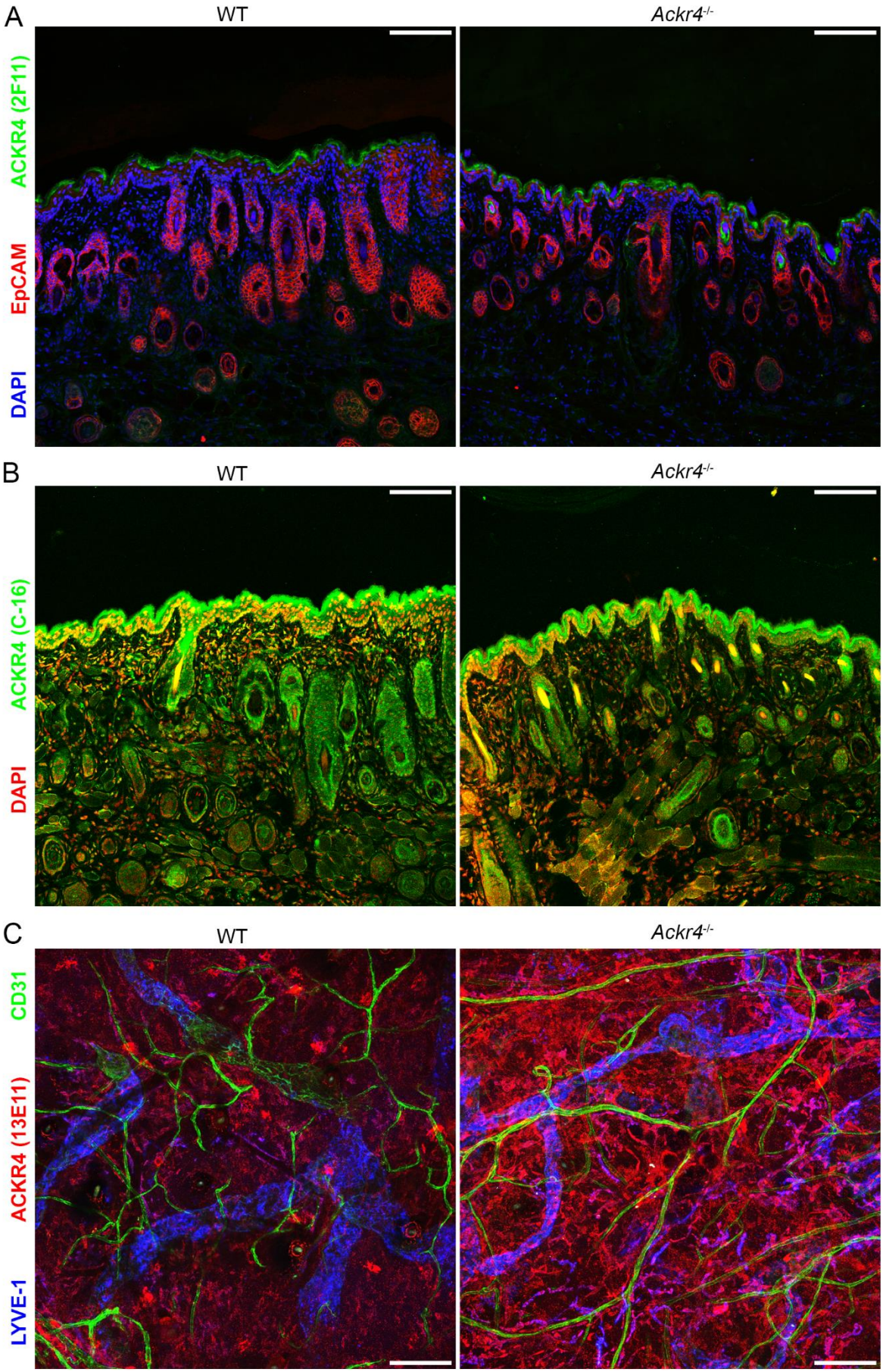
A
WT
Ackr4-/-
ACKR4 (2F11)
EpCAM
DAPI
B
WT
Ackr4-/-
ACKR4 (C-16)
DAPI
C
WT
Ackr4-/-
CD31
ACKR4 (13E11)
LYVE-1

Figure 3.8: Antibody detection of ACKR4 in skin sections and whole-mount ear sheets

(A) Representative PFA-fixed lip skin sections from WT and *Ackr4*$^{-/-}$ mice stained for EpCAM (red), ACKR4 via clone 2F11 (green), and cell nuclei (DAPI, blue). Scale bar: 200µm. Images representative of Chiba laboratory antibody clones 2F11 and 13E11 from two experiments, WT n=5 and *Ackr4*$^{-/-}$ n=4 total. **(B)** Representative acetone-fixed lip skin sections from WT and *Ackr4*$^{-/-}$ mice stained for ACKR4 via Santa Cruz clone C-16 (green), and cell nuclei (DAPI, red). Scale bar: 200µm. Images representative of two experiments, WT n=5 and *Ackr4*$^{-/-}$ n=4 total. **(C)** Z-stack projections of unfixed, non-permeabilised whole-mount ear sheets from WT and *Ackr4*$^{-/-}$ mice, stained for LYVE-1 (blue), ACKR4 via clone 13E11 (red), and CD31 (green). Scale bar: 200µm. Images representative of Chiba laboratory antibody clones 2F11 and 13E11 from two experiments, WT n=6 and *Ackr4*$^{-/-}$ n=3 total.

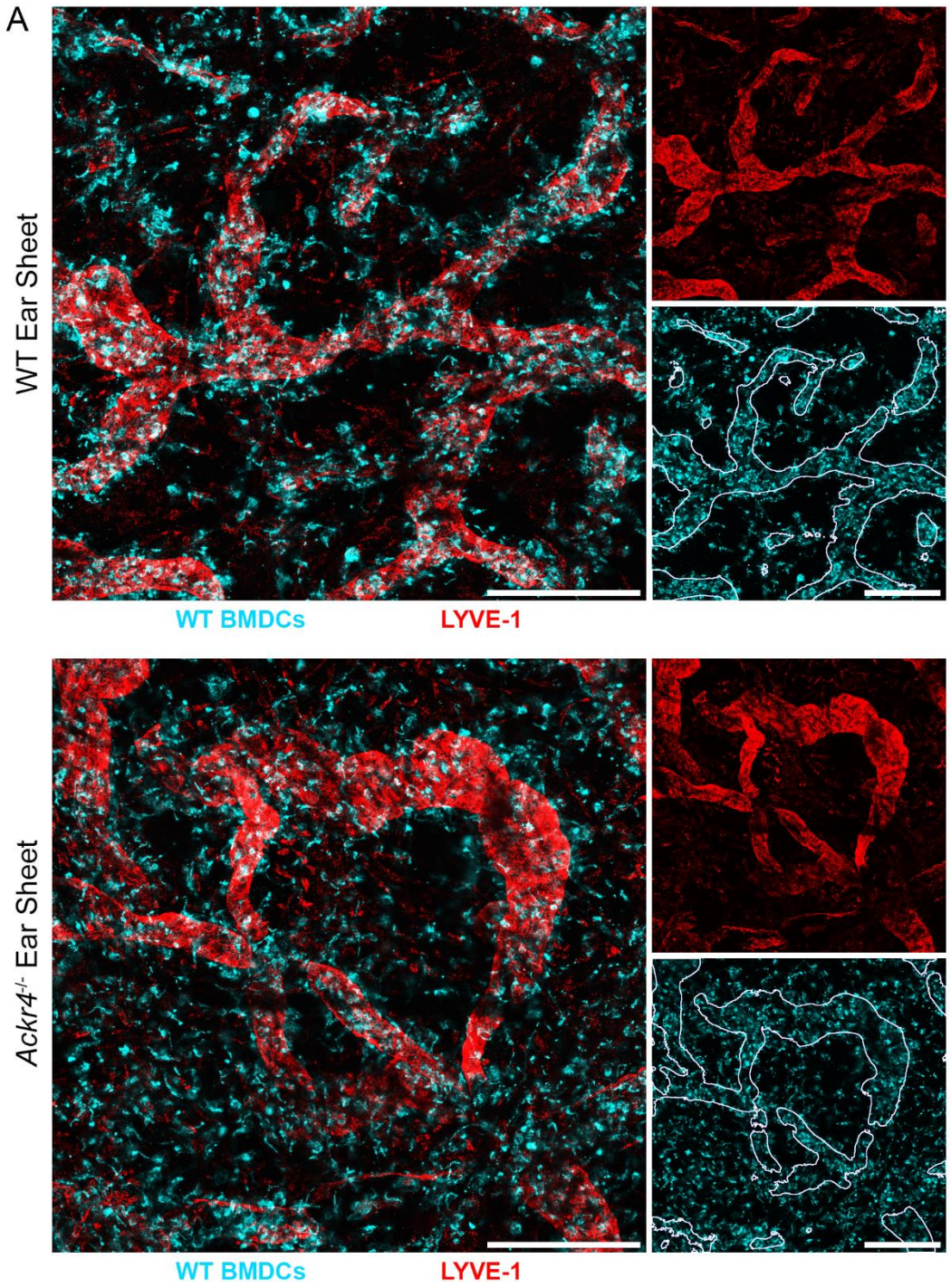
A
WT Ear Sheet
WT BMDCs
LYVE-1
Ackr4-/- Ear Sheet
WT BMDCs
LYVE-1
B
BMDC mean grey intensity inside:outside LYVE-1+ mask
**
WT
Ackr4-/-

Figure 3.9: Intradermal dendritic cell migration is perturbed in *Ackr4*$^{-/-}$ ear sheets

(A) Representative Z-stack projections of WT BMDC crawl-in assay on WT (top row) and *Ackr4*$^{-/-}$ (bottom row) whole-mount ear sheets after 45 mins, stained LYVE-1 (red), WT BMDCs (cyan), with single channel images (right) and lymphatic vessel mask (bottom right). Scale bar: 200µm. **(B)** Representative quantitation of WT BMDC Cell Proliferation Dye mean grey intensity inside:outside lymphatic vessel masks from (A). (A, B) Data representative of 2 independent experiments, n=9 mice/strain total, ±SEM, two-tailed unpaired Student's t test. **p<0.01.

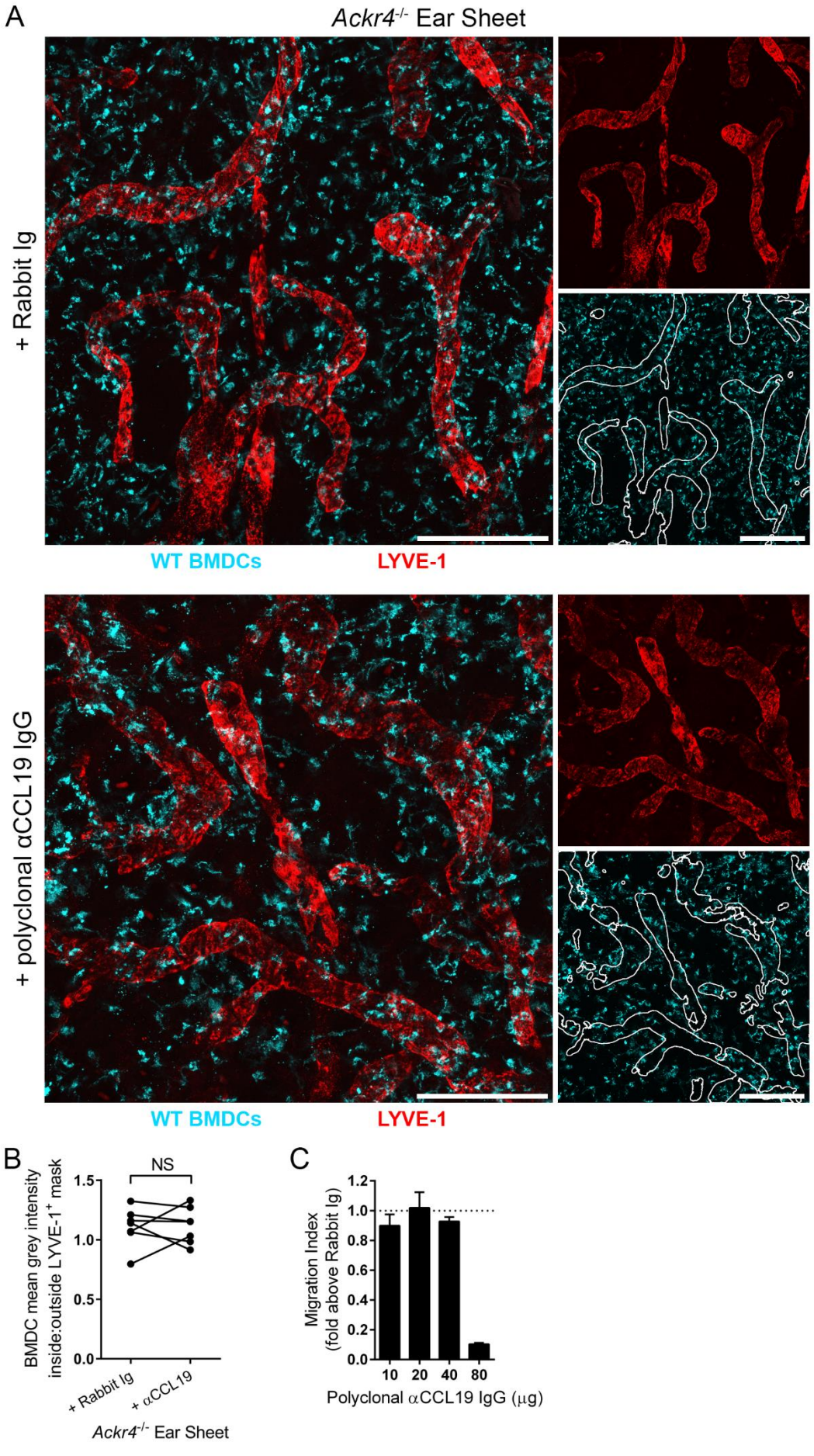
A
Ackr4-/- Ear Sheet
+ Rabbit Ig
WT BMDCs
LYVE-1
+ polyclonal αCCL19 IgG
WT BMDCs
LYVE-1
B
BMDC mean grey intensity inside:outside LYVE-1+ mask
NS
1.5
1.0
0.5
0.0
+ Rabbit Ig
+ αCCL19
Ackr4-/- Ear Sheet
C
Migration Index (fold above Rabbit Ig)
1.2
1.0
0.8
0.6
0.4
0.2
0.0
10
20
40
80
Polyclonal αCCL19 IgG (μg)

Figure 3.10: Neutralisation of hyperabundant CCL19 in *Ackr4*$^{-/-}$ ear sheets does not rescue aberrant dendritic cell migration

(A) Representative Z-stack projections of WT BMDC crawl-in assay after 45 mins on *Ackr4*$^{-/-}$ whole-mount ear sheets pre-treated with isotype control (top row) or 300µg polyclonal anti-CCL19 (bottom row), stained LYVE-1 (red), WT BMDCs (cyan), with single channel images (right) and lymphatic vessel mask (bottom right). Scale bar: 200µm. Images representative of two independent experiments, n=7 mice receiving both treatments. **(B)** Quantitation of WT BMDC Cell Proliferation Dye mean grey intensity inside:outside lymphatic vessel mask from (A). Each dot represents the average of technical replicates from one ear sheet, and each line represents one mouse, two-tailed paired Student's t test. **(C)** Transwell migration of naïve splenocytes from WT mice to 75ng/mL recombinant CCL19 in the presence of increasing concentrations of neutralising polyclonal anti-CCL19 or control immunoglobulin. Migration index is presented as fold above immunoglobulin control, n=3, ±SEM, one-way ANOVA with Tukey's multiple comparisons test.

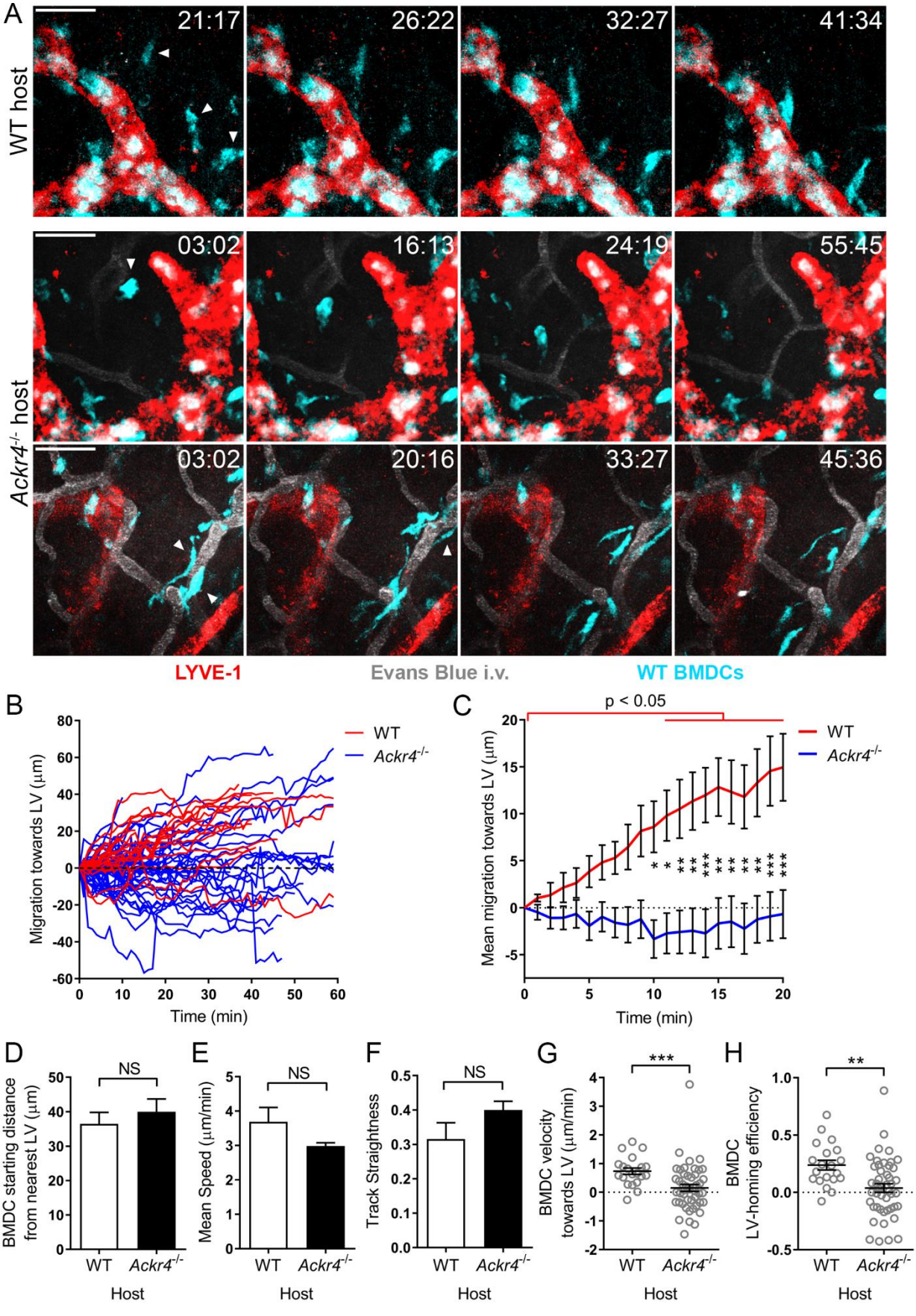
A
WT host
Ackr4-/- host
21:17
26:22
32:27
41:34
03:02
16:13
24:19
55:45
03:02
20:16
33:27
45:36
LYVE-1
Evans Blue i.v.
WT BMDCs
B
Migration towards LV (µm)
Time (min)
WT
Ackr4-/-
C
p < 0.05
Mean migration towards LV (µm)
Time (min)
WT
Ackr4-/-
D
BMDC starting distance from nearest LV (µm)
NS
WT
Ackr4-/-
Host
E
Mean Speed (µm/min)
NS
WT
Ackr4-/-
Host
F
Track Straightness
NS
WT
Ackr4-/-
Host
G
BMDC velocity towards LV (µm/min)
***
WT
Ackr4-/-
Host
H
BMDC LV-homing efficiency
**
WT
Ackr4-/-
Host

Figure 3.11: Lymphatic vessel homing of dendritic cells is impaired in *Ackr4*$^{-/-}$ skin *in vivo*

(A) Representative Z-stack projections and time stamps (mm:ss) of emigrating WT BMDCs in WT and *Ackr4*$^{-/-}$ host footpads, 18 hours post s.c. transfer. White arrows highlight migrating WT BMDCs (cyan) relative to LYVE-1^{+} lymphatic vessels (red) or blood vessels (Evans Blue dye i.v., grey). Scale bar: 50µm. Images representative of 2 independent experiments, n=4 mice/host strain total. **(B)** Displacement of tracked WT BMDCs in WT and *Ackr4*$^{-/-}$ hosts over time, relative to nearest lymphatic vessel. Each line represents one tracked BMDC. **(C)** Mean displacement of tracked WT BMDCs in WT and *Ackr4*$^{-/-}$ hosts over time, relative to nearest lymphatic vessel. Only tracks ≥20 mins were included, analysing the first 20 mins of longer tracks. All statistical comparisons in WT mice between time-point 0mins and time-points 11-20mins inclusive were $p<0.05$. There were no significant differences across time-points in *Ackr4*$^{-/-}$ mice. Comparisons between WT and *Ackr4*$^{-/-}$ hosts at a given time-point delineated by asterisks. **(D)** Starting distance of tracked WT BMDCs from nearest lymphatic vessel in WT and *Ackr4*$^{-/-}$ hosts. **(E)** Mean speed of tracked WT BMDCs in WT and *Ackr4*$^{-/-}$ hosts. **(F)** Straightness of WT BMDC tracks in WT and *Ackr4*$^{-/-}$ hosts. **(G)** Mean velocity of tracked WT BMDCs towards lymphatic vessels in WT and *Ackr4*$^{-/-}$ hosts. Each dot represents one tracked WT BMDC. **(H)** Lymphatic vessel homing efficiency of tracked WT BMDCs in WT and *Ackr4*$^{-/-}$ hosts. Each dot represents one tracked WT BMDC. (B-H) Data pooled from two independent experiments, n=4 mice/host strain, ±SEM, (C) two-way ANOVA with Sidak's multiple comparison test. (D-H) two-tailed unpaired Student's t test. *$p<0.05$, **$p<0.01$, ***$p<0.001$.

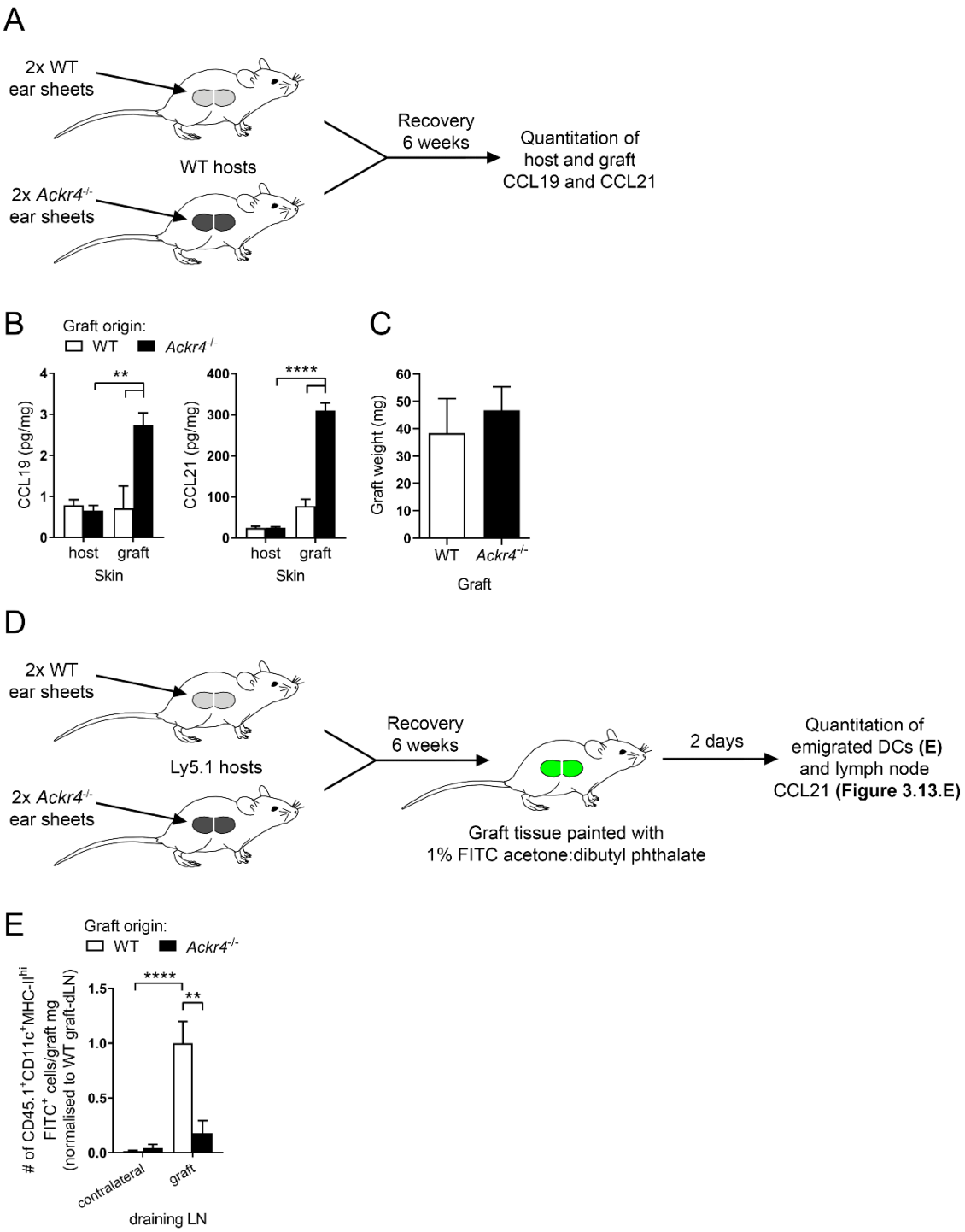
A
2x WT
ear sheets
WT hosts
2x Ackr4-/-
ear sheets
Recovery
6 weeks
Quantitation of
host and graft
CCL19 and CCL21
B
Graft origin:
WT
Ackr4-/-
CCL19 (pg/mg)
CCL21 (pg/mg)
**
****
host
graft
Skin
C
Graft weight (mg)
WT
Ackr4-/-
Graft
D
2x WT
ear sheets
Ly5.1 hosts
2x Ackr4-/-
ear sheets
Recovery
6 weeks
2 days
Quantitation of
emigrated DCs (E)
and lymph node
CCL21 (Figure 3.13.E)
Graft tissue painted with
1% FITC acetone:dibutyl phthalate
E
Graft origin:
WT
Ackr4-/-
# of CD45.1+CD11c+MHC-IIhi
FITC+ cells/graft mg
(normalised to WT graft-dLN)
****
**
contralateral
graft
draining LN

Figure 3.12: Skin-restricted ACKR4-deficiency is sufficient to drive dermal CCL21 accumulation and perturb dendritic cell egress

(A) Schematic for experiment in (B). WT or *Ackr4*$^{-/-}$ graft donor mice were humanely killed and ear sheets were harvested for transplantation. WT graft recipient mice were anaesthetised and two ear sheets were grafted on their right abdominal flank. After a recovery period of 6 weeks, WT graft recipient mice were humanely killed for analysis. **(B)** Amount of CCL19 and total CCL21 in contralateral host flank skin and grafted skin (pg/mg) from WT graft recipients 6 weeks post-tissue engraftment, as determined by ELISA. **(C)** Weights (mg) of grafted tissue in (B). **(D)** Schematic for experiments in (E and Figure 3.13.E). WT or *Ackr4*$^{-/-}$ graft donor mice were humanely killed and ear sheets were harvested for transplantation. Ly5.1 graft recipient mice were anaesthetised and two ear sheets were grafted on their right abdominal flank. After a recovery period of 6 weeks, grafted tissue was painted with 1% FITC for analysis after 2 days. **(E)** Number of CD45.1^{+} host-derived migratory dendritic cells emigrated from FITC-painted grafts (CD45.1^{+}CD11c^{+}MHC-II^{hi}FITC^{+}) in contralateral lymph nodes and graft-draining lymph nodes after 2 days, per graft weight (mg). Values are normalised to the number of emigrated dendritic cells in WT graft-draining lymph nodes. (B, C) n=3 WT graft recipients, n=4 *Ackr4*$^{-/-}$ graft recipients, ±SEM, (B) two-way ANOVA with Sidak's multiple comparison test, (C) two-tailed unpaired Student's t test. (E) Data pooled from 3 independent experiments, n=14 WT graft recipients, n=4 *Ackr4*$^{-/-}$ graft recipients, ±SEM, two-way ANOVA with Sidak's multiple comparison test. *p<0.05, **p<0.01, ****p<0.0001.

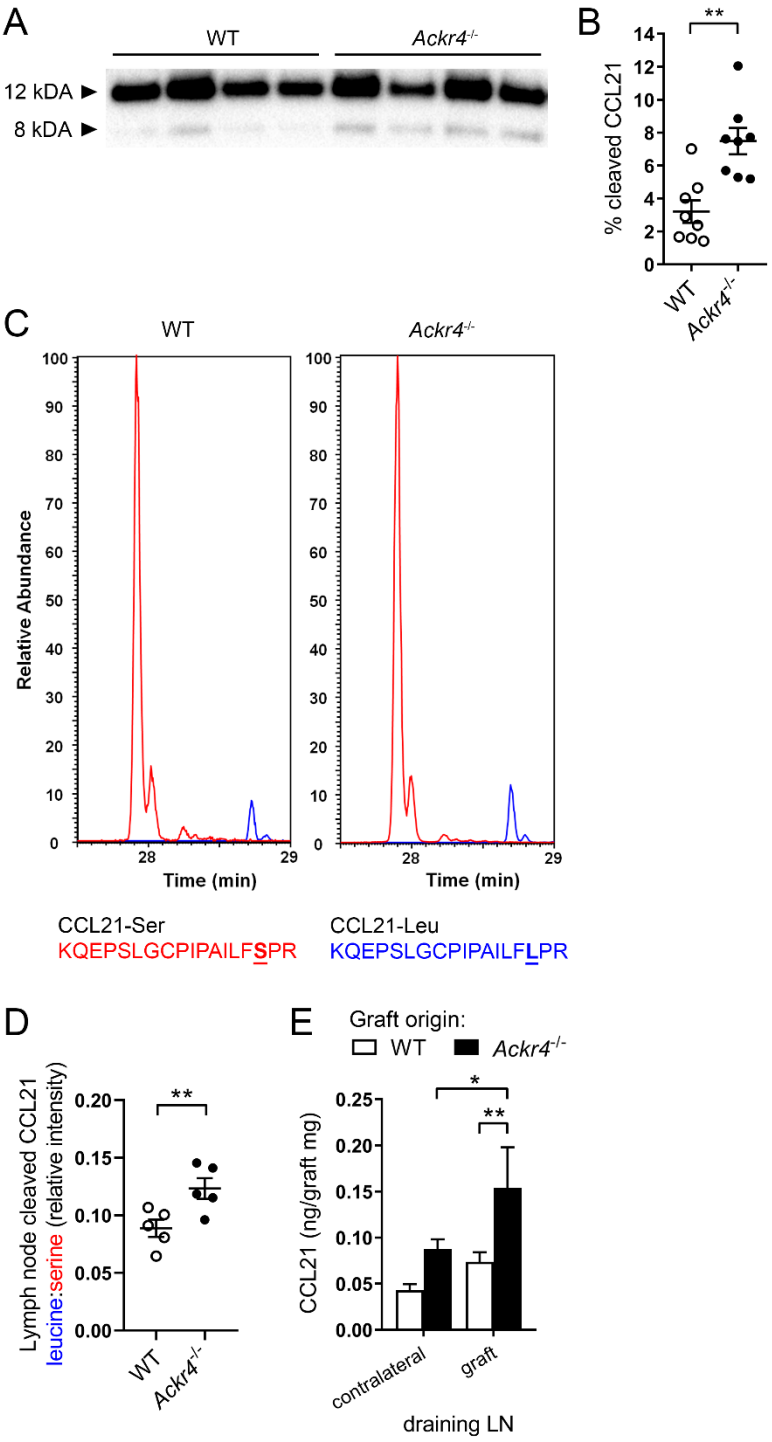
A
WT
Ackr4-/-
12 kDA ►
8 kDA ►
B
**
% cleaved CCL21
WT
Ackr4-/-
C
WT
Ackr4-/-
Relative Abundance
Time (min)
Time (min)
CCL21-Ser
KQEPSLGCPIPAILFSPR
CCL21-Leu
KQEPSLGCPIPAILFLPR
D
**
Lymph node cleaved CCL21
leucine:serine (relative intensity)
WT
Ackr4-/-
E
Graft origin:
WT
Ackr4-/-
*
**
CCL21 (ng/graft mg)
contralateral
graft
draining LN

Figure 3.13: ACKR4-deficiency drives accumulation of peripheral CCL21 in draining lymph nodes

(A) Detection of full-length (12kDA) and cleaved (8kDA) CCL21 leached out from skin-draining lymph nodes (inguinal, axillary and deep cervical) of steady-state WT and *Ackr4*$^{-/-}$ mice by immunoprecipitation then western blot. **(B)** Percent of cleaved CCL21 amongst total CCL21 in skin-draining lymph nodes from (A). **(C)** Representative LC-MS chromatograms detecting unique CCL21-Serine (red) and CCL21-Leu (blue) tryptic peptides from cleaved CCL21 leached out and immunoprecipitated from skin-draining lymph nodes of steady-state wildtype and *Ackr4*$^{-/-}$ mice. Unique CCL21-Serine and CCL21-Leucine tryptic peptide sequences are listed with the single amino acid difference underlined. **(D)** Relative intensity of CCL21 leucine:serine isoforms quantitated from LC-MS analysis in (C). **(E)** Quantity of CCL21 in contralateral and graft-draining lymph node supernatant from Figure 3.12.D, as determined by ELISA. (A) Blot representative of two independent experiments, n=8 biological samples of two pooled mice per genotype total, each lane is a biological sample. (B) Data pooled from two independent experiments, n=8 biological samples of two pooled mice per genotype. Each dot represents a biological replicate, ±SEM, two-tailed unpaired Student's t test. (C) LC-MS chromatograms representative of two independent experiments, n=8 biological samples of 2 pooled mice per genotype total. (D) Data representative of two independent experiments, n=8 biological samples of 2 pooled mice per genotype total. Each dot represents a biological sample from one experiment, ±SEM, two-tailed unpaired Student's t test. (E) Data pooled from 3 independent experiments, n=14 WT graft recipients, n=5 *Ackr4*$^{-/-}$ graft recipients, ±SEM, two-way ANOVA with Sidak's multiple comparison test. *$p<0.05$, **$p<0.01$.

Video files are included as digital files or on CD-ROM

Video 3.1: BMDC lymphatic homing in wildtype hosts

Time-lapse video of WT LPS-activated BMDCs (cyan) in WT host footpads post s.c. transfer and imaged for 60 minutes at one-minute intervals by two-photon microscopy. Emigrating BMDCs are visible in the top right-hand corner migrating towards the nearest LYVE-1^+ lymphatic vessel (red). Scale bar: 50µm, time stamp (h:mm:ss), tracking tails are displayed. Video representative of two independent experiments, n=4 mice/host strain total.

Video 3.2: Impaired BMDC lymphatic homing in *Ackr4*$^{-/-}$ hosts

Time-lapse video of WT LPS-activated BMDCs (cyan) in *Ackr4*$^{-/-}$ host footpads post s.c. transfer and imaged for 60 minutes at one-minute intervals by two-photon microscopy. A central BMDC within the interstitial space and close to blood capillaries (white) fails to sense and migrate towards the nearest LYVE-1^+ lymphatic vessel (red). Scale bar: 50µm, time stamp (h:mm:ss), tracking tails are displayed. Video representative of two independent experiments, n=4 mice/host strain total.

Video 3.3: Abnormal BMDC blood capillary crawling in *Ackr4*$^{-/-}$ hosts

Time-lapse video of WT LPS-activated BMDCs (cyan) in *Ackr4*$^{-/-}$ host footpads post s.c. transfer and imaged for 60 minutes at one-minute intervals by two-photon microscopy. Migrating BMDCs in the bottom right-hand corner send out long processes to crawl along blood capillaries (white) instead of migrating towards proximal LYVE-1^+ lymphatic vessels (red). Scale bar: 50µm, time stamp (h:mm:ss), tracking tails are displayed. Video representative of two independent experiments, n=4 mice/host strain total.

Chapter 4
Results- GCT cell migratory cues

Chapter 4 - Results - GCT cell migratory cues

4.1 Overview

Extensive T and B cell interactions underpin the formation and propagation of germinal centre responses that produce high-affinity antibodies. Central to these interactions are dynamic migratory events to initially overcome T and B cell segregation in lymphoid organs, then deliver responding cells to the correct microanatomical niches necessary for their differentiation, function and survival. T_{FH} and T_{FR} cells are essential in supporting and regulating the quality of germinal centre antibody responses. Their migration during the propagation of antibody responses has largely been attributed to CXCR5 expression, however CXCR5-deficient T_{FH} and T_{FR} cells are still capable of localising to the germinal centre[186,243]. This suggests that additional chemotactic axes contribute to the trafficking of GCT cells during antibody responses, however the complete chemokine receptor expression profiles of these subsets remain uncharacterised.

4.2 Chemokine receptor profiling of GCT cells

To comprehensively investigate expression of chemokine receptors by GCT cells, $CXCR5^{+}PD\text{-}1^{+}$ T-helper cells were sorted 5 and 8 days post-SRBC immunisation (Figure 4.1.A), and the relative expression of key GCT cell genes and chemotactic receptors was determined by qPCR (Figure 4.1.B-E). SRBC i.p. immunisation was selected as the immunological stimulus as the kinetics of this response are well characterised and it produces a robust humoral response generating many splenic GCT cells required for sorting and mRNA isolation. Given the dynamic changes in chemokine receptor expression profile already characterised in germinal centre subsets, GCT cells were sorted at two timepoints following immunisation, before the peak of the response (day 5) and after the peak response (day 8), to identify whether additional chemokine receptors displayed dynamic kinetics. In comparison to sorted splenic naïve CD4 T cells ($CD4^{+}CD44^{-}CD62L^{+}$), GCT cells had greater expression of *Bcl6*, encoding the master regulator of GCT cell differentiation, and *Il21*, encoding a key cytokine of the T_{FH} repertoire (Figure 4.1.B). As anticipated, GCT cells had greater expression of transcripts for the follicle/germinal centre-tropic chemokine receptors CXCR5 and CXCR4, and had downregulated *Ccr7* transcript relative to naïve T cells (Figure 4.1.C). Transcript for the chemotactic receptor *Ebi2* appeared progressively downregulated by GCT cells relative to naïve CD4 T cells throughout the duration of the response as reported elsewhere during the course of this project[187] (Figure 4.1.C). Having validated the expression of key germinal centre transcripts in our sorted GCT cells, the relative expression of all other known chemokine receptors (Figure 4.1.D) and atypical chemokine receptors (Figure 4.1.E) was determined. The limited chemokine receptor repertoire of naïve T-helper cells provided a useful comparison to evaluate whether GCT cells had upregulated/downregulated typical or atypical chemokine receptors upon differentiation. Compared to naïve T cells, GCT cells reproducibly expressed higher levels of *Ccr2*, *Ccr6*, and *Cxcr3* transcripts on days 5 and 8, transiently upregulated of *Ccr4* on day

5, and had downregulated *Ccr9* expression (Figure 4.1.D). There was negligible expression of atypical chemokine receptors in all T cell populations examined (Figure 4.1.E).

Of the chemokine receptor transcripts detected in GCT cells, an interesting avenue of novel investigation was *Ccr6*. This was consistently expressed in GCT cells at both timepoints, is poorly characterised with regard to T cell function in the germinal centre, and a range of experimental tools were available in the lab to study CCR6 expression and function. While CCR6 expression had been identified in early antigen-engaged B cells[180–183], its function in events underpinning antibody responses remain incompletely understood. As GCT- and GCB cells co-opt migratory programs throughout the germinal centre response, investigating the role of CCR6 in GCT cell biology may also provide insights to its respective function in early B cell activation. Furthermore, CCR6 is known to be expressed and utilised by Tregs[269,270], which raised the possibility that T_{FR} cells which differentiate from nTregs may express and utilise CCR6. Therefore, an investigation into the expression and function of CCR6 on T_{FH} and T_{FR} cells was embarked upon.

4.3 CCR6 is differentially expressed by T_{FH} and T_{FR} cells

First, the question of whether T_{FH} and T_{FR} cells differentially express CCR6 was investigated by flow cytometry. To interrogate CCR6 expression by GCT cells, wildtype mice were immunised with SRBC and CCR6 expression was analysed via flow cytometry on T_{FH} cells ($CXCR5^{hi}PD\text{-}1^{hi}Foxp3^{-}$) and T_{FR} cells ($CXCR5^{hi}PD\text{-}1^{hi}Foxp3^{+}$; Figure 4.2.A), and respective precursor populations, naïve CD4 T cells and nTregs (Figure 4.2.B). Here, nTregs were distinguished from peripheral Tregs by high neuropillin-1 expression[271,272]. As no difference in *Ccr6* transcript abundance was observed between an early and late timepoint post-immunisation (Figure 4.1.D), flow cytometry analysis was performed at the peak of the humoral response to SRBC on day 6 post immunisation. In this experiment, the additional GCT cell negative-marker PSGL-1 was included to identify GCT cell subsets as the preferred method for detecting CXCR5 with secondary antibody amplification was not compatible with the CCR6 staining method (Figure 4.2.A). Interestingly, CCR6 expression differed significantly between T_{FH} and T_{FR} populations by both measures of CCR6 geometric mean fluorescence intensity (gMFI; Figure 4.2.C) and proportion of CCR6-positive cells, approximately 15% T_{FH} cells compared to >50% T_{FR} cells expressing CCR6 (Figure 4.2.D). Within precursor populations, few naïve T-helper cells expressed CCR6 (Figure 4.2.D), whilst over 25% of nTregs were CCR6-positive (Figure 4.2.D), however there was no statistically significant difference in CCR6 gMFI between these subsets (Figure 4.2.C). Collectively, both gMFI and proportion measures of CCR6 expression significantly increased from the precursor nTreg population to germinal centre effector T_{FR} cell population (Figure 4.2.C, D), implicating a possible role for CCR6 in T_{FR} biology.

Co-expression of additional chemokine receptors with CXCR5 is known to regulate fine anatomical niche localisation of germinal centre populations during the humoral response. Additionally, the ratio of T_{FH} to T_{FR} cells is critical for the correct regulation of antibody responses, and when perturbed, can result in abnormal germinal centre kinetics, affinity maturation and antibody isotype switching, which may drive autoantibody generation[225,237,238,240,273]. As different proportions of T_{FH} and T_{FR} cells expressed CCR6, it was determined whether the ratio of T_{FH} to T_{FR} cells was significantly altered when further distinguishing these populations by CCR6 expression. This was achieved by gating CCR6-positive and -negative cells within the GCT cell gate ($CD4^+B220^-PSGL\text{-}1^{lo}CXCR5^{hi}PD\text{-}1^{hi}$), then delineating T_{FH} and T_{FR} cells by Foxp3 expression (Figure 4.2.E). Without any CCR6 pre-gating, the ratio of T_{FH}:T_{FR} was approximately 5:1 (Figure 4.2.F), as previously reported[43,221]. Interestingly, the T_{FH}:T_{FR} ratio significantly differed when segregated by CCR6 expression, from approximately 1:1 within $CCR6^+$ populations, to approximately 9:1 within $CCR6^-$ populations (Figure 4.2.F). This posed a question whether CCR6-driven migratory cues establish finer germinal centre niches that differentially support or suppress local cell activation through altering the ratio of T_{FH} to T_{FR} cells in that niche. Distinct CCR6 expression patterns between T_{FH} and T_{FR} were not a product of the SRBC immunisation strategy, as similar proportions of T_{FH} and T_{FR} cells (15% and 50% respectively) expressed CCR6 following NP-KLH/Alum immunisation (Figure 4.2.G). Likewise, CCR6 was expressed by a greater proportion of T_{FR} cells compared to T_{FH} cells following NP-KLH/Alum immunisation (Figure 4.2.G). Throughout the propagation of the germinal centre response to NP-KLH/Alum, the proportion of CCR6-expressing cells within each GCT cell compartment was steady, with only a slight but significant increase in CCR6-expressing T_{FR} cells from 48% to 54% on days 7 to 10 post immunisation (Figure 4.2.G). Together, CCR6 expression identified at the transcriptional level in GCT cells was validated by flow cytometry and identification of T_{FH} and T_{FR} cell subsets identified greater CCR6 expression in T_{FR} cells.

4.4 CCR6 expression facilitates GCT cell chemotaxis *in vitro*

To determine whether CCR6 expression in GCT cell populations could facilitate cell migration, *in vitro* transwell chemotaxis assays to the sole CCR6 ligand CCL20 were performed with splenocytes from day 6 SRBC-immunised mice. Migrated cells were subsequently identified and enumerated by flow cytometry, then the migration index of each cell population was calculated relative to control samples without chemokine. CCR6-deficient splenocytes from day 6 SRBC-immunised mice were also included as a control to demonstrate that migration was CCR6-dependent and not facilitated by expression of additional chemokines produced during the assay. Naïve CD4 T cells, which expressed minimal levels of *Ccr6* at the mRNA level (Figure 4.1.D) and minimal surface CCR6 protein (Figure 4.2.B-D) did not migrate to CCL20 (Figure 4.3.A). Conversely B cells, which were included as a positive-control[183,274], demonstrated migration to CCL20 in a CCR6- and dose-dependent manner (Figure 4.3.B). nTreg cells, approximately a quarter of which express CCR6 (Figure 4.2.B, D), demonstrated CCR6-dependent migration towards CCL20

(Figure 4.3.C). Within GCT cell populations, both T_{FH} cells (Figure 4.3.D) and T_{FR} cells (Figure 4.3.E) migrated to CCL20 in a CCR6-dependent manner. These experiments demonstrated that CCR6 expression by GCT cell subsets enabled chemotaxis to CCL20, however the migration of these subsets was not as robust as that observed for B cells.

4.5 CCL20 is induced in the spleen at low levels following immunisation

Given the ability of T_{FH} and T_{FR} cells to utilize CCR6 for migration *in vitro*, the availability of CCL20 in the spleen during the humoral response was determined, as this was the major site of antibody responses for the immunisation strategies utilised throughout this study. *Ccl20* transcript was present, albeit at low levels, in the spleen during the steady-state and 6 days post-SRBC immunisation (Figure 4.4.A). At the peak of the SRBC response, there was a significant, approximately 4-fold increase in extracellular CCL20 protein that leached out of the spleen, as determined by ELISA (Figure 4.4.B). To understand how CCR6 may influence the localisation of GCT cells during the humoral response, immunofluorescence imaging was performed to identify the distribution of CCL20 in the spleen during the steady-state and the peak of the germinal centre response, for which sections from day 14 NP-KLH/Alum i.p. immunised mice were utilised. Using a commercial polyclonal-goat antibody from R&D Systems published elsewhere[215,275], CCL20 was visualised in both fixed (4% PFA) and fixed/permeabilised (4% PFA, 0.05% saponin) spleen sections to visualise both extracellular, bioavailable CCL20, and total CCL20 respectively. The peri-arteriole lymphatic sheath (PALS) was identified by CD4 staining (red), and germinal centre-restricted N-acetylneuraminic acid (Neu5Ac) was detected in immunised spleens with the GL7 antibody clone (blue). In fixed spleen sections, isotype controls for all antibodies revealed no background staining other than non-specific AlexaFluor647 fluorescence restricted to the red pulp (left panel, Figure 4.5.A, B). However, this background staining was easily distinguishable from $CD4^+$ T cells localised in the white pulp (right panel, Figure 4.5.A, B). In steady-state fixed spleen sections (Figure 4.5.A), CCL20 staining was observed on central arterioles (examples highlighted with asterisks), and structures resembling trabecular/penicillar arteries[276] (examples highlighted with hashtags). This pattern of staining was reminiscent of CCL20 staining previously described in the inflamed lung that was immobilised on vascular heparan sulfate moieties[277]. In fixed, immunised spleen sections, similar CCL20 staining patterns to steady-state spleen sections were observed (right panel, Figure 4.5.B). Interestingly, small clusters of bright CCL20-positive cells were present in some peri-vascular areas (examples highlighted with arrows). These cells could not be definitively identified with the antibody panel utilised in this experiment; however they were CD4-negative and had dendritic cell-like morphology.

Fixation and permeabilisation of spleen sections again resulted in non-specific AlexaFluor647 fluorescence in the red pulp using this same antibody panel (left panel, Figure 4.6.A, B). Permeabilisation of steady-state spleen sections increased CCL20 staining intensity at the sites observed in non-permeabilised tissue, and revealed punctate staining

throughout the white pulp (right panel, Figure 4.6.A). Similarly, permeabilisation of immunised spleen sections also increased CCL20 staining and revealed punctate staining throughout the white pulp and $GL7^+$ germinal centres (right panel, Figure 4.6.B). This was surprising given the low levels of CCL20 detected at the transcriptional and protein level in spleens from identically-treated mice (Figure 4.4). However, this could be explained by *Ccl20* expression within a cell population that makes up a minor proportion of the spleen, such as stromal cells. Additionally, CCL20 quantification performed here by ELISA only measured extracellular, bioavailable CCL20, thus may have underestimated the total quantity extracellular and intracellular of splenic CCL20. Together, the staining pattern of bioavailable CCL20 suggested that CCR6 may facilitate migration to the splenic vasculature and peri-vascular spaces, whilst intracellular stores of CCL20 in the white pulp may be secreted locally during both the steady-state and inflammation upon additional as yet uncharacterised signals.

4.6 CCR6-deficient mice do not display gross GCT cell abnormalities or differences in splenic $Foxp3^+$ cell localisation

To investigate the overall contribution of CCR6 on the germinal centre reaction, wildtype and *Ccr6*$^{-/-}$ mice were immunised with SRBC and germinal centre populations were analysed at an early (day 4) and peak (day 6) time-point. Importantly, CCR6-deficiency does not affect steady-state trafficking of splenic B cells, naïve T cells or Tregs[278–280]. At both 4 and 6 days post-immunisation there were no significant differences in the proportion or number of naïve T-helper (Figure 4.7.A, B) or nTreg (Figure 4.7.A, C) populations between wildtype and *Ccr6*$^{-/-}$ mice. Similarly, there was no significant difference in the proportion or number of T_{FH} (Figure 4.7.D, E) and T_{FR} (Figure 4.7.D, F) cells between wildtype and *Ccr6*$^{-/-}$ mice at both time-points analysed. Consequently, there was no difference between the ratio of T_{FH}:T_{FR} cells at either timepoint between wildtype and *Ccr6*$^{-/-}$ mice (Figure 4.7.G). As the role of CCR6 in early GCB cell biology is not fully understood, the effects of CCR6-deficiency on GCB cell biology were also investigated in these mice (Figure 4.8). There was a small but significant increase in the proportion of splenic naïve B cells at 6 days post SRBC immunisation in *Ccr6*$^{-/-}$ compared to wildtype mice, however there was no difference in total naïve B cell numbers between wildtype and *Ccr6*$^{-/-}$ mice at either 4 or 6 days post-immunisation (Figure 4.8.A, B). Whilst no significant differences were observed between the proportion and number of GCB cells at both time-points (Figure 4.8.A, C), on day 6 there was a trend towards fewer GCB cells in *Ccr6*$^{-/-}$ mice that did not reach statistical significance. Similarly, there was a trend towards fewer IgM^+ plasma cells in *Ccr6*$^{-/-}$ mice, however the proportions and numbers of IgM^+ plasma cells ($B220^{mid}CD138^{hi}$intracellular IgM^+) between strains were not significantly altered (Figure 4.8.D, E). Conversely, both the proportion and number of splenic isotype-switched plasma cells, ($B220^{mid}CD138^{hi}$intracellular IgM^-) was significantly reduced in *Ccr6*$^{-/-}$ mice at day 6 of the antibody response (Figure 4.8.D, F). Together, analysis of the germinal centre reaction in *Ccr6*$^{-/-}$ mice revealed no gross defects in T_{FH} or T_{FR} cell biology dependent on CCR6, but rather differences were observed in antibody-producing subsets during the peak

of the germinal centre response. Specifically, isotype-switched plasma cell populations were reduced in CCR6-deficient mice.

Whilst flow cytometry data did not highlight any differences in the proportion and number of T_{FR} cells in CCR6-deficient mice, the microanatomical location of these cells during the antibody response facilitates interactions with other immune cells and is essential for their regulatory function. To interrogate the effect of CCR6-deficiency on T_{FR} cell localisation, immunofluorescence microscopy was performed on spleen sections from wildtype and *Ccr6*$^{-/-}$ mice at the peak of the germinal centre response to SRBC immunisation. Utilising a core stain of antibodies against CD4 (red), IgD (blue) and Foxp3 (green), total splenic Foxp3^{+} cells were visualised as additional antibodies against CXCR5 and PD-1 required to discriminate between nTregs and T_{FR} cells could not be incorporated due to the limited fluorescence channels on the microscope. Subsequently, the PALS (red outline), T-B border (magenta outline), follicles (blue outline) and germinal centres (green outline) were defined in spleen sections (Figure 4.9.A), then Foxp3^{+} cells in each of these areas were identified (Figure 4.9.B). There was no statistically significant difference in the size (mm^2) of each compartment between wildtype and *Ccr6*$^{-/-}$ mice (Figure 4.10.A). CCR6-deficiency had no significant effect on Foxp3^{+} cell location within each splenic compartment when quantified as the percentage of total Foxp3^{+} cells in the image (Figure 4.10.B), or density (number/mm^2; Figure 4.10.C). These results suggested that CCR6 deficiency did not affect the microanatomy of splenic niches, nor the gross localisation of splenic Foxp3^{+} cell subsets during the humoral response to SRBC immunisation.

4.7 Cell-intrinsic CCR6 expression is dispensable for T_{FH} and T_{FR} differentiation

The data described above appeared to eliminate a role for CCR6 in T_{FH} or T_{FR} cell differentiation and localisation during the germinal centre response. However, extensive cell-cell interactions underpin the differentiation of both GCT- and GCB cell populations. Thus, to eliminate possible CCR6-dependent cell-extrinsic effects that impact on GCT cell differentiation resultant of global CCR6-deficiency, mixed bone marrow chimeras were generated. Here, irradiated Ly5.1 hosts were reconstituted with 50% Ly5.1 bone marrow (CD45.1^{+}), and 50% bone marrow from either WT or *Ccr6*$^{-/-}$ donor mice (both CD45.2^{+}). Resulting chimeric mice contained a CD45.1^{+} immune cell compartment present throughout the germinal centre reaction to support the differentiation of CD45.2^{+} WT or CD45.2^{+}*Ccr6*$^{-/-}$ germinal centre subsets. Therefore, the intrinsic role of CCR6 on the development of germinal centre populations could be determined as any knock-on defects resultant of CCR6-deficiency would be eliminated by supporting CD45.1^{+} cells. Chimeric mice were immunised with SRBC and analysed by flow cytometry at the peak of the humoral response 6 days later. At this time point, the percentage of CD45.2^{+} naïve CD4 and nTreg precursor populations (Figure 4.11.A), was determined in chimeras reconstituted with WT (top row) and *Ccr6*$^{-/-}$ (bottom row) bone marrow. Despite bone marrow reconstitution with 1:1 mix of CD45.1 and CD45.2 bone marrow (WT or *Ccr6*$^{-/-}$) in irradiated Ly5.1 hosts,

there was a disadvantage for CD45.2 bone marrow to differentiate into T cells as <50% of CD4 T cells were CD45.2$^+$ (Figure 4.11.A). However, as both WT and *Ccr6*$^{-/-}$ bone marrow were on the CD45.2 genetic background, this disadvantage was controlled for in comparisons between WT and *Ccr6*$^{-/-}$ germinal centre populations. Thus, the percentage of CD45.2$^+$ T_{FH} and T_{FR} cells was determined in WT (top row) and *Ccr6*$^{-/-}$ (bottom row) mixed chimeras (Figure 4.11.B) and the ratio of CD45.2$^+$effector population:CD45.2$^+$precursor population was calculated to normalise for any differences in the reconstitution efficiency of CD45.2$^+$ bone marrow between individual chimeric mice. As there was no change in the ratio of precursors (naïve or nTreg) to effector cells (T_{FH} or T_{FR} cells) between WT and *Ccr6*$^{-/-}$ chimeras, this demonstrated that there was no intrinsic requirement for CCR6 in the development of T_{FH} cells (Figure 4.11.C) or T_{FR} cells (Figure 4.11.D).

Mixed chimeras were also utilised further to investigate any cell-intrinsic requirements for CCR6 in activated B cells during the splenic germinal centre reaction as this was incompletely understood. Subsequently, the percentages of CD45.2$^+$ precursor naïve B cells and effector GCB cells were determined in chimeras (Figure 4.12.A), then expressed as the ratio of CD45.2$^+$GCB cells:CD45.2$^+$naïve B cells (Figure 4.12.B). This revealed that B cell-intrinsic CCR6 expression was dispensable for the formation of GCB cells (Figure 4.12.B). Similarly, IgM$^+$ plasma cells and isotype-switched plasma cell populations were identified in chimeras (Figure 4.13.A). CCR6 was required for optimal splenic IgM$^+$ plasma cell differentiation, as the ratio of CD45.2$^+$IgM$^+$plasma cells:naïve B cells was decreased in *Ccr6*$^{-/-}$ chimeras compared to control chimeras (Figure 4.13.B), but CCR6 was redundant in isotype-switched plasma cell differentiation (Figure 4.13.C). This suggested that the previously identified defects in isotype-switched plasma cells observed in global *Ccr6*$^{-/-}$ mice (Figure 4.8.D, F) may be a knock-on effect.

4.8 Restricting CCR6-deficiency to T_{FR} cells in a bone marrow chimera model with Treg transfer

The data above rule out a requirement for CCR6 in the generation of T_{FR} cells and indicate that it does not play a major role in governing their localisation during the germinal centre response. However, given the high level of expression of CCR6 by these cells, it was next determined whether this chemokine receptor played a role in the functionality of T_{FR} cells during the germinal centre response. This required development of a model to specifically delete CCR6 in T_{FR} cells. As there are currently no genetic means of restricting gene deletion to T_{FR} cells without also impacting T_{FH} cells or Tregs, a bone marrow chimera model was designed where the Treg precursors of T_{FR} cells were ablated without triggering systemic autoimmunity, then restored via cell transfer with either wildtype or *Ccr6*$^{-/-}$ Tregs from which T_{FR} cells would differentiate following immunological challenge (Figure 4.14.A). Importantly, with this approach all other germinal centre populations including T_{FH} cells are CCR6-sufficient, thus any defects in the response would be attributable to CCR6-deficiency on T_{FR} cells. The foundation of this chimeric model were irradiated *Rag1*$^{-/-}$ hosts

reconstituted with a 1:1 mix of bone marrow from *Sh2d1a*$^{-/-}$ and *Foxp3*$^{DTR\text{-}GFP}$ donor mice. *Rag1*$^{-/-}$ mice were used as hosts as they lacked mature T- and B cells, thus would not contribute to the mature T- and B cell pool if bone marrow depletion was incomplete. *Sh2d1a*$^{-/-}$ mice are deficient for the gene encoding SAP, an essential factor for differentiation of T_{FH} and T_{FR} cells, thus mature T cells generated from *Sh2d1a*$^{-/-}$ bone marrow cannot participate in germinal centre reactions[43,135]. Importantly, bone marrow from *Sh2d1a*$^{-/-}$ mice was utilised to generate a pool of Treg cells that would prevent systemic autoimmunity upon Treg ablation, but would be unable to contribute to germinal centre reactions established upon immunisation[43]. Additionally, B cells generated from the *Sh2d1a*$^{-/-}$ strain utilised here do not exhibit germinal centre defects[281,282]. *Foxp3*$^{DTR\text{-}GFP}$ mice generate Tregs with a fusion protein of the diphtheria toxin receptor and GFP via an IRES-driven coding sequence knocked-in to the 3' untranslated region of the *Foxp3* gene. This construct facilitates the depletion of Foxp3-expressing cells upon administration of diphtheria toxin, and given the co-expression of GFP, depletion efficiency can be determined via loss of GFP^+ cells in circulation (Figure 4.14.B). Cells that do not express Foxp3 in these mice are otherwise normal[247]. Thus, *Foxp3*$^{DTR\text{-}GFP}$ bone marrow generated mature T cells and nTregs capable of differentiating into T_{FH} and T_{FR} cells, respectively. However, upon administration of diphtheria toxin, *Foxp3*$^{DTR\text{-}GFP}$-derived nTregs capable of differentiating into T_{FR} cells would be depleted. As *Sh2d1a*-deficient nTregs could not differentiate into T_{FR} cells, diphtheria toxin-treated *Rag1*$^{-/-}$(*Sh2d1a*$^{-/-}$:*Foxp3*$^{DTR\text{-}GFP}$) chimeric mice are T_{FR} cell-deficient. Subsequently, MACS-purified Tregs ($CD4^+CD25^+$) from secondary lymphoid organs of steady-state *Foxp3*^{GFP} or *Ccr6*$^{-/-}$*Foxp3*^{GFP} mice were transferred into chimeras to provide a pool of Tregs capable of recapitulating T_{FR} cell differentiation, and thereby restricting CCR6-deficiency to T_{FR} cells. This model is depicted in Figure 4.14.A.

Chimeric *Rag1*$^{-/-}$(*Sh2d1a*:*Foxp3*$^{DTR\text{-}GFP}$) mice were split into four groups (Figure 4.14.A). Group 1 received saline vehicle control i.p. on indicated diphtheria toxin treatment days and no Treg transfer. These mice generated endogenous T_{FR} cells from *Foxp3*$^{DTR\text{-}GFP}$ bone marrow and served as a control for diphtheria toxin-mediated Treg depletion. Group 2 received diphtheria toxin and no Treg transfer, thus the germinal centre reaction of these mice was dysregulated due to a lack of T_{FR} cells. Groups 3 and 4 received diphtheria toxin and i.v. transfer of $5x10^5$ Tregs from steady-state *Foxp3*^{GFP} or *Ccr6*$^{-/-}$*Foxp3*^{GFP} hosts, respectively. Purities of >95% $CD4^+CD25^+$ were achieved via MACS, >85% of which were *Foxp3*^{GFP}-positive for both strains (Figure 4.14.C). Successful recapitulation of T_{FR} cells by transferred wildtype Tregs in Group 3 could be identified by comparing the germinal centre reactions of mice in Group 3 to T_{FR}-deficient mice in Group 2, and the effect of CCR6-deficiency on T_{FR} cells could be interpreted by comparing Groups 3 and 4.

To determine the effect of T_{FR}-restricted CCR6-deficiency on germinal centre populations, chimeric mice were immunised with $2x10^9$ SRBCs i.p. and spleens were harvested 8 days post-immunisation for flow cytometric analysis (Figure 4.14.A). It was intended that flow cytometric detection of Foxp3 would be via GFP reporter expression, as i) T_{FR} cells in the

saline control group would express GFP via the *Foxp3*$^{DTR\text{-}GFP}$ construct, ii) no T_{FR} cells, thus no GFP signal, would be observed in the diphtheria toxin-only group, and iii) T_{FR} cells within cell transfer groups would express GFP via the *Foxp3*^{GFP} allele. Unexpectedly however, GFP-positive T cells could only be detected in saline controls, not Treg transfer mice (Figure 4.14.D). It is likely the low numbers of transferred Tregs and difference in GFP expression levels between the *Foxp3*^{GFP} and *Foxp3*$^{DTR\text{-}GFP}$ constructs contributed to this outcome. This is discussed further in Chapter 5.2. Regardless, meaningful analyses were achieved by quantifying total GCT cells without further delineation of T_{FH} and T_{FR} cells. There were no statistically significant differences between groups in the percentage or number of GCT- and GCB cells (Figure 4.14.E, F). This was surprising as a loss of germinal centre regulation was anticipated in experimental Group 2 which lacked T_{FR} cells, as T_{FR} cells in this model have been shown previously to be essential in regulating T_{FH} and GCB cell populations[43]. Similarly, there were no significant differences in IgM^+ and IgM^- splenic plasma cells between any of the chimeras (Figure 4.14.G, H), indicating that T_{FR} cell-dependent regulation of these populations was not apparent in this model.

In parallel, the effect of T_{FR}-restricted CCR6-deficiency on the generation of memory B cells and plasma cells, antibody production, and affinity maturation was determined by immunising chimeric mice with NP-KLH/Alum (Figure 4.15.A). NP-KLH/Alum was used as the immunising antigen as it permitted the identification of antigen-specific memory B cells and plasma cells by flow cytometry, and antibody titre and affinity maturation could be measured by ELISA. Previously, this model of T_{FR} cell-deficiency resulted in defective affinity maturation of antibodies towards the immunising antigen[43]. Thus, serum was collected from chimeric mice via tail-vein bleeding on days 7, 14, 21 and 28 post-immunisation for antibody analysis, and spleens and bone marrow were harvested on day 28 to quantify memory B cells and plasma cells. Whilst group numbers were initially equal, several chimeric mice did not respond to NP-KLH/Alum immunisation, evident by low anti-NP antibody titres, thus these mice were excluded from further analyses. NP-specific memory B cells ($B220^+CD38^+IgD^-GL7^-NP^+$) were identified in flow cytometry analyses by their ability to bind NP hapten conjugated to the fluorescent protein R-phycoerythrin (NP-PE; Figure 4.15.B). There was no significant difference in the proportion or number of NP-specific splenic memory B cells between groups (Figure 4.15.C). Additionally, NP-specific bone marrow plasma cells ($B220^-CD138^+$intracellular NP^+) were identified by intracellular NP-PE staining (Figure 4.15.D). Whilst there were no statistically significant differences in the proportion of NP-specific plasma cells in the bone marrow, reconstitution of the T_{FR} cell precursor pool with wildtype *Foxp3*^{GFP} Tregs produced a greater number of NP-specific plasma cells compared to all other experimental groups (Figure 4.15.E). Importantly, this result comes with the caveat that the experimental group was restricted to n=2 following the exclusion of non-responding mice, thus greater experimental power will be required to validate this conclusion. NP-KLH/Alum immunisation also facilitated the quantitation of both high- and low-affinity anti-NP antibodies via the use of different ELISA coating substrates. Total anti-NP IgG was measured using the densely-haptenated coating substrate BSA-NP_{32} as it

provided abundant NP-antigen for anti-NP antibodies with a range of specificities to bind[283]. Alternatively, the sparsely haptenated coating substrate BSA-NP_5 restricted NP-antigen abundance, thus favoured the detection of high-affinity anti-NP antibodies[283]. Both total (Figure 4.15.F) and high-affinity (Figure 4.15.G) anti-NP antibody titres increased from 7 days post-immunisation to 14 days, before plateauing for the remainder of the time course with no significant differences observed between groups. The average affinity of anti-NP antibodies was calculated by the ratio of high-affinity to low-affinity antibody titres[283], thus comparison between experimental groups at a given timepoint compared the extent of affinity maturation between chimeras. On day 7, the average affinity of anti-NP antibodies in the *Ccr6*$^{-/-}$*Foxp3*^{GFP} Treg transfer experimental group was significantly greater than saline controls, however this was resolved by day 14, and no significant differences in the average anti-NP affinity between groups were observed for the remainder of the time course (Figure 4.15.H). Again, contrary to the publication on which this model was based[43], depletion of T_{FR} cells had no effect on the quantity or quality of antigen-specific antibodies. As this model was unable to recapitulate the effects of T_{FR} cell depletion observed by Linterman and colleagues, specifically the dysregulation of GCT and B cell responses following SRBC immunisation and dysregulated antigen-specific antibody responses upon NPKLH immunisation, further experimentation with this model was discontinued. Collectively, these experiments with a novel T_{FR}-restricted CCR6-knockout model provided valuable insight into the nuances of this approach and alternative strategies to restrict gene deficiency to T_{FR} cells are discussed in Chapter 5.2.

4.9 Conclusions

This study identified multiple novel chemokine receptors expressed by GCT cells together with previously characterised CXCR5 and CXCR4 expression. Subsequently, CCR6 expression identified by qPCR within GCT cell subsets was validated by flow cytometry and functionality was demonstrated by *in vitro* chemotaxis assays. Interestingly, a greater proportion and level of CCR6 was expressed by T_{FR} cells compared to T_{FH} cells, however there was no intrinsic requirement for CCR6 in differentiation of T_{FH} or T_{FR} cells. Quantitation of CCL20 in the spleen, the site of immune priming in the models used in this study, revealed a small but significant increase in abundance following immunisation, and visualisation of CCL20 in spleen sections revealed localisation to vasculature and intracellular white pulp stores. A model to specifically test gene function in the T_{FR} cell compartment was also designed and tested. Lastly, a cell-intrinsic requirement for CCR6 in efficient splenic plasma cell formation was observed, prompting a future novel line of investigation.

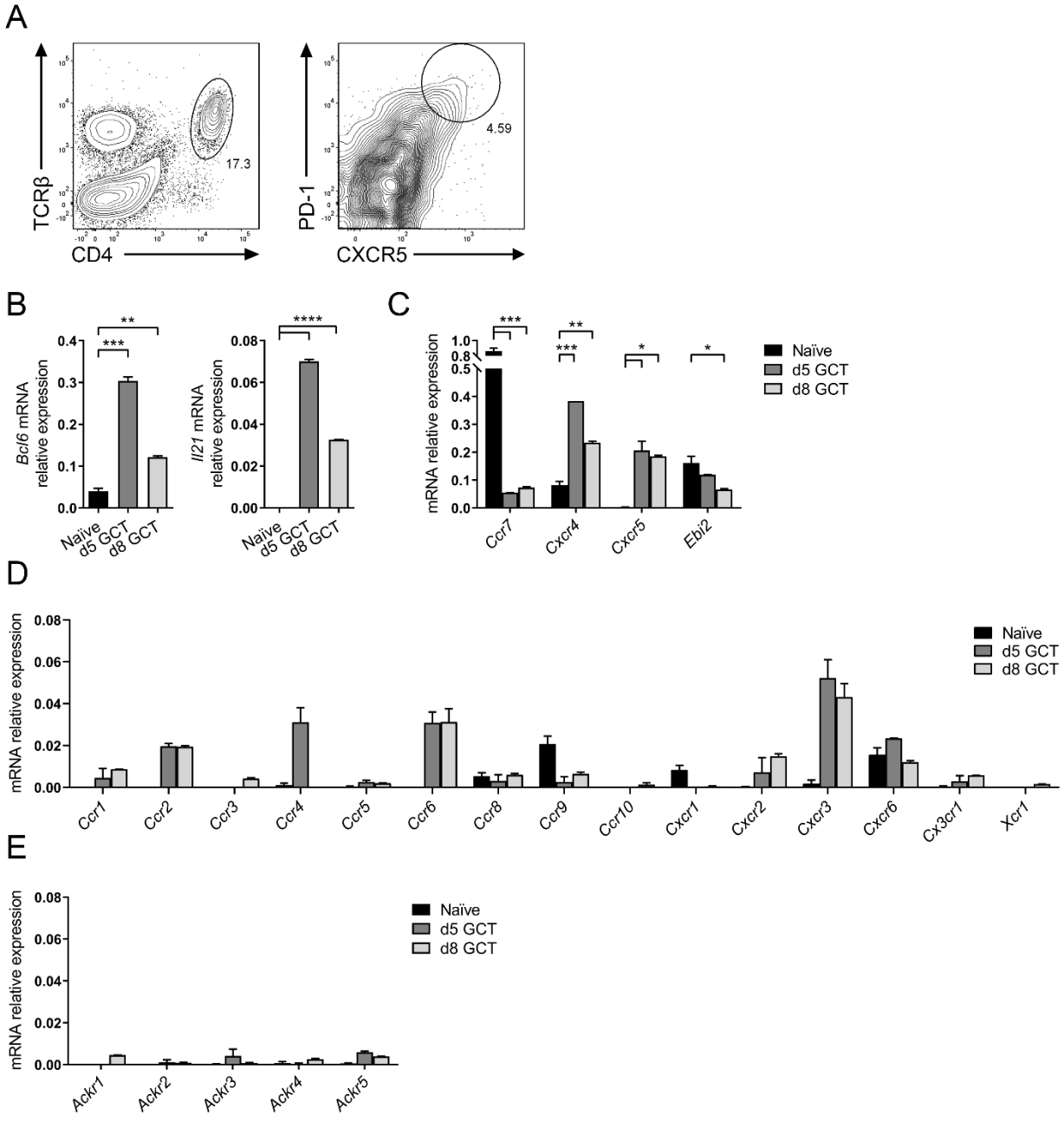

Figure 4.1: Complete chemokine receptor expression analysis of GCT cells

(A) Representative gating strategy for sorting GCT cells ($CD4^+TCR\beta^+CXCR5^{hi}PD\text{-}1^{hi}$) from day 5 and 8 SRBC i.p. immunised mice. Relative expression of **(B)** key GCT cell transcripts, **(C)** characterised germinal centre chemotactic receptors, **(D)** all known chemokine receptors, and **(E)** atypical chemokine receptors in sorted GCT cells 5 and 8 days after SRBC immunisation. (B-E) Expression relative to *Gapdh*, and naïve CD4 T cells ($CD4^+CD44^-CD62L^+$) are included for comparison. Data pooled from two independent experiments with 3 mice pooled per time point ±SEM. (B, C) one-way ANOVA with Tukey's multiple comparison test for each gene. *p<0.05, **p<0.01, ***p<0.001, ****p<0.0001.

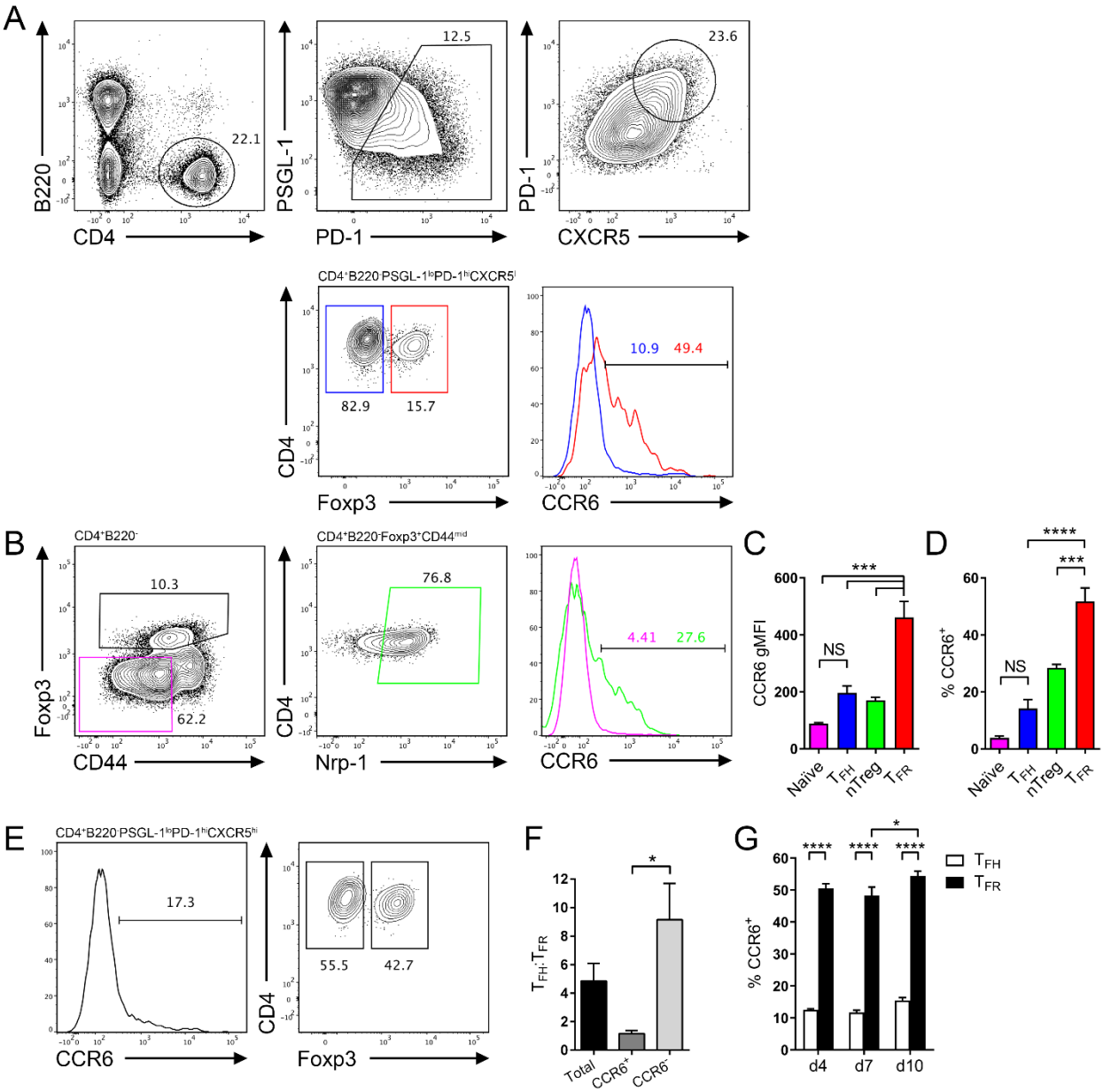

Figure 4.2: CCR6 expression varies among GCT cell populations

Representative gating for CCR6$^+$ **(A)** T_{FH} cells (CD4$^+$B220$^-$PSGL1^{lo}PD-1^{hi}CXCR5^{hi}Foxp3$^-$) and T_{FR} cells (CD4$^+$B220$^-$PSGL1^{lo}PD-1^{hi}CXCR5^{hi}Foxp3$^+$), and CCR6$^+$ **(B)** naïve CD4 T cells (CD4$^+$B220$^-$CD44^{lo}Foxp3$^-$) and nTregs (CD4$^+$B220$^-$CD44^{mid}Foxp3$^+$Nrp-1$^+$) 6 days after SRBC immunisation. **(C)** gMFI of CCR6 and, **(D)** percentage of CCR6$^+$ cells within populations from (A) and (B). **(E)** Representative gating strategy for T_{FH} and T_{FR} cells within CCR6$^+$ GCT cells (CD4$^+$B220$^-$PSGL1^{lo}PD-1^{hi}CXCR5^{hi}CCR6$^+$). **(F)** Ratio of T_{FH}:T_{FR} cells within gating strategies from (A) and (E). **(G)** Frequency of CCR6$^+$ T_{FH} and T_{FR} cells at indicated time points after i.p. NP-KLH/Alum immunisation. (A-F) Data representative of two independent experiments, n=4 mice ±SEM, one-way ANOVA with Tukey's multiple comparisons test, (G) data from n=4-5 mice per time-point ±SEM, two-way ANOVA with Sidak's multiple comparison test. *p<0.05, ***p<0.001, ****p<0.0001.

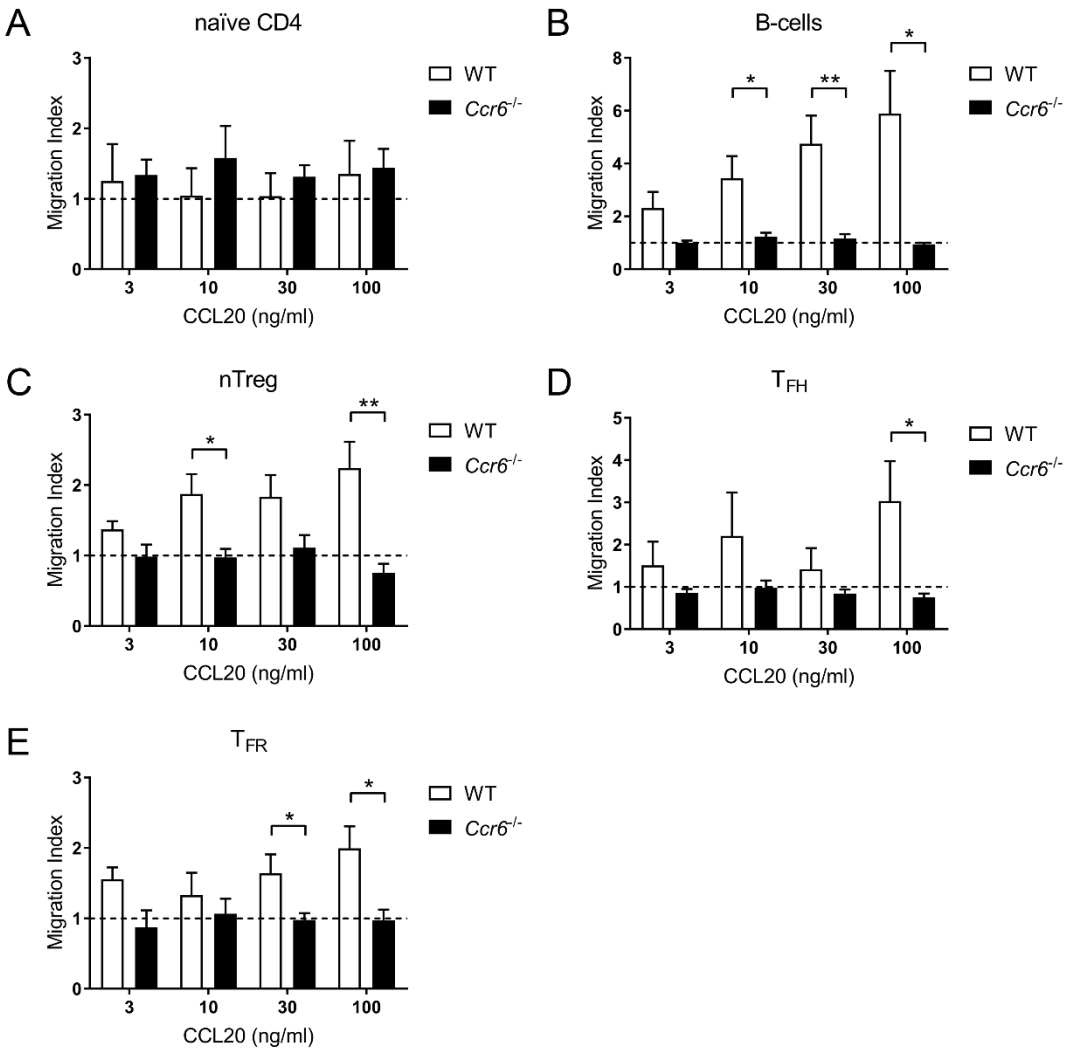

Figure 4.3: GCT cell populations migrate to CCL20 *ex vivo*

Transwell migration of splenocytes from day 6 SRBC immunised WT or *Ccr6*$^{-/-}$ mice to increasing concentrations of CCL20. Cell populations were identified within total migrated splenocytes by flow cytometry and migration index was calculated relative to controls without chemokine. **(A)** Naïve CD4 T cells, **(B)** B cells (CD4^{-}B220^{+}), **(C)** nTregs, **(D)** T_{FH} cells, and **(E)** T_{FR} cells. (A-E) Data pooled from two independent experiments, n=3-5 mice/strain ±SEM, two-tailed unpaired Student's t test between strains for each CCL20 concentration. *p<0.05, **p<0.01.

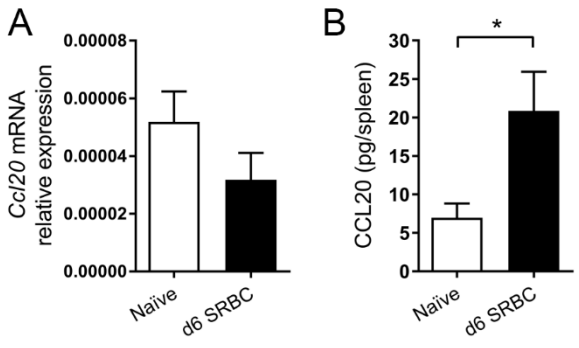

Figure 4.4: CCL20 is expressed in the spleen during the steady-state and following immunisation

(A) Expression of *Ccl20* mRNA in whole spleen samples from steady-state and day 6 SRBC-immunised WT mice relative to *Rplp0*. **(B)** Quantity of CCL20 (pg) in spleen supernatant from steady-state and day 6 SRBC-immunised WT mice, as determined by ELISA. (A) Data pooled from two independent experiments, n=3-6 mice/condition, ±SEM. (B) Data pooled from two independent experiments, n=6/condition ±SEM, two-tailed unpaired Student's t test with Welch's correction. *$p<0.05$.

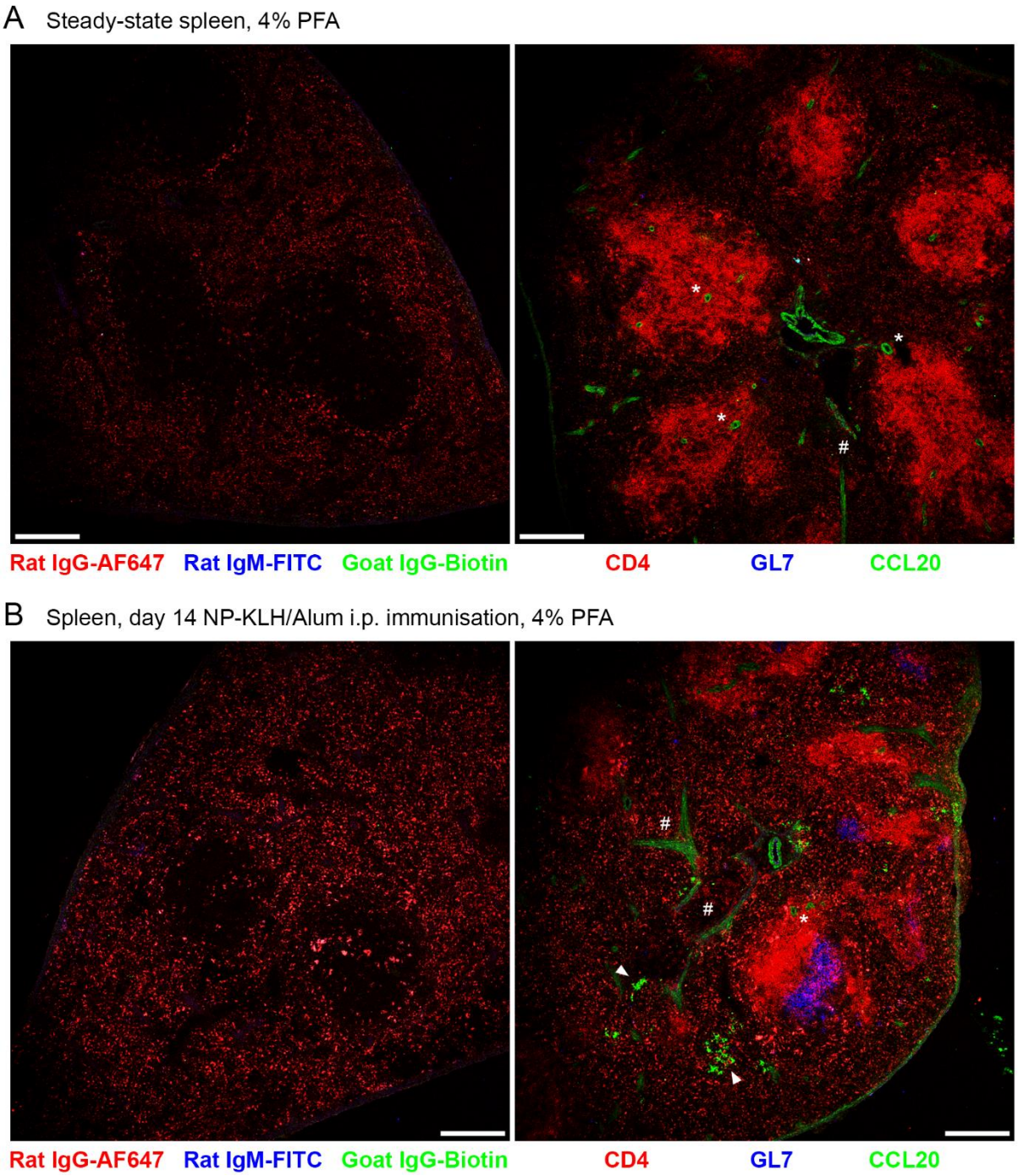

Figure 4.5: Extracellular CCL20 is localised to splenic vasculature during the steady-state and following immunisation

Localisation of CCL20 protein in fixed, non-permeabilised spleen sections from wildtype mice **(A)** during the steady-state, and **(B)** 14 days post NP-KLH/Alum immunisation. (A, B) Sections are stained with isotype control antibodies (left), or antibodies (right) against CD4 (red), Neu5Ac (GL7, blue) and CCL20 (green), scale bar: 200µm. CCL20 staining on the following structures are highlighted accordingly: central arterioles (*), splenic arteries (#), perivascular cells (arrowheads). Images representative of four experiments, n=4 mice total.

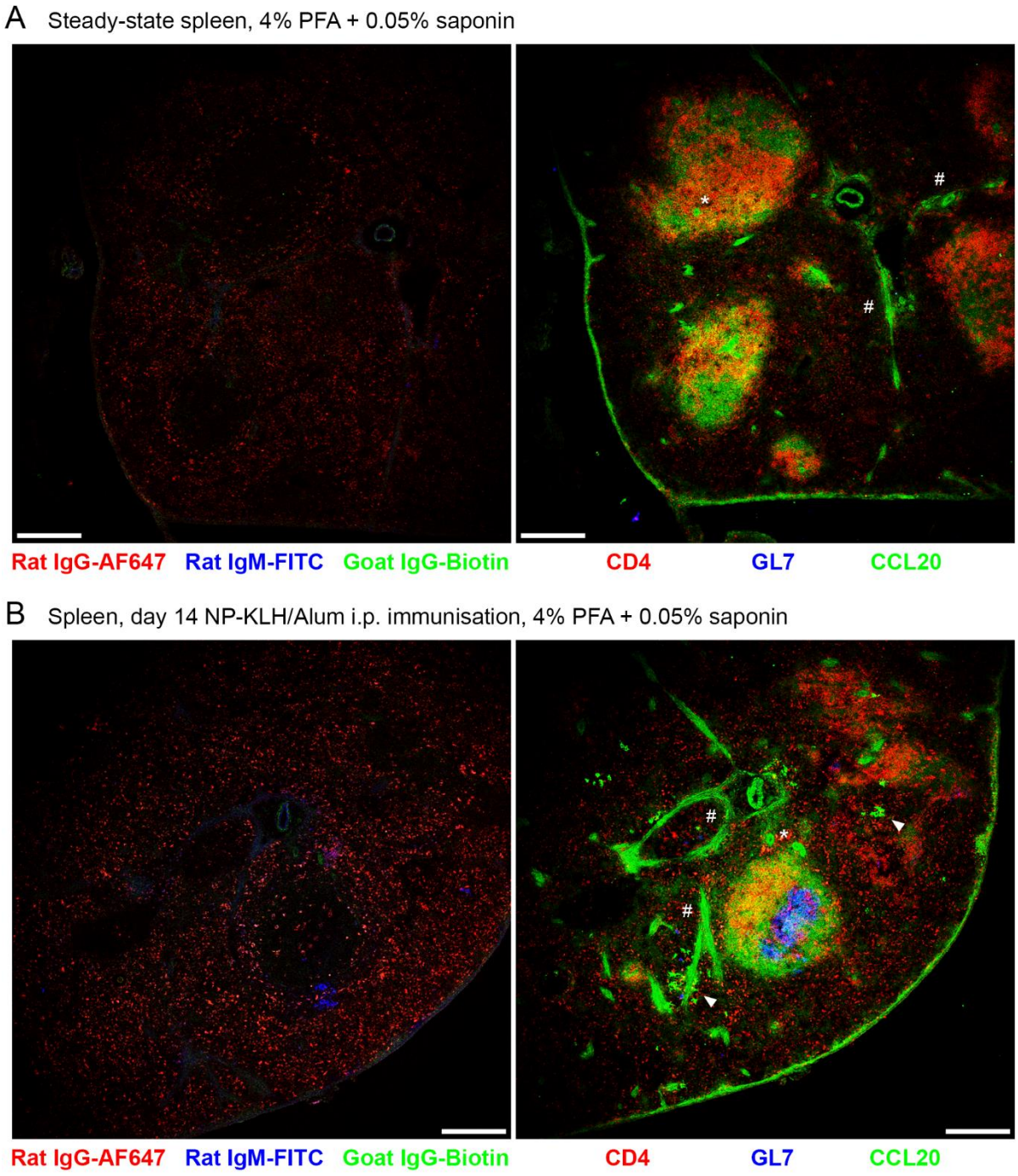

Figure 4.6: Intracellular stores of CCL20 are located in the splenic white pulp during the steady-state and following immunisation

Localisation of CCL20 protein in fixed, permeabilised spleen sections from wildtype mice **(A)** during the steady-state, and **(B)** 14 days post NP-KLH/Alum immunisation. (A, B) Sections are stained with isotype control antibodies (left), and antibodies (right) against CD4 (red), Neu5Ac (GL7, blue) and CCL20 (green), scale bar: 200µm. CCL20 staining on the following structures are highlighted accordingly: central arterioles (*), splenic arteries (#), perivascular cells (arrowheads). Images representative of four experiments, n=4 mice total.

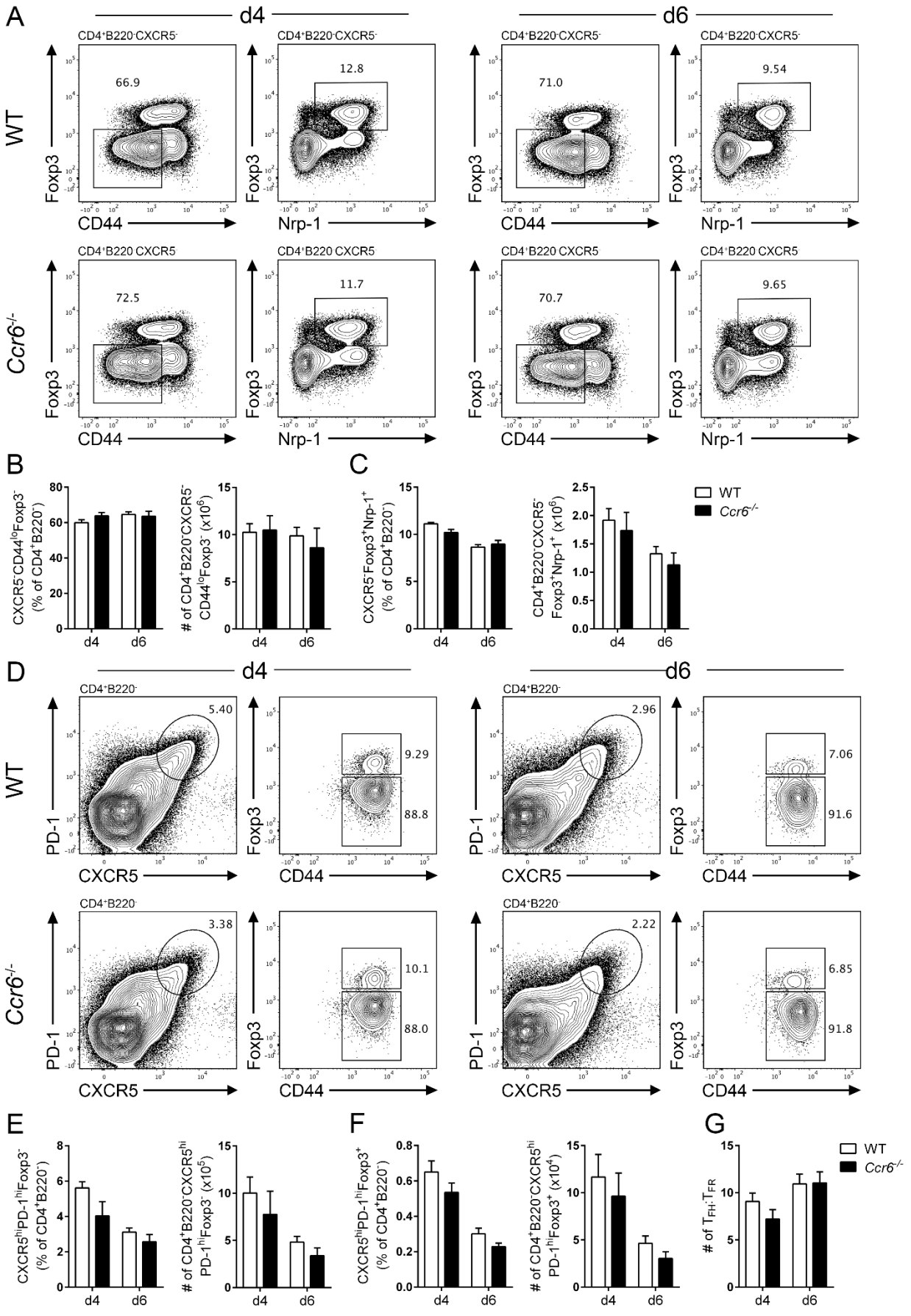
A
d4
d6
WT
Ccr6-/-
CD4+B220-CXCR5-
66.9
12.8
71.0
9.54
72.5
11.7
70.7
9.65
Foxp3
CD44
Nrp-1
B
C
CXCR5-CD44loFoxp3-
(% of CD4+B220-)
# of CD4+B220-CXCR5-
CD44loFoxp3- (x10^6)
CXCR5-Foxp3+Nrp-1+
(% of CD4+B220-)
CD4+B220-CXCR5-
Foxp3+Nrp-1+ (x10^6)
WT
Ccr6-/-
d4
d6
D
CD4+B220-
5.40
9.29
88.8
2.96
7.06
91.6
3.38
10.1
88.0
2.22
6.85
91.8
PD-1
CXCR5
Foxp3
CD44
E
F
G
CXCR5hiPD-1hiFoxp3-
(% of CD4+B220-)
# of CD4+B220-CXCR5hi
PD-1hiFoxp3- (x10^5)
CXCR5hiPD-1hiFoxp3+
(% of CD4+B220-)
# of CD4+B220-CXCR5hi
PD-1hiFoxp3+ (x10^4)
# of TFH:TFR
WT
Ccr6-/-
d4
d6

Figure 4.7: CCR6-deficient mice mount normal GCT cell responses to protein antigen

(A) Representative gating strategy of naïve CD4 T cells and nTregs 4 and 6 days post SRBC immunisation in WT and *Ccr6*$^{-/-}$ mice. Frequency and number of **(B)** naïve T cells, and **(C)** nTregs from (A). **(D)** Representative gating strategy of T_{FH} and T_{FR} cells 4 and 6 days post SRBC immunisation in WT and *Ccr6*$^{-/-}$ mice. Frequency and number of **(E)** T_{FH} cells, and **(F)** T_{FR} cells from (D). **(G)** Ratio of T_{FH}:T_{FR} cells 4 and 6 days post SRBC immunisation in WT and *Ccr6*$^{-/-}$ mice. (A-G) Data representative of 3 independent experiments, n=6-7 mice/time point ±SEM, two-tailed unpaired Student's t test between strains at each time point.

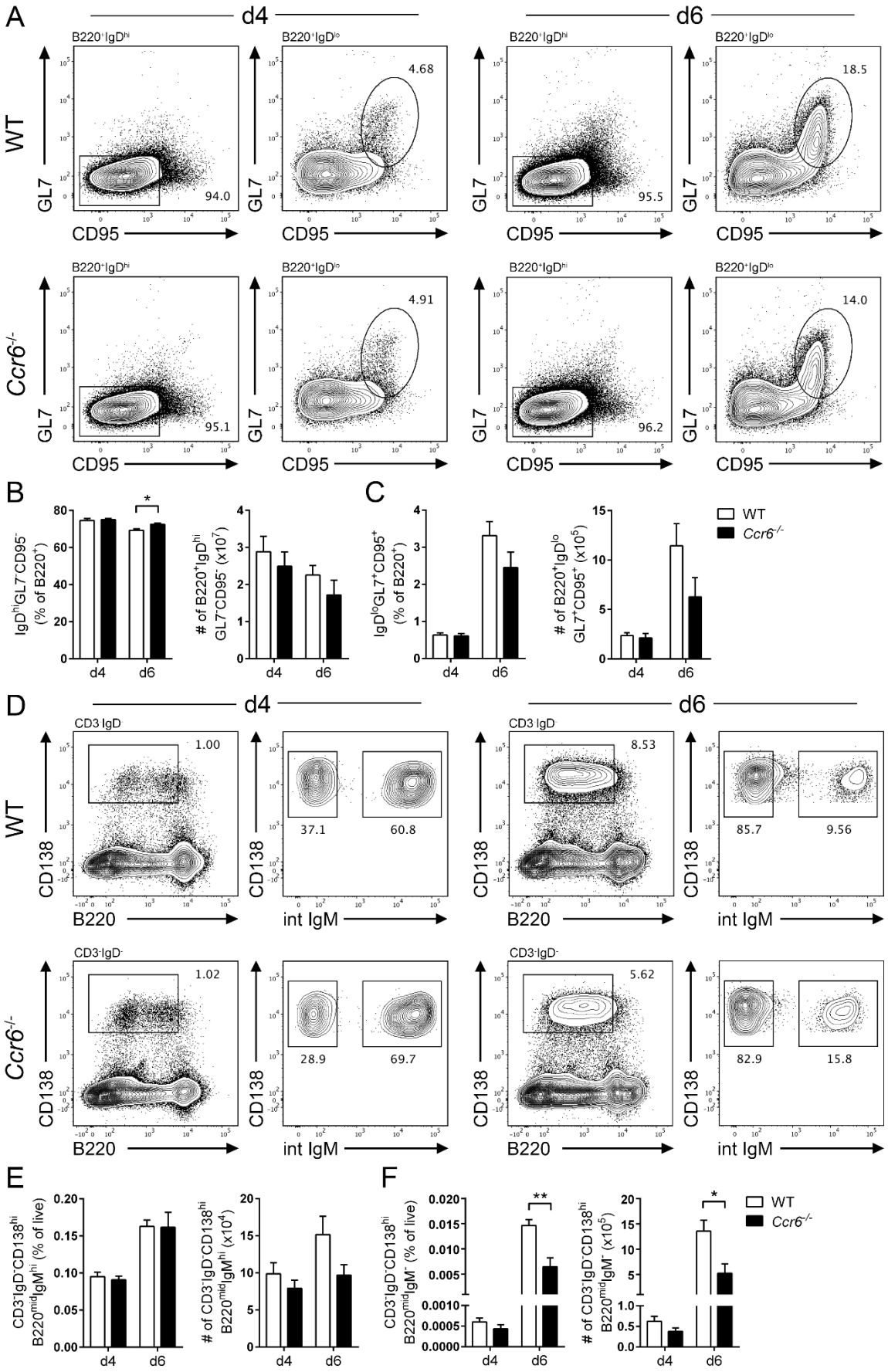
A
d4
d6
WT
Ccr6-/-
B220+IgDhi
B220+IgDlo
GL7
CD95
4.68
94.0
18.5
95.5
4.91
95.1
14.0
96.2
B
C
IgDhiGL7-CD95-
(% of B220+)
# of B220+IgDhi
GL7-CD95- (x10^7)
IgDloGL7+CD95+
(% of B220+)
# of B220+IgDlo
GL7+CD95+ (x10^5)
WT
Ccr6-/-
d4
d6
D
CD3 IgD
CD138
B220
int IgM
1.00
37.1
60.8
8.53
85.7
9.56
CD3-IgD-
1.02
28.9
69.7
5.62
82.9
15.8
E
F
CD3-IgD-CD138hi
B220mid IgMhi (% of live)
# of CD3-IgD-CD138hi
B220mid IgMhi (x10^4)
CD3-IgD-CD138hi
B220mid IgM- (% of live)
# of CD3-IgD-CD138hi
B220mid IgM- (x10^5)

Figure 4.8: Switched plasma cell responses to protein antigen are impaired in CCR6-deficient mice

(A) Representative gating strategy of naïve B cells ($B220^{+}IgD^{hi}GL7^{-}CD95^{-}$) and GCB cells ($B220^{+}IgD^{lo}GL7^{+}CD95^{+}$) 4 and 6 days post SRBC immunisation in WT and *Ccr6*$^{-/-}$ mice. Frequency and number of **(B)** naïve B cells, and **(C)** GCB cells, from (A). **(D)** Representative gating strategy of IgM^{+} plasma cells (IgM^{+}PC: $CD3^{-}IgD^{-}CD138^{hi}B220^{mid}intIgM^{+}$) and isotype-switched plasma cells (swPC: $CD3^{-}IgD^{-}CD138^{hi}B220^{mid}intIgM^{-}$) 4 and 6 days post SRBC immunisation in WT and *Ccr6*$^{-/-}$ mice. Frequency and number of **(E)** IgM^{+}PCs, and **(F)** swPCs, from (D). Data representative of 3 independent experiments, n=6-7 mice/time point ±SEM, two-tailed unpaired Student's t test between strains at each time point. *$p<0.05$, **$p<0.01$.

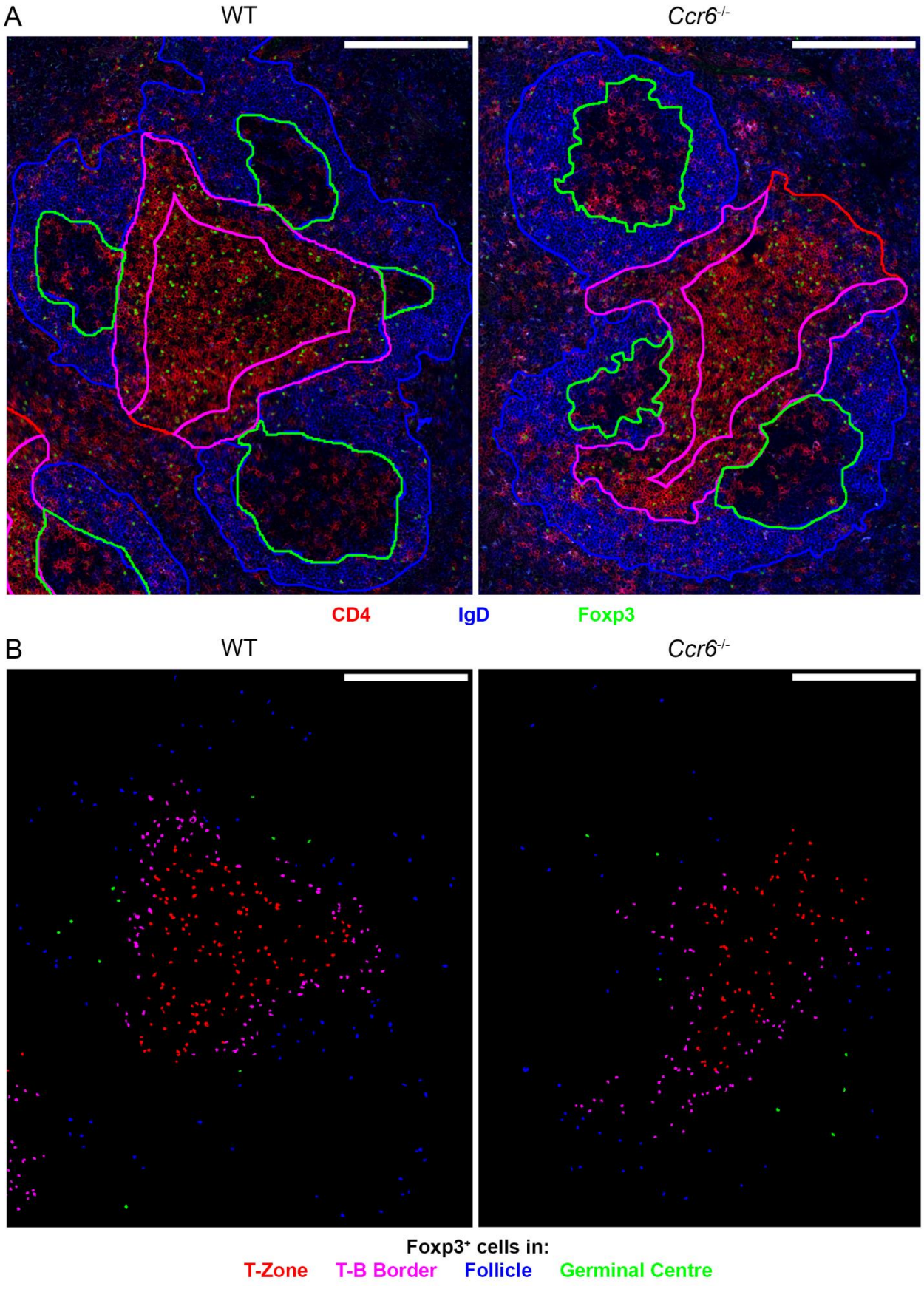
A
WT
Ccr6-/-
CD4
IgD
Foxp3
B
WT
Ccr6-/-
Foxp3+ cells in:
T-Zone
T-B Border
Follicle
Germinal Centre

Figure 4.9: Localisation of splenic Foxp3^{+} cells during the peak of SRBC immunisation in wildtype and CCR6-deficient mice

(A) Localisation of Foxp3^{+} cells in PFA and acetone fixed/permeabilised spleen sections from day 6 i.p. SRBC immunised WT and *Ccr6*$^{-/-}$ mice. Sections were stained with antibodies against CD4 (red), IgD (blue) and Foxp3 (green). Based on CD4 and IgD staining, the following areas are outlined: follicles (blue), germinal centres (green), T-B border (magenta), and T-zone (red). Scale bar: 200µm. **(B)** Identification of Foxp3^{+} cells from (A), colour-coded based on localisation within the T-zone (red), T-B border (magenta), follicle (blue), or germinal centre (green). Scale bar: 200µm. (A, B) Images representative of n=5 mice/strain, 2-6 images/mouse.

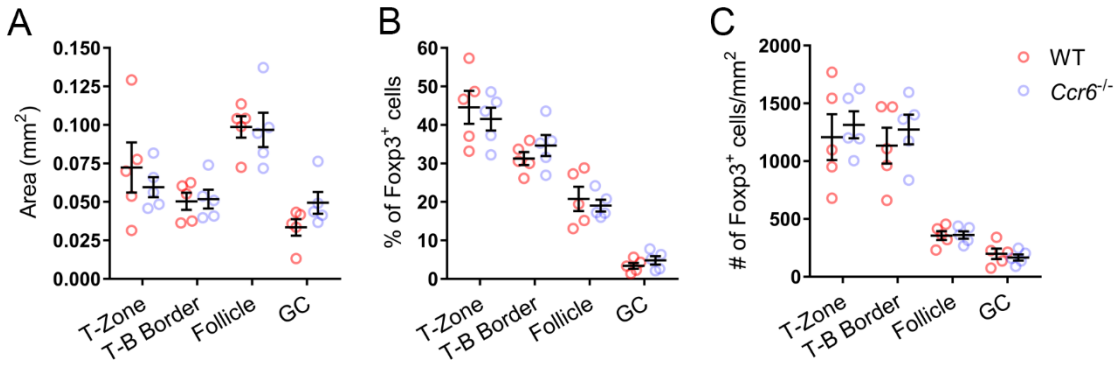

Figure 4.10: CCR6-deficiency does not grossly alter Foxp3$^+$ cell distribution within splenic compartments during the humoral response

(A) Average area (mm^2) of the splenic niches delineated in Figure 4.9.A. **(B)** Percentage and **(C)** number/mm^2 of Foxp3$^+$ cells within each splenic niche, quantified from Figure 4.9.B. (A-C) Each dot represents the average of technical replicates per biological replicate, n=5 mice/strain ±SEM, two-tailed unpaired Student's t test.

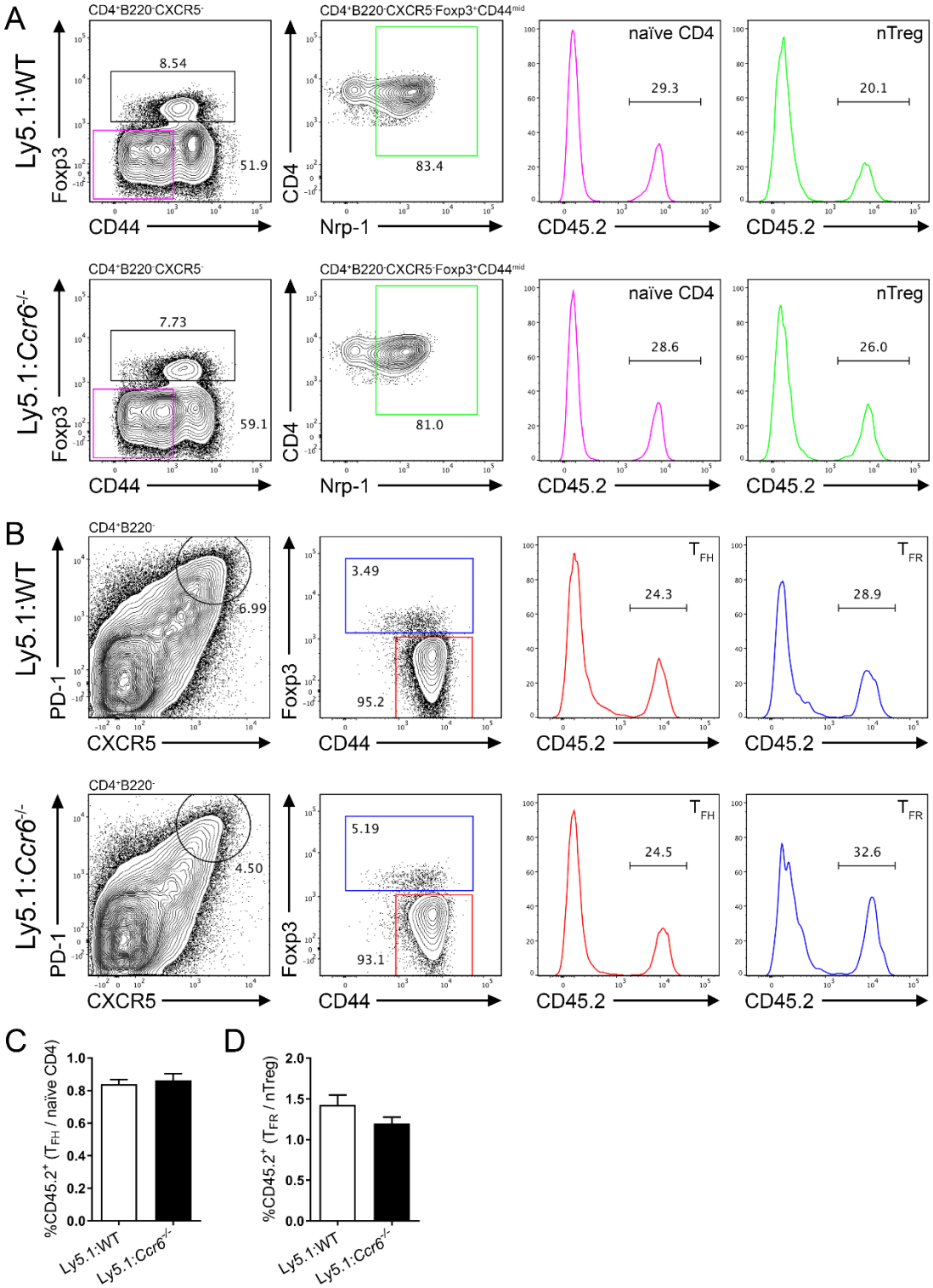
A
Ly5.1:WT
Ly5.1:Ccr6-/-
CD4+B220-CXCR5-
CD4+B220-CXCR5-Foxp3+CD44mid
Foxp3
CD44
CD4
Nrp-1
CD45.2
naïve CD4
nTreg
8.54
51.9
83.4
29.3
20.1
7.73
59.1
81.0
28.6
26.0
B
CD4+B220-
PD-1
CXCR5
TFH
TFR
6.99
3.49
95.2
24.3
28.9
4.50
5.19
93.1
24.5
32.6
C
%CD45.2+ (TFH / naive CD4)
D
%CD45.2+ (TFR / nTreg)
Ly5.1:WT
Ly5.1:Ccr6-/-

Figure 4.11: Cell-intrinsic CCR6 function is not required for formation of GCT cell populations

Representative gating strategies for **(A)** CD45.2$^+$ naïve CD4 T cells and nTregs, and **(B)** CD45.2$^+$ T_{FH} and T_{FR} cells 6 days post SRBC immunisation in irradiated Ly5.1 hosts reconstituted with a 1:1 ratio of Ly5.1:WT (top row) or Ly5.1:*Ccr6*$^{-/-}$ (bottom row) bone marrow. **(C)** Ratio of CD45.2$^+$ T_{FH} cells:CD45.2$^+$ naïve CD4 T cells in Ly5.1:WT and Ly5.1:*Ccr6*$^{-/-}$ chimeras. **(D)** Ratio of CD45.2$^+$ T_{FR} cells:CD45.2$^+$ nTregs in Ly5.1:WT and Ly5.1:*Ccr6*$^{-/-}$ chimeras. (A-D) n=6/chimera group, ±SEM, two-tailed unpaired Student's t test.

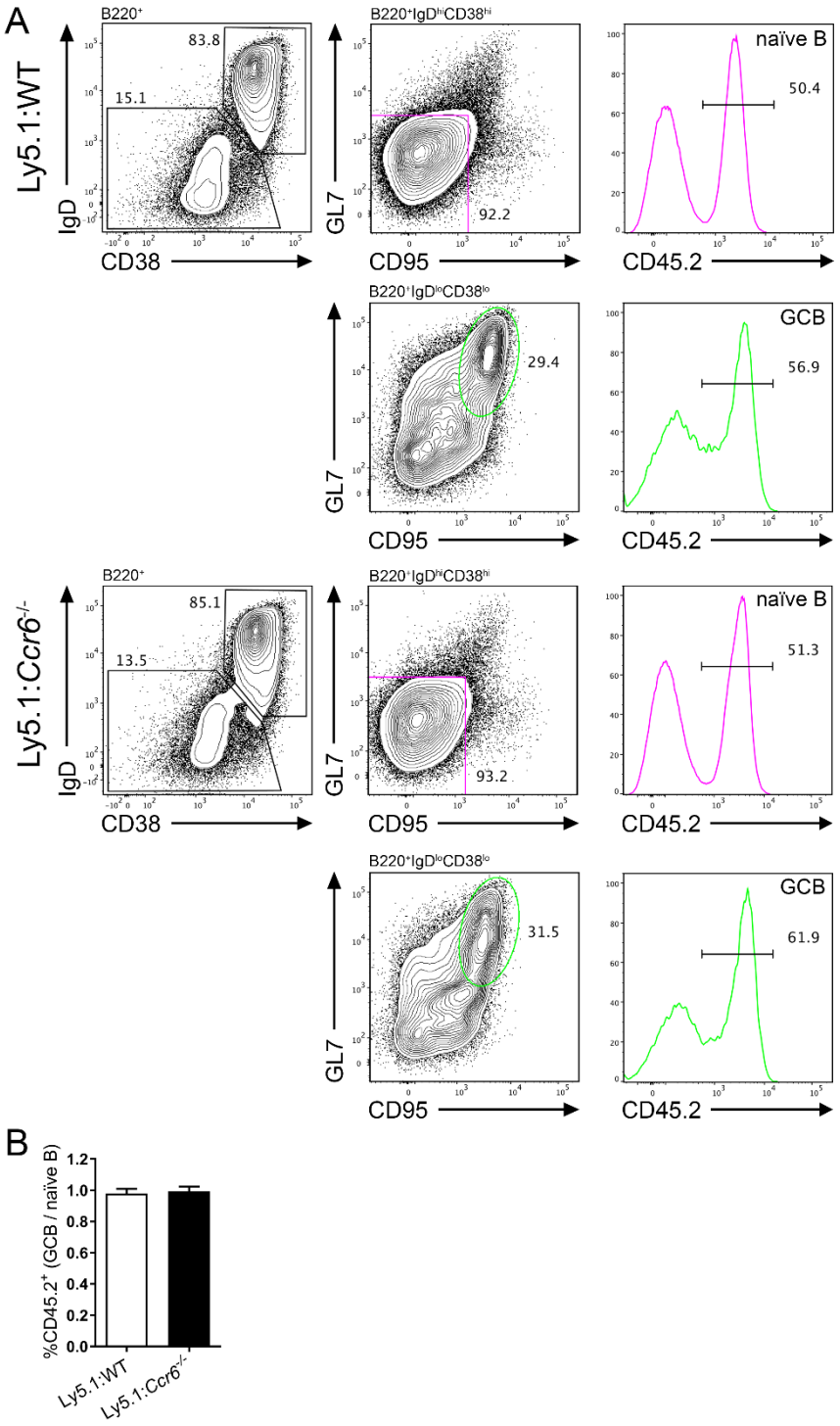

Figure 4.12: Cell-intrinsic CCR6 function is redundant for GCB cell development

(A) Representative gating strategies for CD45.2$^+$ naïve B cells and GCB cells 6 days post SRBC immunisation in irradiated Ly5.1 hosts reconstituted with a 1:1 ratio of Ly5.1:WT (top row) or Ly5.1:*Ccr6*$^{-/-}$ (bottom row) bone marrow. **(B)** Ratio of CD45.2$^+$ GCB cells:CD45.2$^+$ naïve B cells in Ly5.1:WT and Ly5.1:*Ccr6*$^{-/-}$ chimeras. (A,B) n=6/chimera group, ±SEM, two-tailed unpaired Student's t test.

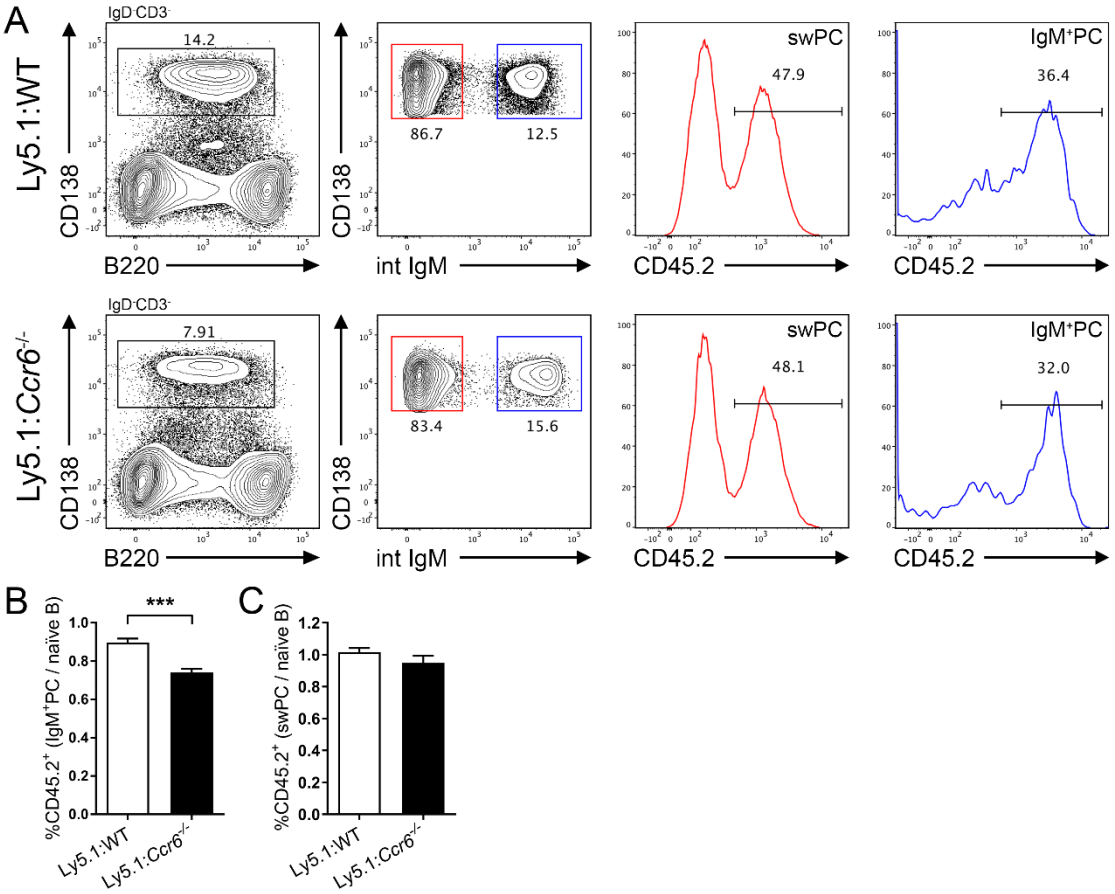

Figure 4.13: Cell-intrinsic CCR6 function is required for optimal plasma cell development

(A) Representative gating strategies of CD45.2$^+$ IgM$^+$PCs and swPCs 6 days post SRBC immunisation in irradiated Ly5.1 hosts reconstituted with a 1:1 ratio of Ly5.1:CD45.2$^+$ (top row) or Ly5.1:CD45.2$^+$*Ccr6*$^{-/-}$ (bottom row) bone marrow. **(B)** Ratio of CD45.2$^+$ IgM$^+$PCs:CD45.2$^+$ naïve B cells in Ly5.1:WT and Ly5.1:*Ccr6*$^{-/-}$ chimeras. **(C)** Ratio of CD45.2$^+$ swPCs:CD45.2$^+$ naïve B cells in Ly5.1:WT and Ly5.1:*Ccr6*$^{-/-}$ chimeras. (A-C) n=6/chimera group, ±SEM, two-tailed unpaired Student's t test. ***p<0.001.

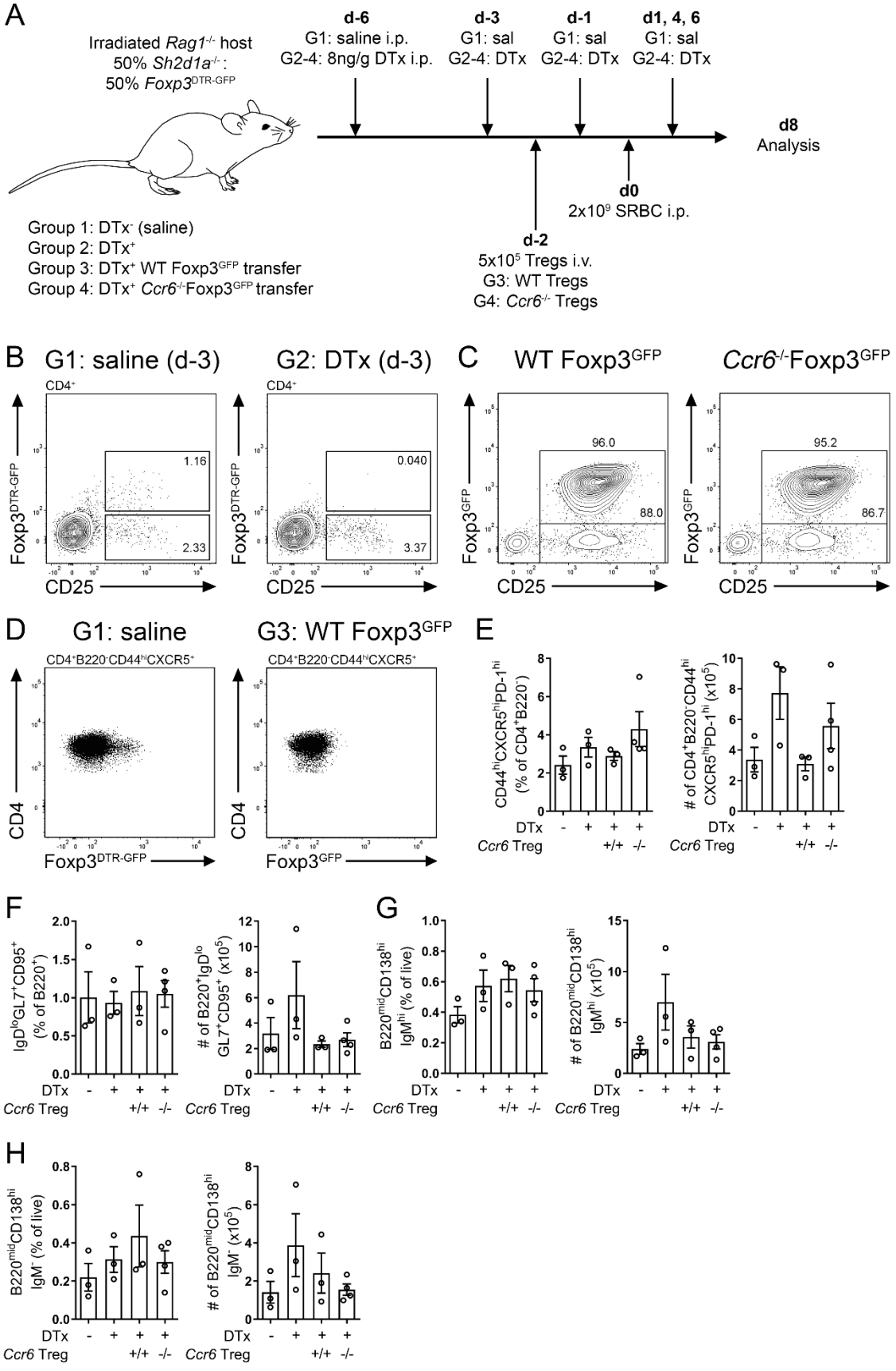
A
Irradiated Rag1-/- host
50% Sh2d1a-/-:
50% Foxp3DTR-GFP
d-6
G1: saline i.p.
G2-4: 8ng/g DTx i.p.
d-3
G1: sal
G2-4: DTx
d-1
G1: sal
G2-4: DTx
d1, 4, 6
G1: sal
G2-4: DTx
d8
Analysis
d0
2x10^9 SRBC i.p.
d-2
5x10^5 Tregs i.v.
G3: WT Tregs
G4: Ccr6-/- Tregs
Group 1: DTx- (saline)
Group 2: DTx+
Group 3: DTx+ WT Foxp3GFP transfer
Group 4: DTx+ Ccr6-/-Foxp3GFP transfer
B
G1: saline (d-3)
G2: DTx (d-3)
CD4+
Foxp3DTR-GFP
CD25
1.16
2.33
0.040
3.37
C
WT Foxp3GFP
Ccr6-/-Foxp3GFP
Foxp3GFP
96.0
88.0
95.2
86.7
D
G1: saline
G3: WT Foxp3GFP
CD4+B220-CD44hiCXCR5+
CD4
Foxp3DTR-GFP
Foxp3GFP
E
CD44hiCXCR5hiPD-1hi (% of CD4+B220-)
# of CD4+B220-CD44hi CXCR5hiPD-1hi (x10^5)
DTx
Ccr6 Treg
+/+
-/-
F
IgDloGL7+CD95+ (% of B220+)
# of B220+IgDlo GL7+CD95+ (x10^5)
G
B220midCD138hi IgMhi (% of live)
# of B220midCD138hi IgMhi (x10^5)
H
B220midCD138hi IgM- (% of live)
# of B220midCD138hi IgM- (x10^5)

Figure 4.14: T_{FR} cell CCR6 expression is dispensable for the regulation of splenic germinal centre cell populations

(A) Irradiated *Rag1*$^{-/-}$ host mice were reconstituted with a 1:1 ratio of *Sh2d1a*$^{-/-}$ and *Foxp3*$^{DTR\text{-}GFP}$ bone marrow, rested for 8 weeks, then allocated into one of four groups. Group 1 received saline vehicle control i.p. on indicated diphtheria toxin (DTx) treatment days and no Treg transfer (DTx^{-}). Group 2 received DTx i.p. on indicated days and no Treg transfer (DTx^{+}). Groups 3 and 4 received DTx treatments and i.v. transfer of 5x10^{5} MACS-purified CD4^{+}CD25^{+} cells from *Foxp3*^{GFP} mice (DTx^{+} *Ccr6*$^{+/+}$Treg) or *Ccr6*$^{-/-}$*Foxp3*^{GFP} mice (DTx^{+} *Ccr6*$^{-/-}$Treg) respectively. Chimeric mice were immunised with SRBC i.p. for analysis on day 8. **(B)** Representative plots from day 3 tail-bleeds of chimeric mice demonstrating the depletion of circulating *Foxp3*$^{DTR\text{-}GFP}$ Tregs in Group 2 after DTx administration compared to Group 1 Saline controls. **(C)** Purity of CD25^{+} and *Foxp3*$^{GFP+}$ cells isolated via CD4^{+}CD25^{+} positive-selection from WT *Foxp3*^{GFP} and *Ccr6*$^{-/-}$ *Foxp3*^{GFP} spleens for transfer into chimeric Groups 3 and 4, respectively. **(D)** Representative plots from chimeric mice demonstrating difficulties identifying *Foxp3*^{GFP}-positive T_{FR} cells in Group 3 WT *Foxp3*^{GFP} transfer chimeras compared to *Foxp3*$^{DTR\text{-}GFP}$-positive T_{FR} cells in Group 1 Saline chimeras. Percentage and number of **(E)** GCT cells, **(F)** GCB cells, **(G)** IgM^{+}PCs, and **(H)** swPCs across treatment groups. (B, D) Representative of n=3-4 mice/experimental group. (E-H) Each dot represents one chimeric mouse, n=3-4 mice/experimental group ±SEM, one-way ANOVA with Tukey's multiple comparison test.

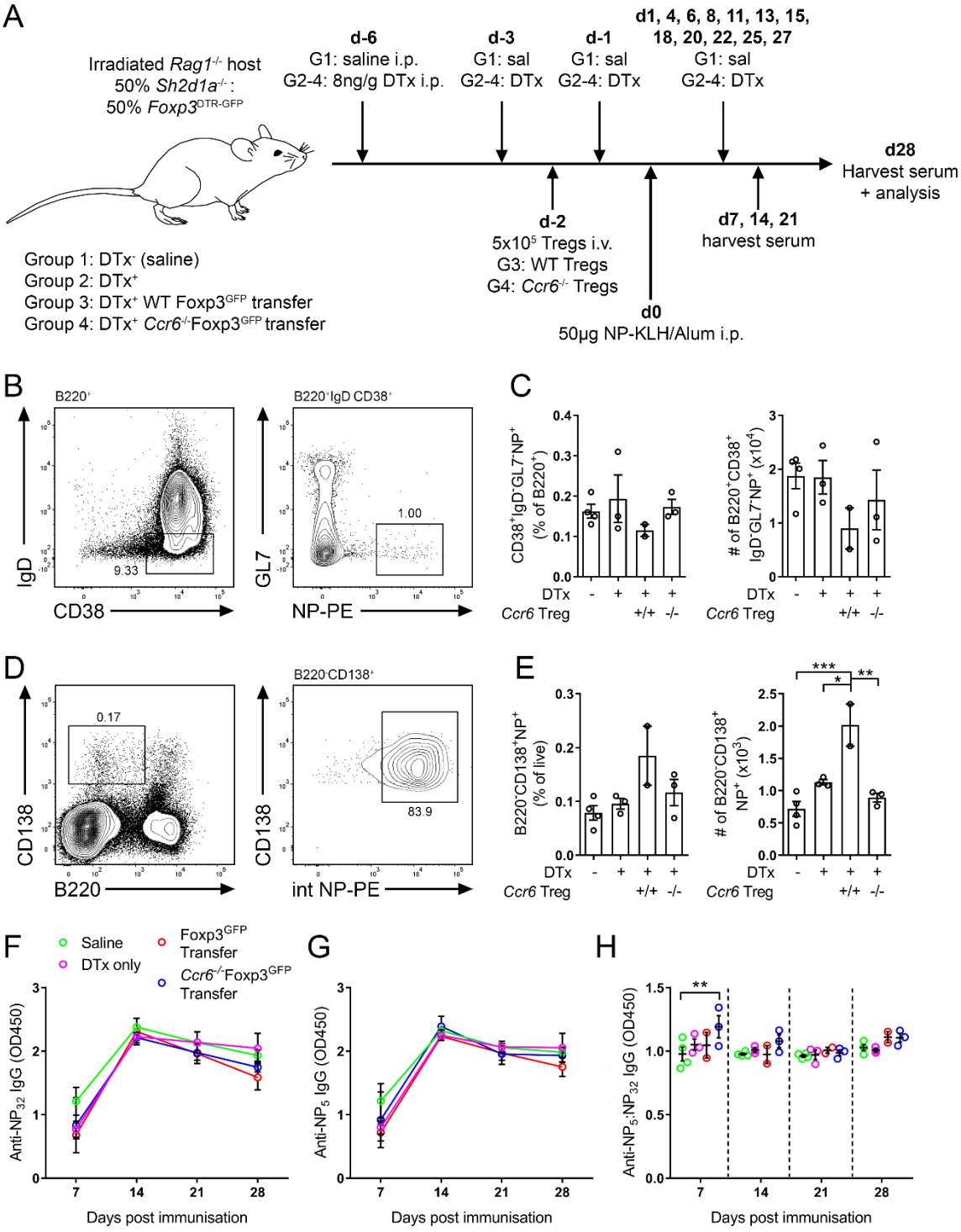
A
Irradiated Rag1-/- host
50% Sh2d1a-/- :
50% Foxp3DTR-GFP
d-6
G1: saline i.p.
G2-4: 8ng/g DTx i.p.
d-3
G1: sal
G2-4: DTx
d-1
G1: sal
G2-4: DTx
d1, 4, 6, 8, 11, 13, 15, 18, 20, 22, 25, 27
G1: sal
G2-4: DTx
d28
Harvest serum
+ analysis
d-2
5x10⁵ Tregs i.v.
G3: WT Tregs
G4: Ccr6-/- Tregs
d7, 14, 21
harvest serum
d0
50µg NP-KLH/Alum i.p.
Group 1: DTx- (saline)
Group 2: DTx+
Group 3: DTx+ WT Foxp3GFP transfer
Group 4: DTx+ Ccr6-/-Foxp3GFP transfer
B
B220+
IgD
CD38
9.33
B220+IgD-CD38+
GL7
NP-PE
1.00
C
CD38+IgD-GL7-NP+ (% of B220+)
# of B220+CD38+ IgD-GL7-NP+ (x10⁴)
DTx
Ccr6 Treg
+/+
-/-
D
CD138
B220
0.17
B220-CD138+
int NP-PE
83.9
E
B220-CD138+NP+ (% of live)
# of B220-CD138+ NP+ (x10³)
***
*
**
F
Saline
DTx only
Foxp3GFP Transfer
Ccr6-/-Foxp3GFP Transfer
Anti-NP32 IgG (OD450)
Days post immunisation
G
Anti-NP5 IgG (OD450)
H
Anti-NP5,NP32 IgG (OD450)

Figure 4.15: T_{FR} cell CCR6 expression is dispensable for antigen-specific antibody production

(A) Irradiated *Rag1*$^{-/-}$ host mice were reconstituted with a 1:1 ratio of *Sh2d1a*$^{-/-}$ and *Foxp3*$^{DTR\text{-}GFP}$ bone marrow, rested for 8 weeks, then allocated into one of four groups as described in Figure 4.14.A. Chimeric mice were immunised with NP-KLH/Alum i.p. to analyse antibody titre and antigen-specific germinal centre output. **(B)** Representative gating strategy for splenic NP-specific memory B cells ($B220^+CD38^+IgD^-GL7^-NP^+$) in chimeric mice. **(C)** Percentage and number of splenic NP-specific memory B cells between chimera groups. **(D)** Representative gating strategy for NP-specific bone marrow plasma cells ($B220^-CD138^+intNP^+$) in chimeric mice. **(E)** Percentage and number of NP-specific bone marrow plasma cells between chimera groups. **(F)** Low-affinity ($BSA\text{-}NP_{32}$) and **(G)** high-affinity ($BSA\text{-}NP_5$) anti-NP IgG antibody levels in the sera of chimeric mice at indicated time points following NP-KLH/Alum immunisation as detected by ELISA. **(H)** Ratio of high-affinity to low-affinity anti-NP IgG at indicated time points following NP-KLH/Alum immunisation. (B, D) Representative of n=2-4 chimeric mice/experimental group. (C, E, F-H) n=2-4 chimeric mice/experimental group, ±SEM, one-way ANOVA with Tukey's multiple comparison test. Each dot represents one chimeric mouse, except (F, G) each dot is the average of chimeric mice per treatment group. *p<0.05, **p<0.01, ***p<0.001.

Chapter 5
Discussion

Chapter 5.1 Discussion- ACKR4 regulates peripheral CCL21

The work presented in Chapter 3 identified novel modes of chemokine regulation by ACKR4 in barrier sites that profoundly influence dendritic cell migration (summarised in Figure 5.1). Additionally, this study identified new reagents and methods to distinguish full-length/soluble forms of CCL21, and serine/leucine isoforms of CCL21, revealing often ignored complexities in CCL21 biology resultant of biological differences between CCL21 variants. Subsequently, this work challenges initial paradigms established from studies with broad *Ackr4*$^{-/-}$ mice and raises multiple outstanding questions and research directions. Whilst skin CCL21 hyperabundance was dependent on local CCL21 and ACKR4 activity, the origin of ACKR4 function and hyperabundant CCL21 remains unknown for a number of barrier tissues and organs. This study has questioned the specificity of ACKR4 antibody reagents in the detection of ACKR4, thus alternate methods of detection are required to identify key ACKR4-expressing populations in other tissues. The identification of hyperabundant soluble CCL21 in steady-state *Ackr4*$^{-/-}$ mice raises outstanding questions regarding which processes regulate CCL21 cleavage *in vivo*, and what role solubilisation may serve in the maintenance of immobilised gradients and migratory events governing dendritic cell egress from barrier tissues.

5.1.1 Differential regulation of ACKR4 ligands in barrier tissues and internal major organs

The results in this thesis demonstrated widespread dysregulation of CCL21 in barrier tissues, the blood and multiple major internal organs in *Ackr4*$^{-/-}$ mice (Figure 3.1.A, D, E), that were consistent with a chemokine scavenging function of ACKR4 (Figure 3.2). Interestingly, differences in the level of CCL21 hyperabundance in skin was site-dependent, as skin harvested from *Ackr4*$^{-/-}$ ears contained substantially more CCL21 per milligram than *Ackr4*$^{-/-}$ dorsal skin (Figure 3.1.A). It is likely that both the greater density of lymphatic vessels in the ear[284], and greater abundance of subcutaneous fat in dorsal skin contributing to overall tissue weight, resulted in this observation. Investigation into the discrepancies within the literature surrounding CCL21 quantitation via ELISA identified reagents able to distinguish full-length and cleaved CCL21 quantitatively. Use of these reagents in ELISA revealed that hyperabundant CCL21 present in *Ackr4*$^{-/-}$ tissues is predominantly cleaved, however a caveat to the quantitation of CCL21 performed here is that isolation of chemokines via leaching out of the tissue potentially enriches for soluble, cleaved CCL21 whilst full-length CCL21 would predominantly remain immobilised within the dermis. To measure all extracellular immobilised CCL21 in barrier tissues in future studies, wildtype and *Ackr4*$^{-/-}$ tissues could be treated with heparinase to cleave heparan sulfate moieties, thus freeing immobilised CCL21 for quantitation via ELISA. This would provide some insight to the quality of immobilised gradients in barrier tissues where their visualisation via immunofluorescent microscopy is not possible.

The mechanisms underlying CCL21 hyperabundance in the blood and internal organs remain unknown. Previously, steady-state CCL21 expression was identified within the heart, liver and kidney[69,92,93,285], varying levels of *Ackr4* transcript was identified in the heart and kidneys[26,27,286], and most recently, ACKR4 function was demonstrated in cardiac fibroblasts utilising fluorescently-tagged ligands[123]. Thus, CCL21 hyperabundance in these organs could arise from local ACKR4-deficiency driving local CCL21 dysregulation, the accumulation of peripheral CCL21 from a distant tissue where ACKR4 function is required, or a combination of both. Additionally, hyperabundant CCL21 in the sera of *Ackr4*$^{-/-}$ mice was identified as soluble (Figure 3.1.D), yet the source(s) of CCL21 in the blood remain unknown. Given the dissemination of CCL21 observed from the skin (Figure 3.13), it is possible that dysregulated CCL21 from multiple peripheral tissues leaches into the blood via lymphatic recirculation. Experiments with tissue/organ targeted ACKR4-deficiency would provide insight to these outstanding questions.

Whilst CCL19 was detected in all barrier tissues, ACKR4 only regulated its abundance in the skin (Figure 3.1.A). The quantity of CCL19 was at least 10-fold lower than that of CCL21 in respective tissues, however given its 10-100 fold greater potency than CCL21 in CCR7-dependent chemotaxis[7,33,104], the levels of CCL19 observed in these tissues may be within a biologically active range. During the steady-state, CCL19 is predominantly expressed in lymphoid tissues[86,87,97], and lower CCL19 expression has been identified at the mRNA level or by the *Ccl19*-Cre.Rosa26-EYFP reporter in the small intestine, colon, trachea, appendix and lung[86,96]. However, few non-redundant CCR7-dependent functions of CCL19 have been identified in mice and studies identifying essential functions of CCL19 outside of lymphoid tissues are limited. Studies with CCL19-deficient mice have not found a role for CCL19 in dendritic cell egress from the skin or lungs during the steady-state, a process dependent on CCL21[101,107]. Rather, CCL19 expression can be induced during inflammation in dendritic cells[97,98] or cells of the non-haematopoietic compartment[96,99–101]. Interestingly, the study by Bryce *et al.*, demonstrated that aberrant cutaneous dendritic cell homing in *Ackr4*$^{-/-}$ mice following inflammation by topic TPA treatment was rescued in *Ccl19*$^{-/-}$*Ackr4*$^{-/-}$ mice[100]. In that model, TPA inflammation induced cutaneous CCL19 production, and hyperabundant CCL19 and full-length CCL21 was subsequently detected in *Ackr4*$^{-/-}$ mice relative to wildtype controls. In light of the results of our study, the observations of Bryce *et al.* raise the question of how hyperabundant CCL21 that is generated during the steady-state is ignored by mature dendritic cells leaving the skin of *Ccl19*$^{-/-}$*Ackr4*$^{-/-}$ mice. Future studies should investigate the abundance of both full-length and cleaved CCL21 in inflammatory settings to determine how these forms of CCL21 function with CCL19 to regulate dendritic cells migration in inflammation.

ACKR4 did not appear to regulate CCL25 abundance in the small intestine. At this site, CCL25 expression is restricted to epithelial cells spanning the crypts and the lower third of the villus, and the SED of Peyer's patches[211,287]. Recently, intestinal ACKR4 expression was identified within submucosal fibroblasts localised in close proximity to CCL21-producing

lymphatic vessels[118], but spatially separated from the epithelial source of CCL25 by the muscularis mucosa and lamina propria. This difference in localisation of ACKR4-expressing fibroblasts relative to the sources of these chemokines in the small intestine potentially explains their differential regulation by ACKR4 identified here. The effect of ACKR4 deficiency on CCL25 and CCR9-dependent migration has also been investigated in the thymus, a major site of CCL25 production. ACKR4-deficiency did not result in CCL25 hyperabundance in the thymus, however defects in localisation of CCR9-expressing thymocytes were consistently observed[103,112,117]. How CCR9-mediated migration in the thymus is disrupted without perturbations in CCL25 abundance remains unknown. However, like CCL21, CCL25 also has an elongated C-terminal tail, yet the function of this domain in CCL25 is unknown. Thus, perhaps like the phenomenon observed here in CCL21 quantitation, the current ELISA detection methods may not capture all biologically-active CCL25 if it is also cleaved like CCL21. Further investigation is therefore required to determine the contribution of ACKR4 in regulating CCL25 with additional methods of quantitation.

During the preparation of this thesis, CCL20 was identified as an additional ligand of ACKR4 in mice[110]. The CCR6-CCL20 axis is redundant for steady-state dendritic cell renewal and function within the skin[288,289], however upon inflammation, this axis is critical in recruiting dendritic cell precursors out of the blood and into the inflamed skin[289]. Future studies could investigate how ACKR4 regulates the abundance of CCL20 during this process with a particular focus on the resolution of inflammation when CCL20 signals are no longer required in the skin.

5.1.2 Identification of ACKR4-expressing populations in barrier tissues

A surprising finding of this study was the identification of greater *Ackr4* expression in the dermis than the epidermis (Figure 3.6.C), the opposite to what had previously been reported by imaging and flow cytometry experiments with the *Ackr4*^{EGFP} mouse[100,112]. Whilst we did observe *Ackr4* mRNA in IE keratinocytes, the greatest *Ackr4* expression was observed in dermal papillary fibroblasts (Figure 3.6.C, G), which is in support of human data[262]. Interestingly, this population of fibroblasts declines with age and is not replaced in human skin[290], raising a question as to whether CCL21 abundance in the skin will increase naturally with age and whether this may affect barrier immune function, which also deteriorates with aging[291]. Expression of additional atypical chemokine receptors was also identified on fibroblast subpopulations distinguished by CD26 and Sca-1 expression (Figure 3.6.H). During the wound healing process, CD26^{+} fibroblasts contribute to collagen deposition and scar formation[292]. Additional expression of ACKR1, ACKR2 and ACKR3 by CD26^{+} fibroblasts may further contribute to the regulation of wound healing, as ligands of these receptors are already implicated in multiple aspects of healing including the recruitment of immune cells, fibroplasia, angiogenesis and re-epithelialisation[293]. Lastly, similar sorting

strategies utilised here may be employed to identify ACKR4-expressing populations in the lung, kidney and vaginal mucosa where the identify of ACKR4^{+} cells remain unknown.

To support the identification of *Ackr4* expression in cells at the mRNA level, antibody staining of ACKR4 was attempted with multiple antibody clones by both flow cytometry and imaging. However, no specific staining was observed in wildtype cell populations above background determined with *Ackr4*$^{-/-}$ mice via flow cytometry (Figure 3.7). This is likely due to the low levels of surface receptor resultant of constitutive ACKR4 cycling through endosomes[116]. Despite previously reported ACKR4 staining in imaging experiments[80,100,117], specific ACKR4 staining above negative controls could not be reproduced with the same reagents and methods, or different antibody clones and skin preparations (Figure 3.8). Again, low levels of receptor expression are likely responsible for this observation, and this is supported by the literature which demonstrates that detection of ACKR4 via antibody staining is not as sensitive as detection with the *Ackr4*^{EGFP} reporter strain[80,100,117]. Given the lack of reliable antibody agents for ACKR4 demonstrated by this study, efforts to generate reliable antibodies against murine ACKR4 are ongoing, and future experiments to identify ACKR4-expressing cells in barrier tissues will include analysis of the *Ackr4*^{EGFP} or other ACKR4 reporter strains in development. Whilst these methods would identify ACKR4 expression, alternate approaches are required to demonstrate ACKR4 scavenging function. Unfortunately our attempts to show functional chemokine scavenging *in vitro* by primary dermal fibroblasts *in lieu* of ACKR4 protein detection were inconclusive, thus not presented here. This was likely due to the cellular stress imparted during lengthy tissue digestion and sorting protocols that were required, with the resultant cells unsuitable for subsequent functional assays. Thus, alternate strategies are required to demonstrate ACKR4 chemokine scavenging function by cell populations *in situ*. Recently, a chimeric CCL25-CCL19y fusion protein which selectively binds ACKR4 and not CCR9 or CCR7 was generated to visualise ACKR4 expression and scavenging function[110]. This has the advantage over similar reagents such as CCL19-AlexaFluor647 which require additional controls including *Ccr7*$^{-/-}$ and *Ackr4*$^{-/-}$*Ccr7*$^{-/-}$ mice to eliminate binding of CCL19-AlexaFluor647 to CCR7-expressing cells[100,118]. Fluorophore-labelled CCL25-CCL19y could be injected intradermally or painted epicutaneously onto the ears of wildtype and *Ackr4*$^{-/-}$ mice to identify ACKR4 expressing cells. Alternatively, *Ackr4*$^{fl/fl}$ mouse strains in development could be crossed to K14-Cre-ER^{T2} or *Pdgfra*-CreER^{T2} mice to restrict ACKR4-deficiency to keratinocytes[294] or fibroblasts[263,295] respectively, and the contribution of these cell populations to chemokine scavenging *in vivo* could be determined.

5.1.3 Unravelling the contributions of full-length and cleaved CCL21 in dendritic cell egress from the skin

To understand the importance of ACKR4 scavenging soluble CCL21, the contributions of immobilised haptotactic and soluble chemotactic CCL21 in dendritic cell egress during the steady-state must be understood. Previous studies with *St8sia4*$^{-/-}$ and *Grk6*$^{-/-}$ mice have

demonstrated the essential role for immobilised full-length CCL21 gradients in directing interstitial dendritic cell migration towards lymphatic vessels. The sialyltransferase ST8SIA4 is required by dendritic cells to reconfigure full-length CCL21 from an autoinhibitory to an active confirmation[9], whilst the G protein-coupled receptor kinase GRK6 is required for CCR7 signal transduction following ligation with full-length CCL21, but not cleaved CCL21[13]. Both *St8sia4*$^{-/-}$ and *Grk6*$^{-/-}$ dendritic cells show impaired migration to full-length CCL21 *in vitro*, however neither are required for chemotaxis to cleaved CCL21 and CCL19[9,13]. *In vivo*, *St8sia4*$^{-/-}$ and *Grk6*$^{-/-}$ dendritic cells show impaired interstitial migration towards lymphatic vessels in the skin, but subsequent intralymphatic migration and migration within draining lymph nodes is intact[9,13]. Collectively, these observations have led to the conclusion that immobilised CCL21 is essential for initial lymphatic vessel homing in the skin, whilst cleaved CCL21 is sufficient for migration within the lymph node.

Results here identified that soluble CCL21 is generated in barrier tissues during the steady-state and that ACKR4-scavenging was required to regulate its abundance. Originally, CCL21 cleavage was thought to be restricted to activated dendritic cells, however detection of soluble CCL21 in the absence of inflammatory stimuli here challenge this model. How CCL21 is cleaved in barrier tissues during the steady-state is unknown. Mature dendritic cells cleave CCL21 through an uncharacterised serine protease[7], but it is unknown whether dendritic cells matured in the absence of inflammatory stimuli are capable of cleaving CCL21 during basal steady-state emigration from the skin. To determine whether steady-state cleaved CCL21 is generated by dendritic cells, abundance of the cleaved form of CCL21 should be determined after long-term depletion of dendritic cells via diphtheria toxin in CD11c.DOG mice[296]. The biological function of cleaved CCL21 in interstitial migration of dendritic cells within peripheral tissues is also unknown. Given the increased chemotactic potency of cleaved CCL21[33], it has been postulated that CCL21 is cleaved by "leading" dendritic cells to transiently boost trailing dendritic cell recruitment in scenarios where dendritic cells are co-activated[33,297]. To determine whether dendritic cells employ *de novo* solubilized gradients during egress *in vivo*, varying ratios of differentially labelled wildtype and *St8sia4*$^{-/-}$ BMDCs could be co-injected into the dermis to study lymphatic homing via live imaging. As *St8sia4*$^{-/-}$ BMDCs cannot migrate to full-length CCL21 *in vitro* or home to dermal lymphatic vessels *in vivo* when transferred alone, migration within the interstitial areas could only be facilitated by cleaved CCL21 generated by co-injected wildtype BMDCs. Additionally, wildtype BMDCs could be substituted for *Ccl19*$^{-/-}$ or *Ccr7*$^{-/-}$ BMDCs to eliminate a role for dendritic cell-derived CCL19 or demonstrate any requirement for directional lymphatic homing of "leading" dendritic cells, respectively.

A second possibility is that soluble dermal CCL21 has limited function in interstitial dendritic cell migratory events, but is generated to facilitate scavenging by ACKR4 and maintenance of functional immobilised CCL21 gradients. This hypothesis fits with current observations that soluble CCL21 alone cannot support lymphatic vessel homing[9,13], and potentially answers an important question as to how largely-immobile ACKR4-expressing

cells regulate a spatially-segregated immobilised gradient. In the study by Ulvmar *et al.*, cLECs residing in the lymph node SCS were proposed to scavenge immobilised CCL21 within interfollicular areas up to 40μm away[80]. Similarly, the results here implicated papillary fibroblasts and interfollicular epidermal keratinocytes, localised adjacent to the dermal-epidermal junction, in the regulation of lymphatic vessel-derived CCL21 within the deeper dermis. It is now conceivable that ACKR4-expressing cells are not required to be adjacent to immobilised gradients if the cells utilising these gradients cleave CCL21 for local scavenging. Whether dendritic cells groom the immobilised gradient in this manner could be determined by visualising immobilised gradients in dendritic cell-depleted CD11c.DOG mice as outlined above. Ultimately, experiments to determine the biological significance of solubilised CCL21 either in dendritic cell egress or immobilised gradient regulation require identification of the protease(s) which facilitate CCL21 cleavage, and subsequent studies with mice deficient in these proteases.

5.1.4 Additional CCL21-dependent egress events potentially regulated by ACKR4 in the skin

In addition to the immediate function of guiding dendritic cells to lymphatic vessels, CCL21 plays a multitude of supplementary roles in dendritic cell egress from the skin. Dendritic cells first cross through preformed portals in the discontinuous basement membrane lining lymphatic capillaries, then transmigrate through specialised button junctions into the lymphatic lumen[72,73]. It is hypothesised that local CCL21 release by LECs proximal to basement membrane portals may facilitate adhesion to the lymphatic endothelium, propel dendritic cells into vessels to physically open button junctions, and/or recruit trailing dendritic cells to preformed portals[74,75]. If local LEC CCL21 secretion also guides dendritic cells through pre-existing portals, it is anticipated that hyperabundant CCL21 in *Ackr4*$^{-/-}$ skin may further impair this process. Additionally, immobilised CCL21 promotes adhesion of dendritic cells to surfaces through β_2 integrins[7]. However, transmigration across lymphatic endothelium is only integrin-dependent during inflammation when LECs upregulate ICAM and VCAM[298]. Conversely, during the steady-state, ICAM expression is reserved to blood vasculature[298] and cutaneous dendritic cell egress is integrin-independent[299]. Given the apparent abundance of CCL21 on blood vasculature in *Ackr4*$^{-/-}$ mice (Figure 3.4), immobilised CCL21 may have facilitated integrin-dependent crawling of activated wildtype BMDCs observed in *Ackr4*$^{-/-}$ skin (Figure 3.11.A and Video 3.3). In future studies, the intravital imaging experiments performed here could be further optimised to ensure sufficient BMDCs can be tracked in wildtype and *Ackr4*$^{-/-}$ hosts to interrogate differences in the duration of attachment to lymphatic vessels and pathing through preformed lymphatic portals.

Within the lymphatic vessel lumen, immobilised CCL21 gradients generated by lymph flow facilitate dendritic cell migration downstream towards larger lymphatic collecting vessels where increased lymph flow subsequently drives dendritic cells passively to lymph

nodes[74,76,77]. It is conceivable that hyperabundant CCL21 leaching from ACKR4-deficient skin via the lymphatics to the draining lymph nodes may impair this process (depicted in Figure 5.1). Unfortunately, luminal dendritic cell migration within lymphatic vessels was difficult to analyse in the intravital imaging experiments here as BMDCs often clumped together in vessels making it difficult to track individual cells. Additionally, without markers to identify LYVE-1^{-} lymphatic collector vessels during imaging, this study was unable to distinguish upstream or downstream luminal migration. To determine whether increased luminal CCL21 in ACKR4-deficient skin disrupts downstream migration, live imaging experiments performed here could be adapted by i) reducing the number of injected wildtype BMDCs to allow tracking of single luminal dendritic cells, and ii) including additional fluorophore-tagged antibodies alongside anti-LYVE-1, such as anti-gp38 (podoplanin) or anti-VE-Cadherin, to identify lymphatic collector vessels. Subsequently, upstream/downstream migration of luminal dendritic cells could be calculated and compared between wildtype and *Ackr4*$^{-/-}$ hosts. Together, refinements to the imaging methods utilised in this study could identify the requirement for ACKR4 in regulating additional CCL21-dependent migratory events which facilitate skin dendritic cell egress.

5.1.5 Dendritic cell egress defects in *Ackr4*$^{-/-}$ mice

Despite significant disruption to CCL21 regulation and drastic dendritic cell migratory defects observed in this study, only minor differences in migratory dendritic cell populations are reported in the lymph nodes of steady-state *Ackr4*$^{-/-}$ mice. These defects are most evident in the skin-draining lymph nodes[80,100,112], but no differences have been observed in mesenteric lymph nodes draining the small intestine[118], and it is unknown whether dendritic cell trafficking to the mediastinal and iliac lymph nodes that drain the lung and vaginal mucosa respectively, are perturbed. Importantly, ACKR4 deficiency *delays* egress, not completely abrogate egress. Thus, studies quantitating the number of dendritic cells in steady-state lymphoid tissue may not identify defects in the kinetics of dendritic cell trafficking given that basal dendritic cell emigration is a continuous process. To accurately determine the delay in dendritic cell egress during the steady-state, mouse strains that express endogenous photoconvertible fluorescent proteins are required so dendritic cells can be photoconverted in the periphery without inflammation, then subsequently identified in draining lymph nodes. KikGR mice are suitable for these experiments given their efficacy in tracking steady-state egress of dendritic cells from wildtype skin without inducing phototoxicity and inflammation[300–302]. Comparing the accumulation of peripherally-photoconverted dendritic cells in draining lymph nodes of KikGR and KikGR.*Ackr4*$^{-/-}$ mice would allow the quantification of delays in steady-state dendritic cell egress from various barrier tissues.

This study revealed that BMDCs in *Ackr4*$^{-/-}$ skin are unable to be guided towards lymphatic vessels by immobilized CCL21 and exhibit path-persistent migration likely triggered by LPS activation (Figure 3.11). Thus, a caveat to the imaging approaches in this study is that the

migratory behaviour of LPS-activated BMDCs may not recapitulate those of dendritic cells matured in the absence of inflammatory stimuli that traffic within the skin during the steady-state. Whilst the signals that regulate steady-state dendritic cell maturation are incompletely understood, inflammation-independent maturation of BMDCs has been achieved following activation with TSLP[57], ligation of surface TREM-2[56], or by disrupting E-cadherin interactions during BMDC culture[58]. Future studies could utilise BMDCs matured via these methods for ear crawl-in and live imaging experiments to better model dendritic cell egress during the steady-state and further demonstrate the requirement of ACKR4 in this process.

Although this study focused on the functions of ACKR4 during the steady-state, ACKR4-deficiency may differentially impact the egress of different dendritic cell subsets following inflammation in a tissue- and immunogen-specific manner. Indeed, *Ackr4*$^{-/-}$ mice display impaired migration of specific dendritic cell subsets in models of cutaneous sensitisation and breast cancer[100,122]. However, it is unknown whether subset-specific dendritic cell migration defects occur in other tissues of *Ackr4*$^{-/-}$ mice following inflammation. Future studies could investigate the impact of ACKR4-deficiency on dendritic cell subset-specific egress from barrier tissues induced by immunogens that preferentially drive cDC1 or cDC2 activation. Importantly, these immunogens should be delivered to each barrier tissue in a manner which reflects the natural route of antigen exposure., e.g. oral administration for activation of dendritic cell subset within the small intestine lamina propria.

5.1.6 Contributions of peripheral and lymph node ACKR4 in restricting the pollution of draining lymph nodes with solubilised peripheral CCL21

The data presented here challenge the current paradigm that SCS cLEC ACKR4 regulates interfollicular CCL21 gradients, as skin ACKR4 deficiency resulted in draining lymph node CCL21 hyperabundance despite intact SCS cLEC ACKR4 function. Furthermore, data here demonstrated that soluble, peripheral CCL21-Leu is increased in the skin-draining lymph nodes of *Ackr4*$^{-/-}$ mice, challenging the model put forth by Ulvmar and colleagues that hyperabundant CCL21 was of lymph node paracortex origin[80]. Mechanistically, hyperabundance of CCL21 in the SCS and interfollicular areas is more likely to arise from upstream lymph fluid, as paracortex-derived CCL21 would need to diffuse against the flow of lymph in the lymph node to reach sites of accumulation observed in *Ackr4*$^{-/-}$ mice. The distribution of CCL21-Leu leaching into *Ackr4*$^{-/-}$ lymph nodes could be visualised by crossing *Ackr4*$^{-/-}$ mice to the recently described *Ccl21a*$^{-/-}$ mouse strain that lacks lymphoid CCL21-Ser expression[303]. As these mice lack lymphoid CCL21-Ser expression, staining of CCL21 in lymph node sections from *Ccl21a*$^{-/-}$ and *Ackr4*$^{-/-}$*Ccl21a*$^{-/-}$ mice would highlight the localisation and relative abundance of CCL21-Leu leaching into lymph nodes in the absence of ACKR4. This approach would support the findings in this study that ACKR4 limits the dissemination of peripheral CCL21 into draining lymph nodes, and demonstrate that aberrant SCS and interfollicular CCL21 is of peripheral origin.

Based on the discussion above and the data in this thesis, it is now hypothesised that cLEC ACKR4 complements the functions of peripheral ACKR4 in scavenging afferent lymph-borne chemokines to prevent local hyperabundance in the SCS and interfollicular areas. This is likely critical given the reliance on soluble CCL21 for CCR7-mediated migration within these areas, as implied from studies using both *St8sia4*$^{-/-}$ and *Grk6*$^{-/-}$ BMDCs[9,13]. To determine the contribution of cLEC ACKR4 in restricting lymph node pollution by upstream chemokines, the chimeric and selective ACKR4 ligand CCL25-CCL19y could be injected into the afferent lymphatics of wildtype and *Ackr4*$^{-/-}$ mice, then quantitated in the draining lymph node shortly after injection to identify the threshold of SCS ACKR4 scavenging function. To determine the effect of cLEC ACKR4-deficiency on dendritic cell localisation within the lymph node, another transplant approach could be utilised where wildtype or *Ackr4*$^{-/-}$ lymph nodes are transplanted into the ear pinnae of wildtype mice. In this setting, host immune cells populate the transferred lymph node within 3-4 weeks[304] and transferred lymph nodes can subsequently be excised and imaged to determine differences in CCL21 and dendritic cell distribution between wildtype and *Ackr4*$^{-/-}$ lymph nodes. A strength of this approach is that it can be internally controlled by transplanting both wildtype and *Ackr4*$^{-/-}$ lymph nodes into separate ears of hosts, and the synergistic effect of ACKR4 deficiency in the skin and lymph nodes could be recapitulated by transplanting lymph nodes into *Ackr4*$^{-/-}$ ears. Alternatively, conditional *Ackr4*$^{fl/fl}$ strains in development could be crossed to *Prox1*-Cre^{ERT2} mice to restrict ACKR4 deficiency to LECs[305] and eliminate the technicalities associated with intralymphatic injection or transplant methods.

5.1.7 Conclusions- ACKR4 regulates peripheral CCL21

In summary, this study has revealed several important biological functions of ACKR4 in the regulation of CCL21 and subsequent dendritic cell migration *in vivo*. This study demonstrated that ACKR4 was crucial in regulating both immobilised and soluble CCL21 in barrier tissues, and resolved various conflicting reports on the *in vivo* scavenging activity of ACKR4 by revealing shortcomings with commercial ELISA detection methods for CCL21. This study also demonstrated the need for better reagents or methods for reliable detection of endogenous ACKR4, either by generation of new antibodies, reporter strains, or the use of synthetic ACKR4-specific ligands. Going forward, this work poses new questions regarding the dynamics of soluble and immobilised CCL21 gradients *in vivo* and their importance in the migratory events that underpin dendritic cell egress. Given the widespread dysregulation of soluble CCL21 in *Ackr4*$^{-/-}$ mice, new models are required for targeting ACKR4-deficiency to specific tissues and/or cell lineages to demonstrate tissue-specific functions of ACKR4. Together, these studies will broaden understanding of molecular control of cell migratory signals *in vivo*, which could shape strategies aiming to modulate immune cell migration for health and prevention of disease.

Chapter 5.2 Discussion- GCT cell migratory cues

Work conducted in Chapter 4 identified differential expression of CCR6 between GCT cell subsets, with the greatest expression identified within T_{FR} cells. Here, CCR6 expression facilitated migration to sole ligand CCL20 *in vitro*, yet the distribution of $Foxp3^+$ cells in splenic germinal centre compartments *in vivo* was unaffected by CCR6-deficiency. This occurred despite upregulation of splenic CCL20 following immunisation. Whether CCL20 directs T_{FR} cell migration in other secondary lymphoid organs where CCL20 expression has been better characterised, such as the lymph node or Peyer's patches, remains an open question. To interrogate the function of T_{FR} cell CCR6 expression, a novel model to restrict CCR6-deficiency to T_{FR} cells and their precursors was designed, but revealed unexpected variables with this approach. Therefore, improved strategies published during this work to restrict gene deficiency to T_{FR} cells may be beneficial to future studies investigating CCR6 function in T_{FR} cells. Additionally, the unknown function of CCR6 upregulation by early antigen-activated B cells following T-dependent immunisation was also investigated in experiments when permitted. Through this approach, defects in early plasma cell differentiation were identified. Lastly, initial chemokine receptor profiling of GCT cells identified multiple additional chemokine receptors expressed with uncharacterised function. Given the many studies determining GCT cell function published during this work, new insights into the possible roles of additional chemokine receptors identified here warrant future investigation.

5.2.1 New lines of inquiry into the function of CCR6 in T_{FR} cell localisation and function

Whilst the experiments carried out here utilising a T_{FR}-restricted CCR6-deficiency model were inconclusive in identifying a role for CCR6 in T_{FR} cell biology in the spleen, further work is warranted investigating this chemokine axis in the germinal centre responses of alternate lymphoid organs or following different immunisation strategies and/or infectious models. During the course of this work, CCR6 expression by GCT cells has been verified by other groups[206,306,307]. However, the work presented here is the first to demonstrate i) greater expression by T_{FR} cells compared to T_{FH} cells, ii) functional chemotaxis towards CCL20 by GCT cells, and iii) no intrinsic requirement for CCR6 in T_{FH} and T_{FR} cell differentiation. Given the low quantities of CCL20 observed in the spleen following the immunisation strategies utilised here, other inflammatory models could be utilised which have demonstrated splenic CCL20 induction. Notably, CCL20 upregulation and production have been identified in the spleen following immunisation with synthetic peptidoglycan compounds[278]. In this setting, CCL20 expression was induced in radio-resistant cells downstream of TNFα signalling which has been demonstrated to induce CCL20 expression in a variety of different cell types[274,308–312]. The immunisation strategies utilised in this study, SRBC and NP-KLH/Alum, may not sufficiently induce splenic CCL20 expression as the adjuvant alum does not induce nor act through TNFα[313–315], and it was recently demonstrated that SRBC immunisation initiates antibody responses directly through missing-self CD47 and SIRPα interactions between xenogeneic red blood cells and splenic dendritic cells,

respectively[316]. Whether GCT cell CCR6 function is reserved for splenic antibody responses following bacterial infections remains an open avenue for investigation.

Alternatively, the function of CCR6 on GCT cell subsets could be investigated in other secondary lymphoid organs with characterised CCL20 expression and localisation. Firstly, steady-state CCL20 expression has been identified in the SED of Peyer's patches[288,317–319], and is further upregulated by ingested bacterial products from *Salmonella* species and *Listeria monocytogenes*[320]. Here, CCR6 mediates the migration of B cells and dendritic cells in to the SED and facilitates crucial interactions between these cells necessary for CSR[184], exemplified by reduced IgA responses to gut inflammation in *Ccr6*$^{-/-}$ mice[288]. In the Peyer's patches, T_{FR} cells are crucial in diversifying IgA against gut microbiota and establishing a regulatory loop whereby the healthy microbiome established by T_{FR} cells supports Foxp3^{+} cells and IgA production[164]. Therefore, it is conceivable that T_{FR} cells may also utilise CCR6 to migrate to the SED and influence the diversification of IgA antibodies against the microbiota through interactions with dendritic cells and B cells in this niche (Figure 5.2). Future studies could investigate the function of CCR6 in T_{FR} cell localisation within the Peyer's patches and interrogate microbiota diversity in models that lack CCR6 expression in T_{FR} cells.

Steady-state CCL20 expression has also been identified in the lymph node SCS[215,321] and is further upregulated following SIV infection[321] or LPS administration[317]. At this site, CCR6 drives the migration of innate-like lymphocytes to the SCS[215] and it is hypothesised that high CCR6 expression by memory B cells may contribute their peri-subcapsular localisation in lymph nodes during the steady-state[214], however the latter remains to be formally tested. Upon secondary activation, memory B cells in the peri-subcapsular space interact with memory T_{FH} cells, proliferate, and differentiate into plasma cells[187,214]. CCR6-deficiency results in diminished memory B cell responses characterised by reduced plasma cell differentiation and antibody titres upon secondary challenge[278,322]. As CCR6 is dispensable for memory B cell development and germinal centre localisation[213,322], memory B cell CCR6 expression may be crucial for localisation to the peri-subcapsular niche preceding secondary activation. Additionally, early-activated B cells upregulate CCR6 and accumulate at the SCS/follicle interface to proliferate during the early phases of the immune response prior to the formation of the germinal centre[132]. Whilst peri-subcapsular localisation of early-activated B cells coincides with CCR6 expression[132,180–183], it is unknown whether CCR6 expression contributes to this relocalisation in addition to cues that are known to drive outer-follicle localisation such as EBI2[174,175]. The importance of localisation adjacent to the SCS for rapid B cell expansion prior to seeding the germinal centre is incompletely understood, but B cells that accumulate at the SCS do not express Bcl6 and many upregulate intracellular immunoglobulin light chain expression, consistent with plasmablast differentiation[132]. Given that T_{FR} cells restrict the emergence of autoantibodies following immune challenge[225,237,238,240], CCR6 may facilitate the recruitment of T_{FR} cells to subcapsular niches to regulate crucial proliferation and differentiation events that underpin plasma cell

differentiation (Figure 5.3). As the subcapsular niche is utilised by both early-activated and memory B cells, T_{FR} cells may colocalised to this niche to regulate both primary and memory antibody responses (Figure 5.3). Whilst the role of T_{FR} cells in regulating antigen-specific antibody production and affinity is widely debated, T_{FR} cells have defined roles in limiting the production of autoantibodies[225,237,238,240], therefore future studies investigating a function of T_{FR} cell CCR6 expression in the lymph node should incorporate measures of both total, antigen-specific, and autoreactive immunoglobulin.

Together, these new hypotheses to investigate T_{FR} cell function outside of the germinal centre fit with a recent publication where human lymph node T_{FR} cells, accurately visualised through high-parameter histocytometry, predominantly resided outside of the germinal centre[323]. Whilst multiple studies have visualised $Foxp3^{+}$ cells within the germinal centre[42-44,221,243,244] the larger phenotyping panel utilised by Sayin *et al.* permitted the differentiation between T_{FR} cells and Tregs in sections, thus permitted quantitation of definitive T_{FR} cells localised outside of the germinal centre for the first time. Therefore, complementary to investigating the function of CCR6 in homing T_{FR} cells to niches outside of the germinal centre in lymph nodes or Peyer's patches, a range of infectious models or immunising antigens with bacterial adjuvants would benefit future studies given their ability to further induce CCL20 in these niches.

5.2.2 Improvements to current approaches restricting gene deletion to T_{FR} cells

Whilst the approach utilised here to restrict CCR6-deficiency to T_{FR} cells was designed with the greatest intent, some unexpected variables limited the interpretation of results. Firstly, incomplete depletion of T_{FR}-competent host Tregs was observed in some mice prior to Treg transfer. Whilst analysis on day 8 SRBC immunised chimeras revealed complete depletion of *Foxp3*$^{DTR\text{-}GFP}$-derived Tregs at the endpoint of analysis, complete depletion is necessary for restriction of CCR6 deficiency to transferred T_{FR} cell precursors and therefore accurate interpretation of results generated by the model. Additionally, longer time courses of diphtheria toxin administration have demonstrated toxicity and/or clearance of toxin by neutralising antibodies in other models[296,324], and these problems may have manifested in the NP-KLH/Alum immunisation model utilised here. Whist diphtheria toxin receptor-mediated transgenic mice are a useful immunological tool, the extensive experimental manipulation required to maintain cell depletion here may be an unnecessary disadvantage given the number of components to the model used here.

A shortcoming identified following the analysis of the chimera model utilised here was the inability to distinguish T_{FH} and T_{FR} cell populations within identified GCT cells using the Foxp3-reporter constructs as intended. Whilst Foxp3-expressing cells were identified in control saline treated *Rag1*$^{-/-}$(*Sh2d1a*$^{-/-}$:*Foxp3*$^{DTR\text{-}GFP}$) chimeras via IRES-driven GFP expression from the *Foxp3*$^{DTR\text{-}GFP}$ locus, transferred *Foxp3*$^{GFP+}$ and *Ccr6*$^{-/-}$*Foxp3*$^{GFP+}$ cells could not be visualised by the expression of the Foxp3-GFP fusion protein within these cells.

One scenario that may explain this is that the lower level of GFP expression when fused with Foxp3 protein is insufficient to detect these cells when the flow cytometer was setup to visualise the greater GFP signal resultant from IRES-driven expression in *Foxp3*$^{DTR-GFP}$-derived T_{FR} cells. In future, this could be easily resolved by directly staining Foxp3 in flow cytometry analyses. An alternate scenario is that insufficient numbers of Tregs may have been transferred to recapitulate the pool of Tregs capable of differentiating into T_{FR} cells to regulate the immune response. Whilst the number of transferred Tregs was based on previous studies[42,44], these studies transferred Tregs into T cell deficient mice, thus the optimal number of transferred Tregs for the chimeric model used in this study may differ. This is further compounded by the possibility that transferred Tregs may have been outcompeted by endogenous *Sh2d1a*$^{-/-}$ Tregs for survival signals and failed to persist in chimeras for the duration of the experiment. A previous study demonstrated that upon depletion of 50% of the Treg compartment via diphtheria toxin, surviving Tregs proliferate to overfill the Treg niche before contracting back to initial steady-state numbers[325]. Here, Treg expansion was induced by increased IL-2 produced by activated T cells upon the easing of Treg-mediated immunosuppression, and subsequent contraction was facilitated by competition for the limited IL-2 which drove pro-survival signals in expanded Tregs[325]. This may be problematic in the *Rag1*$^{-/-}$(*Sh2d1a*$^{-/-}$:*Foxp3*$^{DTR-GFP}$) chimera model used in this study, as depletion of *Foxp3*$^{DTR-GFP}$-derived Tregs may trigger overexpansion of *Sh2d1a*$^{-/-}$ Tregs. Whilst *Sh2d1a*$^{-/-}$ Tregs cannot participate in the germinal centre response, expansion of *Sh2d1a*$^{-/-}$ Tregs to reconstitute the Treg niche in chimeric mice may starve transferred *Foxp3*$^{GFP+}$ or *Ccr6*$^{-/-}$*Foxp3*$^{GFP+}$ Tregs of limited IL-2 and thus impede the survival of T_{FR}-compatible Tregs that are central to the model.

To overcome limitations of models utilising diphtheria toxin-induced depletion and possible issues regarding transferred Treg cell longevity, chimera models where *Ccr6*$^{-/-}$ T_{FR} cell precursors are present during the steady-state could be utilised. The simplest approach here would be *Rag1*$^{-/-}$(80% *Foxp3*$^{-/-}$:20% WT or *Ccr6*$^{-/-}$) chimeras. However, the *Ccr6*$^{-/-}$ chimeras may exhibit gut inflammation given a partial requirement for CCR6 in efficient Treg migration to the Peyer's patches[269]. As Tregs can also limit autoantibody formation[229] and all Tregs in this chimera would also be generated from *Ccr6*$^{-/-}$ bone marrow, differences could not be solely attributed to T_{FR} cell CCR6-deficiency. The effects of Treg CCR6-deficiency could be minimised by generating *Rag1*$^{-/-}$(45% *Foxp3*$^{-/-}$:45% *Sh2d1a*$^{-/-}$:10% WT or *Ccr6*$^{-/-}$) chimeras, where *Sh2d1a*$^{-/-}$ bone marrow is included to generate CCR6-sufficient Tregs necessary for peripheral tolerance but excluded from germinal centre reactions, akin to the chimera model used in this study. In this chimeric model, the T cell compartment would consist of T_{FH} cells derived from 80% *Foxp3*$^{-/-}$ and 20% WT or *Ccr6*$^{-/-}$ bone marrow, non T_{FR}-competent Tregs derived from 80% *Sh2d1a*$^{-/-}$ and 20% WT or *Ccr6*$^{-/-}$ bone marrow, and all T_{FR} cells would be generated from WT or *Ccr6*$^{-/-}$ bone marrow. The caveat with both of these approaches is that a small proportion of T_{FH} cells will differentiate from *Ccr6*$^{-/-}$ bone marrow. Precise genetic-targeting of Treg/T_{FR} cells without off-target deletion in T_{FH} cells has been achieved recently utilising *Foxp3*$^{Cre-ERT2}$*Cxcr5*$^{fl/fl}$ mice[243], where administration of tamoxifen to activate *Foxp3*-driven Cre expression prevented off target deletion in

Foxp3^{-} cells that has been observed with other *Foxp3*-Cre mouse strains[243,326,327]. Generation of *Ccr6*$^{fl/fl}$ mice would allow a similar approach can be utilised to efficiently target CCR6 deletion to Treg and T_{FR} cells. There are currently no methods to restrict gene-deficiency to T_{FR} cells without disrupting T_{FH} cell or Treg expression as the commonly used *Bcl6*^{Cre} and *Foxp3*^{Cre} strains also target these populations, respectively. However, a recent paper by Clement *et al.* restricted diphtheria toxin receptor expression to T_{FR} cells using *Foxp3*^{Cre}*Cxcr5*^{LoxSTOPLoxDTR} constructs[237]. Together with the adoption of sequential dual-recombinase models utilised in other research fields[328–330] the additional precision required to restrict *Ccr6* gene deletion to only T_{FR} cells could be provided by dual recombinase activity under both *Foxp3* and *Cxcr5* promoters in a similar manner to Clement *et al*. For example, *Foxp3*^{Dre}*Cxcr5*^{RoxSTOPRoxCre}*Ccr6*$^{fl/fl}$ mice could be generated where Dre recombinase drives the recombination of Rox sequences to permit Cre expression from the *Cxcr5* locus which subsequently knocks-out *Ccr6* in cells expressing both *Foxp3* and *Cxcr5*. As dual-recombination models become more available and readily used by the immunological research community, these approaches will greatly benefit the study of T_{FR} cell differentiation, function and localisation.

5.2.3 Cell-intrinsic requirement for CCR6 in plasma cell differentiation

Unexpectedly, a requirement for cell-intrinsic CCR6 expression was identified in IgM^{+} and isotype-switched plasma cell differentiation during this study (Figure 4.13). This was surprising given that plasma cells reportedly do not express CCR6[119,183,322], no defects in primary immunisation plasma cells responses have previously been reported in *Ccr6*$^{-/-}$ mice[183,322] and defects in plasma cell number appear contradictory to reports of greater titres of low-affinity antibody generated in *Ccr6*$^{-/-}$ mice following model antigen immunisation[182]. Differences to these published studies may have been observed due to the different immunisation strategies utilised here. Unfortunately, the effect of CCR6-deficiency on antibody affinity was not determined as SRBC immunisation was utilised in broad-knockout and mixed chimera experiments, and methods to determine the overall affinity of this response are not available. As plasma cells do not express CCR6, the results here suggest that CCR6 may be required by a precursor population not identified in our analyses. Indeed, early activated B cells upregulate CCR6 and seed both germinal centre and early germinal-centre independent plasma cell responses[180,181]. However, as no complementary increase in GCB cell differentiation was observed in chimeras, it is unlikely that CCR6 facilitates fate decisions of activated B cells down germinal centre or plasma cell differentiation pathways, but rather CCR6 may optimally position developing plasma cells or precursor populations in niches supporting their survival and differentiation. Like the lymph node, early antigen-activated B cells in the spleen migrate to the outer-follicle where they rapidly proliferate[132,191], however the contribution of this migration to plasma cell differentiation is unclear from these studies as early antigen-activated B cells migrated back into the follicle to seed germinal centres[191]. It is also unknown whether early activated B cell CCR6 expression contributes to outer-follicle localisation in the spleen. Additionally, CCL20 expression patterns in the spleen are poorly characterised, with limited evidence

demonstrating that CCR6-deficiency results in misplacement of switched memory B cells in the spleen[322]. Future studies should utilise imaging experiments interrogating incremental timepoints to track localisation of wildtype and *Ccr6*$^{-/-}$ antigen-specific B cells following immunisation to determine whether CCR6 is required for outer-follicle localisation. If studied in the spleen, generation of a CCL20-reporter strain will assist with determining the cellular source of CCL20 given the uncertainty in intracellular CCL20 staining encountered in this study. Together, these experimental approaches could finally identify any roles for the temporal CCR6 upregulation by early activated B cells.

5.2.4 Migratory implications for additional chemokine receptors identified in GCT cells

Whilst *Ccr6* expression by GCT cells was investigated in this study, expression of other chemokine receptors with unknown functions in GCT cell biology were also identified in initial qPCR experiments. Relative to naïve CD4 T cells, GCT cells displayed increased expression of *Ccr2*, *Ccr4* and *Cxcr3*. High expression of *Ccr2* was observed in GCT cells at both peak and late time points during the germinal centre reaction. A recent study identified *Ccr2* expression in neonatal GCT cells[331], however its function in germinal centre biology remains unknown. Like CCR6, some Tregs express CCR2[332–336] where it has been demonstrated to regulate CD25 expression and thus sensitivity to IL-2 signalling[336]. Given recent studies demonstrating that IL-2 signalling is detrimental to the stability of the GCT cell transcriptome[225,226,337] and that T_{FR} cells downregulate CD25[225,226], CCR2 expression may contribute to the regulation of T_{FR} cell differentiation through limiting IL-2 signalling. Together, these observations justify future investigation into the role of this chemokine axis in GCT cell biology.

Transient expression of *Ccr4* was observed in GCT cells 5 days post SRBC immunisation before being undetectable by day 8. CCR4 expression has been identified in Tregs[332,333,338,339] and one of its ligands, CCL22, is a potent Treg attractant expressed by lymph node dendritic cells and further upregulated upon inflammation[338,339]. CCL22 facilitates essential interactions between dendritic cells and Treg cells that when disrupted, results in excessive T cell activation[339]. During the preparation of this thesis, CCR4 expression was reported on both T_{FH} and T_{FR} cells where it facilitated interactions between T_{FH} cells and CCL22-expressing high-affinity GCB cells crucial for affinity maturation[340]. Whether CCR4 regulates early dendritic cell-dependent differentiation cues for GCT cells is unknown, thus future studies could investigate the function of this chemokine axis during early stages of the humoral response in lymph nodes with a focus on early GCT cell and dendritic cell interactions.

During this study, multiple groups identified CXCR3 expression by T_{FH} cells during antibody responses to viral infection[166,341,342]. Whether CXCR3 was required for T_{FH}

localisation to specific lymph node niches during the response was not the focus of these studies. However, a later study demonstrated that dysregulated CXCR3 expression by T_{FH} cells was detrimental to germinal centre localisation and relocated T_{FH} cells into the follicle[165]. Conversely, scarce CXCR3 expression was identified on T_{FR} cells during initial characterisation of this subset[42], suggesting CXCR3 expression may be limited to T_{FH} cells. CXCR3 ligands CXCL9 and CXCL10 are induced in the lymph node upon inflammation, where they drive early CD4 T cell migration to the interfollicular and medullary regions, respectively[216]. In the spleen, CXCL9 expression has been identified in the marginal zone where it attracted CD8 T cells in response to viral infection[343]. Both the interfollicular and outer-follicle areas of the lymph node and spleen respectively, are key niches for the early development of humoral responses[132,191]. Thus, CXCR3 may facilitate migration to the CXCL9 signals in interfollicular or outer-follicle areas during events preceding germinal centre formation, or as postulated by Shi *et al.*, facilitate the dynamic migration of GCT cells observed between the germinal centre and follicle[165,187]. Further studies into the effect of CXCR3-deficiency on T_{FH} and T_{FR} cell localisation are necessary to determine whether CXCR3 facilitates key GCT cell differentiation events in the interfollicular zone, and/or dynamic T_{FH} cell germinal centre to follicle migration that is typical of memory T_{FH} cell responses[187]. Ultimately, the chemokine receptor expression profiling of GCT cells performed here has identified new avenues of inquiry into chemokine receptors that may further contribute to GCT cell biology and humoral immunity.

5.2.5 Conclusions- GCT cell migratory cues

In summary, the work in Chapter 4 revealed novel differences in the migratory capacities of T_{FH} and T_{FR} cells during the germinal centre reaction. Whilst the ultimate function of CCR6 in T_{FR} cells remains elusive, this study demonstrated that it could facilitate chemotaxis *in vitro*, and it was not required for T_{FR} cell differentiation. Together with additional chemokine receptors identified here and a greater understanding of T_{FR} cell function arising from studies published during this work, multiple new lines of inquiry have been identified regarding the migratory events underpinning GCT cell development and function. This study also highlighted a requirement for careful choice of immunisation strategies and immunisation models when studying these chemokine/chemokine receptor axes given the differences in early migratory events governing germinal centre formation between the spleen, lymph nodes and mucosal lymphoid organs. Going forward, improved models to target gene-deficiency to T_{FR} cells are required to elucidate the function of T_{FR} cell-CCR6 expression during the germinal centre reaction. Given the recently described functions of T_{FR} cells in restricting the early outgrowth of autoreactive antibodies upon immunisation and ability to diversify gut microbiota, attention should be given to these measures in future work. Ultimately, these studies will add to the growing body of work understanding the functions of T_{FR} cells and how defects in their biology may underpin autoantibody-driven autoimmune diseases or dysbalanced gut microbiota and resulting pathogenic diseases.

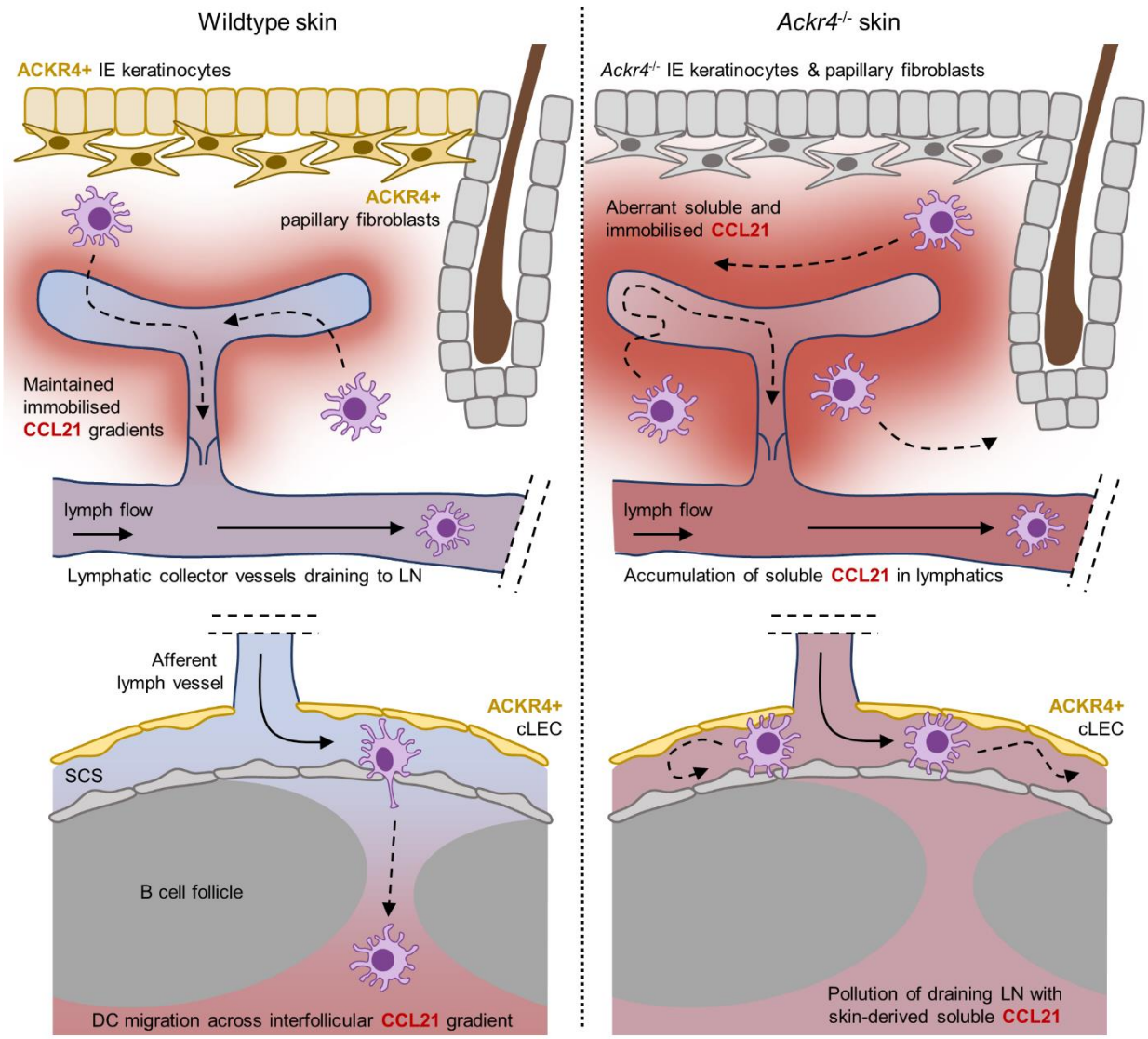

Figure 5.1: Functions of cutaneous ACKR4 expression

In wildtype skin (left), ACKR4 is largely expressed by IE keratinocytes and underlying papillary fibroblasts. Here, ACKR4 regulates immobilised CCL21 gradients and soluble CCL21 produced during the steady-state to facilitate optimal dendritic cell egress to draining lymph nodes. ACKR4 functions within cLECs lining the lymph node SCS to maintain immobilised CCL21 gradients in interfollicular areas which guide dendritic cells into the paracortex. In the absence of cutaneous ACKR4 (right), both soluble and immobilised CCL21 aberrantly accumulate. Resulting hyperabundant immobilised CCL21 gradients are unable to direct dendritic cell migration to lymphatic vessels, and soluble CCL21 leaches out of the skin via the lymphatics, potentially impairing luminal dendritic cell migration within lymphatic capillary vessels. Despite intact ACKR4 function within lymph node SCS cLECs, it is not sufficient to prevent upstream hyperabundant soluble CCL21 from polluting the lymph node. It remains to be determined whether cutaneous ACKR4-deficiency alone results in dendritic cell accumulation in the SCS and disrupted interfollicular immobilised CCL21 gradients as observed with *Ackr4*$^{-/-}$ mice.

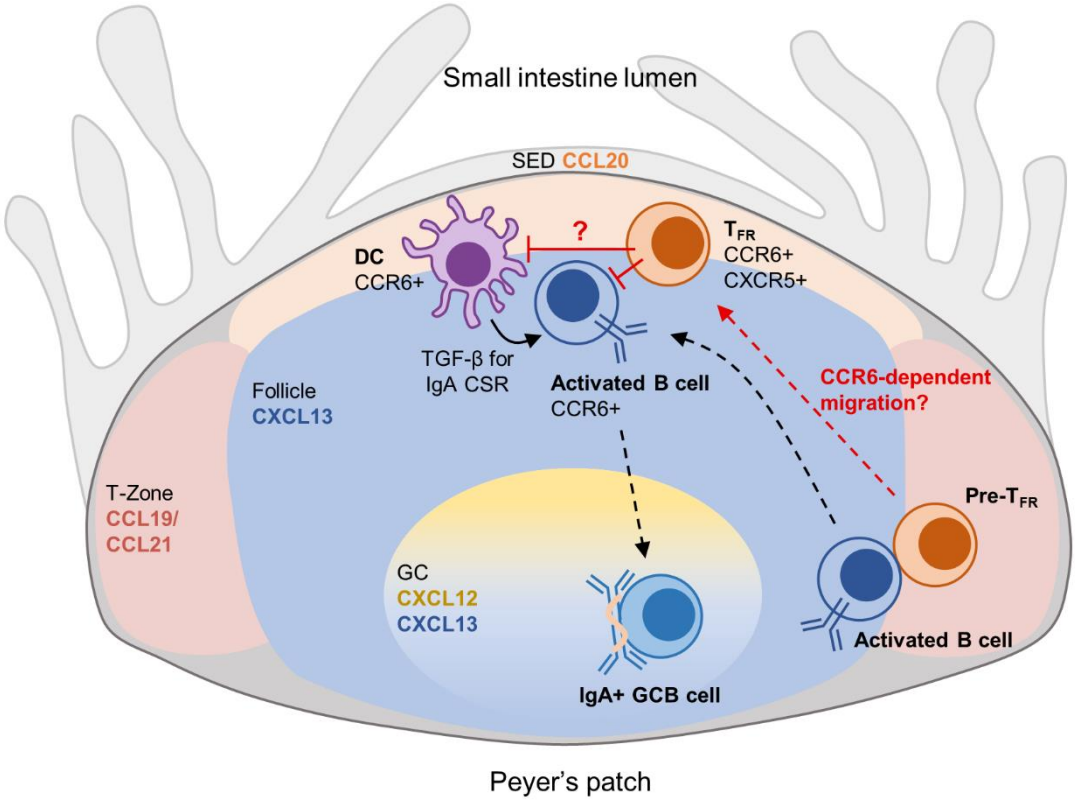

Figure 5.2: Hypothesised function of T_{FR} cell CCR6 expression in Peyer's patches

Within the Peyer's patches, CCL20 (orange) is expressed by epithelial cells lining the SED proximal to the intestinal lumen. At this site, CCL20 facilitates crucial interactions between $CCR6^+$ dendritic cells and activated B cells necessary for IgA CSR instructed by dendritic cell-derived TGF-β. In the gut, T_{FR} cells are crucial in diversifying IgA to promote a healthy microbiome and support gut regulatory T cell expansion. Therefore, CCR6 expression by T_{FR} cells may promote relocation to the SED and facilitate interactions with dendritic cells and/or activated B cells to promote or supress antibody responses.

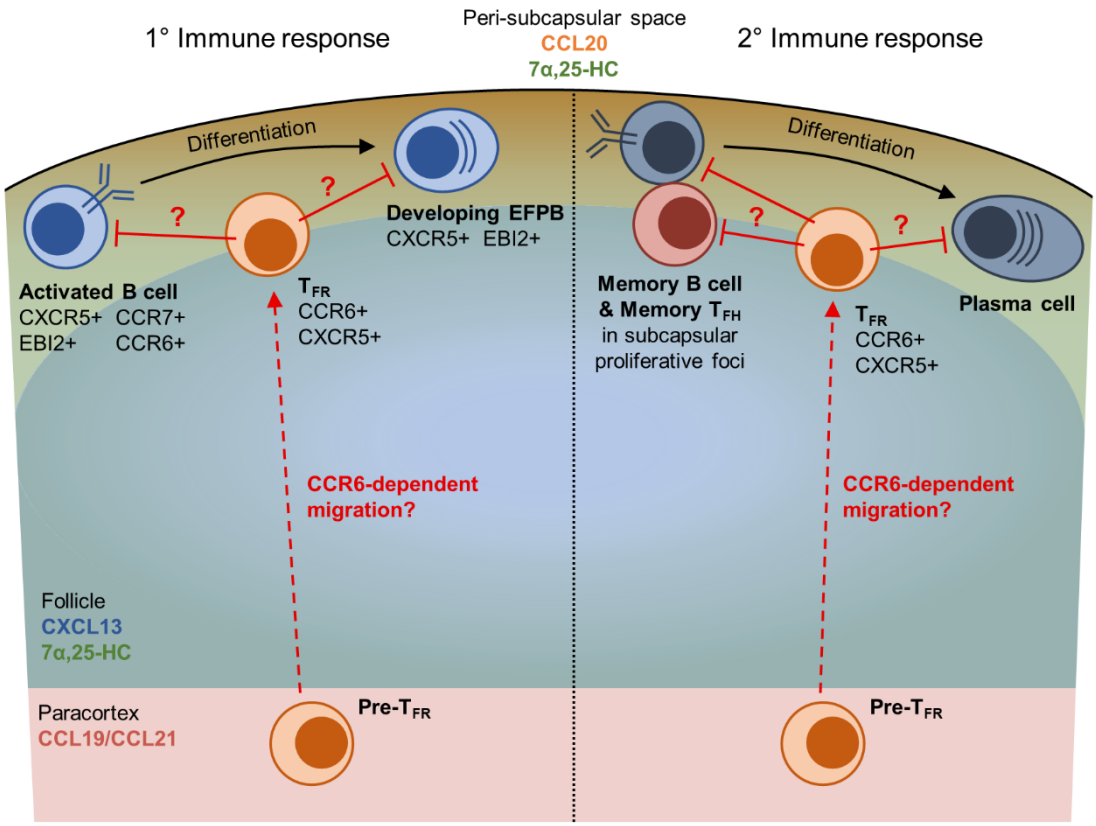

Figure 5.3: Hypothesised function of T_{FR} cell CCR6 expression in the lymph node

In the lymph node, CCL20 (orange) is expressed by epithelial cells lining the subcapsular sinus. Whether CCL20 at this location is important for antibody responses is unknown. However, B cell relocalisation to peri-subcapsular niches coincides with dynamic CCR6 expression during primary antibody responses (left), and memory B cell CCR6 expression is anticipated to facilitate their residence in subcapsular foci upon secondary activation (right). T_{FR} cells can restrict the emergence of autoantibodies, thus CCR6 expression may recruit T_{FR} cells to subcapsular niches to suppress autoreactive activated B cells or plasma cells. As the subcapsular niche is utilised for plasma cell differentiation during both primary and secondary antibody responses, T_{FR} cells may supress antibody responses during both of these phases.

Chapter 6
References

1. Murphy, P. M. *et al.* International Union of Pharmacology. XXII. Nomenclature for Chemokine Receptors. *Pharmacol. Rev.* **52**, 145–176 (2000).
2. Zlotnik, A. & Yoshie, O. Chemokines: A New Classification System and Their Role in Immunity. *Immunity* **12**, 121–127 (2000).
3. Salanga, C. L. & Handel, T. M. Chemokine Oligomerization and Interactions with Receptors and Glycosaminoglycans: The Role of Structural Dynamics in Function. *Exp. Cell Res.* **317**, 590–601 (2011).
4. Weber, M. *et al.* Interstitial Dendritic Cell Guidance by Haptotactic Chemokine Gradients. *Science* **339**, 328–332 (2013).
5. Patel, D. D. *et al.* Chemokines Have Diverse Abilities to Form Solid Phase Gradients. *Clin. Immunol.* **99**, 43–52 (2001).
6. de Paz, J. L. *et al.* Profiling Heparin–Chemokine Interactions Using Synthetic Tools. *ACS Chem. Biol.* **2**, 735–744 (2007).
7. Schumann, K. *et al.* Immobilized Chemokine Fields and Soluble Chemokine Gradients Cooperatively Shape Migration Patterns of Dendritic Cells. *Immunity* **32**, 703–713 (2010).
8. Hauser, M. A. *et al.* Distinct CCR7 glycosylation pattern shapes receptor signaling and endocytosis to modulate chemotactic responses. *J. Leukoc. Biol.* **99**, 993–1007 (2016).
9. Kiermaier, E. *et al.* Polysialylation controls dendritic cell trafficking by regulating chemokine recognition. *Science* **351**, 186–190 (2016).
10. Hughes, C. E. & Nibbs, R. J. B. A guide to chemokines and their receptors. *Febs J.* **285**, 2944–2971 (2018).
11. Lämmermann, T. & Sixt, M. Mechanical modes of 'amoeboid' cell migration. *Curr. Opin. Cell Biol.* **21**, 636–644 (2009).
12. Okada, T. & Cyster, J. G. CC Chemokine Receptor 7 Contributes to Gi-Dependent T Cell Motility in the Lymph Node. *J. Immunol.* **178**, 2973–2978 (2007).
13. Schwarz, J. *et al.* Dendritic Cells Interpret Haptotactic Chemokine Gradients in a Manner Governed by Signal-to-Noise Ratio and Dependent on GRK6. *Curr. Biol. CB* **27**, 1314–1325 (2017).
14. Bonecchi, R. & Graham, G. J. Atypical Chemokine Receptors and Their Roles in the Resolution of the Inflammatory Response. *Front. Immunol.* **7**, (2016).
15. Bachelerie, F. *et al.* International Union of Pharmacology. LXXXIX. Update on the Extended Family of Chemokine Receptors and Introducing a New Nomenclature for Atypical Chemokine Receptors. *Pharmacol. Rev.* **66**, 1–79 (2014).
16. Mercier, A. L. *et al.* GPR182 is an endothelium-specific atypical chemokine receptor that maintains hematopoietic stem cell homeostasis. *Proc. Natl. Acad. Sci.* **118**, (2021).
17. Lee, J. S. *et al.* The Duffy Antigen Modifies Systemic and Local Tissue Chemokine Responses following Lipopolysaccharide Stimulation. *J. Immunol.* **177**, 8086–8094 (2006).
18. Fra, A. M. *et al.* Cutting Edge: Scavenging of Inflammatory CC Chemokines by the Promiscuous Putatively Silent Chemokine Receptor D6. *J. Immunol.* **170**, 2279–2282 (2003).
19. Jamieson, T. *et al.* The chemokine receptor D6 limits the inflammatory response in vivo. *Nat. Immunol.* **6**, 403–411 (2005).

20. Torre, Y. M. de la *et al.* Increased inflammation in mice deficient for the chemokine decoy receptor D6. *Eur. J. Immunol.* **35**, 1342–1346 (2005).
21. Lee, J. S. *et al.* Duffy Antigen Facilitates Movement of Chemokine Across the Endothelium In Vitro and Promotes Neutrophil Transmigration In Vitro and In Vivo. *J. Immunol.* **170**, 5244–5251 (2003).
22. Pruenster, M. *et al.* The Duffy antigen receptor for chemokines transports chemokines and supports their promigratory activity. *Nat. Immunol.* **10**, 101–108 (2009).
23. McKimmie, C. S. *et al.* An analysis of the function and expression of D6 on lymphatic endothelial cells. *Blood* **121**, 3768–3777 (2013).
24. Lee, K. M. *et al.* The chemokine receptors ACKR2 and CCR2 reciprocally regulate lymphatic vessel density. *EMBO J.* **33**, 2564–2580 (2014).
25. Burns, J. M. *et al.* A novel chemokine receptor for SDF-1 and I-TAC involved in cell survival, cell adhesion, and tumor development. *J. Exp. Med.* **203**, 2201–2213 (2006).
26. Gosling, J. *et al.* Cutting Edge: Identification of a Novel Chemokine Receptor That Binds Dendritic Cell- and T Cell-Active Chemokines Including ELC, SLC, and TECK. *J. Immunol.* **164**, 2851–2856 (2000).
27. Townson, J. R. & Nibbs, R. J. B. Characterization of mouse CCX-CKR, a receptor for the lymphocyte-attracting chemokines TECK/mCCL25, SLC/mCCL21 and MIP-3β/mCCL19: comparison to human CCX-CKR. *Eur. J. Immunol.* **32**, 1230–1241 (2002).
28. Venkiteswaran, G. *et al.* Generation and Dynamics of an Endogenous, Self-Generated Signaling Gradient across a Migrating Tissue. *Cell* **155**, 674–687 (2013).
29. Levoye, A., Balabanian, K., Baleux, F., Bachelerie, F. & Lagane, B. CXCR7 heterodimerizes with CXCR4 and regulates CXCL12-mediated G protein signaling. *Blood* **113**, 6085–6093 (2009).
30. Schioppa, T. *et al.* Molecular Basis for CCRL2 Regulation of Leukocyte Migration. *Front. Cell Dev. Biol.* **8**, (2020).
31. Zabel, B. A. *et al.* Mast cell–expressed orphan receptor CCRL2 binds chemerin and is required for optimal induction of IgE-mediated passive cutaneous anaphylaxis. *J. Exp. Med.* **205**, 2207–2220 (2008).
32. Lorenz, N. *et al.* Plasmin and regulators of plasmin activity control the migratory capacity and adhesion of human T cells and dendritic cells by regulating cleavage of the chemokine CCL21. *Immunol. Cell Biol.* **94**, 955–963 (2016).
33. Hjortø, G. M. *et al.* Differential CCR7 Targeting in Dendritic Cells by Three Naturally Occurring CC-Chemokines. *Front. Immunol.* **7**, (2016).
34. Moussouras, N. A. *et al.* Structural Features of an Extended C-Terminal Tail Modulate the Function of the Chemokine CCL21. *Biochemistry* (2020) doi:10.1021/acs.biochem.0c00047.
35. Breitfeld, D. *et al.* Follicular B Helper T Cells Express Cxc Chemokine Receptor 5, Localize to B Cell Follicles, and Support Immunoglobulin Production. *J. Exp. Med.* **192**, 1545–1552 (2000).
36. Schaerli, P. *et al.* Cxc Chemokine Receptor 5 Expression Defines Follicular Homing T Cells with B Cell Helper Function. *J. Exp. Med.* **192**, 1553–1562 (2000).

37. Kim, C. H. *et al.* Subspecialization of Cxcr5+ T Cells: B Helper Activity Is Focused in a Germinal Center–Localized Subset of Cxcr5+ T Cells. *J. Exp. Med.* **193**, 1373–1382 (2001).
38. Johnston, R. J. *et al.* Bcl6 and Blimp-1 Are Reciprocal and Antagonistic Regulators of T Follicular Helper Cell Differentiation. *Science* **325**, 1006–1010 (2009).
39. Nurieva, R. I. *et al.* Bcl6 Mediates the Development of T Follicular Helper Cells. *Science* **325**, 1001–1005 (2009).
40. Yu, D. *et al.* The Transcriptional Repressor Bcl-6 Directs T Follicular Helper Cell Lineage Commitment. *Immunity* **31**, 457–468 (2009).
41. Liu, X. *et al.* Bcl6 expression specifies the T follicular helper cell program in vivo. *J. Exp. Med.* **209**, 1841–1852 (2012).
42. Chung, Y. *et al.* Follicular regulatory T cells expressing Foxp3 and Bcl-6 suppress germinal center reactions. *Nat. Med.* **17**, 983–988 (2011).
43. Linterman, M. A. *et al.* Foxp3 + follicular regulatory T cells control the germinal center response. *Nat. Med.* **17**, 975–982 (2011).
44. Wollenberg, I. *et al.* Regulation of the Germinal Center Reaction by Foxp3+ Follicular Regulatory T Cells. *J. Immunol.* **187**, 4553–4560 (2011).
45. Eisenbarth, S. C. Dendritic cell subsets in T cell programming: location dictates function. *Nat. Rev. Immunol.* **19**, 89–103 (2019).
46. Swiecki, M. & Colonna, M. The multifaceted biology of plasmacytoid dendritic cells. *Nat. Rev. Immunol.* **15**, 471–485 (2015).
47. Hadeiba, H. *et al.* Plasmacytoid Dendritic Cells Transport Peripheral Antigens to the Thymus to Promote Central Tolerance. *Immunity* **36**, 438–450 (2012).
48. Goubier, A. *et al.* Plasmacytoid Dendritic Cells Mediate Oral Tolerance. *Immunity* **29**, 464–475 (2008).
49. Kohli, K., Janssen, A. & Förster, R. Plasmacytoid dendritic cells induce tolerance predominantly by cargoing antigen to lymph nodes. *Eur. J. Immunol.* **46**, 2659–2668 (2016).
50. Coillard, A. & Segura, E. Antigen presentation by mouse monocyte-derived cells: Re-evaluating the concept of monocyte-derived dendritic cells. *Mol. Immunol.* **135**, 165–169 (2021).
51. Romani, N., Clausen, B. E. & Stoitzner, P. Langerhans cells and more: langerin-expressing dendritic cell subsets in the skin. *Immunol. Rev.* **234**, 120–141 (2010).
52. Satpathy, A. T., Wu, X., Albring, J. C. & Murphy, K. M. Re(de)fining the dendritic cell lineage. *Nat. Immunol.* **13**, 1145–1154 (2012).
53. Alloatti, A., Kotsias, F., Magalhaes, J. G. & Amigorena, S. Dendritic cell maturation and cross-presentation: timing matters! *Immunol. Rev.* **272**, 97–108 (2016).
54. Hawiger, D. *et al.* Dendritic Cells Induce Peripheral T Cell Unresponsiveness under Steady State Conditions in Vivo. *J. Exp. Med.* **194**, 769–780 (2001).
55. Ohl, L. *et al.* CCR7 Governs Skin Dendritic Cell Migration under Inflammatory and Steady-State Conditions. *Immunity* **21**, 279–288 (2004).
56. Bouchon, A., Hernández-Munain, C., Cella, M. & Colonna, M. A Dap12-Mediated Pathway Regulates Expression of Cc Chemokine Receptor 7 and Maturation of Human Dendritic Cells. *J. Exp. Med.* **194**, 1111–1122 (2001).

57. Watanabe, N. *et al.* Hassall's corpuscles instruct dendritic cells to induce CD4 + CD25 + regulatory T cells in human thymus. *Nature* **436**, 1181–1185 (2005).
58. Jiang, A. *et al.* Disruption of E-Cadherin-Mediated Adhesion Induces a Functionally Distinct Pathway of Dendritic Cell Maturation. *Immunity* **27**, 610–624 (2007).
59. Dieu, M.-C. *et al.* Selective Recruitment of Immature and Mature Dendritic Cells by Distinct Chemokines Expressed in Different Anatomic Sites. *J. Exp. Med.* **188**, 373–386 (1998).
60. Sallusto, F. *et al.* Rapid and coordinated switch in chemokine receptor expression during dendritic cell maturation. *Eur. J. Immunol.* **28**, 2760–2769 (1998).
61. Förster, R. *et al.* CCR7 Coordinates the Primary Immune Response by Establishing Functional Microenvironments in Secondary Lymphoid Organs. *Cell* **99**, 23–33 (1999).
62. Martín-Fontecha, A. *et al.* Regulation of Dendritic Cell Migration to the Draining Lymph Node Impact on T Lymphocyte Traffic and Priming. *J. Exp. Med.* **198**, 615–621 (2003).
63. Johansson-Lindbom, B. *et al.* Functional specialization of gut CD103+ dendritic cells in the regulation of tissue-selective T cell homing. *J. Exp. Med.* **202**, 1063–1073 (2005).
64. Worbs, T. *et al.* Oral tolerance originates in the intestinal immune system and relies on antigen carriage by dendritic cells. *J. Exp. Med.* **203**, 519–527 (2006).
65. Jang, M. H. *et al.* CCR7 Is Critically Important for Migration of Dendritic Cells in Intestinal Lamina Propria to Mesenteric Lymph Nodes. *J. Immunol.* **176**, 803–810 (2006).
66. Hintzen, G. *et al.* Induction of Tolerance to Innocuous Inhaled Antigen Relies on a CCR7-Dependent Dendritic Cell-Mediated Antigen Transport to the Bronchial Lymph Node. *J. Immunol.* **177**, 7346–7354 (2006).
67. Yanagihara, S., Komura, E., Nagafune, J., Watarai, H. & Yamaguchi, Y. EBI1/CCR7 Is a New Member of Dendritic Cell Chemokine Receptor That Is Up-Regulated upon Maturation. *J. Immunol.* **161**, 3096–3102 (1998).
68. Kriehuber, E. *et al.* Isolation and Characterization of Dermal Lymphatic and Blood Endothelial Cells Reveal Stable and Functionally Specialized Cell Lineages. *J. Exp. Med.* **194**, 797–808 (2001).
69. Gunn, M. D. *et al.* A chemokine expressed in lymphoid high endothelial venules promotes the adhesion and chemotaxis of naive T lymphocytes. *Proc. Natl. Acad. Sci.* **95**, 258–263 (1998).
70. Hirose, J. *et al.* Chondroitin sulfate B exerts its inhibitory effect on secondary lymphoid tissue chemokine (SLC) by binding to the C-terminus of SLC. *Biochim. Biophys. Acta BBA - Gen. Subj.* **1571**, 219–224 (2002).
71. Chen, S.-C. *et al.* Ectopic Expression of the Murine Chemokines CCL21a and CCL21b Induces the Formation of Lymph Node-Like Structures in Pancreas, But Not Skin, of Transgenic Mice. *J. Immunol.* **168**, 1001–1008 (2002).
72. Baluk, P. *et al.* Functionally specialized junctions between endothelial cells of lymphatic vessels. *J. Exp. Med.* **204**, 2349–2362 (2007).
73. Pflicke, H. & Sixt, M. Preformed portals facilitate dendritic cell entry into afferent lymphatic vessels. *J. Exp. Med.* **206**, 2925–2935 (2009).

74. Tal, O. *et al.* DC mobilization from the skin requires docking to immobilized CCL21 on lymphatic endothelium and intralymphatic crawling. *J. Exp. Med.* **208**, 2141–2153 (2011).
75. Vaahtomeri, K. *et al.* Locally Triggered Release of the Chemokine CCL21 Promotes Dendritic Cell Transmigration across Lymphatic Endothelia. *Cell Rep.* **19**, 902–909 (2017).
76. Russo, E. *et al.* Intralymphatic CCL21 Promotes Tissue Egress of Dendritic Cells through Afferent Lymphatic Vessels. *Cell Rep.* **14**, 1723–1734 (2016).
77. Nitschké, M. *et al.* Differential requirement for ROCK in dendritic cell migration within lymphatic capillaries in steady-state and inflammation. *Blood* **120**, 2249–2258 (2012).
78. Martens, R. *et al.* Efficient homing of T cells via afferent lymphatics requires mechanical arrest and integrin-supported chemokine guidance. *Nat. Commun.* **11**, 1–16 (2020).
79. Braun, A. *et al.* Afferent lymph–derived T cells and DCs use different chemokine receptor CCR7–dependent routes for entry into the lymph node and intranodal migration. *Nat. Immunol.* **12**, 879–887 (2011).
80. Ulvmar, M. H. *et al.* The atypical chemokine receptor CCRL1 shapes functional CCL21 gradients in lymph nodes. *Nat. Immunol.* **15**, 623–630 (2014).
81. Kabashima, K. *et al.* CXCL12-CXCR4 Engagement Is Required for Migration of Cutaneous Dendritic Cells. *Am. J. Pathol.* **171**, 1249–1257 (2007).
82. Ouwehand, K. *et al.* CXCL12 is essential for migration of activated Langerhans cells from epidermis to dermis. *Eur. J. Immunol.* **38**, 3050–3059 (2008).
83. Johnson, L. A. & Jackson, D. G. The chemokine CX3CL1 promotes trafficking of dendritic cells through inflamed lymphatics. *J. Cell Sci.* **126**, 5259–5270 (2013).
84. Sokol, C. L., Camire, R. B., Jones, M. C. & Luster, A. D. The Chemokine Receptor CCR8 Promotes the Migration of Dendritic Cells into the Lymph Node Parenchyma to Initiate the Allergic Immune Response. *Immunity* **49**, 449-463.e6 (2018).
85. Stutte, S. *et al.* Requirement of CCL17 for CCR7- and CXCR4-dependent migration of cutaneous dendritic cells. *Proc. Natl. Acad. Sci.* **107**, 8736–8741 (2010).
86. Yoshida, R. *et al.* Molecular Cloning of a Novel Human CC Chemokine EBI1-ligand Chemokine That Is a Specific Functional Ligand for EBI1, CCR7. *J. Biol. Chem.* **272**, 13803–13809 (1997).
87. Luther, S. A., Tang, H. L., Hyman, P. L., Farr, A. G. & Cyster, J. G. Coexpression of the chemokines ELC and SLC by T zone stromal cells and deletion of the ELC gene in the plt/plt mouse. *Proc. Natl. Acad. Sci.* **97**, 12694–12699 (2000).
88. Chai, Q. *et al.* Maturation of Lymph Node Fibroblastic Reticular Cells from Myofibroblastic Precursors Is Critical for Antiviral Immunity. *Immunity* **38**, 1013–1024 (2013).
89. Cremasco, V. *et al.* B cell homeostasis and follicle confines are governed by fibroblastic reticular cells. *Nat. Immunol.* **15**, 973–981 (2014).
90. Hedrick, J. A. & Zlotnik, A. Identification and characterization of a novel beta chemokine containing six conserved cysteines. *J. Immunol.* **159**, 1589–1593 (1997).
91. Tanabe, S. *et al.* Identification of a new mouse beta-chemokine, thymus-derived chemotactic agent 4, with activity on T lymphocytes and mesangial cells. *J. Immunol.* **159**, 5671–5679 (1997).

92. Nagira, M. *et al.* Molecular Cloning of a Novel Human CC Chemokine Secondary Lymphoid-Tissue Chemokine That Is a Potent Chemoattractant for Lymphocytes and Mapped to Chromosome 9p13*. *J. Biol. Chem.* **272**, 19518–19524 (1997).
93. Vassileva, G. *et al.* The Reduced Expression of 6ckine in the plt Mouse Results from the Deletion of One of Two 6ckine Genes. *J. Exp. Med.* **190**, 1183–1188 (1999).
94. Nakano, H. & Gunn, M. D. Gene Duplications at the Chemokine Locus on Mouse Chromosome 4: Multiple Strain-Specific Haplotypes and the Deletion of Secondary Lymphoid-Organ Chemokine and EBI-1 Ligand Chemokine Genes in the plt Mutation. *J. Immunol.* **166**, 361–369 (2001).
95. Lo, J. C. *et al.* Differential regulation of CCL21 in lymphoid/nonlymphoid tissues for effectively attracting T cells to peripheral tissues. *J. Clin. Invest.* **112**, 1495–1505 (2003).
96. Cheng, H.-W. *et al.* CCL19-producing fibroblastic stromal cells restrain lung carcinoma growth by promoting local antitumor T-cell responses. *J. Allergy Clin. Immunol.* **142**, 1257-1271.e4 (2018).
97. Ngo, V. N., Lucy Tang, H. & Cyster, J. G. Epstein-Barr Virus–induced Molecule 1 Ligand Chemokine Is Expressed by Dendritic Cells in Lymphoid Tissues and Strongly Attracts Naive T Cells and Activated B Cells. *J. Exp. Med.* **188**, 181–191 (1998).
98. Piqueras, B., Connolly, J., Freitas, H., Palucka, A. K. & Banchereau, J. Upon viral exposure, myeloid and plasmacytoid dendritic cells produce 3 waves of distinct chemokines to recruit immune effectors. *Blood* **107**, 2613–2618 (2006).
99. Rangel-Moreno, J., Moyron-Quiroz, J. E., Hartson, L., Kusser, K. & Randall, T. D. Pulmonary expression of CXC chemokine ligand 13, CC chemokine ligand 19, and CC chemokine ligand 21 is essential for local immunity to influenza. *Proc. Natl. Acad. Sci.* **104**, 10577–10582 (2007).
100. Bryce, S. A. *et al.* ACKR4 on Stromal Cells Scavenges CCL19 To Enable CCR7-Dependent Trafficking of APCs from Inflamed Skin to Lymph Nodes. *J. Immunol.* **196**, 3341–3353 (2016).
101. Fleige, H. *et al.* Manifold Roles of CCR7 and Its Ligands in the Induction and Maintenance of Bronchus-Associated Lymphoid Tissue. *Cell Rep.* **23**, 783–795 (2018).
102. Comerford, I. *et al.* The atypical chemokine receptor CCX-CKR scavenges homeostatic chemokines in circulation and tissues and suppresses Th17 responses. *Blood* **116**, 4130–4140 (2010).
103. Bunting, M. D. *et al.* CCX-CKR deficiency alters thymic stroma impairing thymocyte development and promoting autoimmunity. *Blood* **121**, 118–128 (2013).
104. Ricart, B. G., John, B., Lee, D., Hunter, C. A. & Hammer, D. A. Dendritic Cells Distinguish Individual Chemokine Signals through CCR7 and CXCR4. *J. Immunol.* **186**, 53–61 (2011).
105. Zidar, D. A., Violin, J. D., Whalen, E. J. & Lefkowitz, R. J. Selective engagement of G protein coupled receptor kinases (GRKs) encodes distinct functions of biased ligands. *Proc. Natl. Acad. Sci.* **106**, 9649–9654 (2009).
106. Kohout, T. A. *et al.* Differential Desensitization, Receptor Phosphorylation, β-Arrestin Recruitment, and ERK1/2 Activation by the Two Endogenous Ligands for the CC Chemokine Receptor 7*. *J. Biol. Chem.* **279**, 23214–23222 (2004).

107. Britschgi, M. R., Favre, S. & Luther, S. A. CCL21 is sufficient to mediate DC migration, maturation and function in the absence of CCL19. *Eur. J. Immunol.* **40**, 1266–1271 (2010).
108. Bax, M., Vliet, S. J. van, Litjens, M., García-Vallejo, J. J. & Kooyk, Y. van. Interaction of Polysialic Acid with CCL21 Regulates the Migratory Capacity of Human Dendritic Cells. *PLOS ONE* **4**, e6987 (2009).
109. Britschgi, M. R., Link, A., Lissandrin, T. K. A. & Luther, S. A. Dynamic Modulation of CCR7 Expression and Function on Naive T Lymphocytes In Vivo. *J. Immunol.* **181**, 7681–7688 (2008).
110. Matti, C. *et al.* CCL20 is a novel ligand for the scavenging atypical chemokine receptor 4. *J. Leukoc. Biol.* **107**, 1137–1154 (2020).
111. Meyrath, M., Reynders, N., Uchański, T., Chevigné, A. & Szpakowska, M. Systematic reassessment of chemokine-receptor pairings confirms CCL20 but not CXCL13 and extends the spectrum of ACKR4 agonists to CCL22. *J. Leukoc. Biol.* **109**, 373–376 (2021).
112. Heinzel, K., Benz, C. & Bleul, C. C. A silent chemokine receptor regulates steady-state leukocyte homing in vivo. *Proc. Natl. Acad. Sci.* **104**, 8421–8426 (2007).
113. Watts, A. O. *et al.* β-Arrestin Recruitment and G Protein Signaling by the Atypical Human Chemokine Decoy Receptor CCX-CKR*. *J. Biol. Chem.* **288**, 7169–7181 (2013).
114. Matti, C. *et al.* ACKR4 Recruits GRK3 Prior to β-Arrestins but Can Scavenge Chemokines in the Absence of β-Arrestins. *Front. Immunol.* **11**, (2020).
115. Comerford, I., Milasta, S., Morrow, V., Milligan, G. & Nibbs, R. The chemokine receptor CCX-CKR mediates effective scavenging of CCL19 in vitro. *Eur. J. Immunol.* **36**, 1904–1916 (2006).
116. Purvanov, V., Matti, C., Samson, G. P. B., Kindinger, I. & Legler, D. F. Fluorescently Tagged CCL19 and CCL21 to Monitor CCR7 and ACKR4 Functions. *Int. J. Mol. Sci.* **19**, (2018).
117. Lucas, B. *et al.* CCRL1/ACKR4 is expressed in key thymic microenvironments but is dispensable for T lymphopoiesis at steady state in adult mice. *Eur. J. Immunol.* **45**, 574–583 (2015).
118. Thomson, C. A. *et al.* Expression of the Atypical Chemokine Receptor ACKR4 Identifies a Novel Population of Intestinal Submucosal Fibroblasts That Preferentially Expresses Endothelial Cell Regulators. *J. Immunol.* **201**, 215–229 (2018).
119. Shi, W. *et al.* Transcriptional profiling of mouse B cell terminal differentiation defines a signature for antibody-secreting plasma cells. *Nat. Immunol.* **16**, 663–673 (2015).
120. Kara, E. E. *et al.* Atypical chemokine receptor 4 shapes activated B cell fate. *J. Exp. Med.* **215**, 801–813 (2018).
121. Kealy, L. *et al.* The Histone Methyltransferase DOT1L Is Essential for Humoral Immune Responses. *Cell Rep.* **33**, 108504 (2020).
122. Whyte, C. E. *et al.* ACKR4 restrains antitumor immunity by regulating CCL21. *J. Exp. Med.* **217**, (2020).

123. Zhang, M. *et al.* Inhibition of fibroblast IL-6 production by ACKR4 deletion alleviates cardiac remodeling after myocardial infarction. *Biochem. Biophys. Res. Commun.* **547**, 139–147 (2021).
124. Mintz, M. A. & Cyster, J. G. T follicular helper cells in germinal center B cell selection and lymphomagenesis. *Immunol. Rev.* **296**, 48–61 (2020).
125. Deng, J., Wei, Y., Fonseca, V. R., Graca, L. & Yu, D. T follicular helper cells and T follicular regulatory cells in rheumatic diseases. *Nat. Rev. Rheumatol.* **15**, 475–490 (2019).
126. Claman, H. N., Chaperon, E. A. & Triplett, R. F. Thymus-Marrow Cell Combinations. Synergism in Antibody Production. *Proc. Soc. Exp. Biol. Med.* **122**, 1167–1171 (1966).
127. Miller, J. F. A. P. & Mitchell, G. F. CELL TO CELL INTERACTION IN THE IMMUNE RESPONSE : I. HEMOLYSIN-FORMING CELLS IN NEONATALLY THYMECTOMIZED MICE RECONSTITUTED WITH THYMUS OR THORACIC DUCT LYMPHOCYTES. *J. Exp. Med.* **128**, 801–820 (1968).
128. Kusam, S., Toney, L. M., Sato, H. & Dent, A. L. Inhibition of Th2 Differentiation and GATA-3 Expression by BCL-6. *J. Immunol.* **170**, 2435–2441 (2003).
129. Baumjohann, D. *et al.* Persistent Antigen and Germinal Center B Cells Sustain T Follicular Helper Cell Responses and Phenotype. *Immunity* **38**, 596–605 (2013).
130. Fazilleau, N., McHeyzer-Williams, L. J., Rosen, H. & McHeyzer-Williams, M. G. The function of follicular helper T cells is regulated by the strength of T cell antigen receptor binding. *Nat. Immunol.* **10**, 375–384 (2009).
131. Song, W. & Craft, J. T follicular helper cell heterogeneity: Time, space, and function. *Immunol. Rev.* **288**, 85–96 (2019).
132. Kerfoot, S. M. *et al.* Germinal Center B Cell and T Follicular Helper Cell Development Initiates in the Interfollicular Zone. *Immunity* **34**, 947–960 (2011).
133. Choi, Y. S. *et al.* ICOS Receptor Instructs T Follicular Helper Cell versus Effector Cell Differentiation via Induction of the Transcriptional Repressor Bcl6. *Immunity* **34**, 932–946 (2011).
134. Kitano, M. *et al.* Bcl6 Protein Expression Shapes Pre-Germinal Center B Cell Dynamics and Follicular Helper T Cell Heterogeneity. *Immunity* **34**, 961–972 (2011).
135. Qi, H., Cannons, J. L., Klauschen, F., Schwartzberg, P. L. & Germain, R. N. SAP-controlled T–B cell interactions underlie germinal centre formation. *Nature* **455**, 764–769 (2008).
136. Cannons, J. L. *et al.* Optimal Germinal Center Responses Require a Multistage T Cell:B Cell Adhesion Process Involving Integrins, SLAM-Associated Protein, and CD84. *Immunity* **32**, 253–265 (2010).
137. Yusuf, I. *et al.* Germinal Center T Follicular Helper Cell IL-4 Production Is Dependent on Signaling Lymphocytic Activation Molecule Receptor (CD150). *J. Immunol.* **185**, 190–202 (2010).
138. Bauquet, A. T. *et al.* The costimulatory molecule ICOS regulates the expression of c-Maf and IL-21 in the development of follicular T helper cells and TH-17 cells. *Nat. Immunol.* **10**, 167–175 (2009).

139. Gigoux, M. *et al.* Inducible costimulator promotes helper T-cell differentiation through phosphoinositide 3-kinase. *Proc. Natl. Acad. Sci.* **106**, 20371–20376 (2009).
140. Rolf, J. *et al.* Phosphoinositide 3-Kinase Activity in T Cells Regulates the Magnitude of the Germinal Center Reaction. *J. Immunol.* **185**, 4042–4052 (2010).
141. Reinhardt, R. L., Liang, H.-E. & Locksley, R. M. Cytokine-secreting follicular T cells shape the antibody repertoire. *Nat. Immunol.* **10**, 385–393 (2009).
142. Lüthje, K. *et al.* The development and fate of follicular helper T cells defined by an IL-21 reporter mouse. *Nat. Immunol.* **13**, 491–498 (2012).
143. King, I. L. & Mohrs, M. IL-4–producing CD4+ T cells in reactive lymph nodes during helminth infection are T follicular helper cells. *J. Exp. Med.* **206**, 1001–1007 (2009).
144. Zaretsky, A. G. *et al.* T follicular helper cells differentiate from Th2 cells in response to helminth antigens. *J. Exp. Med.* **206**, 991–999 (2009).
145. Hsu, H.-C. *et al.* Interleukin 17–producing T helper cells and interleukin 17 orchestrate autoreactive germinal center development in autoimmune BXD2 mice. *Nat. Immunol.* **9**, 166–175 (2008).
146. McCoy, K. D. *et al.* Polyclonal and Specific Antibodies Mediate Protective Immunity against Enteric Helminth Infection. *Cell Host Microbe* **4**, 362–373 (2008).
147. Di Noia, J. M. & Neuberger, M. S. Molecular Mechanisms of Antibody Somatic Hypermutation. *Annu. Rev. Biochem.* **76**, 1–22 (2007).
148. Klein, U. & Dalla-Favera, R. Germinal centres: role in B-cell physiology and malignancy. *Nat. Rev. Immunol.* **8**, 22–33 (2008).
149. Shlomchik, M. *et al.* Anti-DNA antibodies from autoimmune mice arise by clonal expansion and somatic mutation. *J. Exp. Med.* **171**, 265–292 (1990).
150. Ray, S. K., Putterman, C. & Diamond, B. Pathogenic autoantibodies are routinely generated during the response to foreign antigen: a paradigm for autoimmune disease. *Proc. Natl. Acad. Sci.* **93**, 2019–2024 (1996).
151. Nussenzweig, A. & Nussenzweig, M. C. Origin of Chromosomal Translocations in Lymphoid Cancer. *Cell* **141**, 27–38 (2010).
152. Shaffer, A. L. *et al.* BCL-6 Represses Genes that Function in Lymphocyte Differentiation, Inflammation, and Cell Cycle Control. *Immunity* **13**, 199–212 (2000).
153. Phan, R. T. & Dalla-Favera, R. The BCL6 proto-oncogene suppresses p53 expression in germinal-centre B cells. *Nature* **432**, 635–639 (2004).
154. Good, K. L., Bryant, V. L. & Tangye, S. G. Kinetics of Human B Cell Behavior and Amplification of Proliferative Responses following Stimulation with IL-21. *J. Immunol.* **177**, 5236–5247 (2006).
155. Saito, M. *et al.* BCL6 suppression of BCL2 via Miz1 and its disruption in diffuse large B cell lymphoma. *Proc. Natl. Acad. Sci.* **106**, 11294–11299 (2009).
156. Arguni, E. *et al.* JunD/AP-1 and STAT3 are the major enhancer molecules for high Bcl6 expression in germinal center B cells. *Int. Immunol.* **18**, 1079–1089 (2006).
157. Ranuncolo, S. M. *et al.* Bcl-6 mediates the germinal center B cell phenotype and lymphomagenesis through transcriptional repression of the DNA-damage sensor ATR. *Nat. Immunol.* **8**, 705–714 (2007).

158. Ci, W. *et al.* The BCL6 transcriptional program features repression of multiple oncogenes in primary B cells and is deregulated in DLBCL. *Blood* **113**, 5536–5548 (2009).
159. Zotos, D. *et al.* IL-21 regulates germinal center B cell differentiation and proliferation through a B cell–intrinsic mechanism. *J. Exp. Med.* **207**, 365–378 (2010).
160. Linterman, M. A. *et al.* IL-21 acts directly on B cells to regulate Bcl-6 expression and germinal center responses. *J. Exp. Med.* **207**, 353–363 (2010).
161. Takahashi, Y. *et al.* Relaxed Negative Selection in Germinal Centers and Impaired Affinity Maturation in bcl-xL Transgenic Mice. *J. Exp. Med.* **190**, 399–410 (1999).
162. Kusam, S., Vasanwala, F. H. & Dent, A. L. Transcriptional repressor BCL-6 immortalizes germinal center-like B cells in the absence of p53 function. *Oncogene* **23**, 839–844 (2004).
163. Victora, G. D. *et al.* Germinal Center Dynamics Revealed by Multiphoton Microscopy with a Photoactivatable Fluorescent Reporter. *Cell* **143**, 592–605 (2010).
164. Kawamoto, S. *et al.* Foxp3+ T Cells Regulate Immunoglobulin A Selection and Facilitate Diversification of Bacterial Species Responsible for Immune Homeostasis. *Immunity* **41**, 152–165 (2014).
165. Shi, J. *et al.* PD-1 Controls Follicular T Helper Cell Positioning and Function. *Immunity* **49**, 264-274.e4 (2018).
166. Sheikh, A. A. *et al.* Context-Dependent Role for T-bet in T Follicular Helper Differentiation and Germinal Center Function following Viral Infection. *Cell Rep.* **28**, 1758-1772.e4 (2019).
167. Arpin, C. *et al.* Generation of memory B cells and plasma cells in vitro. *Science* **268**, 720–722 (1995).
168. Kwon, H. *et al.* Analysis of Interleukin-21-Induced Prdm1 Gene Regulation Reveals Functional Cooperation of STAT3 and IRF4 Transcription Factors. *Immunity* **31**, 941–952 (2009).
169. Jourdan, M. *et al.* An in vitro model of differentiation of memory B cells into plasmablasts and plasma cells including detailed phenotypic and molecular characterization. *Blood* **114**, 5173–5181 (2009).
170. Wang, Y. *et al.* Germinal-center development of memory B cells driven by IL-9 from follicular helper T cells. *Nat. Immunol.* **18**, 921–930 (2017).
171. Rodda, L. B. *et al.* Single-Cell RNA Sequencing of Lymph Node Stromal Cells Reveals Niche-Associated Heterogeneity. *Immunity* **48**, 1014-1028.e6 (2018).
172. Reif, K. *et al.* Balanced responsiveness to chemoattractants from adjacent zones determines B-cell position. *Nature* **416**, 94–99 (2002).
173. Okada, T. *et al.* Antigen-Engaged B Cells Undergo Chemotaxis toward the T Zone and Form Motile Conjugates with Helper T Cells. *PLOS Biol.* **3**, e150 (2005).
174. Pereira, J. P., Kelly, L. M., Xu, Y. & Cyster, J. G. EBI2 mediates B cell segregation between the outer and centre follicle. *Nature* **460**, 1122–1126 (2009).
175. Gatto, D., Wood, K. & Brink, R. EBI2 Operates Independently of but in Cooperation with CXCR5 and CCR7 To Direct B Cell Migration and Organization in Follicles and the Germinal Center. *J. Immunol.* **187**, 4621–4628 (2011).

176. Kelly, L. M., Pereira, J. P., Yi, T., Xu, Y. & Cyster, J. G. EBI2 Guides Serial Movements of Activated B Cells and Ligand Activity Is Detectable in Lymphoid and Nonlymphoid Tissues. *J. Immunol.* **187**, 3026–3032 (2011).
177. Liu, C. *et al.* Oxysterols direct B-cell migration through EBI2. *Nature* **475**, 519–523 (2011).
178. Hannedouche, S. *et al.* Oxysterols direct immune cell migration via EBI2. *Nature* **475**, 524–527 (2011).
179. Yi, T. *et al.* Oxysterol Gradient Generation by Lymphoid Stromal Cells Guides Activated B Cell Movement during Humoral Responses. *Immunity* **37**, 535–548 (2012).
180. Schwickert, T. A. *et al.* A dynamic T cell–limited checkpoint regulates affinity-dependent B cell entry into the germinal center. *J. Exp. Med.* **208**, 1243–1252 (2011).
181. Taylor, J. J., Pape, K. A. & Jenkins, M. K. A germinal center–independent pathway generates unswitched memory B cells early in the primary response. *J. Exp. Med.* **209**, 597–606 (2012).
182. Wiede, F. *et al.* CCR6 is transiently upregulated on B cells after activation and modulates the germinal center reaction in the mouse. *Immunol. Cell Biol.* **91**, 335–339 (2013).
183. Reimer, D. *et al.* Early CCR6 expression on B cells modulates germinal centre kinetics and efficient antibody responses. *Immunol. Cell Biol.* **95**, 33–41 (2017).
184. Reboldi, A. *et al.* IgA production requires B cell interaction with subepithelial dendritic cells in Peyer's patches. *Science* **352**, (2016).
185. Hardtke, S., Ohl, L. & Förster, R. Balanced expression of CXCR5 and CCR7 on follicular T helper cells determines their transient positioning to lymph node follicles and is essential for efficient B-cell help. *Blood* **106**, 1924–1931 (2005).
186. Haynes, N. M. *et al.* Role of CXCR5 and CCR7 in Follicular Th Cell Positioning and Appearance of a Programmed Cell Death Gene-1High Germinal Center-Associated Subpopulation. *J. Immunol.* **179**, 5099–5108 (2007).
187. Suan, D. *et al.* T Follicular Helper Cells Have Distinct Modes of Migration and Molecular Signatures in Naive and Memory Immune Responses. *Immunity* **42**, 704–718 (2015).
188. Poholek, A. C. *et al.* In Vivo Regulation of Bcl6 and T Follicular Helper Cell Development. *J. Immunol.* **185**, 313–326 (2010).
189. Veerman, K. M. *et al.* Interaction of the selectin ligand PSGL-1 with chemokines CCL21 and CCL19 facilitates efficient homing of T cells to secondary lymphoid organs. *Nat. Immunol.* **8**, 532–539 (2007).
190. Baumjohann, D., Okada, T. & Ansel, K. M. Cutting Edge: Distinct Waves of BCL6 Expression during T Follicular Helper Cell Development. *J. Immunol.* **187**, 2089–2092 (2011).
191. Coffey, F., Alabyev, B. & Manser, T. Initial Clonal Expansion of Germinal Center B Cells Takes Place at the Perimeter of Follicles. *Immunity* **30**, 599–609 (2009).
192. Chan, T. D. *et al.* Antigen Affinity Controls Rapid T-Dependent Antibody Production by Driving the Expansion Rather than the Differentiation or Extrafollicular Migration of Early Plasmablasts. *J. Immunol.* **183**, 3139–3149 (2009).

193. Roco, J. A. *et al.* Class-Switch Recombination Occurs Infrequently in Germinal Centers. *Immunity* **51**, 337-350.e7 (2019).
194. Blink, E. J. *et al.* Early appearance of germinal center–derived memory B cells and plasma cells in blood after primary immunization. *J. Exp. Med.* **201**, 545–554 (2005).
195. Tangye, S. G. & Tarlinton, D. M. Memory B cells: Effectors of long-lived immune responses. *Eur. J. Immunol.* **39**, 2065–2075 (2009).
196. MacLennan, I. C. M. *et al.* Extrafollicular antibody responses. *Immunol. Rev.* **194**, 8–18 (2003).
197. Hargreaves, D. C. *et al.* A Coordinated Change in Chemokine Responsiveness Guides Plasma Cell Movements. *J. Exp. Med.* **194**, 45–56 (2001).
198. Gatto, D., Paus, D., Basten, A., Mackay, C. R. & Brink, R. Guidance of B Cells by the Orphan G Protein-Coupled Receptor EBI2 Shapes Humoral Immune Responses. *Immunity* **31**, 259–269 (2009).
199. Allen, C. D. C. *et al.* Germinal center dark and light zone organization is mediated by CXCR4 and CXCR5. *Nat. Immunol.* **5**, 943–952 (2004).
200. Green, J. A. *et al.* The sphingosine 1-phosphate receptor S1P2 maintains the homeostasis of germinal center B cells and promotes niche confinement. *Nat. Immunol.* **12**, 672–680 (2011).
201. Muppidi, J. R. *et al.* Loss of signalling via Gα13 in germinal centre B-cell-derived lymphoma. *Nature* **516**, 254–258 (2014).
202. Muppidi, J. R., Lu, E. & Cyster, J. G. The G protein–coupled receptor P2RY8 and follicular dendritic cells promote germinal center confinement of B cells, whereas S1PR3 can contribute to their dissemination. *J. Exp. Med.* **212**, 2213–2222 (2015).
203. Lu, E., Wolfreys, F. D., Muppidi, J. R., Xu, Y. & Cyster, J. G. S-Geranylgeranyl-l-glutathione is a ligand for human B cell-confinement receptor P2RY8. *Nature* **567**, 244–248 (2019).
204. Lu, E. & Cyster, J. G. G-protein coupled receptors and ligands that organize humoral immune responses. *Immunol. Rev.* **289**, 158–172 (2019).
205. Bannard, O. *et al.* Germinal Center Centroblasts Transition to a Centrocyte Phenotype According to a Timed Program and Depend on the Dark Zone for Effective Selection. *Immunity* **39**, 912–924 (2013).
206. Moriyama, S. *et al.* Sphingosine-1-phosphate receptor 2 is critical for follicular helper T cell retention in germinal centers. *J. Exp. Med.* **211**, 1297–1305 (2014).
207. Kroenke, M. A. *et al.* Bcl6 and Maf Cooperate To Instruct Human Follicular Helper CD4 T Cell Differentiation. *J. Immunol.* **188**, 3734–3744 (2012).
208. Elsner, R. A., Ernst, D. N. & Baumgarth, N. Single and Coexpression of CXCR4 and CXCR5 Identifies CD4 T Helper Cells in Distinct Lymph Node Niches during Influenza Virus Infection. *J. Virol.* **86**, 7146–7157 (2012).
209. Kabashima, K. *et al.* Plasma cell S1P1 expression determines secondary lymphoid organ retention versus bone marrow tropism. *J. Exp. Med.* **203**, 2683–2690 (2006).
210. Gohda, M. *et al.* Sphingosine 1-Phosphate Regulates the Egress of IgA Plasmablasts from Peyer's Patches for Intestinal IgA Responses. *J. Immunol.* **180**, 5335–5343 (2008).
211. Kunkel, E. J. *et al.* Lymphocyte Cc Chemokine Receptor 9 and Epithelial Thymus-Expressed Chemokine (Teck) Expression Distinguish the Small Intestinal Immune

CompartmentEpithelial Expression of Tissue-Specific Chemokines as an Organizing Principle in Regional Immunity. *J. Exp. Med.* **192**, 761–768 (2000).
212. Kunkel, E. J. & Butcher, E. C. Plasma-cell homing. *Nat. Rev. Immunol.* **3**, 822–829 (2003).
213. Suan, D. *et al.* CCR6 Defines Memory B Cell Precursors in Mouse and Human Germinal Centers, Revealing Light-Zone Location and Predominant Low Antigen Affinity. *Immunity* **47**, 1142-1153.e4 (2017).
214. Moran, I. *et al.* Memory B cells are reactivated in subcapsular proliferative foci of lymph nodes. *Nat. Commun.* **9**, 3372 (2018).
215. Zhang, Y. *et al.* Migratory and adhesive cues controlling innate-like lymphocyte surveillance of the pathogen-exposed surface of the lymph node. *eLife* **5**, e18156 (2016).
216. Groom, J. R. *et al.* CXCR3 chemokine receptor-ligand interactions in the lymph node optimize CD4+ T helper 1 cell differentiation. *Immunity* **37**, 1091–1103 (2012).
217. Hu, S., Yang, K., Yang, J., Li, M. & Xiong, N. Critical roles of chemokine receptor CCR10 in regulating memory IgA responses in intestines. *Proc. Natl. Acad. Sci.* **108**, E1035–E1044 (2011).
218. Onodera, T. *et al.* Memory B cells in the lung participate in protective humoral immune responses to pulmonary influenza virus reinfection. *Proc. Natl. Acad. Sci.* **109**, 2485–2490 (2012).
219. Allie, S. R. *et al.* The establishment of resident memory B cells in the lung requires local antigen encounter. *Nat. Immunol.* **20**, 97–108 (2019).
220. Campbell, D. J. & Koch, M. A. Phenotypical and functional specialization of FOXP3+ regulatory T cells. *Nat. Rev. Immunol.* **11**, 119–130 (2011).
221. Sage, P. T., Francisco, L. M., Carman, C. V. & Sharpe, A. H. The receptor PD-1 controls follicular regulatory T cells in the lymph nodes and blood. *Nat. Immunol.* **14**, 152–161 (2013).
222. Zhang, R. *et al.* B Cells Drive Autoimmunity in Mice with CD28-Deficient Regulatory T Cells. *J. Immunol.* **199**, 3972–3980 (2017).
223. Sage, P. T., Alvarez, D., Godec, J., Andrian, U. H. von & Sharpe, A. H. Circulating T follicular regulatory and helper cells have memory-like properties. *J. Clin. Invest.* **124**, 5191–5204 (2014).
224. Shen, E. *et al.* Control of Germinal Center Localization and Lineage Stability of Follicular Regulatory T Cells by the Blimp1 Transcription Factor. *Cell Rep.* **29**, 1848-1861.e6 (2019).
225. Botta, D. *et al.* Dynamic regulation of T follicular regulatory cell responses by interleukin 2 during influenza infection. *Nat. Immunol.* **18**, 1249–1260 (2017).
226. Wing, J. B. *et al.* A distinct subpopulation of CD25− T-follicular regulatory cells localizes in the germinal centers. *Proc. Natl. Acad. Sci.* **114**, E6400–E6409 (2017).
227. Ritvo, P.-G. G. *et al.* Tfr cells lack IL-2Rα but express decoy IL-1R2 and IL-1Ra and suppress the IL-1–dependent activation of Tfh cells. *Sci. Immunol.* **2**, (2017).
228. Fonseca, V. R., Ribeiro, F. & Graca, L. T follicular regulatory (Tfr) cells: Dissecting the complexity of Tfr-cell compartments. *Immunol. Rev.* **288**, 112–127 (2019).
229. Wing, J. B., Lim, E. L. & Sakaguchi, S. Control of foreign Ag-specific Ab responses by Treg and Tfr. *Immunol. Rev.* **296**, 104–119 (2020).

230. Maceiras, A. R. *et al.* T follicular helper and T follicular regulatory cells have different TCR specificity. *Nat. Commun.* **8**, 15067 (2017).
231. Ritvo, P.-G. *et al.* High-resolution repertoire analysis reveals a major bystander activation of Tfh and Tfr cells. *Proc. Natl. Acad. Sci.* **115**, 9604–9609 (2018).
232. Aloulou, M. *et al.* Follicular regulatory T cells can be specific for the immunizing antigen and derive from naive T cells. *Nat. Commun.* **7**, 10579 (2016).
233. Heeger, P. S. *et al.* Revisiting Tolerance Induced by Autoantigen in Incomplete Freund's Adjuvant. *J. Immunol.* **164**, 5771–5781 (2000).
234. Korn, T. *et al.* IL-6 controls Th17 immunity in vivo by inhibiting the conversion of conventional T cells into Foxp3+ regulatory T cells. *Proc. Natl. Acad. Sci.* **105**, 18460–18465 (2008).
235. Wu, H. *et al.* Follicular regulatory T cells repress cytokine production by follicular helper T cells and optimize IgG responses in mice. *Eur. J. Immunol.* **46**, 1152–1161 (2016).
236. Xie, M. M. *et al.* T follicular regulatory cells and IL-10 promote food antigen–specific IgE. *J. Clin. Invest.* **130**, 3820–3832 (2020).
237. Clement, R. L. *et al.* Follicular regulatory T cells control humoral and allergic immunity by restraining early B cell responses. *Nat. Immunol.* **20**, 1360–1371 (2019).
238. Fu, W. *et al.* Deficiency in T follicular regulatory cells promotes autoimmunity. *J. Exp. Med.* **215**, 815–825 (2018).
239. Vaeth, M. *et al.* Follicular regulatory T cells control humoral autoimmunity via NFAT2-regulated CXCR5 expression. *J. Exp. Med.* **211**, 545–561 (2014).
240. Xie, M. M. *et al.* Roles of T follicular helper cells and T follicular regulatory cells in Autoantibody Production in IL-2-deficient mice. *ImmunoHorizons* **3**, 306–316 (2019).
241. Sage, P. T., Paterson, A. M., Lovitch, S. B. & Sharpe, A. H. The Coinhibitory Receptor CTLA-4 Controls B Cell Responses by Modulating T Follicular Helper, T Follicular Regulatory, and T Regulatory Cells. *Immunity* **41**, 1026–1039 (2014).
242. Wing, J. B., Ise, W., Kurosaki, T. & Sakaguchi, S. Regulatory T Cells Control Antigen-Specific Expansion of Tfh Cell Number and Humoral Immune Responses via the Coreceptor CTLA-4. *Immunity* **41**, 1013–1025 (2014).
243. Vanderleyden, I. *et al.* Follicular regulatory T cells can access the germinal centre independently of CXCR5. *bioRxiv* 641589 (2019) doi:10.1101/641589.
244. Lim, H. W., Hillsamer, P., Banham, A. H. & Kim, C. H. Cutting Edge: Direct Suppression of B Cells by CD4+CD25+ Regulatory T Cells. *J. Immunol.* **175**, 4180–4183 (2005).
245. Varona, R. *et al.* Molecular cloning, functional characterization and mRNA expression analysis of the murine chemokine receptor CCR6 and its specific ligand MIP-3α 1. *FEBS Lett.* **440**, 188–194 (1998).
246. Fontenot, J. D. *et al.* Regulatory T Cell Lineage Specification by the Forkhead Transcription Factor Foxp3. *Immunity* **22**, 329–341 (2005).
247. Kim, J. M., Rasmussen, J. P. & Rudensky, A. Y. Regulatory T cells prevent catastrophic autoimmunity throughout the lifespan of mice. *Nat. Immunol.* **8**, 191–197 (2007).

248. Czar, M. J. *et al.* Altered lymphocyte responses and cytokine production in mice deficient in the X-linked lymphoproliferative disease gene SH2D1A/DSHP/SAP. *Proc. Natl. Acad. Sci.* **98**, 7449–7454 (2001).
249. Mombaerts, P. *et al.* RAG-1-deficient mice have no mature B and T lymphocytes. *Cell* **68**, 869–877 (1992).
250. Frazer, I. H. *et al.* Tolerance or Immunity to a Tumor Antigen Expressed in Somatic Cells Can Be Determined by Systemic Proinflammatory Signals at the Time of First Antigen Exposure. *J. Immunol.* **167**, 6180–6187 (2001).
251. Shevchenko, A., Tomas, H., Havli, J., Olsen, J. V. & Mann, M. In-gel digestion for mass spectrometric characterization of proteins and proteomes. *Nat. Protoc.* **1**, 2856–2860 (2006).
252. Peterson, A. C., Russell, J. D., Bailey, D. J., Westphall, M. S. & Coon, J. J. Parallel Reaction Monitoring for High Resolution and High Mass Accuracy Quantitative, Targeted Proteomics. *Mol. Cell. Proteomics MCP* **11**, 1475–1488 (2012).
253. Weber, M. & Sixt, M. Live Cell Imaging of Chemotactic Dendritic Cell Migration in Explanted Mouse Ear Preparations. in *Chemokines: Methods and Protocols* (eds. Cardona, A. E. & Ubogu, E. E.) 215–226 (Humana Press, 2013). doi:10.1007/978-1-62703-426-5_14.
254. Reth, M. G., Ammirati, P., Jackson, S. & Alt, F. W. Regulated progression of a cultured pre-B-cell line to the B-cell stage. *Nature* **317**, 353–355 (1985).
255. Kohler, R. E., Caon, A. C., Willenborg, D. O., Clark-Lewis, I. & McColl, S. R. A Role for Macrophage Inflammatory Protein-3α/CC Chemokine Ligand 20 in Immune Priming During T Cell-Mediated Inflammation of the Central Nervous System. *J. Immunol.* **170**, 6298–6306 (2003).
256. Avraham, T. *et al.* Radiation therapy causes loss of dermal lymphatic vessels and interferes with lymphatic function by TGF-β1-mediated tissue fibrosis. *Am. J. Physiol.-Cell Physiol.* **299**, C589–C605 (2010).
257. Iolyeva, M. *et al.* Interleukin-7 is produced by afferent lymphatic vessels and supports lymphatic drainage. *Blood* **122**, 2271–2281 (2013).
258. Malhotra, D. *et al.* Transcriptional profiling of stroma from inflamed and resting lymph nodes defines immunological hallmarks. *Nat. Immunol.* **13**, 499–510 (2012).
259. Miano, J. M. & Olson, E. N. Expression of the Smooth Muscle Cell Calponin Gene Marks the Early Cardiac and Smooth Muscle Cell Lineages during Mouse Embryogenesis (∗). *J. Biol. Chem.* **271**, 7095–7103 (1996).
260. Merad, M. *et al.* Langerhans cells renew in the skin throughout life under steady-state conditions. *Nat. Immunol.* **3**, 1135–1141 (2002).
261. Nagao, K. *et al.* Stress-induced production of chemokines by hair follicles regulates the trafficking of dendritic cells in skin. *Nat. Immunol.* **13**, 744–752 (2012).
262. Janson, D. G., Saintigny, G., Adrichem, A. van, Mahé, C. & Ghalbzouri, A. E. Different Gene Expression Patterns in Human Papillary and Reticular Fibroblasts. *J. Invest. Dermatol.* **132**, 2565–2572 (2012).
263. Driskell, R. R. *et al.* Distinct fibroblast lineages determine dermal architecture in skin development and repair. *Nature* **504**, 277–281 (2013).

264. Proost, P. *et al.* Processing by CD26/dipeptidyl-peptidase IV reduces the chemotactic and anti-HIV-1 activity of stromal-cell-derived factor-1α. *FEBS Lett.* **432**, 73–76 (1998).
265. Comerford, I. & Nibbs, R. J. B. Post-translational control of chemokines: a role for decoy receptors? *Immunol. Lett.* **96**, 163–174 (2005).
266. Takatsuka, S., Sekiguchi, A., Tokunaga, M., Fujimoto, A. & Chiba, J. Generation of a panel of monoclonal antibodies against atypical chemokine receptor CCX-CKR by DNA immunization. *J. Pharmacol. Toxicol. Methods* **63**, 250–257 (2011).
267. Ziegler, E. *et al.* CCL19-IgG Prevents Allograft Rejection by Impairment of Immune Cell Trafficking. *J. Am. Soc. Nephrol.* **17**, 2521–2532 (2006).
268. Yan, A., Avraham, T., Zampell, J. C., Aschen, S. Z. & Mehrara, B. J. Mechanisms of Lymphatic Regeneration after Tissue Transfer. *PLOS ONE* **6**, e17201 (2011).
269. Yamazaki, T. *et al.* CCR6 Regulates the Migration of Inflammatory and Regulatory T Cells. *J. Immunol.* **181**, 8391–8401 (2008).
270. Villares, R. *et al.* CCR6 regulates EAE pathogenesis by controlling regulatory CD4+ T-cell recruitment to target tissues. *Eur. J. Immunol.* **39**, 1671–1681 (2009).
271. Yadav, M. *et al.* Neuropilin-1 distinguishes natural and inducible regulatory T cells among regulatory T cell subsets in vivo. *J. Exp. Med.* **209**, 1713–1722 (2012).
272. Weiss, J. M. *et al.* Neuropilin 1 is expressed on thymus-derived natural regulatory T cells, but not mucosa-generated induced Foxp3+ T reg cells. *J. Exp. Med.* **209**, 1723–1742 (2012).
273. Chowdhury, A. *et al.* Decreased T Follicular Regulatory Cell/T Follicular Helper Cell (TFH) in Simian Immunodeficiency Virus–Infected Rhesus Macaques May Contribute to Accumulation of TFH in Chronic Infection. *J. Immunol.* **195**, 3237–3247 (2015).
274. Meissner, A. *et al.* CC chemokine ligand 20 partially controls adhesion of naive B cells to activated endothelial cells under shear stress. *Blood* **102**, 2724–2727 (2003).
275. Mabuchi, T. *et al.* CCR6 is required for epidermal trafficking of γδ-T cells in an IL-23-induced model of psoriasiform dermatitis. *J. Invest. Dermatol.* **133**, 164–171 (2013).
276. Cheng, H.-W. *et al.* Origin and differentiation trajectories of fibroblastic reticular cells in the splenic white pulp. *Nat. Commun.* **10**, 1739 (2019).
277. Nonaka, M. *et al.* Synthetic di-sulfated iduronic acid attenuates asthmatic response by blocking T-cell recruitment to inflammatory sites. *Proc. Natl. Acad. Sci.* **111**, 8173–8178 (2014).
278. Paradis, M. *et al.* A TNF-α–CCL20–CCR6 Axis Regulates Nod1-Induced B Cell Responses. *J. Immunol.* **192**, 2787–2799 (2014).
279. Bunting, M. D., Comerford, I., Kara, E. E., Korner, H. & McColl, S. R. CCR6 supports migration and differentiation of a subset of DN1 early thymocyte progenitors but is not required for thymic nTreg development. *Immunol. Cell Biol.* **92**, 489–498 (2014).
280. Kitamura, K., Farber, J. M. & Kelsall, B. L. CCR6 Marks Regulatory T Cells as a Colon-Tropic, IL-10–Producing Phenotype. *J. Immunol.* **185**, 3295–3304 (2010).
281. Crotty, S., Kersh, E. N., Cannons, J., Schwartzberg, P. L. & Ahmed, R. SAP is required for generating long-term humoral immunity. *Nature* **421**, 282–287 (2003).

282. Cannons, J. L. *et al.* SAP regulates T cell–mediated help for humoral immunity by a mechanism distinct from cytokine regulation. *J. Exp. Med.* **203**, 1551–1565 (2006).
283. Herzenberg, L., Black, S., Tokuhisa, T. & Herzenberg, L. Memory B cells at successive stages of differentiation. Affinity maturation and the role of IgD receptors. *J. Exp. Med.* **151**, 1071–1087 (1980).
284. Tripp, C. H. *et al.* The lymph vessel network in mouse skin visualised with antibodies against the hyaluronan receptor LYVE-1. *Immunobiology* **213**, 715–728 (2008).
285. Banas, B. *et al.* Roles of SLC/CCL21 and CCR7 in Human Kidney for Mesangial Proliferation, Migration, Apoptosis, and Tissue Homeostasis. *J. Immunol.* **168**, 4301–4307 (2002).
286. Khoja, H. *et al.* Cloning of CCRL1, an orphan seven transmembrane receptor related to chemokine receptors, expressed abundantly in the heart. *Gene* **246**, 229–238 (2000).
287. Wurbel, M.-A. *et al.* The chemokine TECK is expressed by thymic and intestinal epithelial cells and attracts double- and single-positive thymocytes expressing the TECK receptor CCR9. *Eur. J. Immunol.* **30**, 262–271 (2000).
288. Cook, D. N. *et al.* CCR6 Mediates Dendritic Cell Localization, Lymphocyte Homeostasis, and Immune Responses in Mucosal Tissue. *Immunity* **12**, 495–503 (2000).
289. Le Borgne, M. *et al.* Dendritic Cells Rapidly Recruited into Epithelial Tissues via CCR6/CCL20 Are Responsible for CD8+ T Cell Crosspriming In Vivo. *Immunity* **24**, 191–201 (2006).
290. Mine, S., Fortunel, N. O., Pageon, H. & Asselineau, D. Aging Alters Functionally Human Dermal Papillary Fibroblasts but Not Reticular Fibroblasts: A New View of Skin Morphogenesis and Aging. *PLOS ONE* **3**, e4066 (2008).
291. Chambers, E. S. & Vukmanovic-Stejic, M. Skin barrier immunity and ageing. *Immunology* **n/a**, (2019).
292. Rinkevich, Y. *et al.* Identification and isolation of a dermal lineage with intrinsic fibrogenic potential. *Science* **348**, (2015).
293. Rees, P. A., Greaves, N. S., Baguneid, M. & Bayat, A. Chemokines in Wound Healing and as Potential Therapeutic Targets for Reducing Cutaneous Scarring. *Adv. Wound Care* **4**, 687–703 (2015).
294. Indra, A. K. *et al.* Targeted Somatic Mutagenesis in Mouse Epidermis. *Horm. Res. Paediatr.* **54**, 296–300 (2000).
295. Rivers, L. E. *et al.* PDGFRA/NG2 glia generate myelinating oligodendrocytes and piriform projection neurons in adult mice. *Nat. Neurosci.* **11**, 1392–1401 (2008).
296. Hochweller, K., Striegler, J., Hämmerling, G. J. & Garbi, N. A novel CD11c.DTR transgenic mouse for depletion of dendritic cells reveals their requirement for homeostatic proliferation of natural killer cells. *Eur. J. Immunol.* **38**, 2776–2783 (2008).
297. Jørgensen, A. S., Rosenkilde, M. M. & Hjortø, G. M. Biased signaling of G protein-coupled receptors – From a chemokine receptor CCR7 perspective. *Gen. Comp. Endocrinol.* **258**, 4–14 (2018).
298. Johnson, L. A. *et al.* An inflammation-induced mechanism for leukocyte transmigration across lymphatic vessel endothelium. *J. Exp. Med.* **203**, 2763–2777 (2006).

299. Lämmermann, T. *et al.* Rapid leukocyte migration by integrin-independent flowing and squeezing. *Nature* **453**, 51–55 (2008).
300. Tomura, M. *et al.* Monitoring cellular movement in vivo with photoconvertible fluorescence protein "Kaede" transgenic mice. *Proc. Natl. Acad. Sci.* **105**, 10871–10876 (2008).
301. Tomura, M. *et al.* Activated regulatory T cells are the major T cell type emigrating from the skin during a cutaneous immune response in mice. *J. Clin. Invest.* **120**, 883–893 (2010).
302. Tomura, M. *et al.* Tracking and quantification of dendritic cell migration and antigen trafficking between the skin and lymph nodes. *Sci. Rep.* **4**, 1–11 (2014).
303. Kozai, M. *et al.* Essential role of CCL21 in establishment of central self-tolerance in T cells. *J. Exp. Med.* **214**, 1925–1935 (2017).
304. Gibson, V. B. *et al.* A novel method to allow noninvasive, longitudinal imaging of the murine immune system in vivo. *Blood* **119**, 2545–2551 (2012).
305. Bovay, E. *et al.* Multiple roles of lymphatic vessels in peripheral lymph node development. *J. Exp. Med.* **215**, 2760–2777 (2018).
306. Aoki, N. *et al.* Dysregulated Generation of Follicular Helper T Cells in the Spleen Triggers Fatal Autoimmune Hepatitis in Mice. *Gastroenterology* **140**, 1322-1333.e5 (2011).
307. Lee, A. Y. S. *et al.* Expression of Membrane-Bound CC Chemokine Ligand 20 on Follicular T Helper Cells in T-B-Cell Conjugates. *Front. Immunol.* **8**, 1871 (2017).
308. Dieu-Nosjean, M.-C. *et al.* Macrophage Inflammatory Protein 3α Is Expressed at Inflamed Epithelial Surfaces and Is the Most Potent Chemokine Known in Attracting Langerhans Cell Precursors. *J. Exp. Med.* **192**, 705–718 (2000).
309. Matsui, T. *et al.* Selective recruitment of CCR6-expressing cells by increased production of MIP-3α in rheumatoid arthritis. *Clin. Exp. Immunol.* **125**, 155–161 (2001).
310. Nakayama, T. *et al.* Inducible expression of a CC chemokine liver- and activation-regulated chemokine (LARC)/macrophage inflammatory protein (MIP)-3α/CCL20 by epidermal keratinocytes and its role in atopic dermatitis. *Int. Immunol.* **13**, 95–103 (2001).
311. Fujiie, S. *et al.* Proinflammatory cytokines induce liver and activation-regulated chemokine/macrophage inflammatory protein-3α/CCL20 in mucosal epithelial cells through NF-κB. *Int. Immunol.* **13**, 1255–1263 (2001).
312. Sugita, S. *et al.* Induction of Macrophage-Inflammatory Protein-3α Gene Expression by TNF-Dependent NF-κB Activation. *J. Immunol.* **168**, 5621–5628 (2002).
313. Eisenbarth, S. C., Colegio, O. R., O'Connor, W., Sutterwala, F. S. & Flavell, R. A. Crucial role for the Nalp3 inflammasome in the immunostimulatory properties of aluminium adjuvants. *Nature* **453**, 1122–1126 (2008).
314. Marichal, T. *et al.* DNA released from dying host cells mediates aluminum adjuvant activity. *Nat. Med.* **17**, 996–1002 (2011).
315. Rose Ii, W. A., Okragly, A. J., Patel, C. N. & Benschop, R. J. IL-33 released by alum is responsible for early cytokine production and has adjuvant properties. *Sci. Rep.* **5**, 13146 (2015).

316. Yi, T. *et al.* Splenic Dendritic Cells Survey Red Blood Cells for Missing Self-CD47 to Trigger Adaptive Immune Responses. *Immunity* **43**, 764–775 (2015).
317. Tanaka, Y. *et al.* Selective expression of liver and activation-regulated chemokine (LARC) in intestinal epithelium in mice and humans. *Eur. J. Immunol.* **29**, 633–642 (1999).
318. Iwasaki, A. & Kelsall, B. L. Localization of Distinct Peyer's Patch Dendritic Cell Subsets and Their Recruitment by Chemokines Macrophage Inflammatory Protein (Mip)-3α, Mip-3β, and Secondary Lymphoid Organ Chemokine. *J. Exp. Med.* **191**, 1381–1394 (2000).
319. Zhao, X. *et al.* CCL9 Is Secreted by the Follicle-Associated Epithelium and Recruits Dome Region Peyer's Patch CD11b+ Dendritic Cells. *J. Immunol.* **171**, 2797–2803 (2003).
320. Sierro, F. *et al.* Flagellin stimulation of intestinal epithelial cells triggers CCL20-mediated migration of dendritic cells. *Proc. Natl. Acad. Sci.* **98**, 13722–13727 (2001).
321. Choi, Y. K., Fallert, B. A., Murphey-Corb, M. A. & Reinhart, T. A. Simian immunodeficiency virus dramatically alters expression of homeostatic chemokines and dendritic cell markers during infection in vivo. *Blood* **101**, 1684–1691 (2003).
322. Elgueta, R. *et al.* CCR6-Dependent Positioning of Memory B Cells Is Essential for Their Ability To Mount a Recall Response to Antigen. *J. Immunol.* **194**, 505–513 (2015).
323. Sayin, I. *et al.* Spatial distribution and function of T follicular regulatory cells in human lymph nodes. *J. Exp. Med.* **215**, 1531–1542 (2018).
324. Wang, J., Siffert, M., Spiliotis, M. & Gottstein, B. Repeated Long-Term DT Application in the DEREG Mouse Induces a Neutralizing Anti-DT Antibody Response. *Journal of Immunology Research* vol. 2016 e1450398 https://www.hindawi.com/journals/jir/2016/1450398/ (2016).
325. Pierson, W. *et al.* Antiapoptotic Mcl-1 is critical for the survival and niche-filling capacity of Foxp3 + regulatory T cells. *Nat. Immunol.* **14**, 959–965 (2013).
326. Franckaert, D. *et al.* Promiscuous Foxp3-cre activity reveals a differential requirement for CD28 in Foxp3+ and Foxp3− T cells. *Immunol. Cell Biol.* **93**, 417–423 (2015).
327. Bittner-Eddy, P. D., Fischer, L. A. & Costalonga, M. Cre-loxP Reporter Mouse Reveals Stochastic Activity of the Foxp3 Promoter. *Front. Immunol.* **10**, (2019).
328. Schönhuber, N. *et al.* A next-generation dual-recombinase system for time and host specific targeting of pancreatic cancer. *Nat. Med.* **20**, 1340–1347 (2014).
329. Hermann, M. *et al.* Binary recombinase systems for high-resolution conditional mutagenesis. *Nucleic Acids Res.* **42**, 3894–3907 (2014).
330. Weinberg, B. H. *et al.* Large-scale design of robust genetic circuits with multiple inputs and outputs for mammalian cells. *Nat. Biotechnol.* **35**, 453–462 (2017).
331. Mastelic-Gavillet, B. *et al.* Neonatal T Follicular Helper Cells Are Lodged in a Pre-T Follicular Helper Stage Favoring Innate Over Adaptive Germinal Center Responses. *Front. Immunol.* **10**, (2019).
332. Lee, J. H., Kang, S. G. & Kim, C. H. FoxP3+ T Cells Undergo Conventional First Switch to Lymphoid Tissue Homing Receptors in Thymus but Accelerated Second

Switch to Nonlymphoid Tissue Homing Receptors in Secondary Lymphoid Tissues. *J. Immunol.* **178**, 301–311 (2007).

333. Zhang, N. *et al.* Regulatory T Cells Sequentially Migrate from Inflamed Tissues to Draining Lymph Nodes to Suppress the Alloimmune Response. *Immunity* **30**, 458–469 (2009).
334. Kara, E. E. *et al.* CCR2 defines in vivo development and homing of IL-23-driven GM-CSF-producing Th17 cells. *Nat. Commun.* **6**, 8644 (2015).
335. Loyher, P.-L. *et al.* CCR2 Influences T Regulatory Cell Migration to Tumors and Serves as a Biomarker of Cyclophosphamide Sensitivity. *Cancer Res.* **76**, 6483–6494 (2016).
336. Zhan, Y. *et al.* CCR2 enhances CD25 expression by FoxP3 + regulatory T cells and regulates their abundance independently of chemotaxis and CCR2 + myeloid cells. *Cell. Mol. Immunol.* **17**, 123–132 (2020).
337. Ballesteros-Tato, A. *et al.* Interleukin-2 Inhibits Germinal Center Formation by Limiting T Follicular Helper Cell Differentiation. *Immunity* **36**, 847–856 (2012).
338. Iellem, A. *et al.* Unique Chemotactic Response Profile and Specific Expression of Chemokine Receptors Ccr4 and Ccr8 by Cd4+Cd25+ Regulatory T Cells. *J. Exp. Med.* **194**, 847–854 (2001).
339. Rapp, M. *et al.* CCL22 controls immunity by promoting regulatory T cell communication with dendritic cells in lymph nodes. *J. Exp. Med.* **216**, 1170–1181 (2019).
340. Liu, B. *et al.* Affinity-coupled CCL22 promotes positive selection in germinal centres. *Nature* **592**, 133–137 (2021).
341. Iyer, S. S. *et al.* Codelivery of Envelope Protein in Alum with MVA Vaccine Induces CXCR3-Biased CXCR5+ and CXCR5- CD4 T Cell Responses in Rhesus Macaques. *J. Immunol. Baltim. Md 1950* **195**, 994–1005 (2015).
342. Velu, V. *et al.* Induction of Th1-Biased T Follicular Helper (Tfh) Cells in Lymphoid Tissues during Chronic Simian Immunodeficiency Virus Infection Defines Functionally Distinct Germinal Center Tfh Cells. *J. Immunol.* **197**, 1832–1842 (2016).
343. Kurachi, M. *et al.* Chemokine receptor CXCR3 facilitates CD8+ T cell differentiation into short-lived effector cells leading to memory degeneration. *J. Exp. Med.* **208**, 1605–1620 (2011).